Large amplitude quantum mechanics in polyatomic hydrides and multistate electronic potential energy surfaces of highly electronegative F + HX reactive systems

by

Michael Deskevich

B.S., Juniata College, 2000

A thesis submitted to the

Faculty of the Graduate School of the

University of Colorado in partial fulfillment

Of the requirement for the degree of

Doctor of Philosophy

Chemical Physics

2007

This thesis entitled:
Large amplitude quantum mechanics in polyatomic hydrides and multistate electronic potential energy surfaces of highly electronegative reactive F + HX systems
written by Michael Deskevich
has been approved for the Department of Chemistry and Biochemistry

_____
Dr. David J. Nesbitt

_____
Dr. Robert P. Parson

Date_____

The final copy of this thesis has been examined by the signatories, and we find that both the content and the form meet acceptable presentation standards of scholarly work in the above mentioned discipline.

Deskevich, Michael P. (Ph.D., Chemical Physics)

Large amplitude quantum mechanics in polyatomic hydrides and multistate electronic potential energy surfaces of highly electronegative reactive F + HX systems

Thesis directed by Professor David J. Nesbitt

In this work two different areas of study are discussed. First, a novel model is presented for the quantum mechanics of large amplitude motion in floppy hydrides. A framework is developed for converged quantum mechanical calculations on large amplitude dynamics in polyatomic hydrides (XH_n) based on a relatively simple, but computationally tractable, "particles-on-a-sphere" (POS) model for the intramolecular motion of the light atoms. The model assumes independent 2D angular motion of H atoms imbedded on the surface of a sphere with an arbitrary interatomic angular potential, which permits systematic evolution from "free rotor" to "tunneling" to "quasi-rigid" polyatomic molecule behavior for small but finite values of total angular momentum J. Simple tri- and tetra- atom hydrides act as a test suite for the POS model. After successfully modeling these systems, the model is used on systems with 4 and 5 hydrogens surrounding a central heavy atom, with the final focus on the theoretically and experimentally challenging CH_5^+ molecule.

Next, novel methods are introduced for computing multistate potential energy surfaces for the abstraction of hydrogen by fluorine in two different experimentally important systems: $F(^2P) + HCl \rightarrow HF + Cl(^2P)$ and $F(^2P) + H_2O \rightarrow HF + OH(^2\Sigma)$. A novel method of dynamically adjusted weighting factors in state-averaged multiconfigurational self-consistent field calculations (SA-MCSCF) is developed and

tested on the $F(^2P) + H_2O \rightarrow HF + OH\ (^2\Pi)$ reaction. Using the DW-MCSCF approach a new multistate electronic potential energy surface for the $F(^2P) + HCl \rightarrow HF + Cl(^2P)$ reaction is calculated in full dimensionality. The thesis concludes with nonadiabatic quantum nuclear dynamics calculations for the $F(^2P) + HCl \rightarrow HF + Cl(^2P)$ reaction.

Acknowledgments

I would like to acknowledge several people who provided valuable guidance and support for the work in this dissertation. First and foremost, I would like to thank my advisor David Nesbitt, whose rigorous standards for excellence in science have shaped me into a critical observer of all that I encounter. I also wish to thank my collaborators, including Robert Parson, Anne McCoy, Hans-Joachim Werner, and Millard Alexander, and all of the members of the Nesbitt lab. I am grateful to have had the opportunity to work with such intelligent people.

Contents

List of tables

Chapter 2

Chapter 3

Chapter 4

Chapter 5

List of figures:

Chapter 2

geometry. As shown in the inset, the first hydrogen is defined to be at ($\theta = 0$, $\phi = 0$), with the |amplitude|^2 for the second hydrogen plotted for ($\theta = \gamma$, ϕ).

Figure 2.5. $E_{J=0}$ energy level correlation as a function of intermolecular stiffness for XH_3, plotted for the first few energies of the umbrella mode. At small χ, the levels correspond to three independent rigid HX rotors (displayed with greater detail in the inset) but eventually correlate with inversion doubled tunneling splittings in the limit of large χ.

Figure 2.6. $E_{v=0}$ energy level correlation for XH_3 J = 0, 1, 2 as function of intermolecular stiffness, χ. For small χ, the pattern reflects three freely rotating hydrogens, which for large χ smoothly transitions into the rotational energy pattern characteristic of an oblate symmetric top.

Figure 2.7. 2D cuts (in θ, ϕ space) through full 6D XH_3 wave functions for (i) symmetric ground state (left hand side) and (ii) the antisymmetric first excited state (right hand side) of the umbrella mode for increasing values of χ. The contour plot (center bottom) displays the corresponding potential. At χ = 6, 60 and 600, the contour spacings are 1.5 cm^{-1}, 15 cm^{-1}, and 150 cm^{-1}, respectively. As shown in the inset, the first and second hydrogens are fixed at ($\theta = 0$, $\phi = 0$) and ($\theta = \gamma_0$, $\phi = 0$), with amplitude for the third hydrogen plotted as a function of (θ , ϕ).

Figure 2.8. The log of the fractional error (base 10) as a function of j_{max} for several values of stiffness χ. Larger χ converges more slowly as the basis set is optimized for floppy intermolecular potentials. For a given χ, it is worth noting that the n = 2 and n = 3 calculations converge almost at the same rate, which bodes favorably for scaling to a larger number of H atoms.

Chapter 3

Figure 3.1. Particle-on-a-sphere rotation-bending energies for a) n = 2 (XH_2) and b) n = 3 (XH_3) model systems as a function of basis set size (j_{max}). a) In XH_2, the asymmetric top rotational patterns for J = 0,1 corresponding to $J_{KaKc} = 0_{00}$, 1_{01}, 1_{11}, 1_{10} are clearly evident, with the J = 0 energy rapidly converging to the expected DMC limit (dotted line). b) Converged J = 0 energy levels for XH_3 reveal inversion tunneling splittings in good agreement with NH_3 (after which the potential was modeled) and increasing rapidly with symmetric bend excitation. Note the only exception to this pattern (near 5000 cm^{-1}), arising from an interloper vibrational state due to degenerate asymmetric bend excitation, which exhibits a tunneling splitting very similar to the ground state (0.798 cm^{-1}).

Figure 3.2. Angular pair correlation functions for a) XH_2 and b) XH_3 as a function of potential stiffness χ = k/b, where k is the angular well depth and b is the rotational constant for a single X - H rotor. For comparison, the shaded function is calculated from DMC, whereas the dots reflect the fully converged J = 0 POS calculation.

and c) the pairwise additive least squares fit. Note the excellent agreement at the wave function level.

Figure 3.9. Ground-state energies of CH_5^+ as a function of the potential stiffness parameter (α), calculated by DMC and POS with both the 10D (DMC, open squares) and pairwise (POS, dashed line) potentials. The inset shows the difference between the POS and DMC (pairwise) calculations (i.e., the level of convergence) as a function of α.

Figure 3.10. Nonzero statistical symmetries for J = 0, 1, and 2 of XH_5 (with a = .033) as a function of basis set size, j_{max} and $N_{coupled}$ (the number of coupled basis functions in the basis set). Note the slow but steady convergence of J = 0 energies to the RBDMC limit with the size of $N_{coupled}$.

Figure 3.11. The lowest J = 0 internal rotor energies (with respect to the ground state energy, G_2^- Symmetry) of the POS model compared with the RTRF-like model of Bunker and coworkers. Interestingly, the splittings for the two model treatments are roughly the same order of magnitude, despite the stiffness of the potentials varying by a large factor.

Figure 3.12. DMC pair correlation function of CH_5^+ as a function of potential stiffness scale (α).

Chapter 4

β. If β^{-1} is too small, small changes in energies in excited states can cause discontinuities in the ground state (e.g. point P), if β^{-1} is too large, the weights do not decay to 0 in the asymptotes for the excited states. Moderate β^{-1} parameters (*i.e.*,2 - 3eV) produce smooth curves and converge to ground-state-only asymptotes.

Figure 4.5: The lowest 4 states of the smooth DW-MCSCF reaction path. The energies along the reaction path not only vary smoothly, but the degeneracies are correctly reproduced in the asymptotes. Also note that there are a number of states interacting in the transition state region.

Figure 4.6: Converged weights (normalized to sum to 1) for the DW-MCSCF with β^{-1} = 3. The energies along the reaction path are reproduced at the top to help guide the eye. The weights smoothly vary from $(\frac{1}{3}:\frac{1}{3}:\frac{1}{3})$ to approximately $(\frac{1}{2}:\frac{1}{2}:0)$. During the cross-over through the transition state a fourth and fifth state are briefly introduced. DW-MCSCF automatically included the relevant states in the different regions of the PES.

Figure 4.7: MRCI+Q with spin-orbit interactions calculated at the CASSCF reaction path geometries. The smoothly varying DW-MCSCF wave functions are used as reference configurations for MRCI+Q calculations. Note that the lowest barrier (when zero-point energy is included) is experimentally accessible in crossed supersonic jets, but the other barriers are far out of reach.

Chapter 5

θ decreases below ~120°, both the HCl bond length and barrier height increase dramatically from transition state values, characteristic of a shift from an "early" to "late" transition state. b) Trajectory analysis for F-HCl angular deflection (Δθ) as a function of initial bend angle, θ. For J = 0, only a very narrow range (dark grey) of incident scattering angles are successfully "prerotated" (light grey) into the appropriately bent transition state angle to react.

Chapter 6

Figure 6.1: Three lowest adiabats along the reaction path for the F(^{2}P) + HCl → HF + Cl(^{2}P) system, obtained by high-level DW-MCSCF, MRCI+Q and CBS methods. The lowest two correlate with ground state F and Cl, while the highest one correlates asymptotically with spin-orbit excited F* and Cl* species. In the adiabatic limit, only the lowest spin-orbit ground state can react over a barrier accessible at experimental collision energies.

Figure 6.2: 2D slices through two full 3D A' adiabats. a) The region near the conical intersection seam (solid black line) at θ=180°, which by symmetry becomes b) an avoided crossing for any non-collinear geometry (θ=170°).

Figure 6.3: A 1D angular cut through full 3D adiabatic and diabatic surfaces in the exit channel, with R_{HF}=Req and R_{HCl}=6.6 a0. The adiabats and diabats are asymptotically equal at collinear geometries, but strongly avoid as the symmetry is lowered from $C_{\infty v}$.

Figure 6.4: Adiabats (dashed lines) and diabats (solid lines) calculated along the reaction path a) in full 3D and b) with θ constrained at 180^o. In full 3D the adiabats avoid where the diabats cross, whereas for a collinear geometry the adiabats and diabats overlap perfectly at each point along the conical intersection seam due to zero coupling.

Figure 6.5: A 2D R_{HF}, R_{HCl} contour plot for the ground state adiabatic surface at both a) transition state ($\theta=123^o$) and b) collinear ($\theta=180^o$) geometries. In b) the conical intersection seams are shown with dashed lines. Contour spacing is 3 kcal/mol with respect to zero at reactant entrance channel.

Figure 6.6: Grid of distributed Gaussian locations used to fit the β coupling surface. Angular dependence is fitted at each point (R_{HF}, R_{HCl}) by a linear combination of sin(nθ) functions.

Figure 6.7: 2D contours (at $\theta=123^o$) for the a) V_{Σ}, b) $V_{\Pi x}$, and c) $V_{\Pi y}$ diabats with 3 kcal/mol spacing. A sample histogram of residuals for fitting the V_{Σ} function is also shown in a). The values are not distributed normally, which is why the RMS (0.34 kcal/mol) is considerably larger than the FWHM (0.049 kcal/mol).

Figure 6.8: Sample 2D slices through the full 3D β coupling surface between V_{Σ} and $V_{\Pi x}$ diabats at a) $\theta=180^{o}$, b) $\theta=150^{o}$, and c) $\theta=120^{o}$. Note that for collinear geometry, β vanishes identically but grows rapidly as the molecule becomes bent.

Figure 6.9: V_{Σ} and $V_{\Pi x}$ diabats along the reaction path (scale to left), and the β coupling between the diabats (scale to right). Note the strong peaking of diabatic coupling immediately in the *post* transition state region, due to rapid change in electronic character for the newly formed bond.

Figure 6.10: Sample results starting at the transition state (p=0 au, Δp=2 au) for multistate 1D wavepacket propagation along the F + HCl $\rightarrow$ HF + Cl reaction coordinate. The top panel displays adiabatic energies, the middle panels reveal snapshots of $|\Psi|^2$ out to 100 fs, and the bottom panel accounts for the total flux that passed by each point on each surface.

Figure 6.11: Reaction dynamics for ground F and spin-orbit excited F* as a function of energy. a) Reaction probability of F and F* along the reaction path (solid lines), with dotted lines representing probability if non-adiabatic coupling is set to 0. b) Reaction probability of F and F* along a 2D reaction path with θ constrained to be 180^{o}. The dramatically increased reactivity of F* vs F results from the presence of conical intersection seams sampled at collinear geometries.

Chapter 1: Introduction

In the field of theoretical chemical physics, the main focus of research generally falls along one of two paths: 1) the exact study of the very small or 2) the ensemble study of the very large. In the former, the systems are small enough (fewer than 3 particles) that the mathematics allow one to reach exact results. In the large systems (greater than 50 - 100 particles), there are generally enough degrees of freedom that measurements of the bulk can accurately be described by statistical averages where the exact details of each particle are not relevant. These two branches of study leave behind a middle ground of systems that are too big to study exactly, yet are too small to be treated statically. The key to studying these middle-of-the-road systems is to find the correct approximations that capture most of the chemistry and physics, while still being computationally tractable and providing the correct simple physical picture. In this work two different areas of study are presented, both of which fall into this middle ground. First, I present a model for the quantum mechanics of a floppy 6-atom system (CH_5^+) which aims to capture the low-energy dynamics of a system with a large number of large-amplitude degrees of freedom. Then I will introduce novel methods for computing multistate potential energy surfaces for the abstraction of hydrogen by fluorine in two different experimentally important systems: $F(^2P)+HCl \rightarrow HF + Cl(^2P)$ and $F(^2P)+H_2O \rightarrow HF + OH(^2\Sigma)$.

For the CH_5^+ problem, I start by a developing framework for converged quantum mechanical calculations on large amplitude dynamics in polyatomic hydrides (XH_n) based on a relatively simple, but computationally tractable, "particles-on-a-sphere" (POS) model for the intramolecular motion of the light atoms. The

model assumes independent 2D angular motion of H atoms imbedded on the surface of a sphere with an arbitrary interatomic angular potential, which permits systematic evolution from “free rotor” to “tunneling” to “quasi-rigid” polyatomic molecule behavior for small but finite values of total angular momentum J. Chapter 2 focuses on simple triatom (n = 2) and tetratom (n = 3) systems as a function of interatomic potential stiffness, with explicit consideration of H_2O, NH_3, and H_3O^+ as limiting test cases. The POS model also establishes the necessary mathematical groundwork for calculations on dynamically much more challenging XH_n species with n > 3 (e.g., models of CH_5^+), where such a reduced dimensionality approach offers prospects for being quantum mechanically tractable at low J values (i.e., J = 0, 1, 2) characteristic of supersonic jet expansion conditions.

In Chapter 3, the POS framework focuses on systems with many degrees of freedom (i.e., n = 4 and 5). The goal is to probe and elucidate the large amplitude dynamics in low J states (i.e., J = 0, 1, and 2) that will dominate high resolution spectra of such hydrides (e.g., CH_4, CH_5^+) obtained under supersonic jet-cooled conditions. Comparison with experimental data as well as Diffusion Quantum Monte Carlo methods show how this simple reduced-dimensionality model provides potential insight into multidimensional quantum rovibrational dynamics.

Switching gears from quantum dynamics of nuclei to the creation of potential energy surfaces (on which quantum dynamics of nuclei can be modeled), Chapter 4 discusses a novel method of dynamically adjusted weighting factors in state-averaged multiconfigurational self-consistent field calculations (SA-MCSCF) which is applicable to systems of arbitrary dimensionality. The proposed dynamically

weighted approach automatically weights the relevant electronic states in each region of the potential energy surface, smoothly adjusting between these regions with an energy-dependent functional. This method is tested on the $F(^2P) + H_2O \rightarrow HF + OH$ ($^2\Pi$) reaction, which otherwise proves challenging to describe with traditional SA-MCSCF methods due to i) different asymptotic degeneracies of reactant (3-fold) and product (2-fold) channels, and ii) presence of low lying charge transfer configurations near the transition state region. The smoothly varying wave functions obtained by dynamically weighted multiconfigurational self-consistent field (DW-MCSCF) methods represent excellent reference states for high-level multireference configuration interaction (MRCI) calculations and offer an ideal starting point for construction of multiple state potential energy surfaces.

The F + H2O system is still too large to study in full dimensionality, however, the novel DW-MCSCF approach allows one to accurately study smaller reactive systems. Using this approach, Chapter 5 presents a new ground state ($1^2A'$) electronic potential energy surface for the $F(^2P) + HCl \rightarrow HF + Cl(^2P)$ reaction. The *ab inito* calculations are done at the MRCI+Q/CBS level of theory by extrapolation of the MRCI+Q/aug-cc-pVnZ (n = 2,3,4) energies. Due to low-lying charge transfer states in the transition state region, the molecular orbitals are obtained by 6-state DW-MCSCF methods. Additional perturbative refinement of the energies is achieved by implementing simple one-parameter correlation energy scaling to reproduce the experimental exothermicity (ΔE = -33.06 kcal/mol) for the reaction. *Ab initio* points are fit to an analytical function based on sum of 2- and 3-body contributions, yielding an RMS deviation of < 0.3 kcal/mol for all geometries below 10 kcal/mol above the

barrier. Of particular relevance to non-adiabatic dynamics, the MCSCF-MRCI calculations show significant multireference character in the transition state region, which is located 3.8 kcal/mol with respect to F + HCl reactants and features a strongly bent F-H-Cl transition state geometry (123.5^{o}). Finally, the surface also exhibits two conical intersection seams that are energetically accessible at low collision energies. These seams arise naturally from allowed crossings in the $C_{\infty v}$ linear configuration that become avoided in C_s bent configurations of both the reactant and product and should be characteristic of all X-H-Y atom transfer reaction dynamics between (^{2}P) halogen atoms.

Finally, in Chapter 6, the DW-MCSCF approach is used in creating a multi electronic state PES for the F(^{2}P) + HCl → HF + Cl(^{2}P) reaction. This chapter presents benchmark *ab initio* combined calculations and analytical fits for the lowest three adiabatic (1^2A',2^2A',1^2A"), diabatic ($1^2\Sigma$, $1^2\Pi_x$, $1^2\Pi_y$) and spin-orbit corrected potential energy surfaces associated with the fundamental F(^{2}P) + HCl → HF + Cl(^{2}P) reaction. These surfaces are based on high-level MOLPRO multireference configuration interaction (MRCI) calculations performed at the complete basis set (CBS) level by extrapolation of MRCI+Q/aug-cc-pVnZ (n = 2,3,4) energies as a function of R_{HF}, R_{HCl}, and θ_{FHCl} . Molecular orbitals for the MRCI calculations are obtained by 6-state dynamically weighted MCSCF (DW-MCSCF) methods, necessitated by the presence of low-lying (F^- + HCl^+ and HF^+ + Cl^-) charge transfer states in the transition state region. Additional perturbative refinement of the adiabatic potentials is achieved by implementing correlation energy scaling methods to reproduce the experimental exothermicity. Adiabatic surfaces are transformed into a

smooth diabatic representation by explicit maximization of orbital overlap with respect to limiting θ_{FHCl} . = 0^o and 180^o configurations, which reveals seams of conical intersections in both entrance and exit channels and which is energetically accessible at typical reactive collision energies. The resulting diabatic and non-adiabatic coupling surfaces are analytically least-squares fitted with 2- and 3-body terms, with further inclusion of the Breit-Pauli matrix operator yielding spin-orbit splittings in good agreement with experiment. By way of test application, wavepacket calculations along the reaction path for the set of 3D multiple surfaces are used to predict the role of non-adiabatic surface hopping probabilities for reaction of $F(^2P_{3/2, 1/2})$ + HCl to form $Cl(^2P_{3/2, 1/2})$ + HF.

Chapter 2: Large amplitude quantum mechanics in polyatomic hydrides: I. A particles-on-a-sphere model for XH_n

I. Introduction

The quantum mechanics of large amplitude motion have become an increasing focus of experimental and theoretical attention, fueled in part by impressive advances in high-resolution rotational/vibrational spectroscopy of tunneling dynamics in molecules, ions, and hydrogen bonded clusters. Classic paradigms in the field of large amplitude quantum dynamics have been systems such as tunneling inversion in ammonia[1-8] (NH_3) and hydronium ion[9-16] (H_3O^+), as well as numerous demonstrations of large amplitude tunneling phenomena in van der Waals clusters.[17-20] In favorably small n-atom systems, the dynamics can be treated at the level of *exact* quantum calculations for nuclear motion in full (i.e., 3n-6) dimensionality. This has been elegantly demonstrated, for example, in studies of HF and HCl dimers,[21-24] which have permitted converged variational calculations in all inter- (4D) and intramolecular (2D) coordinates, as well reduced dimensionality extensions to H_2O dimer[25-28] (6D intermolecular coordinates with semirigid monomers) for which multiple H atom tunneling pathways of the rigid H_2O monomers are clearly evident. The level of quantitative success in such benchmark hydrogen-bonded clusters is extremely encouraging and bodes well for understanding tunneling dynamics in even more complicated polyatomic systems.

However, as these large amplitude molecular systems increase in size and complexity, they quickly become prohibitive to treat by standard quantum calculation methods. This is unfortunate, as some of the most interesting dynamical processes begin to be possible in these larger systems. Examples include the proposed concerted "race track" tunneling motion of the 3 H atoms around protonated acetylene[29] ($C_2H_3^+$), and, as an even more longstanding spectroscopic challenge, facile intramolecular H atom exchange in protonated methane.[30, 31] Furthermore, this level of theoretical difficulty increases rapidly with J, which makes the interpretation of rotational patterns especially challenging under all but the lowest temperature conditions. In such cases, a more realistic first spectroscopic goal is to learn how to predict and interpret the experimentally observed energy level patterns and thereby infer new insights about the actual intermolecular dynamics.

As background motivation for the present theoretical study, protonated methane (CH_5^+) represents an extreme case of large amplitude quantum dynamics with a rich scientific history. Adding a single proton to the well-studied methane, CH_4, creates a highly fluxional molecule where simple Lewis octet-bonding motifs do not apply, resulting in 5 H atoms connected by 4 electron pairs and requiring the presence of "three-center-two-electron" bonds (3c-2e).[32] Such 3c-2e bonding motifs correspond to a special class of hypercoordinated carbocations, extremely important reactive intermediates in acid-catalyzed electrophilic reactions,[33, 34] for which CH_5^+ represents the simplest prototypic "superacid." CH_5^+ is also believed to be involved in the synthesis of polyatomic species in cold interstellar clouds,[35, 36] fostering astrophysical interest in this simple but spectroscopically elusive molecular ion.

From a theoretical perspective, CH_5^+ is interesting because its small size makes quantum mechanical calculations of the potential computationally feasible. Early calculations of the potential surface[37-39] predicted the lowest energy equilibrium configuration to exhibit C_S symmetry. Later studies[40] predicted an equilibrium structure reminiscent of CH_3^+ "solvated" by a more distant H_2 moiety, but as the level of theory has improved, the equilibrium separation between the CH_3^+ and H_2 has steadily decreased. Most recent high-level calculations suggest that there are, in fact, three low-lying energy structures within about 1 kcal/mol of each other.[30, 41-43] Furthermore, if zero point energy is taken into account, these three configurations are all extensively sampled by the ground-state wave function. Stated semiclassically, the barrier to rearrangement between these low-lying minima is lower than the zero point vibrational energy, thus promoting facile intramolecular scrambling of the hydrogen atoms.[41]

From a spectroscopic perspective, the highly fluxional, nonclassical nature of CH_5^+ begins to account for long-standing difficulties in obtaining and interpreting its high resolution spectrum. Indeed, despite its first observation as a highly abundant ion in mass spectrometers[44] in the early 1950s, optical detection and characterization of CH_5^+ eluded spectroscopists for another 50 years. The breakthrough came in 1999 from Oka and co-workers, who obtained a spectrum[45] in the CH stretch region exploiting velocity modulation methods and made convincing arguments that the extensive, albeit unassigned, spectrum belonged predominantly to CH_5^+. Desire to help in this assignment process has naturally led to considerable emphasis on calculating the near IR spectrum from theoretical first principles. However, despite

intense theoretical efforts [29, 30, 37-41, 46-53] directed toward CH_5^+ and the recent availability of a high-level potential surface,[42, 43] even a qualitatively correct, high-resolution spectrum based on the rovibrational energy levels has proven challenging to calculate.

The reasons for this are at least twofold. On the experimental side, large zero point energies and lack of any substantial barriers between H atom interchange lead to extensive delocalization in the wave function. This delocalization, in turn, can result in large tunneling splittings and rovibrational energy patterns profoundly perturbed away from rigid rotor expectations, especially for the J states thermally populated under discharge conditions. From a theoretical perspective, however, the number of degrees of freedom for CH_5^+ is already too large (i.e., 3n-3 = 15) to achieve fully converged quantum calculation of the rovibrational energy levels in full dimensionality.

In this chapter and the next, I explore a conceptually simple and physically motivated particles-on-a-sphere (POS) model for studying large amplitude quantum dynamics in systems as large as CH_5^+. This model is stimulated by *ab initio* calculations by both Bunker[50, 51] and Bowman,[42, 43] which reveal that each of the C-H bond lengths in CH_5^+ remain nearly constant throughout the full manifold of H atom exchange pathways. Specifically, the distribution of R_{CH} distances on the full dimensional potential surface differ only by ~0.015Å between equilibrium and saddle point configurations, respectively, which is already comparable to zero point displacements (~0.018 Å) in the corresponding radial CH stretch coordinate.[54] This indicates a high degree of decoupling between radial stretch and bend/rotation

coordinates, which I exploit by focusing explicitly on the internal CH bend/rotational degrees of freedom. Simply stated, the model considers the large amplitude quantum dynamics of an effective XH_n molecule (where $m_X >> m_H$) where n identical H atoms are radially constrained to the surface of sphere, with angular motion dictated by a given H-H interaction potential, thus motivating the POS description (see Figure 2.1). This approach reduces the dimensionality of the problem to ~2n (for a sufficiently massive central atom) and therefore makes *numerically converged* bending/internal rotor/tunneling calculations relatively straightforward for triatomic (XH_2) and tetratomic (XH_3) hydrides, as discussed herein. Most importantly, the method makes calculations for J = 0,1,2 computationally feasible even up to systems as large as XH_4 and XH_5 (as discussed in the accompanying paper II).

Though this approximation may at first seem either simplistic or Draconian, it turns out to be neither. As this first paper attempts to illustrate, such a model accurately captures the essential large amplitude bend/rotational dynamics of small XH_n systems specifically corresponding to n = 2,3. Indeed, by systematically varying the interatomic H-H potential "stiffness" and internal rotor constant for a single H atom, the effective molecular system can be tuned from a nearly "free internal rotor," where large amplitude dynamics correspond to fully delocalized wave functions, to a more "rigid molecule" limit with energy-level-splitting patterns characteristic of rovibrational tunneling. It is worth stressing at the outset that *spectroscopically accurate* predictions for rotational/tunneling level splittings are not the goal of this work, nor are they even realistic with any known potentials or current computational methods. Rather my modest aim is threefold: (i) to develop a general computational

formalism for n-particle systems in reduced dimensionality, (ii) to establish numerical confidence in these methods for simple (n = 2,3) systems by comparison with spectroscopically well known triatomic and tetratomic test case molecules, and (iii) to exploit these methods to develop semi-quantitative intuition for internal rotor/tunneling dynamics in larger systems (i.e., n = 4,5), specifically for the lowest few J levels (J = 0,1,2). These low J predictions should complement and provide particularly valuable guidance in the acquisition and analysis of jet-cooled spectra, currently obtained under supersonic expansion conditions in a high-resolution IR laser slit discharge spectrometer.[55]

The organization of this chapter is as follows: Section II describes the general theoretical background necessary for efficiently solving the POS problem, focusing on methods used in this work for the two- and three-particle system. Sections III and IV discuss application of the POS model to two test systems, n = 2 (XH_2) and n = 3 (XH_3), respectively. In Section V, I compare these n = 2,3 POS predictions with experimental results for large amplitude systems such as H_2O, NH_3, and H_3O^+. For n = 2,3, I compare these results with predictions from full dimensional theoretical calculations, which confirm the remarkable quantitative accuracy of the POS model. Concluding comments are briefly summarized in Section VI.

II. Theoretical Background

As mentioned above, the model restricts the total dimensionality by constraining particles radially, while permitting them to execute large amplitude angular motion on the surface of a sphere. The resulting Hamiltonian for n particles can be simply expressed as

$$H_{POS} = \sum_{i=1}^{n} b_i \hat{j}_i^2 + \hat{V}(\Omega) \quad , \qquad (2.1)$$

where $\hat{j}_i$ is the angular momentum of the ith hydrogen with respect to the central stationary atom and b_i is the rotational constant for motion on the sphere. $\hat{V}(\Omega)$ is the potential describing the H atom interactions, where Ω is a 2n dimensional vector of all H atom angular coordinates. Simply stated, this Hamiltonian is expanded in a suitable basis set, and the matrix elements of H_{POS} are calculated, with the resulting matrix diagonalized to generate the desired eigenvalues and eigenfunctions. Details that make such a model practicable to implement, particularly in larger atom systems, are described below.

A. Primitive and coupled basis sets

The choice of a primitive basis set is dictated by the large amplitude nature of the problems I wish to address. Freezing the n X-H stretch coordinates yields a much simpler 2n dimensional Hamiltonian, but one which nevertheless permits arbitrarily strong coupling between overall rotation and H-X-H bending vibration. In the completely "floppy" limit of vanishing interaction between H atoms (V(Ω) = 0), the quantum mechanics is simply that of n free particles constrained to a sphere. In the corresponding "stiff" extreme of strong interatomic interactions, one anticipates the quantum behavior to be described by localized harmonic oscillator wave functions in each of the H-X-H angular coordinates. Since the goal of this work is to provide insight into low-frequency rovibrational modes of molecules in the floppy limit (such as CH_5^+), I choose a primitive basis diagonal in the kinetic energy operator and treat

the potential perturbatively. Such a basis is the direct product of rigid rotor basis functions:

$$\prod_{i=1}^{n} \left| j_i m_i \right\rangle \quad , \qquad (2.2)$$

where j_i is the angular momentum of the i^{th} hydrogen and m_i is the projection of j_i on the z axis.

The n-particle Hamiltonian is diagonal in total angular momentum, J, so it is advantageous to transform this primitive basis into the coupled representation,[56] This permits matrix construction and diagonalization for each quantum number J, with corresponding reduction in computational expense. The coupled basis for the XH_2 system is denoted as

$$\left| (j_1 j_2) JM \right\rangle \qquad (2.3)$$

and for the XH_3 system as

$$\left| ((j_1 j_2) j_{12} j_3) JM \right\rangle \quad , \qquad (2.4)$$

where j_i is the angular momentum of the i^{th} particle, j_{ij} is the vector sum of j_i and j_j, and the parentheses denote which angular momenta are coupled. J is the total angular momentum, and M is the projection of J on the z axis, with standard sums over 3-J symbols[56] to transform between coupled and uncoupled representations. When creating a basis set for a given J, the primitive free particle angular momenta are restricted to $j_i = [0, j_{max}]$, where j_{max} is chosen to achieve maximum convergence while minimizing computational time. In the absence of external fields, all M states for a given J are degenerate; thus M can be taken to be 0 for an additional 2J + 1 reduction of the Hamiltonian matrix.

B. Basis set symmetrization and permutation inversion

For a crucial further reduction in computational effort, the Hamiltonian is block diagonalized using group theoretical methods.[57, 58] Since these systems exemplify large amplitude motion, I use permutation inversion (PI) theory[58, 59] to create symmetry-adapted linear combinations (SALCs) of the coupled basis functions that transform according to each PI symmetry group. The PI group for XH_2 is G_4 (isomorphic to C_{2v}), which yields four irreducible representations (A_1, A_2, B_1, and B_2), all nondegenerate. For XH_3, on the other hand, the permutation inversion group is G_{12} (isomorphic to D_{3h}), characterized by six irreducible representations (A_1', A_2', E', A_1'', A_2'', and E''), two of which (E', E") are intrinsically twofold degenerate. As clearly outlined by Bunker and Jensen,[59] standard quantum projection operator techniques can be used to systematically generate SALCs of the coupled basis functions represented by Equations (2.3) and (2.4) that transform according to a single irreducible representation. This permits block diagonalization of the Hamiltonian and a four- and sixfold reduction in the basis set size, respectively, for calculation of matrix elements. Furthermore, for systems with three or more identical particles and therefore intrinsic degeneracies, one need only calculate these eigenvalues once. Thus, by symmetrizing the basis set such that only one basis function for each degenerate level is included,[60, 61] the matrix size for a given symmetry can be further reduced. Though not a limiting issue for n = 2 and 3 systems, this size reduction becomes important for larger n. For example, in CH_5^+ the state degeneracy can be as high as six, providing an additional 36-fold reduction in matrix element evaluations for a given state symmetry.

The use of permutation inversion-symmetrized basis sets also automatically permits nuclear spin statistics for the identical particles to be implemented. Specifically for XH_n, one constructs a reducible representation of the n identical hydrogen atoms (spin ½ fermions), which is reduced according to standard group theoretical procedures[59] to obtain nuclear spin weights. For n = 2 and n = 3, these weights are readily found to be 3:1:3:1 (for $\Gamma = A_1:A_2:B_1:B_2$) and 2:2:1:2:2:1 (for $\Gamma = A_1':A_2':E':A_1'':A_2'':E''$) respectively. As the energy eigenvalues are automatically sorted by symmetry, this permits immediate assignment of the nuclear spin states and weights.

C. Matrix element evaluation

The use of symmetrized basis functions drastically decreases the matrix size for large n, thereby greatly enhancing the calculational efficiency. However, there is still significant computational cost in evaluation of the resulting matrix elements, which scales rapidly with the complexity of the system. Indeed, to more clearly illustrate the convergence issues and rapid scaling with molecular size, Table 2.1 displays typical results for a given n-atom system, total angular momentum (J) and j_{max} internal rotor value in the uncoupled representation. Also shown in Table 2.1 for a series of n, J and j_{max} values are (i) N_{sym}, the number of irreducible representations for a given n, (ii) $N_{coupled}$, the number of coupled free rotor basis states consistent with a given total J and all $j_i \leq j_{max}$, (iii) N_{SALC}, the average number of linearly independent SALCs per symmetry species, (iv) M_{SALC}, the average number of coupled basis states in a given SALC, and (v) $N_{integral}$ and N_{tot}, the total number of integral evaluations required to generate the matrix per atom pair or for all pairs, respectively.

The resulting matrix size (N_{SALC}) is decreased by as much as 50-fold from the full-coupled basis set ($N_{coupled}$); thus diagonalization and storage are not the limiting issues. Nevertheless, the number of integral evaluations to fill this matrix increases as $N_{integral} \approx 0.5*(N_{SALC})^2 \times (M_{SALC})^2$ per pair of atoms, which yields $N_{tot} \approx 0.25*(N_{SALC})^2 \times (M_{SALC})^2 \times n^2$ for the full sum over all atom pairs. As shown in Table 2.1, the number of integral evaluations for the two- and three-particle systems considered in this work is quite manageable, even up to the large j_{max} values required for numerical convergence with nearly rigid intermolecular anisotropies (e.g., models for H_2O and NH_3). However, the scaling behavior is so steep that an n = 5 system (such as CH_5^+) will require as many as 6×10^{10} integral evaluations for only J = 2 j_{max} = 3. To make larger n calculations feasible with this model, however, these evaluations need to be exceedingly efficient.

Since both the primitive and coupled basis sets are diagonal in j_i^2, the kinetic energy operator matrix elements satisfy this requirement automatically. For XH_2, these matrix elements simply are:

$$\left\langle (j_1 j_2) J \left| \hat{T} \right| (j_1' j_2') J' \right\rangle = \delta_{JJ'} \delta_{j_1 j_1'} \delta_{j_2 j_2'} b\left[j_1 (j_1 + 1) + j_2 (j_2 + 1) \right] \quad , \tag{2.5}$$

with obvious extension to XH_3 (and higher particle) systems:

$$\begin{aligned} &\left\langle ((j_1 j_2) j_{12} j_3) J \left| \hat{T} \right| ((j_1' j_2') j_{12}' j_3') J' \right\rangle = \\ &\delta_{JJ'} \delta_{j_1 j_1'} \delta_{j_2 j_2'} \delta_{j_{12} j_{12}'} \delta_{j_3 j_3'} b\left[j_1 (j_1 + 1) + j_2 (j_2 + 1) + j_3 (j_3 + 1) \right] \end{aligned} \tag{2.6}$$

The potential matrix elements, however, require substantially greater effort. Matrix element evaluation by standard quadrature methods increases times by an additional factor of Q^{2n}, where Q is the number of points on a potential grid, i.e., unacceptable for n > 3. By considering the potential as a multibody expansion, i.e.,

$$V(\Omega) = \sum_{i<j}^{n} V^{(2)}(\Omega_i, \Omega_j) + \sum_{i<j<k}^{n} V^{(3)}(\Omega_i, \Omega_j, \Omega_k) + \sum_{i<j<k<l}^{n} V^{(4)}(\Omega_i, \Omega_j, \Omega_k, \Omega_l) + \ldots \quad , \tag{2.7}$$

where each term represents a sum over all two-body, three-body, and four-body contributions, the work required to evaluate the potential elements can be greatly reduced. Given the rapidly growing number of evaluations required in Table 2.1, however, I restrict this expansion to only the first term, i.e., I consider arbitrary linear combinations of pairwise additive intermolecular potentials between each particle. Such pairwise additive potential depends only on the angle between pairs of particles:

$$V(\Omega) = \sum_{i<j}^{n} V^{(2)}\left(\gamma_{ij}\right) \quad , \tag{2.8}$$

where γ_{ij} is the H-X-H angle between the i^{th} and j^{th} hydrogen.

Although not essential for the n = 2,3 test systems described in the current study, such a pairwise additive approximation provides a crucial advance for treating larger systems, making theoretical studies of XH_4 and XH_5 tractable. Specifically, if I expand any pairwise additive potential in a sum of Legendre polynomials, the matrix element for each term can be calculated analytically via Clebsh-Gordan angular momentum algebra.[62] For the XH_2 problem, this yields:

$$\left\langle (j_1 j_2) J \left| \hat{V} \right| \left(j_1' j_2'\right) J' \right\rangle = \delta_{JJ'} \sum_{\lambda} f_\lambda \left(j_1 j_2; j_1' j_2'; J\right) , \tag{2.9}$$

where f_λ are the Percival-Seaton coefficients:

$$\begin{aligned} f_\lambda \left(j_1 j_2; j_1' j_2'; J\right) &= \left\langle (j_1 j_2) J \left| P_\lambda(\cos\gamma_{12}) \right| \left(j_1' j_2'\right) J' \right\rangle \\ &= (-1)^{j_2 + j_2' + J} \left[(2j_1+1)(2j_2+1)\left(2j_1'+1\right)\left(2j_2'+1\right)\right]^{\frac{1}{2}} \\ &\times \begin{pmatrix} j_1 & \lambda & j_1' \\ 0 & 0 & 0 \end{pmatrix} \begin{pmatrix} j_2 & \lambda & j_2' \\ 0 & 0 & 0 \end{pmatrix} \begin{Bmatrix} j_2 & \lambda & j_2' \\ j_1' & J & j_1 \end{Bmatrix} \end{aligned} \tag{2.10}$$

and $\begin{pmatrix} \cdot & \cdot & \cdot \\ \cdot & \cdot & \cdot \end{pmatrix}$, $\begin{Bmatrix} \cdot & \cdot & \cdot \\ \cdot & \cdot & \cdot \end{Bmatrix}$ are 3-J, 6-J symbols, respectively.[56] For the n = 2 particle system, calculation of these potential matrix elements is very fast, exploiting efficient 3-J and 6-J evaluation routines.[63]

The extension to a larger number of particles is straightforward. The n = 3 potential is expressed as a sum of pairwise interactions, i.e.,

$$V(\Omega) = V^{(2)}(\gamma_{12}) + V^{(2)}(\gamma_{13}) + V^{(2)}(\gamma_{23}) \quad , \qquad (2.11)$$

where the matrix element of the first term is analogous to the two particle matrix element and easily calculated as:

$$\left\langle ((j_1 j_2) j_{12} j_3) J \middle| \hat{V}^{(2)}(\gamma_{12}) \middle| \left((j_1' j_2') j_{12}' j_3' \right) J' \right\rangle = \delta_{JJ'} \delta_{j_3 j_3'} \delta_{j_{12} j_{12}'} \sum_{\lambda} f_{\lambda}\left(j_1 j_2; j_1' j_2'; j_{12}\right) \quad , \qquad (2.12)$$

The other two terms simply require transformation to a different coupling scheme.[56] For example, the $V^{(2)}(\gamma_{13})$ term is calculated by recoupling the j_1 and j_3 angular momenta first to produce j_{13}, i.e.,

$$\left\langle ((j_1 j_2) j_{12} j_3) J \middle| \hat{V}^{(2)}(\gamma_{13}) \middle| \left((j_1' j_2') j_{12}' j_3' \right) J' \right\rangle = \sum_{j_{13}, j_{13}'} C_{j_{13}} C_{j_{13}'} \left\langle ((j_1 j_3) j_{13} j_2) J \middle| \hat{V}^{(2)}(\gamma_{13}) \middle| \left((j_1' j_3') j_{13}' j_2' \right) J' \right\rangle, \qquad (2.13)$$

where the C_i coefficients can be expressed as 6-J symbols and each term evaluated as in Eq. 2.12.

It may seem restrictive to limit the potential to a pairwise additive form; however, it is reasonable to believe that the approximation will work well for the floppy CH_5^+. The large zero-point motion of the bending/rotation degrees of freedom and the low barriers to interconversion of the hydrogens in CH_5^+ are likely the

predominant factors influencing the spectroscopic patterns. The high-quality potential[43] of Bowman and co-workers contains a C_s minimum and two low-lying transitions states: A C_s transition state at 42 cm^{-1} and a C_{2v} transition state at 190 cm^{-1}. Preliminary calculations on the Bowman surface with a restricted R_{CH} coordinate result in a C_{2v} minimum and one C_s transition state at 115cm^{-1}. A fit of a pairwise additive potential to the Bowman surface yields a similar C_{2v} minimum and a similar C_s transition state 300cm^{-1} higher. All of the transition states are an order of magnitude smaller than the zero-point energy of about 11,000cm^{-1} (or 4,100cm^{-1} when freezing the C-H stretch coordinates). The effects of the pairwise potential is investigated in more detail in Chapter 3; however, the large-amplitude coupled bending/rotation patterns should not change significantly. As will be demonstrated later in this chapter, a pairwise additive potential reproduces the full dimensional and bending levels of both NH_3 and H_3O^+ remarkably well**.**

The pairwise additive potential only depends on the angle between each pair of particles, which can be expanded in Legendre polynomials with no loss of generality. In the interest of simplicity, I take this form of the potential for this paper to be

$$V^{(2)}\left(\gamma_{ij}\right)=\frac{k}{2}\left[1-\cos\left(\gamma_{ij}-\gamma_0\right)\right] , \qquad (2.14)$$

which exhibits a minimum at $\gamma = \gamma_0$. The three free parameters in the full Hamiltonian are: (i) b, the rotational constant for a single H atom, (ii) k, the depth of the potential well, and (iii) γ_0, the equilibrium H-X-H angle. I further introduce the parameter χ = k/b, the ratio of the potential well to the rotational constant, which provides a

convenient dimensionless metric for characterizing the "floppiness" vs. "stiffness" of the pairwise interaction.

I conclude this section with an explicit timing example. By exploiting efficient 3-J/6-J evaluations, Equations (2.11) and (2.12), and logical extensions thereof, each potential energy matrix element for a given coupled basis state can be calculated on a single 2.4 GHz Intel processor in 6.5 μs. This rate translates into ~2 hours per 10^9 integral evaluations, or, by inspection of Table 2.1, ~100 hours for a system with n = 5, J = 2, j_{max} = 3. This is encouraging and suggests that such POS calculations may be tractable even past n = 5, at least for systems with intermolecular potentials sufficiently "floppy" to be adequately represented by small values of j_{max}. Symmetry and nuclear-spin-sorted results will be presented in Chapter 3 for n = 4,5 atom systems, benchmarked against CH_4, and will offer an approximate but insightful model of quantum level structure for the highly fluxional CH_5^+ species. To first establish the feasibility of these methods, however, I focus herein on explicit examples of the POS model for the computationally straightforward n = 2,3 systems.

III. Two Particles-On-A-Sphere (XH_2)

The first test system is that of two POS, i.e., XH_2, with Hamiltonian parameters (b_i = 18.00 cm^{-1}, $\gamma_0 = 104^o$) chosen to resemble the equilibrium structure of H_2O in the limit of large anisotropy in the intermolecular pair potential. The strategy is to investigate the large amplitude eigenenergies as a function of the dimensionless stiffness parameter, $\chi = k_i / b_i$, for fixed b_i. With only two particles, one can readily anticipate the limiting behaviors in each of two regimes. Specifically the $\chi << 0$ ("floppy") limit should yield rotation-like energy level patterns characteristic of

two free internal rotors, with characteristic spacings as a function of j_1, j_2. Conversely, the energy levels in the $\chi >> 1$ ("stiff") limit should begin to approach the asymmetric top rotor levels for a harmonic oscillator in the H-X-H bend coordinate.

Figure 2.2 shows a sample energy eigenvalue correlation diagram for two POS (J = 0, A_1 symmetry), as the stiffness of the potential is increased. When χ is small, the progression scales like $j_i(j_i + 1)$ for each of the two independent rigid rotors. For the specific case of J = 0, however, the *angular momenta* of the two hydrogen atoms are perfectly correlated in the coupled basis, i.e., $j_1 = j_2$. Thus, in the limit of low potential anisotropy, the states can be approximately labeled by $|j_1 j_2>_{sym}$ for a given symmetry and one thus observes energies in Figure 2.2 for $\chi \approx 1$ increasing uniformly as $E_{rot} = 2bj(j + 1)$, for j = 0,1,2… In the stiff limit, the intermolecular potential is large enough that the two atomic *displacements* are now correlated and best described as a small amplitude vibration. The appropriate notation in this limit is therefore $|v\rangle_{sym}$, where the ket denotes the number of quanta and symmetry in the bending vibrational mode. As expected, the correlation diagram in Figure 2.2 for $\chi \approx 1000$ (J = 0, A_1 symmetry) demonstrates harmonic behavior, i.e., approximately equal vibrational spacings in the first few energy levels.

If one examines multiple J values for the lowest vibrational state (v = 0) as a function of intermolecular stiffness, an analogous but quite different trend is anticipated. By way of example, Figure 2.3 shows the energies (relative to $E_{J=0}$) of J = 0, 1, and 2 for XH_2 as χ is increased from 1 to 10000. At low χ, the energy spacing is 2b, reflecting uncorrelated rotation of the two hydrogen atoms. As χ is increased, however, evolution to a more localized rotational structure of XH_2 is clearly evident.

Specifically, for $\chi \approx 10000$, the energy levels for XH_2 converge on those of a rigid molecule, with J = 0, 1 and 2 states taking on the characteristic K_a, K_c patterns of an asymmetric top. This is most readily evident in the set of $J_{KaKc} = 1_{01}$, 1_{11}, and 1_{10} levels, which systematically converge (for high χ) on the characteristic asymmetric top values of $E_{rot} = B + C$, $A + C$, $A + B$, respectively.

Additional confirmation for the two-particle dynamics can be obtained from the corresponding wave functions, representative 2D slices for the J = 0 XH_2 ground state which are displayed in Figure 2.4 as a function of χ. To visualize the anisotropy-induced correlation between the hydrogen atoms, I rotate the coordinate system so that one hydrogen is always pointing upwards at $\theta = 0$ and $\varphi = 0$. For an n = 2 system, the probability of finding the second particle is then plotted as a function of γ, the angle between the two hydrogen atoms. Figure 2.4 clearly illustrates the expected behavior for the XH_2 system; the wave functions become more strongly localized as the potential is stiffened, slowly converging on the equilibrium angular separation (γ_0) between the two hydrogen atoms as χ increases.

As a final test of the n = 2 model, the XH_2 system can be mapped onto the well-studied H_2O molecule, for which the full 3D intermolecular potential has been determined to exceptionally high accuracy by Tennyson and co-workers.[64] In the spirit of the POS model, I first fix the two OH bond lengths at equilibrium values ($R_{OH} = 0.958$ Å) and then fit the reduced dimensionality-bending H_2O potential to a 15-term Legendre expansion. The resulting 1D potential is then inserted into the Hamiltonian with b = 18.4 cm^{-1} (obtained from equilibrium bond lengths) and diagonalized to yield the converged rovibrational eigenstates and eigenfunctions for

H_2O in the POS limit. To facilitate direct quantitative comparison, the equivalent asymmetric top rotational constants are extracted from the three lowest J = 1 levels, as indicated in Figure 2.3. Similarly, the HOH vibrational bending levels are estimated via differences in the lowest three J = 0 states of A_1 symmetry, as illustrated in Figure 2.2. The resulting rovibrational predictions are compared with known experimental values for H_2O in Table 2.2, which indicate nearly quantitative agreement (< 0.1% for vibrations, < 1 - 5 % for rotational constants). Given the calculational simplicity of this POS model for n = 2, this level of agreement for H_2O appears promising, especially considering the complete absence in such a model of any stretch-bend coupling.

IV. Three Particles-On-A-Sphere(XH_3)

With these encouraging results for the two-particle Hamiltonian system, I add one more atom to the model to form XH_3. In anticipation of numerical comparison with experimental data, the intermolecular structural parameters for this system have been chosen to best approximate NH_3, with b = 16.63 cm^{-1} and $\gamma_0 = 108^0$. Since this model potential now predicts an equilibrium *nonplanar* C_{3v} structure with a double minimum along the inversion coordinate, one expects to see evidence of (i) symmetric top rotational behavior and (ii) quantum mechanical tunneling through the inversion barrier.

Analogous to the two-particle system, I consider appropriate state labels as a function of low and high intermolecular anisotropy. In the floppy limit ($\chi \approx 1$), the states can be well designated by $\left| j_1 j_2 j_3 \right\rangle_{sym}$ where the symmetry label uniquely

identifies the proper linear combination of the three-particle permutations. In the semirigid molecular limit for XH_3 , there are three vibrational modes: one is the umbrella mode of A_1'/A_2'' symmetry (ν_{umb}) with the remaining pair forming a degenerate bend (ν_{bend}) of E'/E'' symmetry. The most convenient notation in the stiff limit is therefore $\left|\nu_{umb}\nu_{bend}\right\rangle_{sym}$, with the corresponding number of quanta in either the A umbrella or the E bend vibration explicitly denoted.

As in the case of XH_2, I first examine the correlation diagram for energy eigenvalues between floppy and stiff potential limits. Figure 2.5 displays eigenenergies of the first few A_1'/A_2'' symmetry states of XH_3 with J = 0. In the floppy limit ($\chi \approx 1$), a simple progression of rigid rotor energy levels for XH_3 can be easily recognized, although more complicated than for XH_2. This is because there are multiple ways to add the three H atom angular momenta (j_1,j_2,j_3) and still get total J = 0. Nevertheless, the lowest several states of A_1'/A_2'' symmetry (with respect to $E_{J=0}$) are found to be consistent with the free rotor limit of E_{rot} = 4b, 6b, 10b, 12b, etc. The corresponding lowest energy level behavior in the stiff limit ($\chi >>1$) clearly correlates with a simple progression in the umbrella mode, split by tunneling through the planar barrier. (The XH_3 bending modes are present in this energy range as well but only appear as doubly degenerate vibrations of E'/E" symmetries.) Note that the magnitude of these tunneling splittings increases rapidly with ν_{umb}, corresponding semiclassically to vibrational promotion of barrier penetration as one energetically accesses the planar transition state.

By way of confirmation, one can similarly examine low J levels in the ground vibrational v = 0 state as a function of χ . Figure 2.6 displays the correlation diagram

of rotational energies (relative to $E_{J=0}$) for J = 0, 1, and 2 states of XH_3 as a function of increasing χ. At $\chi \approx 1$, the free rotor pattern emerges, with characteristic 2b energy spacings. In the limit of $\chi >> 1$, however, the correlation diagram correctly predicts a convergence toward the familiar energy levels of a rigid symmetric top, specifically, $E_{JK} = B\ J\ (J + 1) + (C - B)\ K^2$. (Note that this requires inclusion of E' symmetry to represent the intrinsically degenerate $K \neq 0$ states.) Since the equilibrium structural parameters of the potential are modeled after NH_3, the energy levels are those of an oblate symmetric top, i.e., energy decreasing with K for a fixed J value.

Further examination of the model behavior can be obtained from 2D slices through the corresponding eigenfunctions. As the total wave function, Ψ_{tot}, is not possible to plot in 6D, I examine a simpler 2D function of one hydrogen coordinate (θ, φ), with the other two hydrogens held fixed at ($\theta = 0$, $\varphi = 0$) and ($\theta = \gamma_0$ $\varphi = 0$), respectively (see insert in Figure 2.7 for relevant details). A series of slices through Ψ_{tot} is shown in Figure 2.7 as a function of χ, with the lowest A_1' and first excited A_2" states for J = 0 on the left and right, with the equivalent slice through the potential contour shown at the bottom. As expected for an increase in potential stiffness (i.e., increasing χ), the wave function probability for the last H atom progressively localizes on the two equilibrium positions ($\gamma = \gamma_0 = 108^0$, $\phi = 120^0$, 240^0). Furthermore, the wave function amplitudes clearly exhibit the expected alternation between symmetric and antisymmetric wave function characteristic of a double well potential.

As a logical benchmark test of these n = 3 POS calculations, I look to the limiting case of ammonia (NH_3), for which the intermolecular potential and energy

term values are well known from previous spectroscopic studies. Currently, the model is only capable of representing a pairwise additive potential, whereas the most accurately determined NH_3 potential[65] requires small three-body terms to fully describe the interaction of the three hydrogens. As I will be unable to include such nonpairwise additive terms for n > 3 (e.g., CH_5^+), I choose instead to fit an effective pairwise potential that most accurately reproduces the true inversion potential for NH_3. Specifically, the k and γ_0 parameters in Eq. 2.6 are fit to reproduce (i) the experimentally known barrier height at planarity and (ii) the equilibrium HNH bend angle for NH_3. Note that this does not represent a fit to the complete tunneling path, as was done in the previous section for H_2O. However, this approach does offer additional insight into the importance of such three-body terms, for which sufficient computational resources will not be available for larger particle systems.

The results of these test calculations for NH_3 are summarized in Table 2.3 for J = 0 vibrational levels up to 2000 cm^{-1}, along with the experimental values. Both the vibrational energies and inversion tunneling splittings for the umbrella mode match experiment remarkably well (< 3–5%), particularly for such a simple two-parameter representation of the ammonia potential. Though still respectable, the agreement is not quite as good (indeed, systematically underestimated by ~9%) in the degenerate bending vibrational predictions. However, this is not entirely surprising, since only barrier height information has been included in formulating the approximate NH_3 surface.

V. Discussion

I first begin with a brief discussion of the convergence properties for my calculations. In Figure 2.8, the fractional error for the ground-state energy is plotted as a function of j_{max} for several values of χ. As expected, the error (relative to fully converged results at $j_{max} = 50$) decreases with increasing j_{max} and basis set size. Furthermore, the size of j_{max} necessary to converge to a given level increases with stiffness in the potential. This is simply the result of a basis set designed to be diagonal at $V(\Omega) = 0$; i.e., as the interatomic potential is increased, the free rotor picture provides a progressively worse zeroth-order description. Also shown in Figure 2.8 for comparison are corresponding convergence tests for the XH_3 system. Particularly noteworthy is that the convergence rate for a given value of χ is remarkably similar for both XH_2 and XH_3. This is extremely encouraging for extension of these studies to n = 4,5 particle systems, for which the basis set size (and hence the Hamiltonian) grows so quickly that calculations for asymptotic values of j_{max} may not be feasible to establish a rigorous level of convergence for a given test potential. For the n = 2,3 systems discussed herein, however, all the calculations have been performed with $j_{max} > 20$, i.e., sufficiently high to ensure negligible fractional errors (< 0.0001 %).

Now that I have demonstrated the capability of the POS model for reasonably accurate predictions in "stiff" XH_2 and XH_3 systems such as H_2O and NH_3, I next turn my attention to the floppier molecular ion, H_3O^+. The hydronium ion has been extensively studied over the past several decades with both high level theoretical and experimental methods. As a result, the intermolecular potential for this ion is known

to nearly spectroscopic accuracy. The barrier height in H_3O^+ (~ 650 cm^{-1}) is considerably lower than for NH_3 (~ 1792 cm^{-1}), which leads to tunneling splittings in the ground state of nearly 60 cm^{-1}. A test study of H_3O^+ via POS methods is therefore helpful in developing further confidence in calculations for other large amplitude tunneling systems, specifically other closed-shell-protonated molecular ions such as CH_5^+.

I start by fitting the theoretical H_3O^+ 1D symmetric inversion potential[66] to a 15-term Legendre expansion, again without including any three-body terms. Fully converged rovibrational energy levels for the resulting potential are then obtained from the POS Hamiltonian treatment, with b = 17.6 cm^{-1}. The results are listed in Table 2.4. Similar to what was observed for the NH_3 test problem, the predicted H_3O^+ energies agree reasonably well with both experiment and exact full 6D calculations by Bowman *et al*. Indeed, the typical error between (i) the POS and (ii) full dimensional calculations is on the order of 3–5%, which is certainly adequate for such a simple model based on (i) an infinitely heavy central atom and (ii) fixed moment of inertia for each HX rotor. Also similar to what was observed in the NH_3 studies, there are noticeably larger errors (8–12%) for predictions in the degenerate-bending vibrational manifold. This may be simply attributable to the fact that the POS potential is only fit to (and thus might be expected to better reproduce) the H_3O^+ potential along the inversion coordinate. Nevertheless, the results are reasonably accurate for such a fit and may indeed be further improved by a better modeling of the potential shape. Most importantly, however, the overall energy level patterns for the umbrella inversion, tunneling, and degenerate bending modes are accurately and

semiquantitatively reproduced. Since one aim of the POS approach has been to develop qualitative intuitions in highly fluxional tunneling systems, this may already prove of substantial value in more challenging molecular ions such as CH_5^+.

VI. Summary and Conclusion

In this chapter, a conceptually simple method has been introduced for approximate but reasonably quantitative treatment of large amplitude quantum motion in small floppy hydrides such as XH_n. This POS method takes advantage of the approximate independence of XH bond length on angular coordinates to motivate a reduced dimensionality Hamiltonian treatment of hydrogenic motion constrained to the surface of a sphere. Despite the simple nature of this approximation, the method is found to work surprisingly well for test n = 2 and n = 3 particle systems. Furthermore, the method yields good quantitative agreement in tests against experimental results for stiff systems with known intermolecular potentials (e.g., H_2O and NH_3) as well as more "floppy," large amplitude systems (e.g., hydronium ion, H_3O^+). The agreement with full dimensional theoretical calculations is extremely promising, particularly in the quantitative reproduction of all patterns relevant to spectroscopic assignment and analysis of highly quantum mechanical systems.

Most importantly, however, the numerical methods developed with this approach lead to favorable scaling properties that offer encouragement toward applications with even larger n atom systems. The test cases shown herein demonstrate the feasibility of extension of these methods up to n = 5, at least for angular momentum states (J = 0, 1 and 2) relevant to spectroscopic studies in a low temperature slit supersonic expansion. As all n = 2,3 test molecules studied with POS

methods in this paper reflect relatively stiff intermolecular potentials, I feel confident that significant progress can be made toward larger systems. In later chapters, I apply these POS methods to n = 4,5 particle systems along with any extra optimizations needed to converge these exponentially much harder problems. The aim is to provide reduced dimensionality tools to develop the necessary insight and intuition for large amplitude dynamical systems, for which calculations in full dimensionality are simply not feasible. The long range goal is to incorporate these reduced dimensionality approaches with high-level *ab initio* potential surfaces to provide valuable information for decoding high-resolution spectra of highly fluxional species such as CH_5^+.

Tables

Table 2.1. Basis set size and matrix calculation time scaling as a function of n, J, and j_{max}.

n	J	j_{max}	N_{sym}[a]	$N_{coupled}$	N_{SALC}	M_{SALC}	$N_{integral}$	N_{tot}	Time
	0			51	51	1	1,326	1,326	0.01 s
2	1	50	4	150	50	2	5,050	5,050	0.03 s
	2			246	62	2	7,750	7,750	0.05 s
	0			2,056	230	5	0.7×10^6	2×10^6	0.22 m
3	1	15	6	6,120	680	10	23×10^6	69×10^6	7.54 m
	2			10,050	1.1×10^3	16	159×10^6	478×10^6	51.97m
	0			5,719	244	28	23×10^6	140×10^6	0.30 h
4	1	6	10	16,688	690	75	$1{,}339 \times 10^6$	$8{,}034 \times 10^6$	14.6 h
	2			26,320	1.1×10^3	113	$7{,}753 \times 10^6$	$46{,}520 \times 10^6$	84.3 h
	0			4,269	67	101	0.02×10^9	0.2×10^9	0.40 h
5	1	3	14	11,925	186	276	1.3×10^9	13×10^9	23.90 h
	2			17,225	268	400	5.7×10^9	57×10^9	104.1 h

[a]N_{sym} refers to the number of irreducible symmetry representations; $N_{coupled}$ is the number of coupled basis set states for a given J, j_{max}; N_{SALC} is the average number of symmetry-adapted linear combinations (SALC) per symmetry species; M_{SALC} is the average number of coupled basis states in a given SALC; $N_{integral}$ is the number of integral evaluations per atom pair; N_{tot} is the total number of integral evaluations over all atom pairs.

Table 2.2. Calculated and experimental H_2O energy levels (cm^{-1}) for the bending mode and rotational constants (cm^{-1}).

	POS	3-D QM[a]	Experiment[b]
$\|1\rangle_{A1}$	1588	1594.7	1594.7
$\|2\rangle_{A1}$	3149	3151.5	3151.6
A	25.67		24.27
B	14.89		14.81
C	9.19		9.20

[a,b] Values from Polansky *et al.*[64]

Table 2.3. Calculated and experimental NH_3 energies and splittings.

State	POS		Full QM[a]		Experiment[b]	
	Energy	Splitting	Energy	Splitting	Energy	Splitting
$\|00\rangle_{A_1'}$	0	0.798	0	0.790	0	0.793
$\|10\rangle_{A_2''}$	0.798		0.790		0.793	
$\|20\rangle_{A_1'}$	895.6	35.3	934.06	35.51	932.43	35.69
$\|30\rangle_{A_2''}$	930.9		969.57		968.12	
$\|01\rangle_{E'}$	1482		1627.91		1626.28	
$\|11\rangle_{E''}$	1483					
$\|40\rangle_{A_1'}$	1536	277	1600.79	284.27	1597.47	284.71
$\|50\rangle_{A_2''}$	1813		1885.06		1882.18	
$\|60\rangle_{A_1'}$	2299		2387.82		2384.15	
$\|21\rangle_{E'}$	2413		2543.43		2540.53	
$\|70\rangle_{A_2''}$	2795		2899.62		2895.51	
$\|02\rangle_{A_1'}$	2938		3220.13		3216.1	
$\|02\rangle_{E'}$	2953		3244.26		3240.44	
$\|80\rangle_{A_1'}$	3345		3467.24		3462	

[a,b] Values from Rajamaki *et al*.[67]

Table 2.4. Calculated and experimental H_3O^+ energies and splittings.

State	POS		Full QM[a]		Experiment[b]	
	Energy	Splitting	Energy	Splitting	Energy	Splitting
$\|00\rangle_{A_1'}$	0	} 54.33	0	} 46	0	} 55.35
$\|10\rangle_{A_2''}$	54.33		46		55.35	
$\|20\rangle_{A_1'}$	529.9	} 347	580	} 354	581.17	} 373.23
$\|30\rangle_{A_2''}$	876.7		934		954.4	
$\|40\rangle_{A_1'}$	1377		1445		1475.84	
$\|01\rangle_{E'}$	1421		1624		1625.95	
$\|11\rangle_{E''}$	1498		1681		1693.87	
$\|50\rangle_{A_2''}$	1918		2005		1882.18	

[a,b] Values from Huang *et al*.[66]

Figures

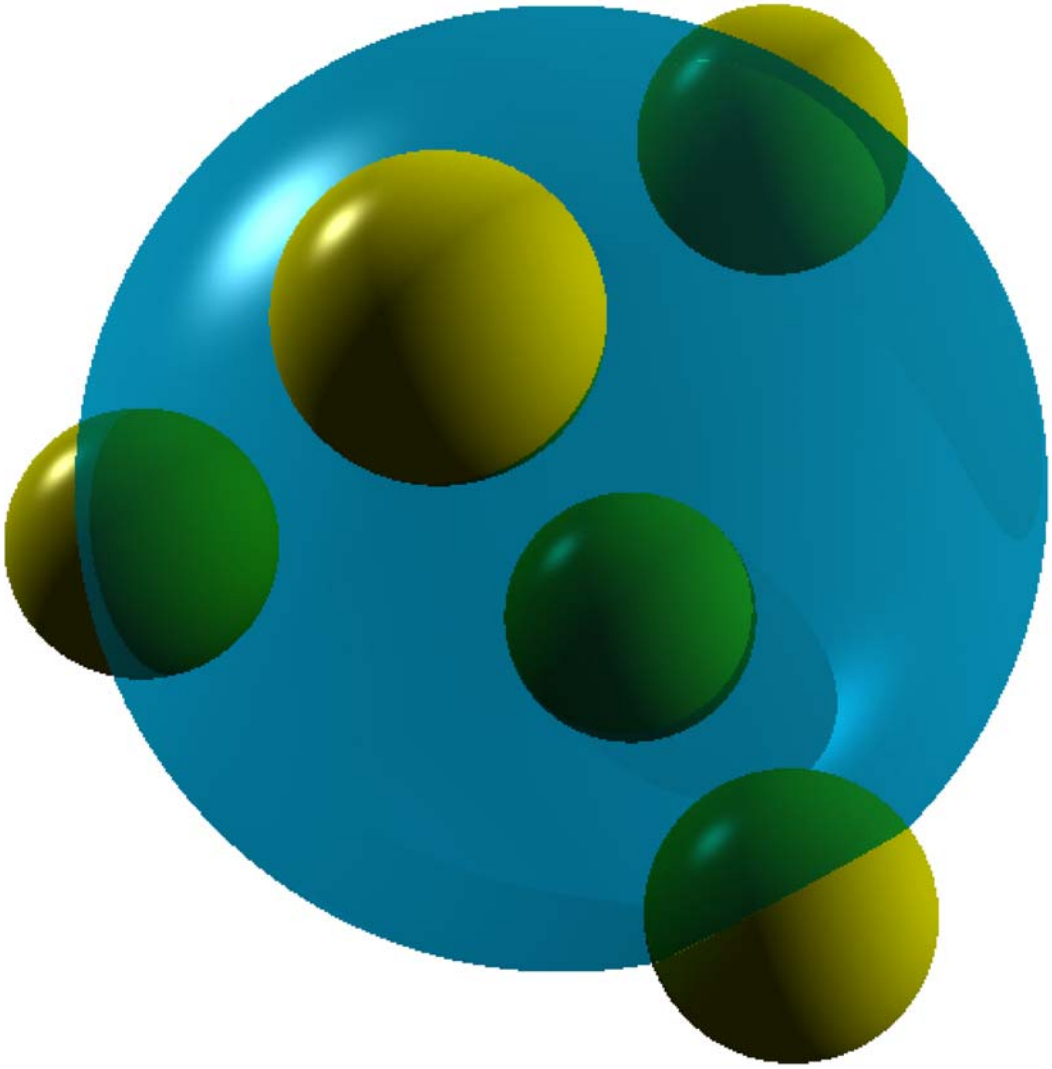

Figure 2.1. Schematic picture of the particles-on-a-sphere (POS) method, which is based on a modeling of polyatomic hydrides (XH_n) as one heavy atom (X) that constrains the motion of n H atoms to the surface of a sphere.

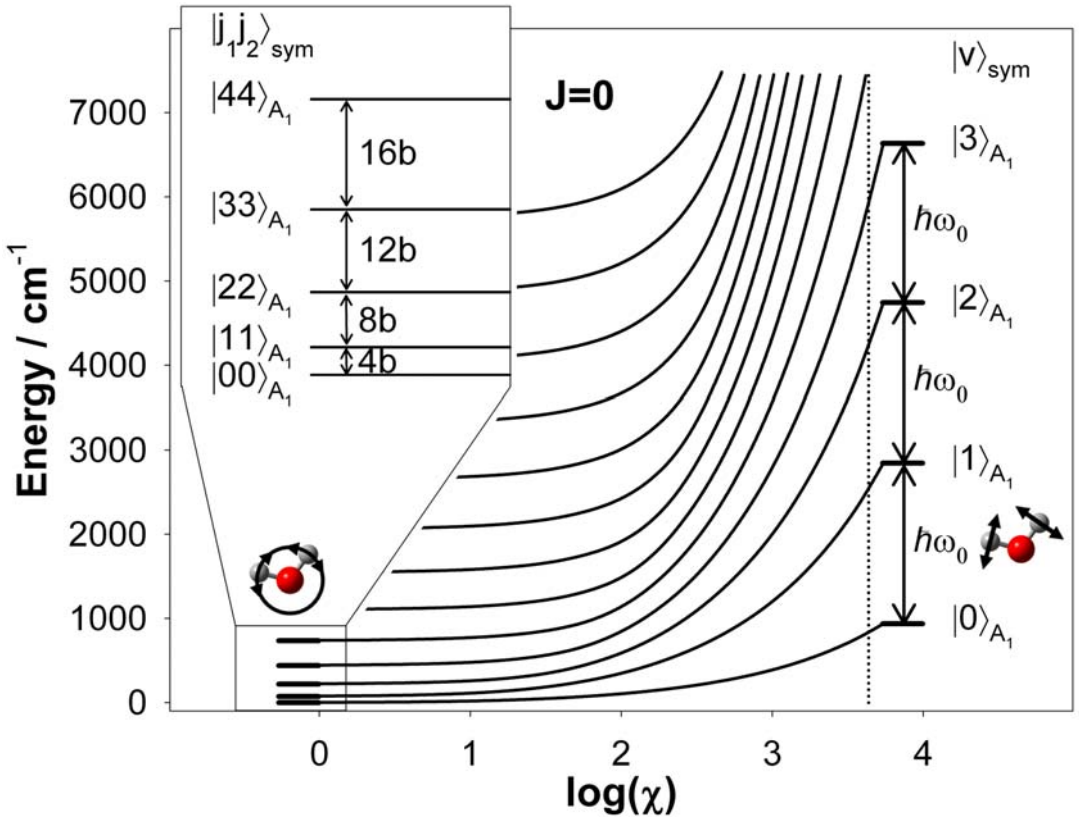

Fig 2.2. $E_{J=0}$ energy level correlations for XH_2, plotted for the first few lowest energies vs. potential stiffness, χ. At small χ, a simple rigid rotor pattern with increasing spacings (4b, 8b, 12b, etc.) is clearly exhibited (the rotational levels are reproduced with greater detail in the inset), but which evolves smoothly to a harmonic pattern of constant energy spacing ($h\omega_0$) in the limit of large χ.

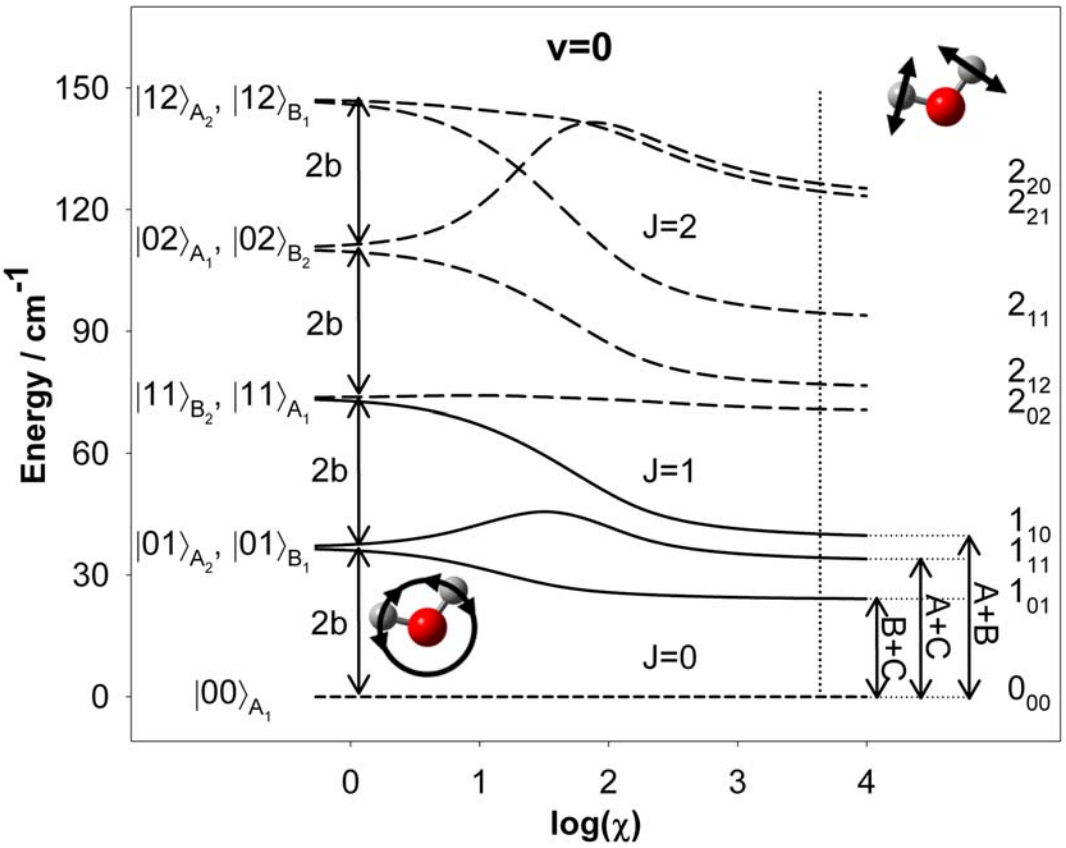

Fig 2.3. $E_{J = 0,1,2}$ energy level correlations for XH_2 in the ground vibrational state, plotted for the first few lowest energies versus potential stiffness, χ. At small χ, the energy separations reflect uncorrelated free rotation of the hydrogen atoms. At large χ, however, this smoothly transitions into the characteristic J_{KaKc} patterns of a rigid asymmetric top.

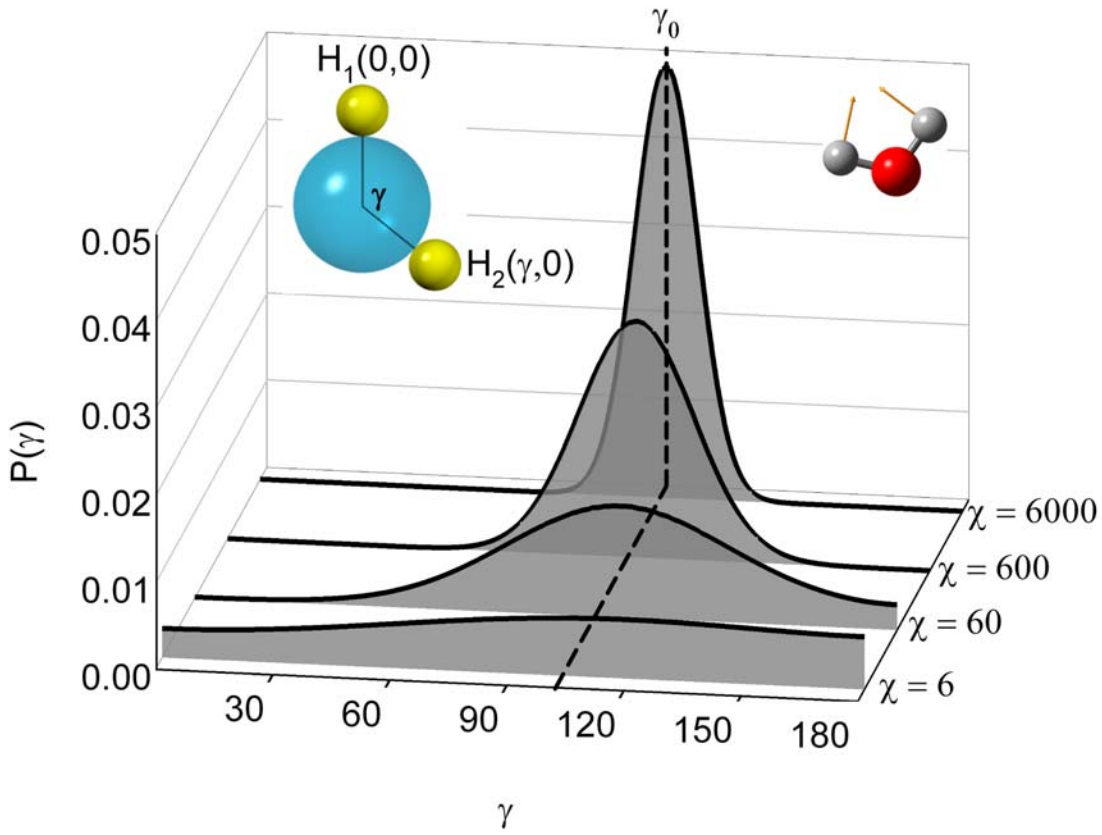

Figure 2.4. 1D wave function probability distribution for the XH_2 ground vibrational state plotted as a function of increasing χ. As the potential stiffness is increased, the width of the HXH angular distribution narrows toward $\gamma = \gamma_0$, i.e., the equilibrium geometry. As shown in the inset, the first hydrogen is defined to be at ($\theta = 0$, $\phi = 0$), with the |amplitude|^2 for the second hydrogen plotted for ($\theta = \gamma$, ϕ).

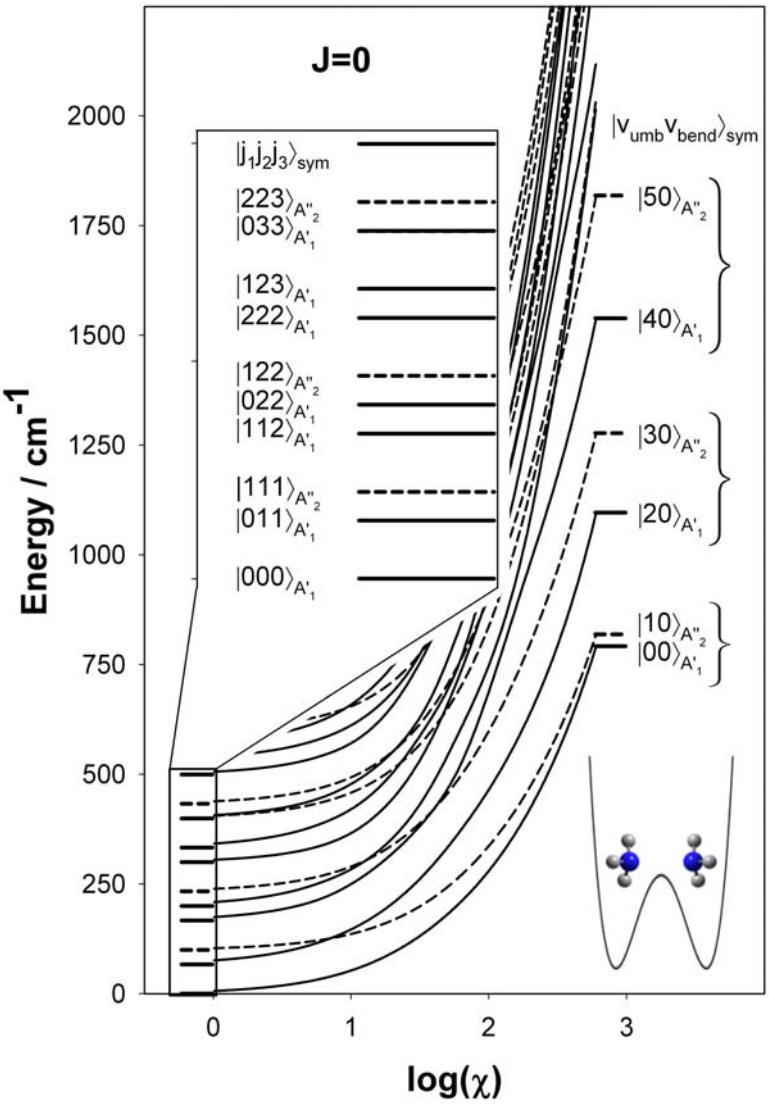

Figure 2.5. $E_{J=0}$ energy level correlation as a function of intermolecular stiffness for XH_3, plotted for the first few energies of the umbrella mode. At small χ, the levels correspond to three independent rigid HX rotors (displayed with greater detail in the inset) but eventually correlate with inversion doubled tunneling splittings in the limit of large χ.

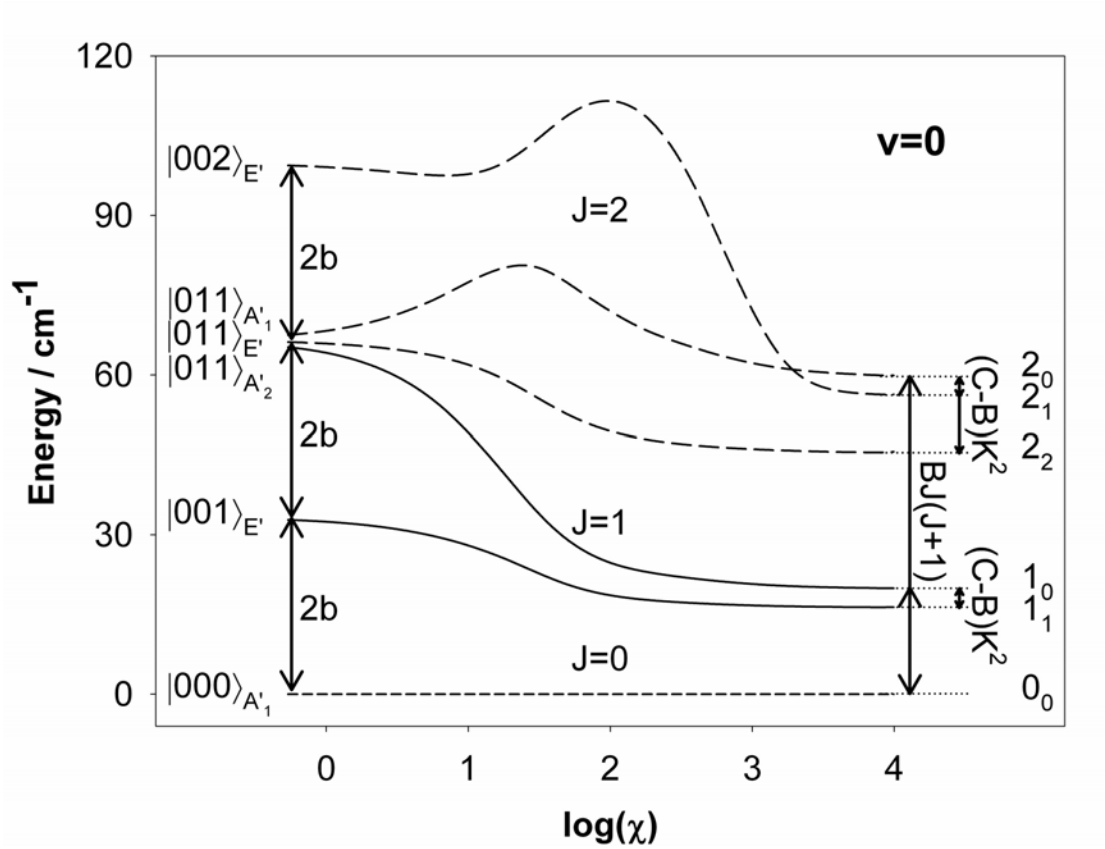

Figure 2.6. $E_{v=0}$ energy level correlation for XH_3 J = 0, 1, 2 as function of intermolecular stiffness, χ. For small χ, the pattern reflects three freely rotating hydrogens, which for large χ smoothly transitions into the rotational energy pattern characteristic of an oblate symmetric top.

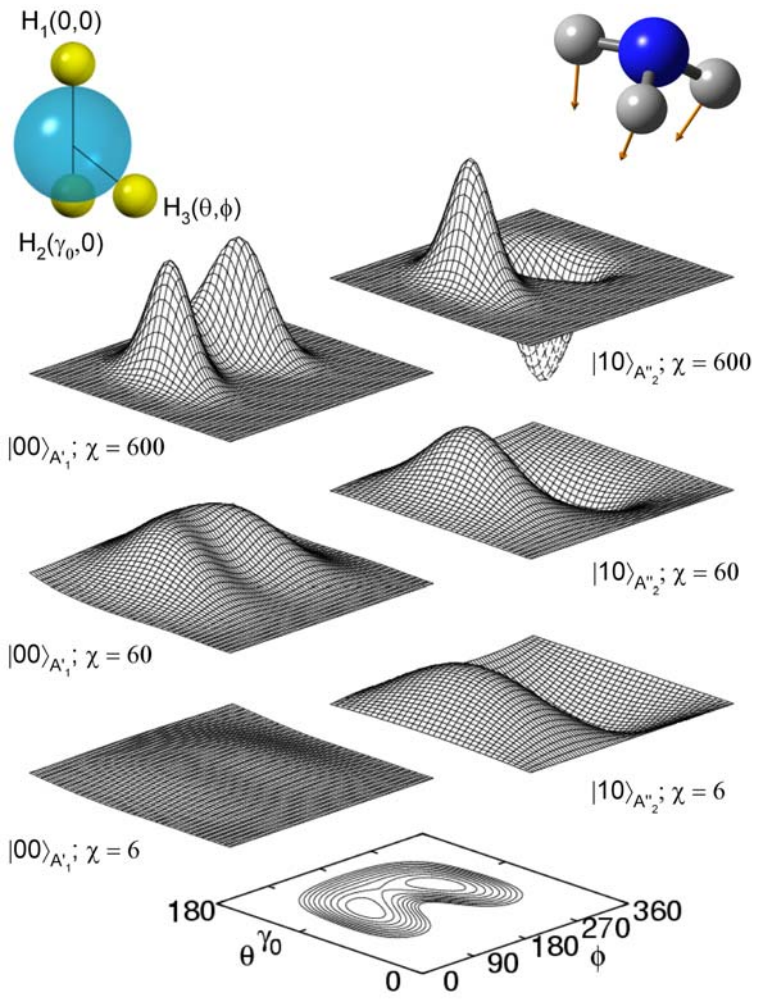

Figure 2.7. 2D cuts (in θ, ϕ space) through full 6D XH_3 wave functions for (i) symmetric ground state (left hand side) and (ii) the antisymmetric first excited state (right hand side) of the umbrella mode for increasing values of χ. The contour plot (center bottom) displays the corresponding potential. At χ = 6, 60 and 600, the contour spacings are 1.5 cm^{-1}, 15 cm^{-1}, and 150 cm^{-1}, respectively. As shown in the inset, the first and second hydrogens are fixed at (θ = 0, ϕ = 0) and (θ = γ_0, ϕ = 0), with amplitude for the third hydrogen plotted as a function of (θ , ϕ).

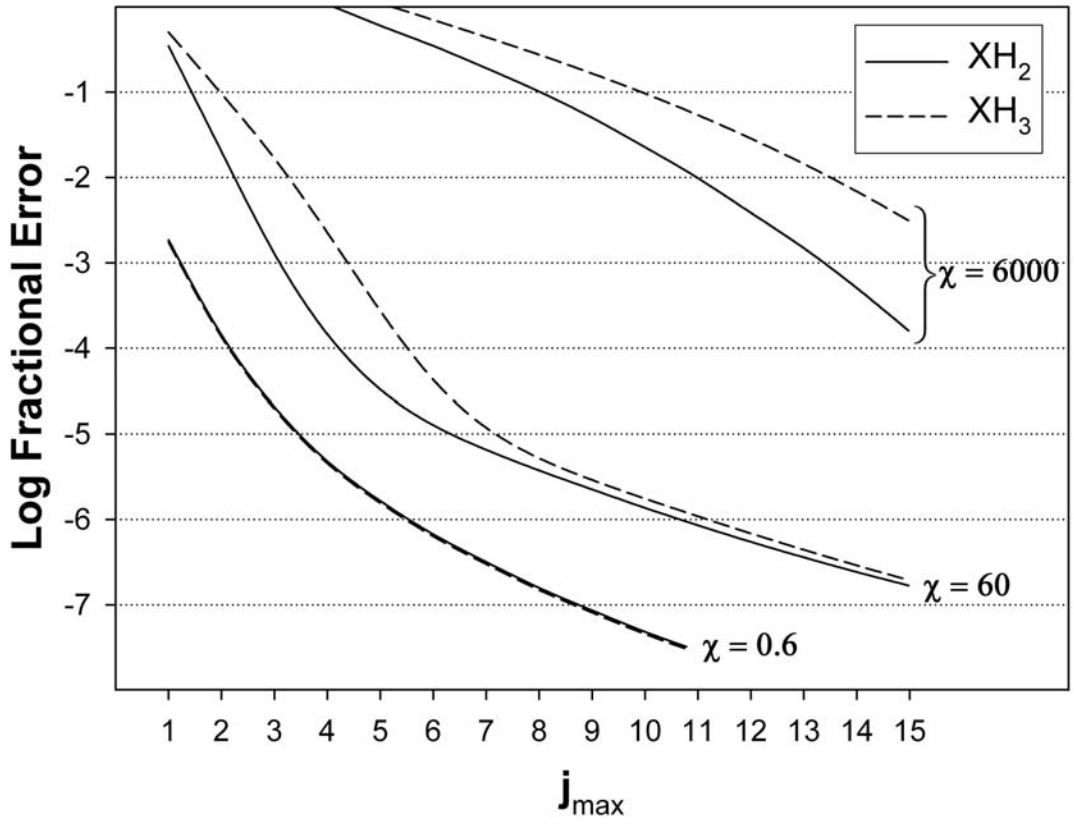

Figure 2.8. The log of the fractional error (base 10) as a function of j_{max} for several values of stiffness χ. Larger χ converges more slowly as the basis set is optimized for floppy intermolecular potentials. For a given χ, it is worth noting that the n = 2 and n = 3 calculations converge almost at the same rate, which bodes favorably for scaling to a larger number of H atoms.

References

[1] V. Spirko, J. Mol. Spectrosc. **101**, 30 (1983).

[2] S. Urban, R. Dcunha, K. N. Rao, and D. Papousek, Can. J. Phys. **62**, 1775 (1984).

[3] S. L. Coy and K. K. Lehmann, Spectroc. Acta Pt. A-Molec. Biomolec. Spectr. **45**, 47 (1989).

[4] V. Spirko and W. P. Kraemer, J. Mol. Spectrosc. **133**, 331 (1989).

[5] S. Urban, N. Tu, K. N. Rao, and G. Guelachvili, J. Mol. Spectrosc. **133**, 312 (1989).

[6] I. Kleiner, G. Tarrago, and L. R. Brown, J. Mol. Spectrosc. **173**, 120 (1995).

[7] I. Kleiner, L. R. Brown, G. Tarrago, Q. L. Kou, N. Picque, G. Guelachvili, V. Dana, and J. Y. Mandin, J. Mol. Spectrosc. **193**, 46 (1999).

[8] C. Cottaz, I. Kleiner, G. Tarrago, L. R. Brown, J. S. Margolis, R. L. Poynter, H. M. Pickett, T. Fouchet, P. Drossart, and E. Lellouch, J. Mol. Spectrosc. **203**, 285 (2000).

[9] J. Tang and T. Oka, J. Mol. Spectrosc. **196**, 120 (1999).

[10] D. J. Liu, T. Oka, and T. J. Sears, J. Chem. Phys. **84**, 1312 (1986).

[11] P. B. Davies, S. A. Johnson, P. A. Hamilton, and T. J. Sears, Chem. Phys. **108**, 335 (1986).

[12] M. H. Begemann and R. J. Saykally, J. Chem. Phys. **82**, 3570 (1985).

[13] M. Gruebele, M. Polak, and R. J. Saykally, J. Chem. Phys. **87**, 3347 (1987).

[14] H. Petek, D. J. Nesbitt, J. C. Owrutsky, C. S. Gudeman, X. Yang, D. O. Harris, C. B. Moore, and R. J. Saykally, J. Chem. Phys. **92**, 3257 (1990).

[15] M. Araki, H. Ozeki, and S. Saito, J. Chem. Phys. **109**, 5707 (1998).

[16] M. Araki, H. Ozeki, and S. Saito, Mol. Phys. **97**, 177 (1999).

[17] M. Farnik, S. Davis, and D. J. Nesbitt, Faraday Discuss. **118**, 63 (2001).

[18] M. J. Weida and D. J. Nesbitt, J. Chem. Phys. **110**, 156 (1999).

[19] D. T. Anderson, M. Schuder, and D. J. Nesbitt, Chem. Phys. **239**, 253 (1998).

[20] D. T. Anderson, S. Davis, and D. J. Nesbitt, J. Chem. Phys. **104**, 6225 (1996).

[21] D. H. Zhang, Q. Wu, J. Z. H. Zhang, M. Vondirke, and Z. Bacic, J. Chem. Phys. **102**, 2315 (1995).

[22] G. W. M. Vissers, G. C. Groenenboom, and A. van der Avoird, J. Chem. Phys. **119**, 277 (2003).

[23] Y. H. Qiu and Z. Bacic, J. Chem. Phys. **106**, 2158 (1997).

[24] Y. H. Qiu, J. Z. H. Zhang, and Z. Bacic, J. Chem. Phys. **108**, 4804 (1998).

[25] P. Eggert, A. Viel, and C. Leforestier, Comput. Phys. Commun. **128**, 315 (2000).

[26] N. Goldman, R. S. Fellers, C. Leforestier, and R. J. Saykally, J. Phys. Chem. A **105**, 515 (2001).

[27] F. N. Keutsch, N. Goldman, H. A. Harker, C. Leforestier, and R. J. Saykally, Mol. Phys. **101**, 3477 (2003).

[28] N. Goldman, C. Leforestier, and R. J. Saykally, J. Phys. Chem. A **108**, 787 (2004).

[29] J. S. Tse, D. D. Klug, and K. Laasonen, Phys. Rev. Lett. **74**, 876 (1995).

[30] P. R. Schreiner, S. J. Kim, H. F. Schaefer, and P. V. Schleyer, J. Chem. Phys. **99**, 3716 (1993).

[31] H. Muller and W. Kutzelnigg, Phys. Chem. Chem. Phys. **2**, 2061 (2000).

[32] D. Marx and M. Parrinello, Nature **375**, 216 (1995).

[33] G. A. Olah, N. Hartz, G. Rasul, and G. K. S. Prakash, J. Am. Chem. Soc. **117**, 1336 (1995).

[34] G. A. Olah and G. Rasul, Accounts Chem. Res. **30**, 245 (1997).

[35] E. Herbst, S. Green, P. Thaddeus, and W. Klemperer, Astrophys. J., 503 (1977).

[36] D. Talbi and R. P. Saxon, Astron. Astrophys. **261**, 671 (1992).

[37] A. Gamba, G. Morosi, and M. Simonetta, Chem. Phys. Lett. **3**, 20 (1969).

[38] G. A. Olah, G. Klopman, and R. H. Schlosberg, J. Am. Chem. Soc. **91**, 3261 (1969).

[39] W. T. A. M. Van der Lugt and P. Ros, Chem. Phys. Lett. **4**, 389 (1969).

[40] W. A. Lathan, W. J. Here, and J. A. People, J. Am. Chem. Soc. **93**, 808 (1971).

[41] H. Muller, W. Kutzelnigg, J. Noga, and W. Klopper, J. Chem. Phys. **106**, 1863 (1997).

[42] A. Brown, B. J. Braams, K. Christoffel, Z. Jin, and J. M. Bowman, J. Chem. Phys. **119**, 8790 (2003).

[43] A. Brown, A. B. McCoy, B. J. Braams, Z. Jin, and J. M. Bowman, J. Chem. Phys. **121**, 4105 (2004).

[44] V. L. Tal'rose and A. K. Lyubimova, Dokl. Akad. Nauk SSSR **86**, 909 (1952).

[45] E. T. White, J. Tang, and T. Oka, Science **284**, 135 (1999).

[46] P. R. Schreiner, Angew. Chem.-Int. Edit. **39**, 3239 (2000).

[47] A. Komornicki and D. A. Dixon, J. Chem. Phys. **86**, 5625 (1987).

[48] W. Klopper and W. Kutzelnigg, J. Phys. Chem. **94**, 5625 (1990).

[49] S. J. Collins and P. J. Omalley, Chem. Phys. Lett. **228**, 246 (1994).

[50] M. Kolbuszewski and P. R. Bunker, J. Chem. Phys. **105**, 3649 (1996).

[51] A. L. L. East, M. Kolbuszewski, and P. R. Bunker, J. Phys. Chem. A **101**, 6746 (1997).

[52] P. R. Bunker, B. Ostojic, and S. Yurchenko, J. Mol. Struct. **695**, 253 (2004).

[53] G. A. Olah, Angew. Chem. Int. Ed. Engl. **34**, 1393 (1995).

[54] A. B. McCoy, B. J. Braams, A. Brown, X. C. Huang, Z. Jin, and J. M. Bowman, J. Phys. Chem. A **108**, 4991 (2004).

[55] C. Savage, F. Dong, and D. J. Nesbitt, work in progress.

[56] R. N. Zare, *Angular Momentum: Understanding Spatial Aspects in Chemistry and Physics*. (John Wiley & Sons, New York, 1988).

[57] F. A. Cotton, *Chemical Applications of Group Theory*, 3rd ed. (Wiley, New York, 1990).

[58] P. R. Bunker, *Molecular Symmetry and Spectrosopy*, 2nd ed. (NRC Research Press, Ottawa, 1998).

[59] P. R. Bunker and P. Jensen, *Molecular Symmetry and Spectroscopy*, 2nd ed. (NRC Research Press, Ottawa, 1998).

[60] J. F. Cornwell, *Group Theory in Physics: An Introduction*. (Academic Press, San Diego, 1987).

[61] I. G. Kaplan, *Symmetry of Many-electron Systems*. (Academic Press, New York, 1975).

[62] J. M. Hutson, in *Advances in Molecular Vibrations and Collision Dynamics*, edited by J. M. Bowman (JAI Press, 1990), Vol. 1A.

[63] K. Schulten and R. G. Gordon, J. Math. Phys. **16**, 1961 (1975).

[64] O. L. Polyansky, P. Jensen, and J. Tennyson, J. Chem. Phys. **105**, 6490 (1996).

[65] T. Rajamaki, A. Miani, and L. Halonen, J. Chem. Phys. **118**, 10929 (2003).

[66] X. C. Huang, S. Carter, and J. Bowman, J. Chem. Phys. **118**, 5431 (2003).

[67] T. Rajamaki, A. Miani, and L. Halonen, J. Chem. Phys. **118**, 6358 (2003).

Chapter 3: Large amplitude quantum mechanics in polyatomic hydrides: II. A particle-on-a-sphere model for XH_n (n = 4,5)

I. Introduction

The quantum mechanics of large amplitude motion has been the focus of experimental and theoretical work for many years. Advances in high-resolution rotational/vibrational spectroscopy have given much experimental evidence of large amplitude dynamics in molecules and ions. The tunneling inversion in ammonia[1-8] (NH_3) and hydronium ion[9-16] (H_3O^+) are two such examples of well-studied systems that exhibit large-amplitude motion. In systems with few enough degrees of freedom ($N \leq 6$), the exact quantum nuclear dynamics can be solved in full dimensionality. For example, this has been achieved in landmark studies of HF and HCl dimers[17-20], as well as reduced-dimensionality extensions to H_2O dimer[21-24] using six-dimensional (6D) intermolecular coordinates with semirigid H_2O molecules.

However, as molecular systems increase in size and complexity, standard quantum-calculation methods rapidly become too difficult to permit treatment in full dimensionality. This is particularly unfortunate from a chemical physics perspective, as some of the most interesting dynamical processes, such as the facile exchange of identical H atoms predicted to occur in protonated methane[25,26], begin to emerge in these larger systems. Furthermore, the level of theoretical difficulty increases rapidly with total angular momentum, J, which makes the high-resolution interpretation of

rovibrational patterns especially challenging under all but the lowest temperature conditions. In such cases, a more realistic first spectroscopic goal is to learn how to predict and interpret the experimentally observed energy level patterns and thereby infer new insights about the actual intermolecular dynamics.

As a specific target of interest, protonated methane (CH_5^+) represents an extreme case of large-amplitude quantum dynamics with a rich scientific history. The addition of a single proton to relatively "rigid" methane, CH_4, creates the highly fluxional CH_5^+ molecule where simple Lewis octet bonding motifs do not apply. Five H atoms are connected by 4 electron pairs and require the presence of "three-center-two-electron bonds" ("3c-2e").[27] Such 3c-2e bonding motifs correspond to a special class of hypercoordinated carbocations, which are extremely important reactive intermediates in acid-catalyzed electrophilic reactions,[28,29] for which CH_5^+ represents the simplest prototypic "superacid." CH_5^+ is also believed to be a key intermediate in the synthesis of polyatomic organic species in cold interstellar clouds,[30,31] further motivating astrophysical interest in this simple, but spectroscopically elusive, molecular ion.

From a theoretical perspective, CH_5^+ is interesting because its relatively small size and high symmetry make quantum mechanical calculations of the potential energy surface computationally tractable, though still quite challenging. The most recent high-level calculations suggest that there are, in fact, three low-lying energy structures within about 1 kcal/mol of each other.[25,32-34] Furthermore, if zero point energy is taken into account, these three configurations are all extensively sampled by the ground-state wave function. Stated simply, the barrier to rearrangement between

these low-lying minima is considerably lower than the quantum zero-point vibrational energy, thus permitting facile intramolecular scrambling of the hydrogen atoms[32] to take place.

From a spectroscopic perspective, the highly fluxional, nonclassical nature of CH_5^+ begins to account for long-standing difficulties in interpreting a high-resolution spectrum. Despite its initial observation as a highly abundant ion in mass spectrometers in the early 1950s,[35] optical detection and characterization of CH_5^+ eluded spectroscopists for another 50 years. The breakthrough came in 1999 from Oka and coworkers, who obtained a spectrum[36] in the CH-stretch region by exploiting velocity modulation methods. They made convincing arguments that the extensive, albeit rovibrationally unassigned, spectrum belonged predominantly to CH_5^+. Recently, exciting progress has been made in obtaining broadband IR action spectra of CH_5^+ by Asvany and coworkers.[37] These spectra yield unresolved vibrational structure from 3500 down to < 1000 cm^{-1}. Our group has also obtained high-resolution jet-cooled IR spectra[38] in the 2820 - 3050 cm^{-1} region.

Desire to help in this assignment process has naturally led to considerable emphasis on direct calculation of near IR spectra from first principles. However, despite intense theoretical efforts directed toward CH_5^+[25,32,39-51] and the recent availability of a high-level potential surface,[33,34] high resolution spectra based on fully converged exact rovibrational energy levels have proven extremely challenging to calculate. The reasons behind this challenge are at least twofold. On the experimental side, large zero-point energies and lack of any substantial barriers between H atom interchange lead to extensive delocalization in the wave function. This in turn can

result in large tunneling splittings and rovibrational energy patterns profoundly perturbed away from rigid rotor expectations, especially for the J states thermally populated under discharge conditions. From a theoretical perspective, however, the number of degrees of freedom for CH_5^+ is already too large (15D) to achieve fully converged quantum calculation of the rovibrational energy levels in full dimensionality.

In Chapter 2,[52] the particle-on-a-sphere (POS) model was introduced as an alternative method for calculating the energies and wave functions for molecules with large amplitude motion in a large number of degrees of freedom. The model was tested on relatively "floppy" molecules (i.e., exhibiting large amplitude bending dynamics) with considerable success for di- and tri-hydride species. In the XH_2 case, the convergence of the energy levels was readily achieved for $J \leq 2$, with the rovibrational levels converged to near spectroscopic ($< 10^{-4}$ cm^{-1}) accuracy. By way of example, Figure 3.1a displays rovibrational energies of the lowest J = 0 and J = 1 states for XH_2 as a function of j_{max}. Here j_{max} is the maximum angular momentum for a single H basis state and therefore a measure of the variational basis set size, where specific parameters for the POS potential and equilibrium bond lengths/bond angles for XH_2 are closely modeled after H_2O. As expected, the variational energies decrease with increasing basis set size, converging on the complete basis set limit to the ground, fundamental, and 1st overtone excited bending states. Agreement at higher resolution is also shown (see Figure 3.1a inset) with the predicted rotational energies for a rigid asymmetric top with H_2O equilibrium bond lengths/angles. As a more significant challenge to the model, energy levels could be similarly converged for

floppy XH_3 molecules modeled after H_3O^+. Indeed, the expected progression of umbrella inversion levels was reproduced even for potentials modeled after the relatively high-tunneling barrier case of NH_3. This pattern is summarized in Figure 3.1b, where the observed tunneling splittings are given for each pair of converged J = 0 energy levels and exhibit a dramatic increase with energy above the barrier. It is worth noting that apparent deviations from this pattern simply arise from a doubly degenerate asymmetric bend state occurring near 5000 cm^-1, which, as expected, exhibits a "normal" tunneling splitting comparable to the ground state.

Most important, the POS model also provides access to rovibrational quantum *eigenfunctions* as well as *eigenenergies*. By way of example, Figure 3.2a displays a 1D projection of the full 4D wavefunction for XH_2 onto the γ coordinate, where γ is the H-X-H bending angle between the two hydrogens. For comparison, I also show a corresponding slice through the J = 0 wave function (shaded in grey) obtained from Diffusion Monte Carlo (DMC) methods, where the stiffness (i.e., anisotropy of the potential) χ of the intermolecular bend potential is systematically incremented between each plot ($\chi \approx 3700$ corresponds to the bending potential in H_2O). Agreement between POS and DMC predictions for XH_2 is excellent, limited only by the intrinsic statistical nature of the DMC wave functions. Similar levels of agreement are evidenced between 1D representations (solid points) of the full 6D XH_3 wave functions and statistical DMC calculations (shaded in grey), which are plotted in Figure 3.2b as a function of increasing stiffness of the intermolecular potential. Here γ refers to the angle between *any pair* of H's with respect to the central atom, and thus both the POS and DMC $\Psi(\gamma)$ should be more appropriately thought of as

pairwise angular-distribution functions. As expected, each of the hydrogen pairs become more tightly correlated with increasing potential stiffness, with the angle strongly localizing around the equilibrium value (104^o for XH_2 and 108^o for XH_3).

However, the potential promise in such a POS approach lies in permitting one to theoretically move past n = 2 and n = 3 to more challenging systems of higher dimensionality, which represent the focus of the present work. The organization of this chapter is as follows. Section II reviews the general theoretical background necessary for efficiently solving the POS problem and focuses explicitly on methods used in this work for the n = 4 and n = 5 particle system. Sections III and IV discuss applications of the particle-on-a-sphere model to two test systems, n = 4 (XH_4) and n = 5 (XH_5), respectively. I specifically model the rotation-bending potentials on suitably scaled versions of i) relatively "stiff" species such as methane (CH_4) and ii) highly fluxional species such as protonated methane (CH_5^+). In Section V, I compare the n = 5 POS predictions with other large amplitude theoretical results for CH_5^+. Concluding comments are summarized in Section VI.

II. Theoretical Background

As discussed more fully in Chapter 2, the POS model assumes a massive central atom ($m_X >> m_H$) and effectively averages over the high-frequency radial stretching of the X-H bond lengths, so that the resulting 2D angular coordinates can be simply represented as motion constrained to the surface of a sphere. The reduction of dimensionality can be simply achieved by freezing the radial coordinates in the full dimensional potential at some average value, or more reasonably, by adiabatically adjusting the radial coordinates to a minimum energy as a function of the remaining

2n angular coordinates. The justification for the latter approach is clearly superior, and in the case of CH_5^+, takes advantage of both the greater than twofold difference in CH stretch vs. torsional / bending frequencies as well as the relatively small spread (< 0.015 Å) in CH equilibrium bond lengths observed for H atoms at typical zero-point energies. The resulting Hamiltonian for the large-amplitude angular motion of n particles can then be simply expressed as

$$H_{POS} = \sum_{i=1}^{n} b_i \hat{j}_i^2 + \hat{V}(\Omega), \qquad (3.1)$$

where $\hat{j}_i$ is the angular momentum of the i^{th} hydrogen with respect to the central stationery atom, and b_i is the rotational constant for motion on the sphere. $\hat{V}(\Omega)$ is the potential describing the H atom interactions, where Ω is a 2n dimensional vector of all n H atom angular coordinates.

One key advantage of this approach is that there is no distinction between angular bending and end-over-end tumbling degrees of freedom. Thus the solutions treat vibration and rotation on a completely equivalent footing (i.e., there are no perturbative assumptions about the magnitude of Coriolis interactions). The method should work best in the limit of extreme large-amplitude quantum motion (e.g., CH_5^+) and relatively weak interparticle interactions, as opposed to the standard decoupling of Ψ_{tot} into a product of rotational and vibrational wave functions describing small amplitude displacements with respect to a zeroth-order body-fixed frame. For example, such a method would be particularly well suited for describing the quantum motion of n He atoms solvating a heavy central atom, as in van der Waals clusters of $XeHe_n$. However, the corresponding cost of equality with respect to rotation/vibration

internal coordinates is a much more rapid scaling of the variational problem with number of particles. Thus, although n = 2 (4D) and n = 3 (6D) systems are theoretically tractable from a variety of approaches, extension of the POS methods to n = 4 and 5 invoke special considerations, which are described below.

A. Primitive and coupled basis sets

As discussed earlier,[52] the goal of the POS model is to describe floppy molecules such as CH_5^+, where the Coriolis coupling between overall rotation and H-X-H angular vibrations is large. In the "floppy" limit, where the potential V(Ω) can be viewed as a perturbation of freely rotating molecules, a natural basis in which to expand the Hamiltonian is simply a direct product of rigid rotor functions:

$$\prod_{i=1}^{n} \left| j_i m_i \right\rangle, \tag{3.2}$$

The full n-particle Hamiltonian is diagonal in total J^2 and J_z, so it is advantageous to transform this primitive basis into an equivalent coupled representation[53] that permits matrix construction and diagonalization for each quantum number J. For increased speed in the potential matrix element evaluation, my choice of a coupled basis for the XH_4 system is

$$\left| \left(\left(j_1 j_2 \right) j_{12} \left(j_3 j_4 \right) j_{34} \right) JM \right\rangle, \tag{3.3}$$

and for the XH_5 system,

$$\left| \left(\left(j_1 \left(j_2 j_3 \right) j_{23} \right) j_{123} \left(j_4 j_5 \right) j_{45} \right) JM \right\rangle, \tag{3.4}$$

In these expressions, j_i represents the angular momentum for the i^{th} particle, j_{ij} is the vector sum of j_i and j_j, parentheses denote the coupling order, and J and M represent the total angular-momentum quantum number and projection on the z axis,

respectively. In the absence of external fields, all M states for a given J are degenerate; thus M can be taken to be 0 for a further factor of 2J + 1 reduction of the Hamiltonian matrix size. To create a basis set for a given J, the primitive free-particle angular momenta are restricted to $j = [0, j_{max}]$.

B. Basis set symmetrization and permutation inversion

To achieve a crucial reduction in computational effort, the Hamiltonian is block diagonalized using group theoretical methods.[54,55] This involves the use of permutation inversion theory[55] to create symmetry-adapted linear combinations (SALCs) of the coupled basis functions that transform according to each permutation inversion symmetry group. The permutation inversion group for XH_4 is G_{48} (isomorphic to the direct product T_d symmetry group with the inversion operation), which yields 10 irreducible representations: A_1^+, A_2^+, E^+, F_1^+, F_2^+, A_1^-, A_2^-, E^-, F_1^-, and F_2^- with nuclear spin weights of 5:1:3 for A_1:E:F_2, respectively, for spin ½ Hs. For XH_5, the permutation inversion group is G_{240}, characterized by 14 irreducible representations: A_1^+, A_2^+, G_1^+, G_2^+, H_1^+, H_2^+, I^+, A_1^-, A_2^-, G_1^-, G_2^-, H_1^-, H_2^-, and I^- with nuclear spin weights of 6:4:2 for A_2:G_2:H_2 symmetries,[50] respectively. Using standard projection operator techniques,[55] the coupled basis functions are transformed into orthonormal SALCs of each irreducible representation. For XH_5 in particular, these irreducible representations reflect high levels of intrinsic degeneracy, specifically E = 2, F = 3, G = 4, H = 5, and I = 6. By exploiting this degeneracy and including only one of the resultant SALCs for each irreducible representation,[56,57] I therefore dramatically reduce the basis set size.

It is important to note that while such a symmetrization need only be performed once, the creation of these SALCs currently represents the limiting step in POS extension to even larger basis sets. The nested loops required to symmetrize and orthogonalize the SALCs quickly grow extremely rapidly with increasing n and j_{max}. Specifically, the time required to create an orthonormal SALC basis set of a *single* irreducible representation increases as $(j_{max})^7$. By way of example, in order to create an orthonormal basis set of SALCs for *one* symmetry with n = 5, J = 0, j_{max} = 5 ($N_{coupled} \approx 75{,}000$) requires about 1 month to symmetrize and orthogonalize on a 2.4 GHz Intel CPU. This translates into a current upper limit for the XH_5 problem of j_{max} = 5, 4 and 3 for J = 0, 1, and 2, respectively. However, this process may be significantly accelerated by parallelization of the code, which represents one of several ongoing directions of further exploration.

C. Matrix element evaluation

The use of symmetrized basis functions significantly decreases matrix size for large n and j_{max}, reducing both memory requirements to store the matrix as well as computational effort for matrix diagonalization. However, calculating the Hamiltonian matrix in a symmetrized basis still requires significant CPU time. Matrix element evaluation in the SALC basis requires calculation of the integral $\left\langle i\left|\hat{H}\right|i'\right\rangle$, that is expanded into a sum of integrals over the direct product of each term in the SALCs. Naively, when the basis function $\left|i\right\rangle$ is a SALC created from a sum of coupled basis functions and the Hamiltonian matrix is too large to store in memory, integral

evaluation might be expected to occur via a process that scales quadratically with SALC size:

$$\left\langle i\left|\hat{H}\right|i'\right\rangle = \sum_{k=1}^{M_{SALC}} \sum_{l=1}^{M_{SALC}} C_k^* C_l \left\langle k\left|\hat{H}\right|l\right\rangle, \tag{3.5}$$

where k and l are indices over each of the M_{SALC} coupled basis functions in each of the N_{SALC} SALC basis functions. Consequently, creation of the symmetrized Hamiltonian matrix would increase roughly as the 4th power, *i.e.,* $O(N^4)$, of basis set size. More specifically, the number of evaluation of integrals required is ½ x N_{SALC}^2 x M_{SALC}^2, where N_{SALC} is the number of SALC basis function for a given symmetry and M_{SALC} is the number of coupled basis functions in the linear combination that comprises the SALC. Even for small values of j_{max}, this number becomes quite large, requiring for J = 0, j_{max} = 5, and n = 5 on the order of 10^9 integral evaluations to create the Hamiltonian matrix; this calculation requires 1 to 2 weeks on a 2.4 GHz Intel CPU, even with analytic matrix elements.

However, by changing the order of evaluation, the matrix element evaluation can be expressed as an $O(N^3)$ operation, which is significantly faster when there are a large number of symmetries into which the SALCs can be distributed. Rather than calculating the full N_{SALC} x N_{SALC} Hamiltonian matrix ($\mathbf{H}_\Gamma$) from direct products of SALCs, the matrix can be expressed as $\mathbf{H}_\Gamma = \mathbf{S}_\Gamma^{\mathbf{T}} \cdot \mathbf{H}' \cdot \mathbf{S}_\Gamma$, where $\mathbf{H}'$ is the nonsparse $N_{coupled}$ x $N_{coupled}$ unsymmetrized Hamiltonian, and $\mathbf{S}_\Gamma$ is a N_{SALC} x $N_{coupled}$ sparse matrix that transforms the coupled (unsymmetrized) basis functions into the SALC basis set. The advantage is that $\mathbf{S}_\Gamma$ is quite sparse (e.g., for XH_5, ~95% of the matrix elements are zero); thus computing terms in $\mathbf{H}'$ (which itself is too large to store for

typical $N_{coupled} \approx 75{,}000$), multiplied by nonzero terms in $\mathbf{S}_\Gamma$ is easily accomplished. Ultimately, this rearrangement of operations results in $N_{coupled}$ x N_{SALC} x M_{SALC} + N_{SALC}^2 x M_{SALC} matrix element evaluations, i.e., reducing to an $O(N^3)$ algorithm. This is approximately $(N_{SALC} \times M_{SALC})/(N_{coupled} + N_{SALC})$ times faster than the naive direct product approach, resulting in a 50- to 100-fold increase in speed for large basis sets with many symmetries.

By careful choice of the potential, the evaluation of both the kinetic energy and potential energy matrix elements is analytic. Since the basis set is diagonal in j_i^2, the kinetic energy operator matrix elements satisfy this requirement automatically. For XH_n, these matrix elements simply are:

$$\left\langle i\left|\hat{T}\right|i'\right\rangle = b\sum_{k=1}^{n}\delta_{ii'}\,j_k\left(j_k+1\right), \tag{3.6}$$

where b is the internal X-H rotational constant and j_k is the angular momentum of the k^{th} X-H rotor. Calculation of the corresponding potential matrix elements involves substantially greater effort. Evaluation of the potential by standard quadrature methods requires Q^{2n} calculations per matrix element, where Q is the number of points on a potential grid and n is the number of hydrogens on the sphere, which scales too rapidly when n > 3. To proceed, therefore, I consider the potential as a multibody expansion, *i.e.,*

$$V(\Omega) = \sum_{i<j}^{n} V^{(2)}(\Omega_i,\Omega_j) + \sum_{i<j<k}^{n} V^{(3)}(\Omega_i,\Omega_j,\Omega_k) + \sum_{i<j<k<l}^{n} V^{(4)}(\Omega_i,\Omega_j,\Omega_k,\Omega_l) + \ldots \tag{3.7}$$

where each successive term represents a sum over all 2-body, 3-body, 4-body, etc., contributions. As a major simplification, I restrict this expansion to the first term, i.e.,

only considering linear combinations of pairwise additive intermolecular potentials between each particle that depends only on the angle between pairs of particles:

$$V(\Omega) = \sum_{i<j}^{n} V^{(2)}\left(\gamma_{ij}\right), \tag{3.8}$$

where γ_{ij} is the H-X-H angle between the i^{th} and j^{th} hydrogen and $V^{(2)}$ is a sum of Legendre polynomials in γ_{ij}. By truncating after the first term in the expansion, the work required to calculate a potential matrix element only grows as n^2 (the number of pairwise interaction for n particles), as opposed to Q^{2n} with numerical quadrature (Q being the number of quadrature points per dimension). As a further bonus, if I expand any pairwise additive potential in a sum of Legendre polynomials, the matrix element for each term can be calculated analytically via Clebsh-Gordan angular momentum algebra.[52,58] The matrix element between two coupled particles and a Legendre function are the Percival-Seaton coefficients[58], which are simply sums over 3- and 6-J symbols. Thus one has gained the advantage of both an n^2 vs. Q^{2n} scaling of integral evaluations as well as a much more efficient analytic evaluation of each matrix element. Although such a pairwise additive approximation to the potential was not essential for calculations in n = 2 and n = 3 systems, it proves absolutely crucial to extension to the larger systems of interest such as XH_4 and XH_5.

D. Rigid-body DMC

In Chapter 2, direct comparison between the POS model and exact full dimensional quantum mechanical calculations proved feasible for low J states in XH_2 and XH_3, due to an acceptably small number of degrees of freedom. For the much more computationally demanding XH_4 and XH_5 systems, exact full dimensional

quantum calculations for J > 0 are simply not available for benchmarking the POS calculations. However, calculations for the nodeless ground rovibrational state (J = 0) are feasible for n = 4 and 5 via DMC methods, which scale much more favorably than variational methods for systems of high dimensionality (roughly linearly in 2n). Thus, I can test the convergence of the J = 0 POS methods against DMC results, specifically exploiting the "rigid body" formulation (RBDMC) to constrain the radial stretching coordinate for the diffusing 2n dimensional "walkers."[59-62]

By way of example, Figures 3.1a and 3.1b show the energies of XH_2 and XH_3 as a function of j_{max} (i.e., basis set size). As j_{max} is increased, the energy of each state decreases variationally, with the ground state J = 0 energy converging on the DMC result (dotted line). The insets show a more detailed picture of agreement between variational POS and DMC POS methods. For both XH_2 and XH_3 calculations, the converged variational calculation equals the DMC result within 1σ statistical uncertainty, where the DMC error estimate reflects 10 ensembles of 2000 walker trajectories starting with different initial conditions.

The distribution of walker angular coordinates also provides a statistical sampling of the wave function. Figure 3.2a displays the DMC wave function for walkers at an angle γ apart from each other in XH_2, binned in 1^o increments and normalized to unity; the black dots represent the wave function results calculated by the variational POS method. Note that when the angular stiffness (χ) is low, the two H atoms rotate independently of each other and the distribution reduces to $sin(\gamma)$, i.e., a uniform sampling of interangular coordinates on a sphere. However, as the stiffness χ is increased, the wave function becomes localized around the equilibrium angle

corresponding to H_2O ($\gamma_o = 104^o$). A similar pair of POS and DMC wavefunction plots for XH_3 is shown in Figure 3.2b, where γ_{ij} represents the angle between *any* two of the particles. Here the equilibrium angle corresponds to that of NH_3 ($\gamma_o = 108^o$), and thus the projection of the wave function peaks near 108^o for a stiff (i.e., large χ) potential and becomes less localized as the potential is softened. Agreement between the DMC and variationally calculated POS wave functions for each value of χ is exact within statistical uncertainty limits.

III. Four Particles-On-A-Sphere(XH_4)

Building on the above successes for XH_2 and XH_3, the next test system to investigate with the POS model is XH_4. The rotor and bending potential parameters ($b_i = 16.63$ cm^{-1} and $\gamma_0 = 109.47^o$) are specifically chosen to recapitulate the equilibrium structure of methane, CH_4, with a $V^{(2)}(\gamma)$ stiffness in the pairwise potential chosen to yield the correct CH-bending frequencies. As I will not in general be able to converge POS calculations for such a strongly localized intermolecular potential, it will be useful to introduce a scaled function, $V_{scaled}(\gamma) = \alpha V^{(2)}(\gamma)$, to reflect an angular potential "softer" than methane by a multiplicative factor of α. In the stiff limit ($\alpha = 1$), my POS model of methane should yield a spherical top rotor with two ν_2 and ν_4 bending states corresponding to the E (~1526 cm^{-1}) and F_2 (~1306 cm^{-1}) symmetry vibrations, respectively. At higher resolution, the 2J + 1 K level degeneracy of a rigid spherical top will be lifted by centrifugal interactions in rotationally excited states, which will lead to additional rotational fine structure for J

> 0. See Table 3.1 for a list of the coefficients used in the Legendre expansion for the CH_4 potential.

I begin the POS investigation of XH_4 by exploring the rate of convergence as a function of basis set size. In Figure 3.3, the vibrationless state energies for J = 0 - 4 are shown as a function of j_{max}, based on a scaled methane potential with a stiffness of $\alpha = 0.033$. By way of comparison, the dashed line in Figure 3.3 represents the J = 0 DMC ground-state energy for the same potential; the inset illustrates agreement of eigenenergies within the 1σ error of the DMC calculation. The size of the basis set increases extremely rapidly with j_{max}. For example, for J = 4, $N_{coupled}$ increases from 16,429 to 39,046 to 80,866 for j_{max} = 5, 6, and 7, respectively. As a result, j_{max} = 7 is the largest calculation that can be performed for the 4 particle POS model with J = 4 (for J = 0, j_{max} can be as large as 9). This choice of α reflects a bending potential that is ~30-fold softer than actual methane, but nevertheless permits systematic convergence of POS calculations for a series of rotationally excited states within computational limits of time and resources. The plots in Figure 3.3 demonstrate that as j_{max} is increased up to the maximum value, the variational POS energies decrease monotonically to an asymptotically converged value. If I empirically characterize convergence by the incremental decrease in POS eigenenergies for an incremental j_{max}- 1 to j_{max} increase in basis set size, then j_{max} = 7 corresponds to a 0.001 cm^{-1} convergence for the lowest rotational state J = 0, with only slightly reduced (0.01 cm^{-1}) levels of convergence for excited rotational states J = 1 - 4. At an even finer level of detail, the j_{max} = 7 energies clearly demonstrate converged spherical top rotational

fine structure, with centrifugal distortion lifting the nominally degenerate 2J + 1 K energy levels for each J.

The progression of the v = 0 energies as a function of α is shown in Figure 3.4a, as the CH_4-like potential is increased from $\alpha = 0.0001$ (i.e., nearly a free rotor limit) up to the stiffest calculations ($\alpha = 0.033$) that can be currently converged. In the $\alpha = 0.0001$ limit, the 4 individual C-H rotors rotate more or less independently, resulting in energy-level spacings characteristic of a large single C-H rotor constant. As the potential is stiffened, these states converge onto what approximates a ~J(J + 1) spherical top progression of energies, with the fine structure splittings in Figure 3.4a (shown in detail in Figure 3.4b) due to centrifugal bend-rotation coupling. Noteworthy is that while the effective B for $\alpha = 0.033$ is only 20% above the true value, the fine structure splittings are ~500 times larger, albeit in the correct symmetry order with even qualitatively correct splitting ratios. This implies that even for a 30-fold scaled-down internal anisotropy, the end-over-end tumbling structure of the 4 particle system is already well defined, with the fine structure effects requiring much larger basis sets (as well as the inclusion of radial degrees of freedom) to converge.

In addition to comparison of POS vs. experimental rotational energies in the ground vibrational state, I can also inspect the low frequency vibrational states of methane (ν_2,E and ν_4,F_2) in the rotationless J = 0 level (see Figure 3.5). Since it was possible to use a larger j_{max} for J = 0 calculations, the energies have been converged with a 10-fold stiffer $\alpha = 0.33$ than for J > 0, but still somewhat short of the full methane potential. As the potential approaches the full methane stiffness, the energy

of the ν_2,E and ν_4,F_2 vibrations increase monotonically towards experimental values,[63] with the order of the ν_2,E and ν_4,F_2 vibrations maintained even for substantially floppier potentials. Similar qualitative agreement is noted with two quanta of bending energy, as shown in Figure 3.5 for $2\nu_2$,A_1 + E, $\nu_2 + \nu_4$,F_1 + F_2, and $2\nu_4$,A_1 + E + F_2. Analogous to the calculations presented earlier, the ordering of the dyads is correctly predicted, with the vibrational fine structure splittings decreasing as the potential stiffens . Although 4 particle POS calculations cannot be fully converged up to $\alpha = 1$, it is important to note that many of the qualitative patterns are already quite visible and correctly predicted at potentials substantially softer than the full potential.

IV. Five Particles-On-A-Sphere (XH_5)

The overall target of the POS model is to expand to 5 particles on a sphere, which I hope will provide initial insight into the challenging fluxional CH_5^+ problem. I model the individual C-H rotor with b = 12.81cm^{-1}, i.e., consistent with expectation values of the C-H bond length from full 15D DMC calculations.[34,64] As discussed earlier in this paper, my choice of i) a pairwise additive potential with ii) each term expressed as a sum of Legendre functions makes matrix element calculation of the potential operator analytic. To take advantage of this, the full 15D MP2/cc-pVTZ Bowman CH_5^+ potential[34] needs to be expressed in this sum of pairwise potentials. To accomplish this, the radial coordinates of the 15D potential are first adiabatically relaxed in the "fast" CH stretch coordinate to create a 10D potential that depends only on the relative angular coordinates. The critical point geometries are shown in Figure

3.6. The minimum energy structure of CH_5^+ on the Bowman potential is of C_s symmetry, consisting of what looks like an H_2 perched on top of a CH_3^+ structure. However, at the wave function level, there is rapid quantum exchange between "H_2" or "CH_3" moieties, resulting in complete delocalization of each of the H atoms between the 120 equivalent geometries separated by low barriers. For example, the H_2 (or CH_3^+) moiety can "rotate" through a C_s transition state (E = 43 cm^{-1}) or "flip" H's between H_2 and CH_3^+ through a slightly higher C_{2v} transition state (E = 192 cm^{-1}). Most importantly, this process ensures that angular geometries and energies of all critical points for the full 15D and reduced 10D potential are identical.

The second step is to represent the 10D potential by a sum of pairwise potentials, which is achieved by least-squares fitting 10,000 randomly selected points with energies below 1,000 cm^{-1}. The energies and angular geometries of these points are then fit to a sum of pairwise terms, with each term described by a sum of Legendre functions (See Table 3.1 for a list of the coefficients used in the Legendre expansion for the CH_5^+ potential). Of crucial relevance is the reproduction quality for critical points and the "flip" and "torsion" reaction paths between C_{2v} and C_s minima. The critical points of the angular coordinates are shown in Figure 3.6 for i) the 10D radially relaxed version of the full 15D Bowman potential and for ii) the pairwise fit potential. Given the enormously simplifying nature of the pairwise additive approximation, the agreement between 10D and pairwise critical points is quite remarkable. Similar accuracy is also demonstrated in Figure 3.7 for both the 10-D potential and the pairwise fit along the C_s (internal rotation) and C_{2v} ("H_2 flip")

reaction paths. Again, the differences between the 10D potential and the pairwise fit are surprisingly small.

The availability of DMC methods provides one more opportunity to test the validity of the pairwise approximation for both the 10D radially relaxed as well as the full 15D potentials. Specifically, DMC is able to calculate the ground state *wave function* at all three levels of dimensionality (POS, 10D and 15D), each of which can then be projected on to the γ coordinate (where γ is the angle between any two particles) for more quantitative comparison. The results from such a comparison are summarized in Figure 3.8, which reveals quite good agreement at the wave function level. (Note that the 10D and 15D histograms are offset from 0 for better visual clarity with respect to the pairwise potential histogram.) The main peak in each of the wave functions near 110^o corresponds to unresolved features due to i) the H-C-H angles in the CH_3^+ motif, as well as ii) the angle between one of the H_2 hydrogens and a CH_3^+ hydrogen. The smaller wavefunction shoulder near 60^o corresponds to contributions from iii) the smaller H-C-H central angle between the H_2 hydrogens. Treatment at the POS, 10D and 15D levels yield reduced interatomic distributions that are nearly identical, and indeed indistinguishable within statistical uncertainty for the pairwise fit and full 10D potential versions of the DMC wave functions. Though clearly not exact, this suggests that the use of a pairwise potential still captures the H-C-H angular correlations at a high level and, at the very least, is not the significant source of error in the reported calculations.

In analogy to the strategy for the n = 4 particle problem, I first look at the ground state (J = 0) zero-point energy for n = 5 particle POS calculations as the

potential (asymptotically the pairwise 10D fit of the full 15D Bowman CH_5^+ potential) is stiffened from $\alpha = 0.0001$ up to $\alpha = 1.0$. Figure 3.9 illustrates the variationally calculated zero-point energy (solid line) from the POS model, with converged DMC energies and uncertainties for the 10D pairwise (solid circles) and nonpairwise 10D potentials (open squares). (The 15D zero-point energy can also be readily calculated from DMC, but is irrelevant for the present comparison due to an additional ~7000 cm^{-1} in the radial stretch coordinates). The agreement between POS eigenvalue predictions for the pairwise and exact 10D results is excellent at low α, confirming the utility of the pairwise approximation to the CH_5^+ potential. Of more quantitative relevance, however, this comparison illustrates the degree of convergence (or lack thereof) of the POS calculations at a *spectroscopic* level as a function of potential stiffness. Up to $\alpha = 0.01$, the ground-state energies appear to be quite converged to < 1 cm^{-1}, with this quality of convergence degrading substantially as α approaches unity.

More specifically, I can monitor the convergence for a particular value of α (0.01) with respect to basis set size (i.e., j_{max}). In Figure 3.10, the ground state energies for each of the 6 nonzero nuclear spin weight symmetries[50] for CH_5^+ are plotted as a function of j_{max}. Note that the totally symmetric ground state (A_1^+), which is the only energy that can be rigorously compared with DMC results (J = 0), is not represented, has zero statistical weight in CH_5^+, and is not shown. Also included along the ordinate axis is the size of the basis set for each j_{max} for J = 0, 1, and 2. Note the rapidly growing size of N_{prim} as j_{max} increases, which is why $j_{max} = 5$ is the largest basis set that can be implemented at the current time for a J = 0 calculation,

with $j_{max} = 4$ and $j_{max} = 3$ for J = 1 and 2, respectively. As mentioned previously, this constraint is due to the maximum size coupled basis set that can currently be symmetrized on a single processor with non-parallelized code.

V. Discussion

The difficult theoretical issues posed by CH_5^+ have been addressed by numerous *ab initio* potential surface investigations over the years; however, efforts to predict detailed rovibrational energy levels for a given potential surface have proven even more challenging. Landmark work by Bunker and co-workers,[50] using a rotation-contortion Hamiltonian,[49] has been used to predict the $J = 0 \leftarrow 1$ microwave spectrum of CH_5^+, exploiting symmetry correlations between the two extremes associated with a rigid C_s and C_{2v} potential minima. In this work, considerable effort was made to calculate energies for states of nonzero statistical weight at a number of different flip and torsion rearrangement barriers, based on a Hamiltonian which adiabatically separates one large amplitude internal contortional mode from the remaining 11 "fast" vibrational modes. The Hamiltonian is a sum H^{rot} (end-over-end tumbling of the molecule), H^{τ} (motion along the contortion degree of freedom), and $H^{rot,\tau}$ (coupling between tumbling and contortion), with all coupling neglected between the "fast" vibrations and overall rotation. As an alternative formulation, the POS model neglects the contributions from only the 5 "fastest" CH-stretching vibrations but does include the 7 low-energy bending vibrations and allows full coupling of these vibrations to end-over-end tumbling of the CH_5^+ molecule. The corresponding disadvantage of the POS model, however, is the significant additional challenge to achieve convergence for realistically stiff versions of the potentials. This

motivates a brief discussion of the POS predictions with the rotation-contortion results, with an eye toward establishing additional insights into the dynamical trends anticipated for CH_5^+.

The 53.9 cm^{-1} torsional and 213.9 cm^{-1} flip barriers from least squares pairwise fits to the full 15D Bowman surface (i.e., $\alpha = 1$) most closely approximate the reduced dimensional rotation-contortion model barriers of 50 cm^{-1} and 200 cm^{-1}, respectively. I am currently unable to converge CH_5^+ calculations for $\alpha = 1$ and therefore compare results as a function of increasing potential stiffness. In this spirit, converged POS eigenenergies for the lowest 10 J = 0 states of nonzero nuclear spin statistical weight are presented in Figure 3.11 for the progression of $\alpha = 0.0001$, $\alpha = 0.001$, and $\alpha = 0.01$. The corresponding J = 0 energy levels obtained from the full rotation-contortion model for the same series of nuclear-spin symmetry states are also shown in Figure 3.11. In each column, the lowest energy state is defined to be zero; thus the relative energies are presented as a function of model and potential stiffness.

At the simplest level, the essentially unhindered free-rotor energy patterns observed at low α evolve to more complex internal rotor splittings with increasing potential stiffness. A general monotonically increasing trend in rotor energy spacings with stiffness is clear, with an energy ordering pattern that is largely (but not entirely) maintained with respect to α. The final extrapolation from $\alpha = .01$ to the rotation-contortion model represents a large change in both the potential and level of dynamical approximation, though much of the energy ordering is maintained as the energy separations increase. However, arguably the most striking aspect is that the converged energy level differences for *stiffest* ($\alpha = 0.01$) POS calculations, though

still far from the full potential (α = 1), have already achieved magnitudes qualitatively comparable (i.e., within 2- to 3-fold) with respect to the rotation-contortion model predictions. We find this result particularly surprising. However, such behavior is likely to be more consistent with more free internal rotor state behavior rather than localized vibrational or librational motion, for which the spacings would presumably continue to scale with the square root of the potential stiffness, $\alpha^{1/2}$.

Since the convergence of the CH_5^+ and CH_4 calculations is limited by the size of the basis set into which the POS Hamiltonian is expanded, the size of the basis set is limited by the amount of time needed to create the orthonormal SALCs from the coupled basis sets. Creating the SALC from standard methods[54,55] requires creating linear combinations of all of the permutations of identical particles in the basis set. For the 4 and 5 particle problems, the length of the linear combinations of these SALCs, M_{SALC}, can be on the order of 1,000 coupled basis functions. For a given symmetry, each of these SALCs must be orthogonalized with respect to each other. As an example, in Table 3.2 the actual time required to create a J = 0 SALC for XH_5 is given as a function of j_{max}. The j_{max} 6 and 7 values are estimated from the time required for j_{max} = 1 - 5. This reinforces the previous assertion that the time required to create the symmetrized basis sets, rather than creation or diagonalization of the resulting Hamiltonian matrix, is currently the rate-limiting factor for achieving converged calculations at higher stiffness parameters. We are currently pursuing several methods to increase the efficiency of this process with parallelization of the code.

As a final note, however, we can roughly estimate the size of j_{max} which will be necessary to achieve convergence for CH_5^+ in the POS model. In Figure 3.12, the RBDMC wave function is projected onto the γ coordinate for α = 0.001, 0.01, 0.1, and 1. As would be expected, the α = 0.001 wave function looks almost identical to the *sin(γ)* Jacobian that would be expected for independent particles. As α is increased to 1, more structure in the wave function appears, which requires sufficient angular flexibility in the multidimensional wave function. Therefore, a crude measure of the j_{max} value required to converge the $\alpha = 1$ POS calculation is to expand the corresponding 1D DMC pair correlation function in the H-C-H angle γ as a sum of Legendre functions $P_l(\gamma)$ and to probe the degree of convergence with respect to l. The physical notion is that angular flexibility in a sum of Legendre functions with $l \leq j_{max}$ mirrors the angular flexibility for a sum of SALCs obtained for the same j_{max}. The assumption is that the SALCs are simply sums of spherical harmonics which are the 2D analog to 1D Legendre polynomials; thus with an expansion of the same size, the flexibility of the two functions should be similar. Figure 3.13 displays the 1D DMC wavefunction along with several expansions in Legendre polynomials, indicating a rapid visual convergence with increasing j_{max}. More quantitatively, if the expectation value of the energy for a 1D rotor in the α = 1 pairwise potential is calculated using the wave functions expanded in Legendre polynomials of increasing order (j_{max}), the convergence of this energy as a function of j_{max} should mirror the number of Legendre functions required to accurately represent the 1D wave function (see Table 3.6). To converge the energy to about 1% requires $j_{max} \approx 9$, which with current basis set creation algorithms would take about 10 CPU-years to create.

However, once a basis is created, the POS method should do exceptionally well reproducing the correct dynamics. The validity of this simple model can be tested with a converged POS wave function of lower dimensionality. For example, the POS model for NH_3 is converged to better than 0.01 cm^{-1} for a $j_{max} = 15$; by expanding this converged n = 3 1D pair correlation function in a sum of Legendre polynomials up to l = 15 and calculating the expectation value of the energy, we can compare the rate of convergence of the energy with respect to j_{max}. Table 3.7 shows the error in the energy of converged POS calculation as a function of j_{max} compared to the error expectation value of the energy of the 1D expansion of the pair correlation function; both energies converge at about the same rate, implying that the 1D expansion gives a good first order estimate of the size of basis set needed to converge a full POS calculation.

VI. Summary and Conclusion

In this paper, a simple, yet surprisingly powerful method for the approximate quantum treatment of large-amplitude motion in systems with many degrees of freedom has been tested with large molecules. The POS method takes advantage of the approximate independence of the XH bond length on the angular coordinates to motivate a reduced dimensionality Hamiltonian treatment of the motion of n hydrogens constrained to the surface of a sphere. For n = 2 and 3, the problem is quite tractable and solutions of very stiff systems are easily converged, although not as efficiently as a method designed for rigid molecules. For the harder n = 4 and 5, the problem space grows so quickly that converged results are obtainable only for very floppy systems. However, the important energy level patterns discovered in the

floppy system have been shown to correlate well to the stiff systems and give insight to the dynamics of these complicated systems. The aim of the POS method is to provide a new tool to gain insight into the quantum dynamics of systems that display large amplitude motion. This reduced dimension method is necessary for systems such as the highly fluxional CH_5^+ where the full dimension quantum calculations are not possible.

Tables

Table 3.1. The Legendre coefficients for the $\alpha = 1$ CH_4 and CH_5^+ potentials

l	CH_4 a_l (cm^{-1})	CH_5^+ a_l (cm^{-1})
0	3892.709	4190.442
1	4999.699	3060.609
2	6942.057	14790.49
3	0	1821.198
4	1561.963	9008.753
5	0	2796.952
6	705.0527	5626.363
7	0	1216.296
8	403.3715	2174.996
9	0	238.9801
10	261.5983	381.5193
11	0	
12	183.5192	
13	0	
14	135.9025	
15	0	
16	104.7094	
17	0	
18	83.15934	
19	0	
20	67.64614	

Table 3.2. Time required to create an orthonormal basis set of one irreducible representation in the G_{240} molecular symmetry group.

j_{max}	Time
1	50 s
2	100 m
3	20 hr
4	3 d
5	30 d
6*	110 d
7*	1 yr

*Predicted time based on scaling observed in previous calculations.

Table 3.3. First five J = 0 energy levels of each nonzero statistical weighted symmetry for n = 5. Energies are given in cm^{-1}, with the estimated error given in parentheses.

Γ	α 0.001	0.01	0.1	1
A_2^+	246.86 (0.02)	479.0 (1.7)	1713 (195)	10752 (3074)
	322.08 (0.01)	545.0 (1.7)	1836 (160)	12125 (3959)
	375.57 (0.11)	609.6 (7.2)	1906 (307)	13120 (3636)
	406.43 (0.20)	622.0 (7.7)	2011 (300)	13789 (3665)
	425.34 (0.00)	630.1 (1.9)	2113 (341)	14343 (4237)
A_2^-	298.44 (0.01)	522.5 (3.0)	1673 (201)	10602 (2997)
	325.38 (0.21)	551.7 (12.0)	1836 (328)	12916 (4125)
	406.30 (0.16)	632.5 (8.5)	2039 (330)	13676 (4974)
	425.88 (0.11)	645.5 (9.8)	2070 (355)	14415 (4500)
	458.43 (0.37)	698.0 (15.1)	2207 (348)	14963 (5199)
G_2^+	250.83 (0.03)	472.5 (1.9)	1493 (198)	9475 (2988)
	255.60 (0.02)	498.5 (3.3)	1669 (312)	10203 (4937)
	306.40 (0.18)	546.8 (7.6)	1777 (257)	11363 (3947)
	322.84 (0.02)	568.1 (3.8)	1793 (266)	11957 (3638)
	329.75 (0.02)	583.1 (10.2)	1837 (270)	12049 (3963)
G_2^-	108.95 (0.04)	304.2 (3.1)	1189 (200)	7695 (2827)
	192.39 (0.05)	399.0 (2.9)	1355 (194)	8547 (2962)
	216.28 (0.01)	425.4 (3.1)	1605 (247)	10392 (3839)
	277.00 (0.04)	506.8 (2.6)	1631 (256)	10699 (3950)
	280.09 (0.04)	527.7 (4.8)	1783 (270)	11417 (3899)
H_2^+	144.94 (0.08)	379.7 (5.7)	1297 (154)	8420 (2015)
	173.88 (0.04)	410.1 (3.1)	1479 (180)	8686 (3034)
	217.60 (0.06)	464.4 (5.2)	1579 (332)	9909 (4362)
	245.34 (0.03)	474.5 (2.6)	1682 (252)	11050 (3639)
	253.30 (0.04)	496.5 (4.0)	1749 (228)	11391 (3880)
H_2^-	191.93 (0.05)	384.1 (1.8)	1273 (133)	8234 (2177)
	198.73 (0.05)	422.3 (3.4)	1408 (265)	8564 (3655)
	214.81 (0.02)	458.1 (5.2)	1623 (283)	9937 (4450)
	276.26 (0.05)	507.9 (1.4)	1712 (254)	11039 (3623)
	279.29 (0.04)	509.5 (5.4)	1730 (307)	11471 (3856)

Table 3.4. First five J = 1 energy levels of each nonzero statistical weighted symmetry for n = 5. Energies are given in cm^{-1}, with the estimated error given in parentheses.

Γ	α 0.001	0.01	0.1	1
	240.19 (0.29)	430.4 (18.1)	1579 (511)	11703 (6311)
	327.76 (0.60)	553.6 (22.4)	1931 (445)	14787 (5301)
A_2^+	349.42 (0.06)	572.6 (10.8)	2138 (447)	16197 (5755)
	373.88 (0.24)	590.6 (15.3)	2170 (487)	16667 (6033)
	375.02 (0.33)	600.9 (27.6)	2284 (491)	17719 (6483)
	269.56 (0.25)	472.4 (15.4)	1679 (371)	12379 (4635)
	292.05 (0.28)	486.0 (16.0)	1966 (299)	15134 (3903)
A_2^-	323.56 (0.18)	548.9 (17.2)	2004 (375)	15332 (4738)
	327.48 (0.13)	569.6 (9.9)	2077 (569)	15715 (6675)
	374.95 (0.34)	597.6 (26.1)	2161 (509)	16574 (6083)
	135.60 (0.03)	331.7 (4.2)	1417 (289)	10280 (4230)
	163.77 (0.25)	373.3 (15.7)	1456 (388)	11225 (4249)
G_2^+	220.12 (0.22)	427.5 (14.4)	1584 (508)	11699 (6016)
	240.29 (0.21)	442.6 (15.4)	1691 (417)	12515 (5395)
	241.92 (0.31)	448.6 (14.7)	1746 (485)	12873 (5780)
	189.27 (0.17)	392.2 (10.7)	1441 (358)	10441 (4471)
	197.61 (0.25)	432.8 (17.3)	1588 (433)	11709 (5004)
G_2^-	221.84 (0.41)	440.2 (16.2)	1716 (372)	12319 (5300)
	269.87 (0.29)	479.9 (15.3)	1730 (484)	12723 (5926)
	271.25 (0.28)	482.4 (15.1)	1913 (369)	14012 (5019)
	138.65 (0.05)	347.4 (9.4)	1419 (346)	10574 (3859)
	163.11 (0.26)	374.1 (11.5)	1482 (357)	10824 (4942)
H_2^+	171.42 (0.31)	403.0 (16.7)	1581 (456)	11644 (5437)
	218.70 (0.18)	442.6 (10.9)	1641 (451)	11902 (5899)
	221.80 (0.22)	447.4 (11.5)	1683 (503)	12318 (6064)
	116.78 (0.05)	335.6 (5.2)	1453 (226)	10587 (3398)
	162.66 (0.01)	382.5 (3.4)	1493 (321)	11154 (3898)
H_2^-	190.46 (0.20)	402.8 (11.2)	1589 (456)	11684 (4898)
	196.12 (0.29)	428.8 (22.4)	1666 (423)	12037 (5743)
	200.71 (0.27)	442.3 (14.5)	1714 (491)	12817 (6154)

Table 3.5. First five J = 2 energy levels of each nonzero statistical weighted symmetry for n = 5. Energies are given in cm^{-1}, with the estimated error given in parentheses.

Γ \ α	0.001	0.01	0.1	1
A_2^+	238.13 (0.24)	435.4 (19.2)	1900 (362)	15832 (3983)
	244.33 (0.33)	484.7 (26.8)	2203 (442)	18616 (5716)
	322.43 (0.39)	517.3 (6.7)	2295 (729)	19598 (8367)
	327.85 (0.48)	547.7 (45.2)	2389 (1100)	20110 (12502)
	340.42 (0.13)	560.8 (78.7)	2452 (1327)	20806 (14431)
A_2^-	185.17 (0.46)	378.8 (32.5)	1869 (537)	16106 (5628)
	289.83 (0.14)	481.4 (10.9)	2105 (637)	17819 (8012)
	296.19 (0.20)	521.2 (37.7)	2312 (871)	19908 (9529)
	320.42 (58.92)	540.4 (131.0)	2480 (1147)	21549 (11662)
	322.52	561.8	2593	22287
G_2^+	167.36 (0.45)	388.6 (21.1)	1835 (576)	15057 (7170)
	214.69 (0.59)	432.2 (35.0)	1912 (882)	16113 (9158)
	239.70 (0.38)	451.4 (27.8)	2039 (833)	16907 (9736)
	244.57 (0.58)	474.7 (40.0)	2078 (896)	17175 (10362)
	245.48 (0.65)	489.1 (40.1)	2159 (835)	18068 (9713)
G_2^-	187.94 (0.62)	390.0 (35.1)	1840 (448)	14873 (5662)
	190.88 (0.65)	411.6 (36.5)	1855 (695)	15635 (7528)
	192.94 (0.98)	423.7 (37.8)	1929 (747)	16458 (8076)
	196.67 (0.93)	441.1 (29.5)	2121 (699)	17916 (8268)
	216.75 (0.30)	452.6 (26.1)	2169 (813)	18322 (9620)
H_2^+	139.78 (1.07)	355.1 (43.9)	1760 (667)	14741 (7174)
	166.38 (0.60)	397.9 (39.5)	1851 (742)	15580 (8266)
	169.84 (0.62)	406.6 (37.7)	1877 (822)	15685 (9396)
	175.52 (0.81)	441.9 (33.5)	2093 (793)	17325 (9406)
	217.08 (0.89)	443.1 (50.1)	2149 (792)	18050 (9285)
H_2^-	113.59 (1.01)	334.3 (46.3)	1816 (512)	14786 (6297)
	190.62 (0.66)	404.2 (26.6)	1838 (755)	15940 (8209)
	191.94 (0.73)	425.1 (35.7)	1923 (782)	16289 (8588)
	196.95 (1.03)	435.7 (36.2)	2055 (923)	17238 (10168)
	198.97 (1.11)	441.8 (45.9)	2121 (877)	17855 (10423)

Table 3.6. The expectation value of the energy of a 1D rotor in the CH_5^+ $\alpha = 1$ pairwise potential.

j_{max}	<E> (cm^{-1})	Error
1	13104.0	371.8%
2	11278.2	306.0%
3	4638.3	67.0%
4	3644.0	31.2%
5	4543.5	63.6%
6	3322.0	19.6%
7	3019.0	8.7%
8	3097.7	11.5%
9	2820.5	1.5%
10	2783.7	0.2%
RBDMC	2777.7	

Table 3.7. The error in ground state energies of the POS model and the 1D Legendre expansion of the pair correlation function for the converged n = 3 NH_3 calculation.

j_{max}	POS Model	1D expansion
2	330%	367%
4	110%	133%
6	41.2%	28.0%
8	13.7%	3.17%
10	3.53%	0.469%
12	0.589%	0.0842%
14	0.00148%	0.00348%

Figures

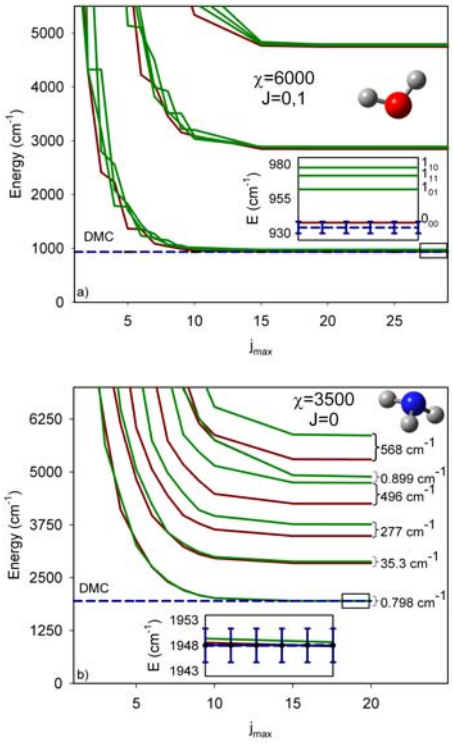

Figure 3.1. Particle-on-a-sphere rotation-bending energies for a) n = 2 (XH_2) and b) n = 3 (XH_3) model systems as a function of basis set size (j_{max}). a) In XH_2, the asymmetric top rotational patterns for J = 0,1 corresponding to $J_{KaKc} = 0_{00}$, 1_{01}, 1_{11}, 1_{10} are clearly evident, with the J = 0 energy rapidly converging to the expected DMC limit (dotted line). b) Converged J = 0 energy levels for XH_3 reveal inversion tunneling splittings in good agreement with NH_3 (after which the potential was modeled) and increasing rapidly with symmetric bend excitation. Note the only exception to this pattern (near 5000 cm^{-1}) arising from an interloper vibrational state due to degenerate asymmetric bend excitation, which exhibits a tunneling splitting very similar to the ground state (0.798 cm^{-1}).

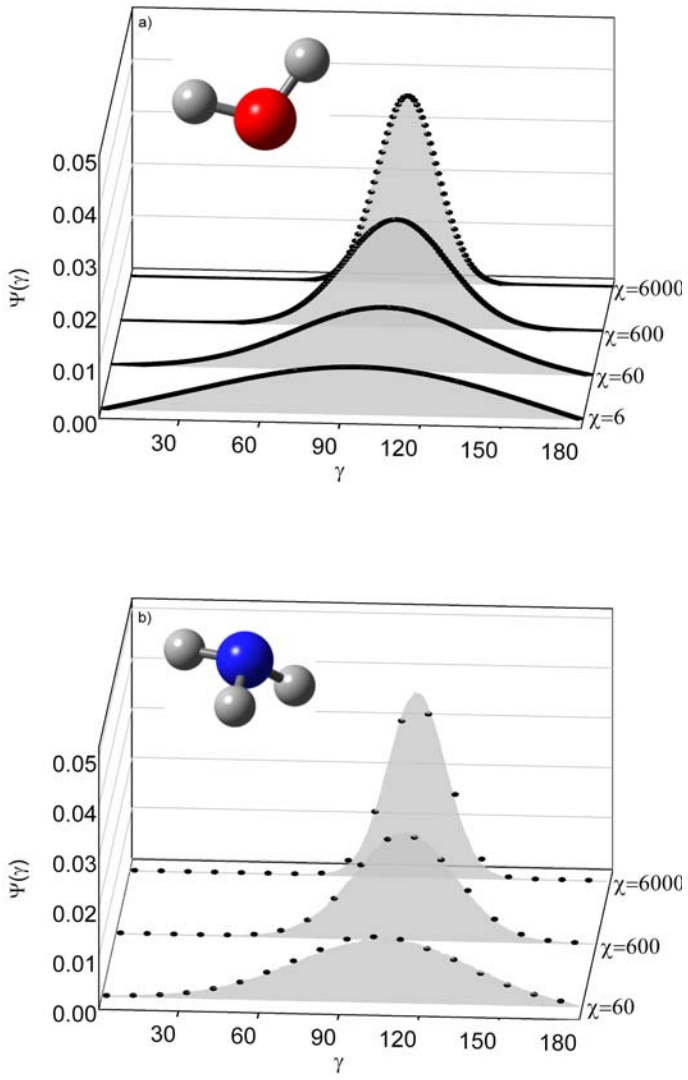

Figure 3.2. Angular pair correlation functions for a) XH_2 and b) XH_3 as a function of potential stiffness χ = k/b, where k is the angular well depth and b the rotational constant for a single X-H rotor. For comparison, the shaded function is calculated from DMC, whereas the dots reflect the fully converged J = 0 POS calculation.

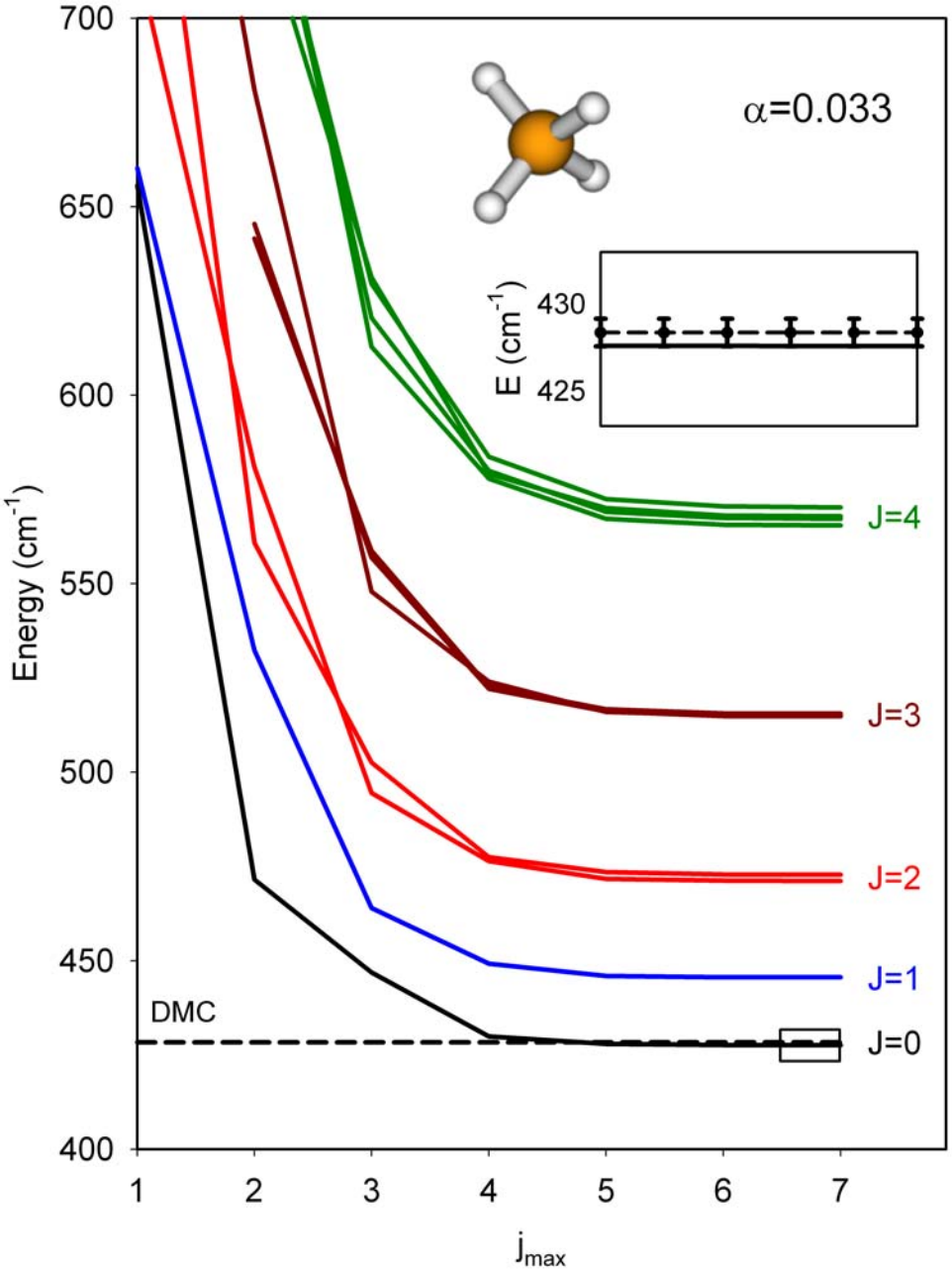

Figure 3.3. Convergence of J = 0, 1, 2, 3, 4 energies for XH_4 as a function of j_{max}. The POS ground state (J = 0) energy is compared against DMC predictions (dotted line).

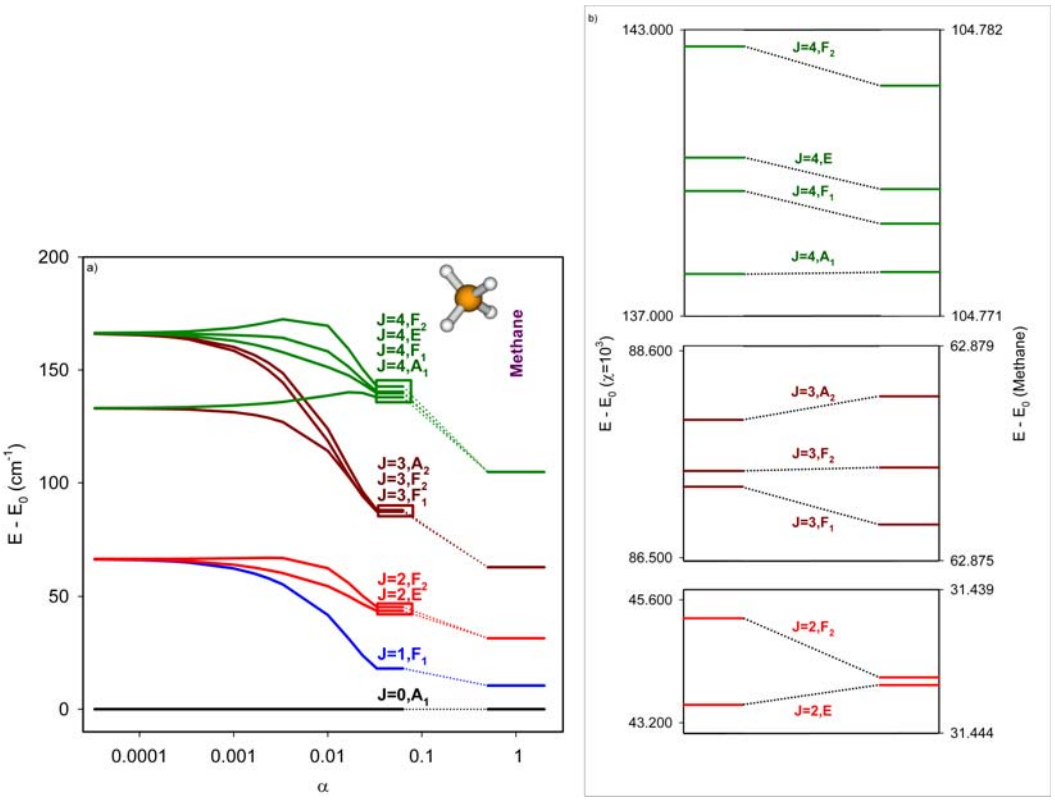

Figure 3.4. a) XH_4 rotational energies of J = 0-4 as a function of potential stiffness scale factor α. b) At higher resolution, centrifugal induced splittings of the nominally degenerate symmetric top levels for XH_4 are shown for $\alpha = 0.033$, which are considerably larger but reveal the same qualitative patterns as experimentally observed.

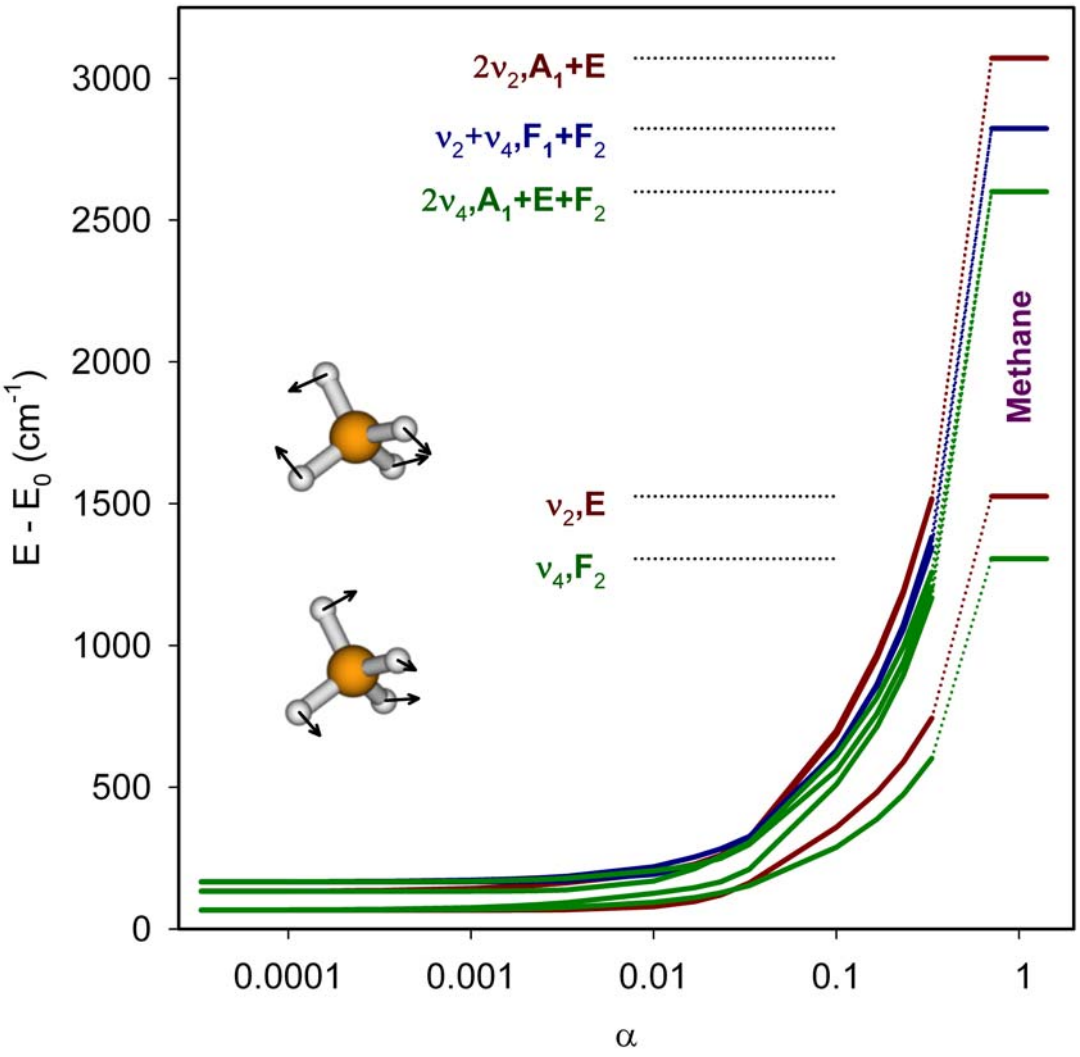

Figure 3.5. Vibrational energies of XH_4 as a function of the potential stiffness scale factor α.

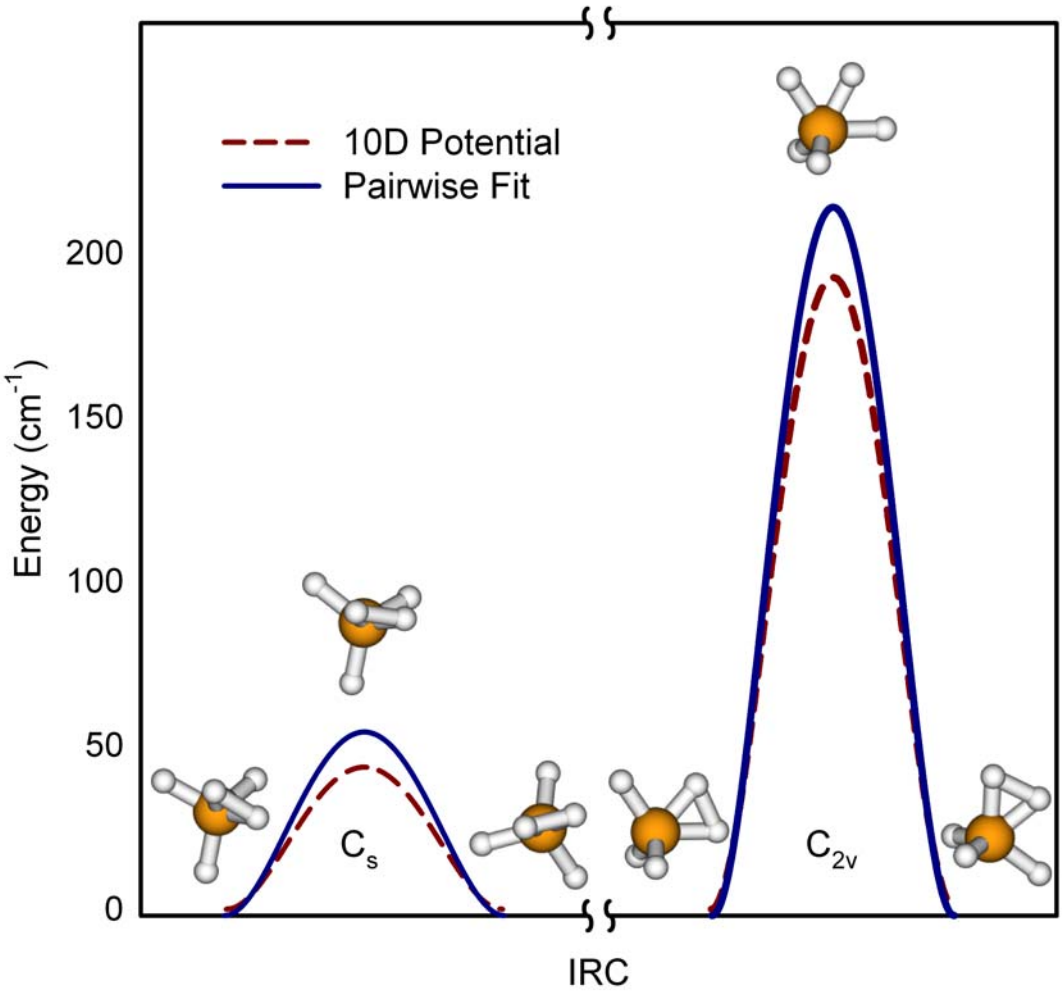

Figure 3.6. Minimum energy paths for CH_5^+ through the C_s and C_{2v} transition states, separating the C_s minimum for both the 10D relaxed potential and the pairwise fit.

C_s Minimum

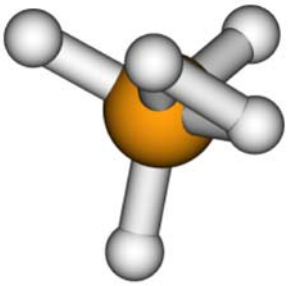

	10D	Pairwise Fit
(θ_1,ϕ_1)	(0.00,0.00)	(0.00,0.00)
(θ_2,ϕ_2)	(75.70,0.00)	(75.52,0.00)
(θ_3,ϕ_3)	(124.47,0.00)	(124.21,0.00)
(θ_4,ϕ_4)	(108.50,-114.13)	(108.28,-114.28)
(θ_5,ϕ_5)	(108.50,114.13)	(108.28,114.28)
E (cm^{-1})	0	-1.9

C_s Transition State

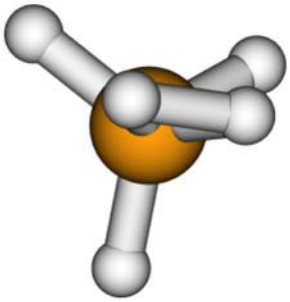

	10D	Pairwise Fit
(θ_1,ϕ_1)	(0.00,0.00)	(0.00,0.00)
(θ_2,ϕ_2)	(108.55,-25.41)	(108.36,-25.39)
(θ_3,ϕ_3)	(108.55,25.41)	(108.36,25.39)
(θ_4,ϕ_4)	(115.62,119.04)	(116.00,-118.03)
(θ_5,ϕ_5)	(115.62,119.04)	(116.00,118.03)
E (cm^{-1})	43.3	53.9

C_{2v} Transition State

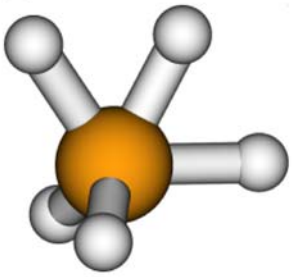

	10D	Pairwise Fit
(θ_1,ϕ_1)	(0.00,0.00)	(0.00,0.00)
(θ_2,ϕ_2)	(61.76,0.00)	(61.89,0.00)
(θ_3,ϕ_3)	(123.52,0.00)	(123.79,0.00)
(θ_4,ϕ_4)	(103.25,-116.00)	(103.18,-115.99)
(θ_5,ϕ_5)	(103.25,116.00)	(103.18,115.99)
E (cm^{-1})	192.5	213.9

Figure 3.7. Geometry comparison of CH_5^+ critical points. Note the surprisingly quantitative agreement between the full 10D relaxed potential and the pairwise additive fit used in the POS model.

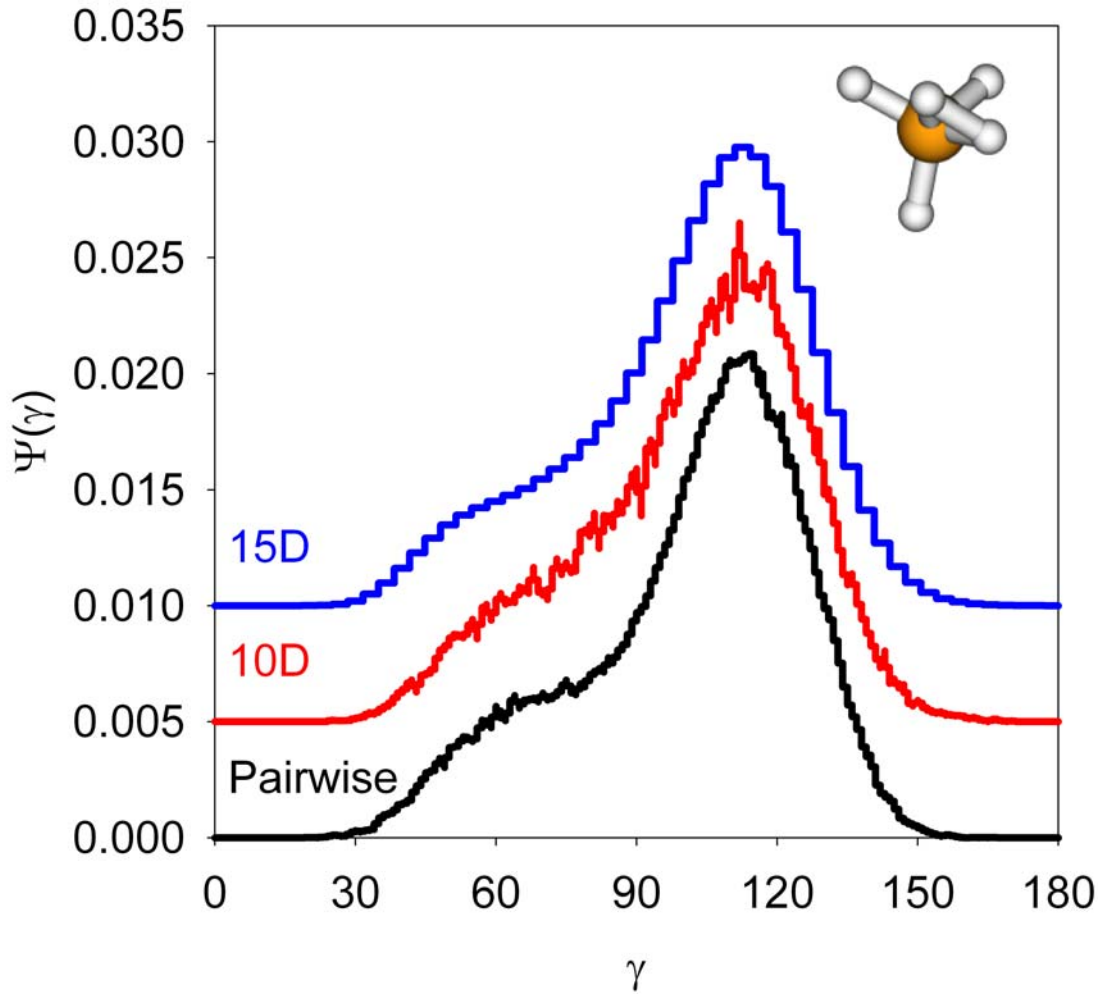

Figure 3.8. Pair correlation functions for J = 0, XH_5 from DMC calculations for a series of potential models: a) 15D full CH_5^+ potential, b) the 10D relaxed potential, and c) the pairwise additive least squares fit. Note the excellent agreement at the wave function level.

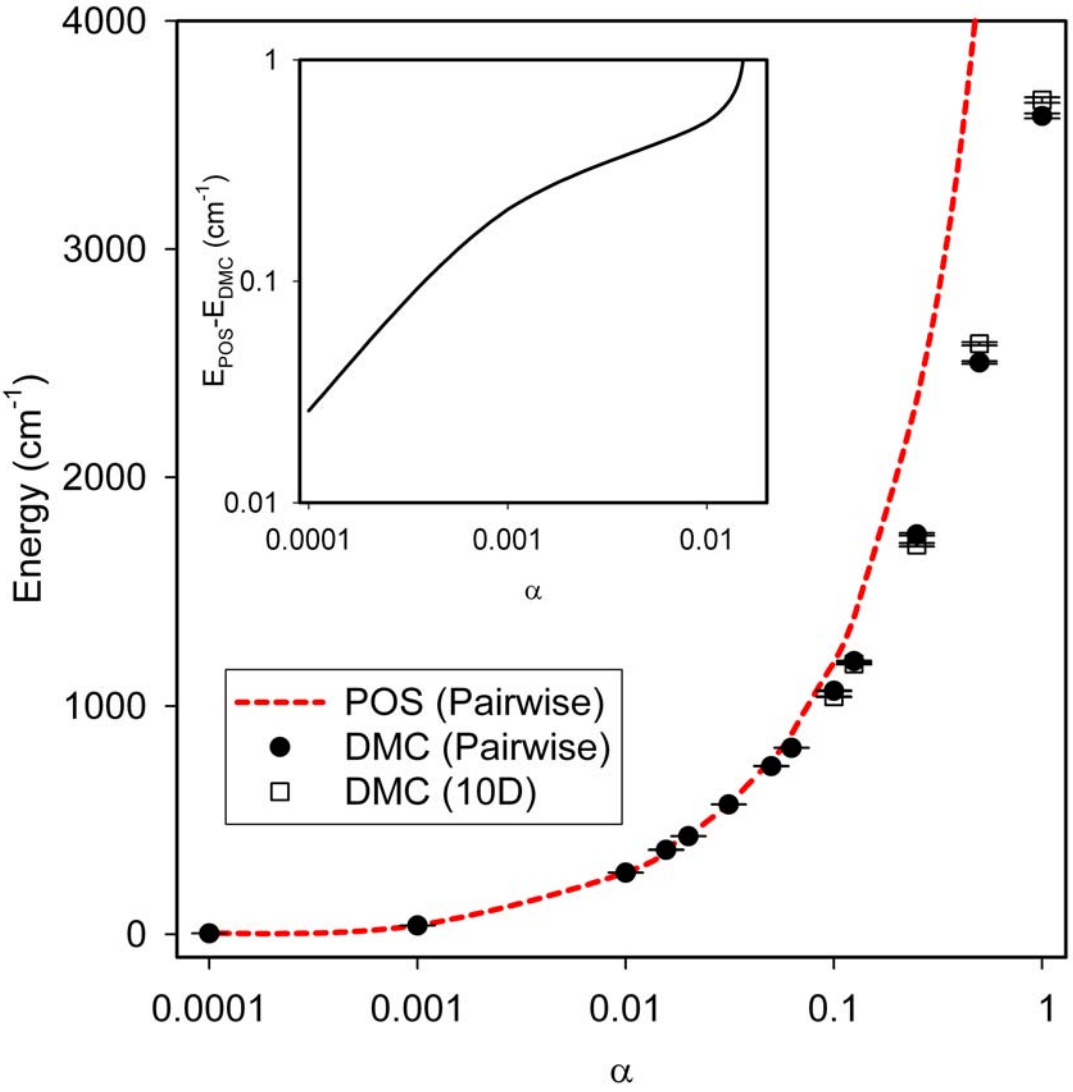

Figure 3.9. Ground-state energies of CH_5^+ as a function of the potential stiffness parameter (α), calculated by DMC and POS with both the 10D (DMC, open squares) and pairwise (POS, dashed line) potentials. The inset shows the difference between the POS and DMC (pairwise) calculations (i.e., the level of convergence) as a function of α.

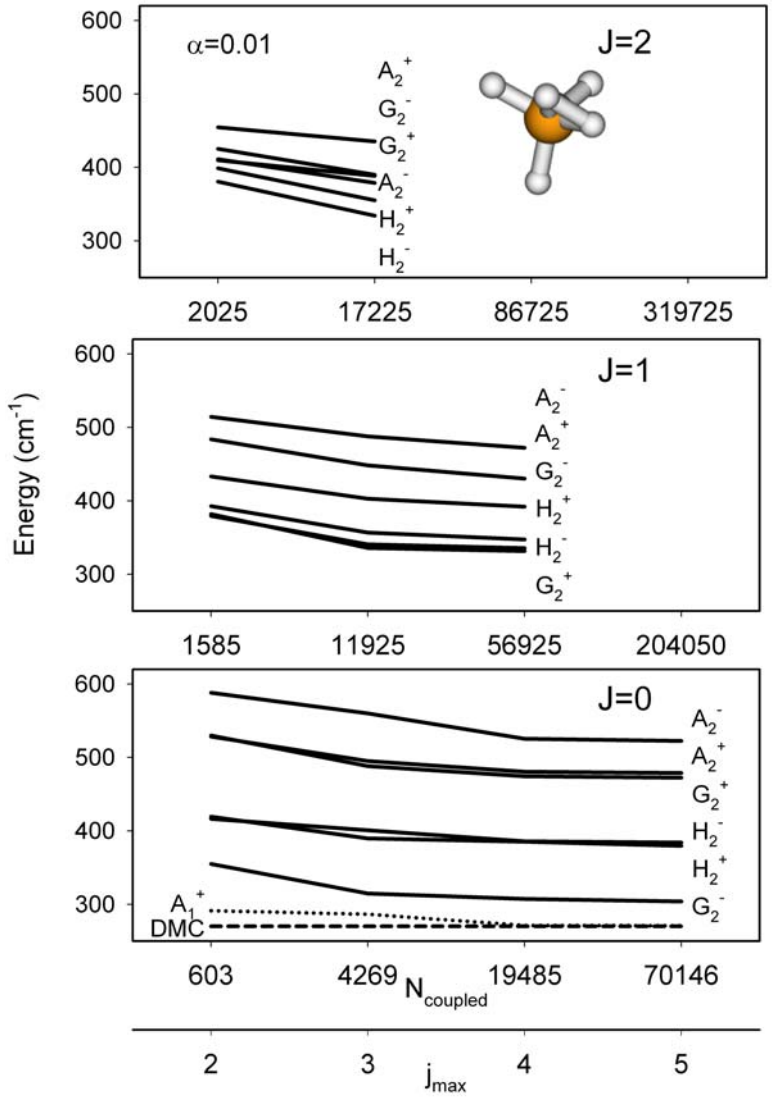

Figure 3.10. Nonzero statistical symmetries for J = 0, 1, and 2 of XH_5 (with a = .033) as a function of basis set size, j_{max} and $N_{coupled}$ (the number of coupled basis functions in the basis set). Note the slow but steady convergence of J = 0 energies to the RBDMC limit with the size of $N_{coupled}$.

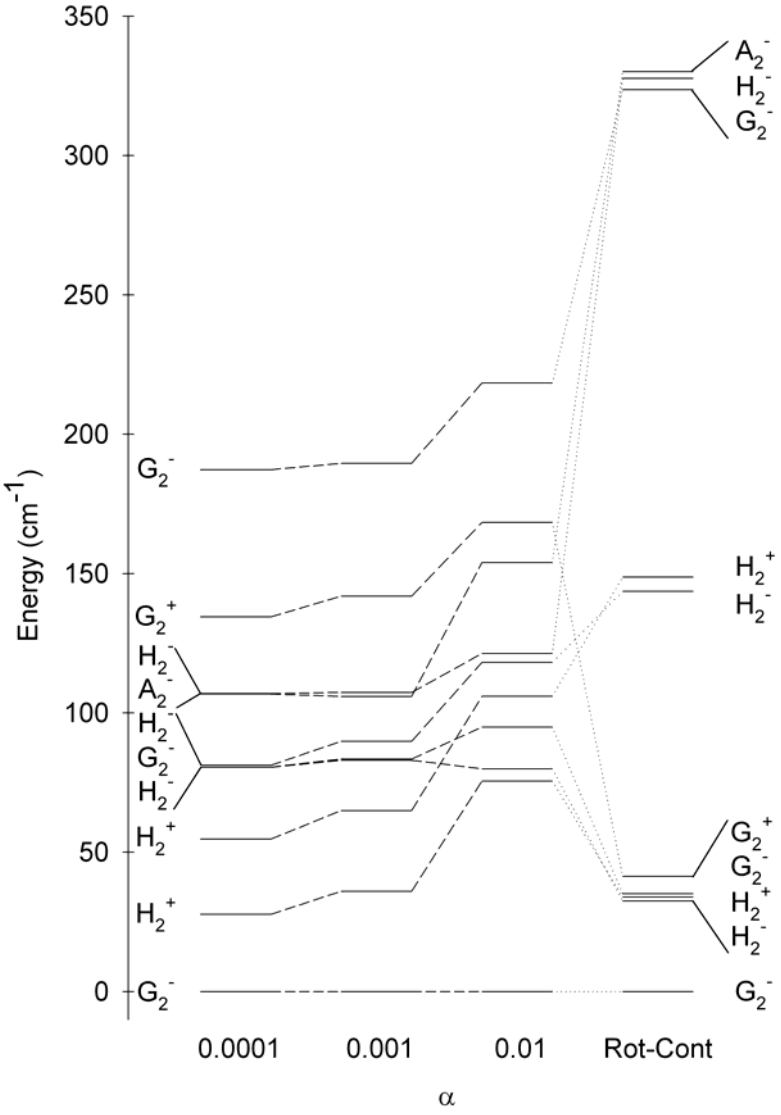

Figure 3.11. The lowest J = 0 internal rotor energies (with respect to the ground state energy, G_2^- Symmetry) of the POS model compared with the RTRF-like model of Bunker and coworkers. Interestingly, the splittings for the two model treatments are roughly the same order of magnitude, despite the stiffness of the potentials varying by a large factor.

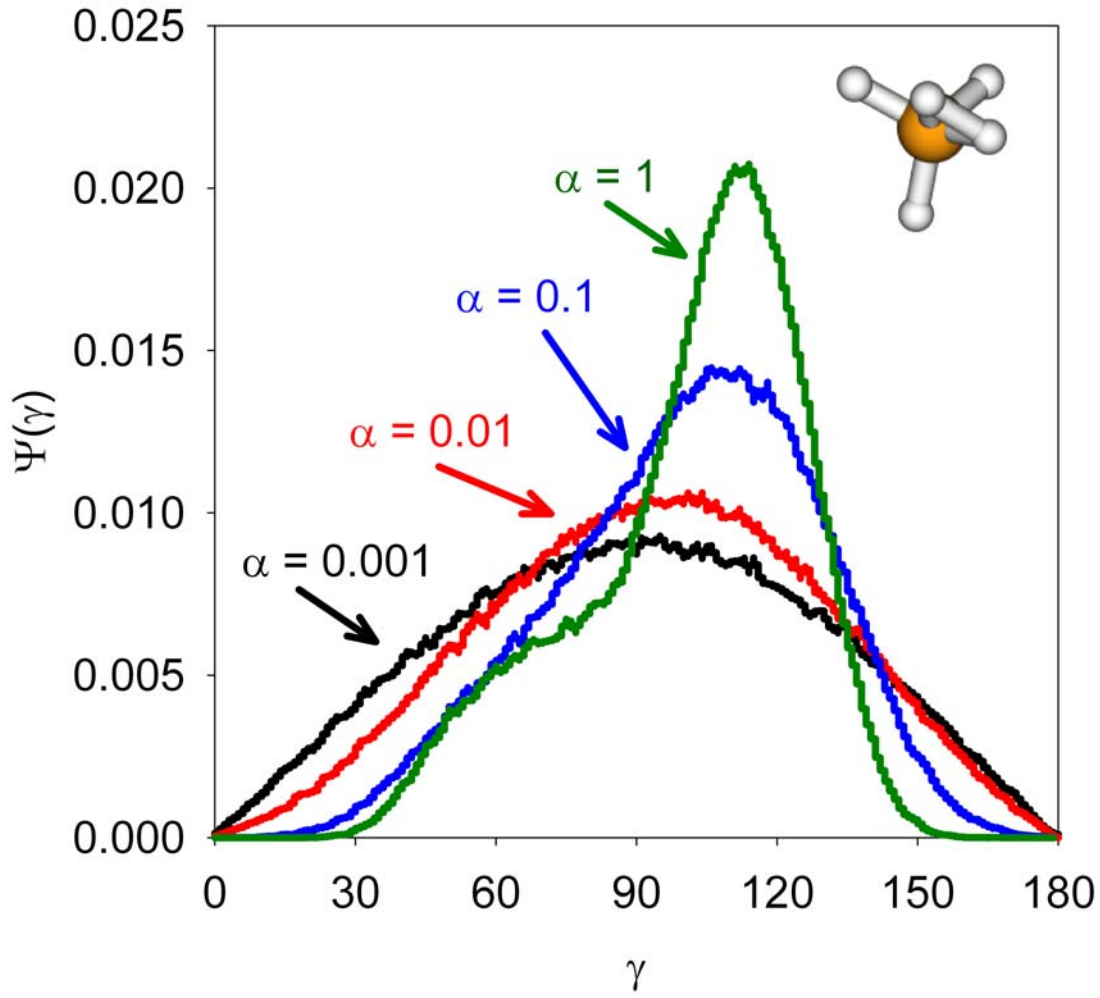

Figure 3.12. DMC pair correlation function of CH_5^+ as a function of potential stiffness scale (α).

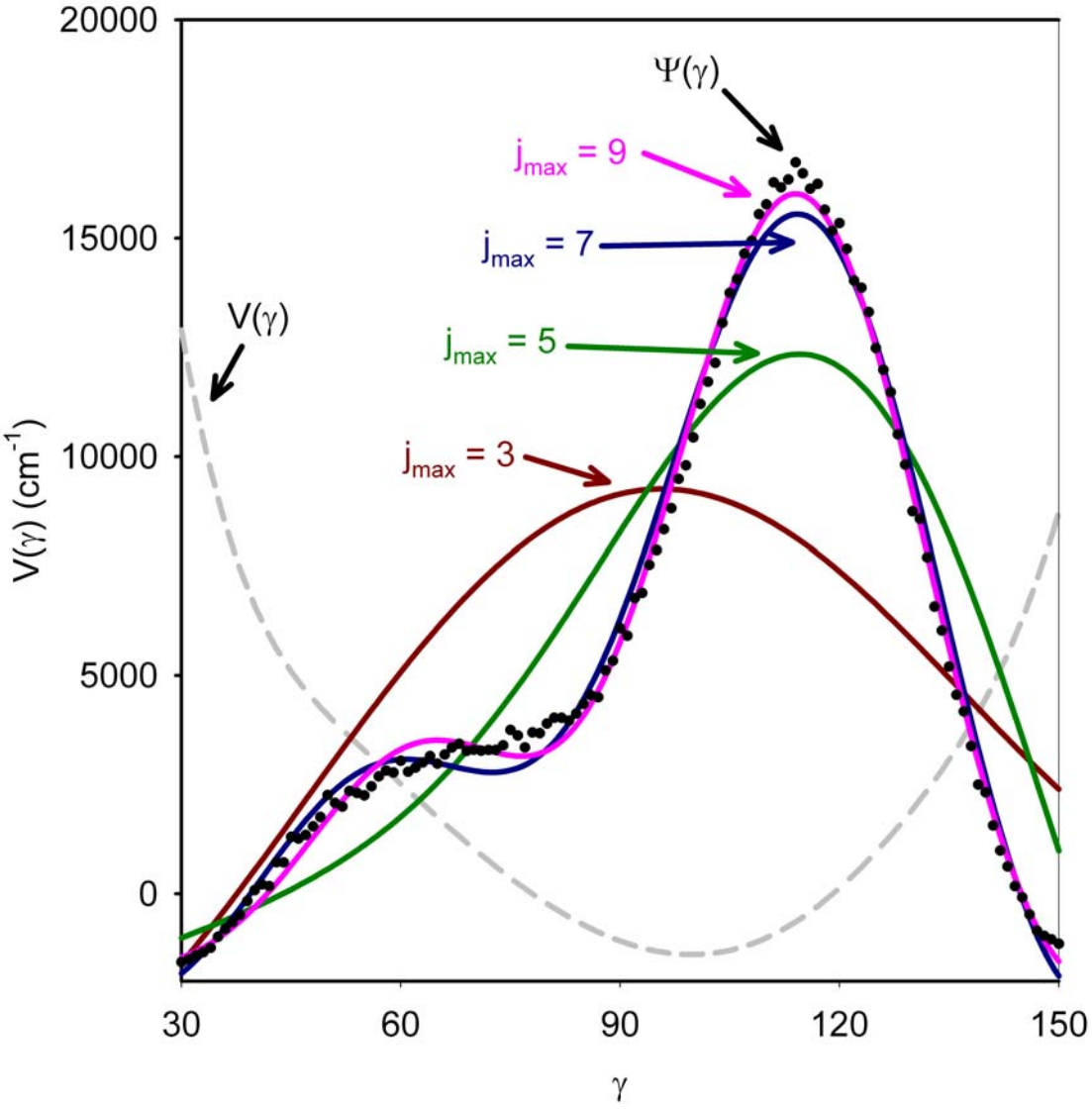

Figure 3.13. Successive fits of the $\alpha = 1$ pair correlation function of CH_5^+ to a sum of Legendre functions. Such behavior suggests a much improved level of convergence for the POS model of CH_5^+ by j_{max} = 7-9.

References

[1] V. Spirko, J. Mol. Spectrosc. **101**, 30 (1983).

[2] S. Urban, R. Dcunha, K. N. Rao, and D. Papousek, Can. J. Phys. **62**, 1775 (1984).

[3] S. L. Coy and K. K. Lehmann, Spectroc. Acta Pt. A-Molec. Biomolec. Spectr. **45**, 47 (1989).

[4] V. Spirko and W. P. Kraemer, J. Mol. Spectrosc. **133**, 331 (1989).

[5] S. Urban, N. Tu, K. N. Rao, and G. Guelachvili, J. Mol. Spectrosc. **133**, 312 (1989).

[6] I. Kleiner, G. Tarrago, and L. R. Brown, J. Mol. Spectrosc. **173**, 120 (1995).

[7] I. Kleiner, L. R. Brown, G. Tarrago, Q. L. Kou, N. Picque, G. Guelachvili, V. Dana, and J. Y. Mandin, J. Mol. Spectrosc. **193**, 46 (1999).

[8] C. Cottaz, I. Kleiner, G. Tarrago, L. R. Brown, J. S. Margolis, R. L. Poynter, H. M. Pickett, T. Fouchet, P. Drossart, and E. Lellouch, J. Mol. Spectrosc. **203**, 285 (2000).

[9] J. Tang and T. Oka, J. Mol. Spectrosc. **196**, 120 (1999).

[10] D. J. Liu, T. Oka, and T. J. Sears, J. Chem. Phys. **84**, 1312 (1986).

[11] P. B. Davies, S. A. Johnson, P. A. Hamilton, and T. J. Sears, Chem. Phys. **108**, 335 (1986).

[12] M. H. Begemann and R. J. Saykally, J. Chem. Phys. **82**, 3570 (1985).

[13] M. Gruebele, M. Polak, and R. J. Saykally, J. Chem. Phys. **87**, 3347 (1987).

[14] H. Petek, D. J. Nesbitt, J. C. Owrutsky, C. S. Gudeman, X. Yang, D. O. Harris, C. B. Moore, and R. J. Saykally, J. Chem. Phys. **92**, 3257 (1990).

[15] M. Araki, H. Ozeki, and S. Saito, Mol. Phys. **97**, 177 (1999).

[16] M. Araki, H. Ozeki, and S. Saito, J. Chem. Phys. **109**, 5707 (1998).

[17] D. H. Zhang, Q. Wu, J. Z. H. Zhang, M. Vondirke, and Z. Bacic, J. Chem. Phys. **102**, 2315 (1995).

[18] G. W. M. Vissers, G. C. Groenenboom, and A. van der Avoird, J. Chem. Phys. **119**, 277 (2003).

[19] Y. H. Qiu, J. Z. H. Zhang, and Z. Bacic, J. Chem. Phys. **108**, 4804 (1998).

[20] Y. H. Qiu and Z. Bacic, J. Chem. Phys. **106**, 2158 (1997).

[21] P. Eggert, A. Viel, and C. Leforestier, Comput. Phys. Commun. **128**, 315 (2000).

[22] N. Goldman, R. S. Fellers, C. Leforestier, and R. J. Saykally, J. Phys. Chem. A **105**, 515 (2001).

[23] F. N. Keutsch, N. Goldman, H. A. Harker, C. Leforestier, and R. J. Saykally, Mol. Phys. **101**, 3477 (2003).

[24] N. Goldman, C. Leforestier, and R. J. Saykally, J. Phys. Chem. A **108**, 787 (2004).

[25] P. R. Schreiner, S. J. Kim, H. F. Schaefer, and P. V. Schleyer, J. Chem. Phys. **99**, 3716 (1993).

[26] H. Muller and W. Kutzelnigg, Phys. Chem. Chem. Phys. **2**, 2061 (2000).

[27] D. Marx and M. Parrinello, Nature **375**, 216 (1995).

[28] G. A. Olah, N. Hartz, G. Rasul, and G. K. S. Prakash, J. Am. Chem. Soc. **117**, 1336 (1995).

[29] G. A. Olah and G. Rasul, Accounts Chem. Res. **30**, 245 (1997).

[30] E. Herbst, S. Green, P. Thaddeus, and W. Klemperer, Astrophys. J. **503**, (1977).

[31] D. Talbi and R. P. Saxon, Astron. Astrophys. **261**, 671 (1992).

[32] H. Muller, W. Kutzelnigg, J. Noga, and W. Klopper, J. Chem. Phys. **106**, 1863 (1997).

[33] A. Brown, B. J. Braams, K. Christoffel, Z. Jin, and J. M. Bowman, J. Chem. Phys. **119**, 8790 (2003).

[34] A. Brown, A. B. McCoy, B. J. Braams, Z. Jin, and J. M. Bowman, J. Chem. Phys. **121**, 4105 (2004).

[35] V. L. Tal'rose and A. K. Lyubimova, Dokl. Akad. Nauk SSSR **86**, 909 (1952).

[36] E. T. White, J. Tang, and T. Oka, Science **284**, 135 (1999).

[37] O. Asvany, P. Kumar, B. Redlich, I. Hegemann, S. Schlemmer, and D. Marx, Science **309**, 1219 (2005).

[38] X. C. Huang, A. B. McCoy, J. M. Bowman, L. M. Johnson, C. Savage, F. Dong, and D. J. Nesbitt, Science **311**, 60 (2006).

[39] J. S. Tse, D. D. Klug, and K. Laasonen, Phys. Rev. Lett. **74**, 876 (1995).

[40] A. Gamba, G. Morosi, and M. Simonetta, Chem. Phys. Lett. **3**, 20 (1969).

[41] G. A. Olah, G. Klopman, and R. H. Schlosberg, J. Am. Chem. Soc. **91**, 3261 (1969).

[42] W. T. A. M. Van der Lugt and P. Ros, Chem. Phys. Lett. **4**, 389 (1969).

[43] W. A. Lathan, W. J. Here, and J. A. People, J. Am. Chem. Soc. **93**, 808 (1971).

[44] P. R. Schreiner, Angew. Chem.-Int. Edit. **39**, 3239 (2000).

[45] A. Komornicki and D. A. Dixon, J. Chem. Phys. **86**, 5625 (1987).

[46] W. Klopper and W. Kutzelnigg, J. Phys. Chem. **94**, 5625 (1990).

[47] S. J. Collins and P. J. Omalley, Chem. Phys. Lett. **228**, 246 (1994).

[48] M. Kolbuszewski and P. R. Bunker, J. Chem. Phys. **105**, 3649 (1996).

[49] A. L. L. East, M. Kolbuszewski, and P. R. Bunker, J. Phys. Chem. A **101**, 6746 (1997).

[50] P. R. Bunker, B. Ostojic, and S. Yurchenko, J. Mol. Struct. **695**, 253 (2004).

[51] G. A. Olah, Angew. Chem. Int. Ed. Engl. **34**, 1393 (1995).

[52] M. P. Deskevich and D. J. Nesbitt, J. Chem. Phys. **123**, (2005).

[53] R. N. Zare, *Angular momentum: Understanding spatial aspects in chemistry and physics*. (John Wiley & Sons, New York, 1988).

[54] F. A. Cotton, *Chemical applications of group theory*, 3rd ed. (Wiley, New York, 1990).

[55] P. R. Bunker and P. Jensen, *Molecular symmetry and spectrosopy*, 2nd ed. (NRC Research Press, Ottawa, 1998).

[56] I. G. Kaplan, *Symmetry of many-electron systems*. (Academic Press, New York, 1975).

[57] J. F. Cornwell, *Group theory in physics: An introduction*. (Academic Press, San Diego, 1987).

[58] J. M. Hutson, edited by J. M. Bowman (JAI Press, 1990), Vol. 1A, pp. 1-45.

[59] V. Buch, J. Chem. Phys. **97**, 726 (1992).

[60] J. B. Anderson, J. Chem. Phys. **63**, 1499 (1975).

[61] M. A. Suhm and R. O. Watts, Phys. Rep.-Rev. Sec. Phys. Lett. **204**, 293 (1991).

[62] A. Vegiri, M. H. Alexander, S. Gregurick, A. B. McCoy, and R. B. Gerber, J. Chem. Phys. **101**, 2577 (1994).

[63] G. Herzberg, *Infrared and raman spectra of polyatomic molecules*. (D. Van Nostrand Company, Inc, New York, 1945).

[64] A. B. McCoy, B. J. Braams, A. Brown, X. C. Huang, Z. Jin, and J. M. Bowman, J. Phys. Chem. A **108**, 4991 (2004).

Chapter 4: Dynamically Weighted MCSCF: Multistate Calculations for F + $H_2O \rightarrow$ HF + OH Reaction Paths

I. Introduction

Chemical reactions represent a complex network of elementary reaction steps, each of which typically proceeds via highly reactive, open shell radical species. Accurate characterization of these elementary chemical reactions from first principles has been a long standing focus for both quantum chemists and dynamicists. This represents a significant challenge on several fronts. As a necessary first step in this process, one must calculate accurate adiabatic (*i.e.,* Born-Oppenheimer) potential energy surfaces as a function of fixed nuclear configurations. There are now many examples of high-level *ab initio* potentials for simple atom + diatom chemical reaction systems[1], though this rapidly becomes a daunting task in higher (*i.e.,*3N - 6) dimensionality. Once an adiabatic potential has been obtained, the next challenge is to perform exact quantum state-to-state dynamics calculations on such a surface. This is an area in which there have been significant advances in the last decade, and it is now more or less straightforward to obtain these calculations for triatomic systems reacting on a single electronic surface. However, extension of these exact quantum scattering methods to polyatomic reaction systems (N > 3) represents the current state-of-the art for chemical dynamics and has thus far only been heroically achieved for special 4 atom systems such as OH + H_2 system with only one "heavy" (*i.e.,* non-hydrogenic) atom[2 3].

Unfortunately, state-to-state chemical reaction dynamics may not be so simply described by quantum wave packet propagation on a *single* electronic potential energy surface. As a result, quantum reactive scattering even for "simple" A + BC triatomic systems can become substantially more complicated by the presence of *non-adiabatic* interactions between various Born-Oppenheimer surfaces. Indeed, there is a growing body of experimental and theoretical evidence (with particular focus on prototypical F + H_2[4,5] and Cl + H_2[6] atom abstraction systems) that non-adiabatic effects can play a finite role in the reactive scattering dynamics. The presence of non-adiabatic interactions even in these relatively simple atom + diatom systems raises obvious questions about the role of such nonadiabatic effects in atom + polyatom systems. This highlights the crucial importance of high-level *ab initio* methods for calculating reaction paths and potential energy surfaces for *multiple* electronically excited states, which is of particular relevance to the present work.

A recent thrust in our group has been the use of high resolution UV lasers in crossed supersonic jets to study quantum state-resolved reaction dynamics for benchmark prototypic 4 atom reactions. The focus of particular interest has been the atom + triatom system $F(^2P) + H_2O \rightarrow HF + OH\ (^2\Pi)$. There are many aspects of this reaction that make it particularly appropriate for combined experimental and theoretical study. First of all, it is strongly exothermic ($\Delta E \approx 17.6$ kcal/mol[7]) and proceeds rapidly at thermal collision energies over a relatively low barrier (~5 kcal/mol), which makes it experimentally convenient for study under crossed molecular beam conditions. Second, the products HF and OH can each be detected with full quantum state resolution, exploiting either LIF [8], or high resolution IR[5,9],

techniques available that are in the group. Thirdly, from a theoretical perspective, the number of electrons (19) is small enough for obtaining accurate reaction paths, potential energy surfaces, and nonadiabatic coupling matrix elements via high-level, multireference *ab initio* methods. Most importantly, such a "heavy + light-heavy-light" system offers the next level of challenge to quantum reactive scattering methods, as well as eventually providing the experimental data with which to facilitate detailed comparison with theory.

In the context of non-adiabatic reaction dynamics, the $F(^2P)$ + H_2O system represents an additional challenge for several reasons. First of all, in the asymptotic regions of the potential, there are nearly degenerate surfaces corresponding to $F(^2P)$ + H_2O reagent (3-fold degenerate) and HF + $OH(^2\Pi)$ product (2-fold degenerate) states. In principle, such close proximity over long reaction path distances could promote significant multiple state mixing in the entrance/exit channels, even for relatively modest non-Born-Oppenheimer coupling matrix elements. Alternatively, strong non-adiabatic coupling could arise in the transition state region due to avoided crossings between electronic surfaces. Indeed, the chemical bond rearrangement occurring near the transition state reflects a rapid evolution of the wave function along the adiabatic reaction path, which as elegantly shown by Butler and coworkers[10], can often dominate the shape and location of the transition state barrier. As also shown by Allison et. al. [11], close avoided crossings lead to strong non-adiabatic behavior. The complex nature of these curve crossings near transition states become especially rich in systems with high electron affinity atoms, where the presence of charge transfer states can be sufficiently low in energy to be important near the transition state

region. This proves to be particularly true for the F + H_2O system, where the transition state region is dominated by avoided crossings between states correlating asymptotically with ionic F^- + H_2O^+ and HF^+ + OH^- surfaces. As this work will illustrate, such strong avoidance of ground and excited state potential surfaces generates special demands on calculating reaction paths via high-level, multireference *ab initio* methods.

In order to investigate the role of non-adiabatic effects on reaction dynamics, one must evaluate matrix elements of the nuclear kinetic energy operator, which requires derivative calculations for ground and multiply excited electronic state wave functions[12]. Such non-adiabatic matrix elements are calculated from the first and second derivatives of the wave function Ψ_i (Q_1, $Q_{2,...}$) for the i^{th} electronic state, where Q_l represents motion along a specific intramolecular coordinate (l = 1, 3N - 6). The full nuclear kinetic energy matrix elements are then obtained from these derivative elements by summing with G matrix analysis[13] and then added to the traditional Born-Oppenheimer (BO) matrix to yield the full non-adiabatic Hamiltonian[12]. The key point is that the reliable calculation of these derivative coupling matrix elements therefore requires *smoothly varying* wave functions and adiabatic energies for each of these ground/excited states, providing crucially important constraints on the fidelity of any high-level multireference calculations.

The conventional way to calculate high-level multireference SCF energies and wave functions for a series of ground and excited states is by a state-averaged variational calculation[14]. In essence, this approach minimizes the weighted average of MCSCF energies for each of the states in question,

$$E^{SA-MCSCF} = \left(\sum_{i=1}^{n} w_i E_i \right) \qquad (4.1)$$

where w_i is a *constant* weight factor for state *i*. The advantage of such an approach is that each of the electronic surfaces is treated equivalently in a variational sense, which is obviously relevant to achieving a balanced wave function description in the limit of asymptotically degenerate reactant (F + H_2O) or product (HF + OH) states. This can lead to small but significant shifts in the ground state energies. When variationally optimizing the ground state(s), any included upper state will lead to a less correct description of the ground state(s).

The fundamental complication of such "statically weighted" *ab initio* methods arises when there is a *different* electronic degeneracy for the product and product asymptotes, as in F + $H_2O \rightarrow$ HF + OH, where the reactants (products) are triply (doubly) degenerate in the absence of spin-orbit coupling. In this case, a 3-state MCSCF calculation will yield the correct exact 3-fold asymptotic degeneracy of the F(^{2}P) reactants, which is broken by inclusion of higher excited states unless all degenerate higher states are included with the same weight. Similarly, a 2-state MCSCF calculation can correctly capture the asymptotic 2-fold degeneracy of the OH($^2\Pi$) products, which is again lifted by variationally averaging in higher state contributions. A 3-state calculation will not describe the 2-fold degenerate OH($^2\Pi$) ground state as well as a 2-state calculation. This situation is further exacerbated in the F + H_2O transition state region, where rapid avoided crossings of determinants in the incomplete MCSCF wave function can result in abrupt discontinuities in both energies and wave functions along the reaction path.

Simply stated, the challenge of such a state-averaged MCSCF calculation is to include a sufficient number of states in the chemically interesting transition region and yet correctly capture the smooth evolution of the wave functions to asymptotic 3-fold (reactant) and 2-fold (product) degeneracy, without introducing discontinuities in potential surface. Toward this end, I propose a simple yet surprisingly robust method, "dynamically weighted" MCSCF (DW-MCSCF), whereby the state weighting is explicitly varied as a continuous, damped function of the relative state energies.

$$E^{DW-MCSCF} = \left(\sum_{i=1}^{n} w_i (E_i - E_1) E_i \right) \qquad (4.2)$$

For a broad range of damping functions, this yields excellent results and automatically achieves the desired goals of i) smoothly varying energies and wave functions along any locally smooth path (e.g. the reaction path) and ii) correct degeneracy behavior out in the asymptotic reagent/product region by including only the relevant states in each region.

The organization of this chapter is as follows. Section II describes details of how the *ab initio* transition state and reaction path calculations are performed, specifically focusing on the F + H_2O system as a test case. Further details of the dynamic weighting algorithm are described in Sec III, with Section IV presenting results using dynamic weighting MCSCF along the F + H_2O reaction path. Concluding comments are summarized in Section V.

II. Ab Initio Calculations

All calculations are performed using the MOLPRO suite of *ab initio* programs[15]. As my focus is on non-adiabatic dynamics, this requires a very high

level of theory capable of accurately describing multiple electronic states: specifically, I perform complete active space self-consistent field calculations (CASSCF)[14] using a full valence active space, followed by inclusion of multireference configuration interaction (MRCI)[16] and Davidson correction (MRCI+Q)[17]. At this level of theory, the choice of basis set is somewhat constrained by computational expense, particularly toward eventual calculation of a 4 atom potential surface. For reference, a single point CASSCF+MRCI+Q energy calculation with Dunning's aug-cc-pVDZ[18] basis takes approximately 3 CPU-hours on an AMD Athlon 2.4 GHz. Timing/convergence tests for absolute energies of reagents and products, as well as harmonic zero point corrected reaction exothermicities for aug-cc-pVDZ, aug-cc-pVTZ, aug-cc-pVQZ, aug-cc-pV5Z basis sets are listed in Table 4.1. This series also permits extrapolation to the complete basis set (CBS) limit[19], based on a conventional $1/n^3$ plot with respect to the zeta basis set index. The timing studies indicate a 2.6-fold increase in computational expense between aug-cc-pVDZ and aug-cc-pVTZ, with steeper incremental penalties (4.2- and 5.2- fold) for each additional zeta. However, acceptably good convergence (< 0.1 kcal/mole with respect to CBS) is already achieved in predicted zero point corrected exothermicities at the aug-cc-pVTZ level, which dictates my choice.

Since my spin-orbit program cannot handle general contractions, a segmented basis set was generated from the correlation-consistent triple-zeta basis set of Dunning. For O and F, the exponents were taken from the aug-cc-pVTZ basis[18], and the first six s and three p-functions were contracted using the 1s and 2p contraction coefficients, respectively. For H, the exponents of the cc-pVTZ basis[18] were used and

the first three s-functions were contracted. Furthermore, the f-functions on O,F and the d-functions on H were neglected. This resulted in a basis [6s4p3d] for O,F and [3s2p] for H (110 contractions). A number of basis contractions were tested for calculational speed and accuracy before the final choice was made. In Table 4.2 are listed a number of different contractions with convergence and timing results. These data indicate the AVTZ[6s3p3d]/VTZ[3s2p] basis demonstrates similar levels of convergence (0.34 kcal/mol above CBS) compared with a standard aug-cc-pVTZ basis (0.12 kcal/mol above CBS), but with an additional 2.1-fold reduction in time. In effect, the contracted aug-cc-pVTZ basis performs comparably for F + H_2O to the standard aug-cc-pVTZ basis, but at a computational speed only 20% slower than aug-cc-pVDZ. For perspective, also shown in Table 4.2 are results including spin-orbit and zero-point energy corrections, which indicate residual discrepancies of 0.7 kcal/mol (4%) between the CBS limit and experimental determined exothermicities. This discrepancy reflects correlation still not taken into account, and is consistent with the residual 0.43 kcal/mol errors in exothermicity for the exhaustively studied F + H_2 potential surface of Stark and Werner[20].

As a longer range goal, I am interested in high-level multistate *ab initio* calculations for the full F + H_2O PES, based on sampling approaches and Shephard interpolation methods outlined by Collins et al[21]. The thrust of the current work, however, is to illustrate the advantages of dynamically weighted MCSCF, which can be adequately elucidated with calculations restricted along the reaction path. I start, therefore, by obtaining the F + H_2O transition state on the lowest electronic surface by CASSCF geometry optimization programs in MOLPRO[22]. The crux of non-

adiabatic interactions for the F + H_2O system arise from rapidly avoided crossings between excited charge transfer states in the transition state region. To take these states into account in zeroth order, I search for this lowest saddle point in a traditional (*i.e.,* non dynamically weighted) 5-state SA-MCSCF calculation; Figure 4.1 shows the geometry of the transition state. Note that the transition state is significantly non-planar (by nearly 60 degrees), and therefore no symmetry element is conserved throughout the reaction coordinate. This most likely reflects additional hyperconjugative interaction between the radical p hole on F and the sp^3 lone pairs on the H_2O subunit, which is further supported by the strongly non-collinear (140 degree) F-H-O bond angle. For comparison, I have also converged the F + H_2O transition state geometry at MRCI+Q level, which yields similar parameters listed in Table 4.3.

From this transition state, a conventional reaction path is mapped in both product and reagent directions by following the path of steepest decent for the lowest state at the 5-state SA-MCSCF level[23]. When the gradient in the asymptotic region becomes too small to follow, the reaction path is defined by simply extending the F – H_2O or HF – OH bonds toward the reactants or products. Figure 4.2 shows the evolution of the nascently formed and broken bonds along this minimum energy path, in bond breaking (R_{OH_1}) and making (R_{FH_1}) coordinates; this curve will be defined as the reaction coordinate for the rest of the paper. It is worth noting that, due to lack of analytic derivatives in the MOLPRO based MRCI code, the reaction coordinate has been obtained only at the CASSCF level, which I next tackle with higher (MRCI+Q) levels of theory. This will lead to additional errors (overestimation by about 0.9

kcal/mol) in the predicted barrier height. However, for the present purposes, the CASSCF reaction path provides an excellent first approximation, which can later be compared with results from a more extensive MRCI+Q mapping of the transition state region.

As a final step, spin-orbit interactions partially lift the degeneracy of the asymptotic F(^{2}P) and OH(^{2}P) states. To capture nonadiabatic effects in the F + H_2O reaction, therefore, spin-orbit interactions are calculated by diagonalizing the 6x6 Breit-Pauli Hamiltonian[24] using the zero order non-spin-orbit wave functions as a basis. Although it is possible to use either SA-MCSCF or MRCI wave functions at this point, I find that the SA-MCSCF wave functions reproduce the experimental spin-orbit splitting as well as the MRCI wave functions, albeit with a factor of 100 reduction in calculation time. As a result, I use the SA-MCSCF wave functions to calculate the spin-orbit interaction along the reaction path. Since the SA-MCSCF wave functions are used as both reference configurations for MRCI calculations and as basis functions for calculating the spin-orbit interaction, a method is clearly needed to calculate SA-MCSCF wave functions and eigenvalues that vary *smoothly* throughout the entire PES. The next section outlines such a method for obtaining this in a non-biased manner and is applicable to PES calculation in any dimensionality.

III. Dynamically Weighted Multiconfiguration Self Consistent Fields Method (DW-MCSCF)

The central issue with the conventional state averaged MCSCF approach to the F + H_2O $\rightarrow$ HF + OH reaction is easily identified. The fluorine atom has a triply degenerate p-hole, thus requiring a 3-state SA-MCSCF calculation to correctly

describe the nature of the reactant channel. However, the lowest OH($^2\Pi$) product channel is only doubly degenerate, which, if I attempt to describe with a 3-state MCSCF calculation, will partially mix in character from the first excited state (5 eV), giving a less accurate description of the OH($^2\Pi$) ground state. By way of example, Figures 4.3a and 4.3b show how the number of states in a SA-MCSCF calculation affects the energies of levels for both reagents and products. In Figure 4.3a, the 3-state calculation achieves the correct degeneracy for both the reactants and products, but closer inspection indicates that the reaction path energies also exhibit strong discontinuities in the transition state region. These are predominantly due to neglect of asymptotically higher energy charge transfer states that decrease rapidly with distance and exhibit multiple avoided crossings with lower lying covalent states in the transition state region. This can be improved by including more state averaging (for example, 5-state results are shown in Fig 4.3b). This produces a much smoother set of surfaces, but with a serious cost; equal variational weighting of these charge transfer states now leads to significantly nondegeneracies for both reactant ground state (110 cm^{-1}).

To correctly maintain asymptotic degeneracies, one requires 3- (or 2-) state calculations for the reactants (or products). However, in the conventional SA-MCSCF approach, this would necessitate an ad hoc "seam" region between the two calculations, creating non-physical discontinuities in both the PES and wave functions, and would thereby prohibit extraction of non-adiabatic coupling matrix elements. An improved method by design would ideally yield a *smooth* transition from a 3-state to a 2-state calculation so that the weights are correct asymptotically,

and yet would also include sufficient states in the transition state region to adequately describe the avoided crossing dynamics. One idea is to set the weights with respect to a smoothly varying function of the nuclear coordinates. This is relatively easy to define for a one-dimensional reaction path

$$w_i = f_i(s), \qquad (4.3)$$

where w_i is the weight of state i and if is a smoothly varying function of s, the reaction coordinate[25].However, this becomes much harder for any higher dimensional potential energy *surface*, and in addition, requires *a priori* knowledge of the number of states important to the calculation in each region of configuration space.

As I care most about the lowest lying surface(s) correlating with reactants and products, a more physically motivated approach is to adjust weights based on energy separation with respect to the ground state at a given geometry. Toward this end, I define an energy dependent weighting function

$$\begin{aligned} w_i &= f(\Delta E) \\ f(0) &= 1 \\ \lim_{\Delta E \to \infty} f(\Delta E) &\to 0 \end{aligned}, \qquad (4.4)$$

where ΔE is the energy with respect to the ground state. By definition, the weights for asymptotically degenerate states will be identical (as required to achieve a proper description of these states), and yet will appropriately decay to zero for sufficiently highly excited states.

The algorithm is implemented iteratively, with initial estimates of energy dependent weights chosen from a closely neighboring geometry (or *a priori* knowledge of the electronic states in the region); the process continues until energies are converged to a specific target value. For the present example, I chose 10^{-5} Hartree

(~0.006 kcal/mol or 2 cm^{-1}), as it is about 1% of the asymptotic spin-orbit splittings. Although the SA-MCSCF program is called more than once per point, the whole process is actually quite efficient; calculations converge within ~2-4 calls of the SA-MCSCF program. This is because the weights change very little along the reaction path, and the starting orbitals are already well optimized from the last SA-MCSCF calculation. It is worth noting that even for bad starting guesses for the weights, e.g. all weight set equal, only 1 or 2 more SA-MCSCF calls are needed for convergence to the same threshold. In this application, the SA-MCSCF calculation is a 6-state calculation with the weights of the first 6 states determined by the weighting function. Throughout the entire reaction path the weight of the 6^{th} state never exceeds approximately 10^{-5}, so increasing to a larger calculation will be of no benefit.

We next investigate the behavior of three possible weighting functions that match the criteria in Eq. 4.3. An obvious first choice for a damping functional form is $f(\Delta E) \propto \exp(-\beta\ (E - E_0))$, but this leads to slower iterative convergence due to a non-zero slope in the exponential at $E = E_0$. An improved functional form is a Gaussian [$f(\Delta E) \propto \exp(-(\beta\ (E - E_0))^2)$], which has a zero derivative at $E = E_0$; this ensures that all nearly degenerate ground states receive equal weighting and therefore the process converges efficiently (~ 2 - 3 iterations). However, for Gaussian damping, the relative weights decay *too* rapidly as near degeneracies begin to lift; this proves undesirable for describing multiple levels near the transition state region accurately. For example, this can result in state weighting coefficients changing nearly discontinuously over relatively short reaction path distances, and thereby introducing non-physical curvature in the calculated potential curves. A good compromise

between these two damping functional forms is empirically found to be $f(\Delta E) \propto \text{sech}^2(-(\beta (E - E_0))$, which has both a zero derivative near $E = E_0$ and yet exhibits a more gradual exponential vs. Gaussian drop off for large ΔE.

The dependence on choice of weighting function is illustrated in Fig 4.4a, explicitly focusing on the ground state surface. Figure 4.4a displays DW-MCSCF results for exponential, Gaussian, and sech^2 weighting functions for a fixed value of $\beta^{-1} = 2\text{eV}$. Noteworthy is the relatively weak sensitivity to choice of weighting function, even near the transition state region. Also included on the plot are the energies of the ground state for the 3- and 5-state constant weight methods. The sensitivity (in shape and absolute energy of the ground state) to weighting function is much smaller than the sensitivity on number of states included in the calculation. On closer inspection, one sees a small but systematic increase in variational energy for exponential weighting. This is due to the slower drop-off in excited state weighting coefficients with increasing $\beta\Delta E$ values, which therefore tends to include more states at the expense of ground state accuracy. Conversely, considerably fewer differences are evident between Gaussian and sech^2 functional weighting, due to more equivalent weighting of states with $\beta\Delta E \approx 0$.

An additional degree of freedom is the choice of β, which characterizes the range of energies weighted appreciably. If β is too large, then the calculations effectively collapse to ~1 (*i.e.,* ground) state MCSCF, which is therefore unable to account for rapidly avoiding adiabatic curve crossings near the transition state. Conversely, for small β, the weights do not decay fast enough with energy in the asymptotic reactant and product regions, which will not satisfy the requirement of a

3-state calculation in the reactant channel and 2-state in the product channel. The sensitivity to choice of energy scale parameter β^{-1} is illustrated in Figure 4.4b for a fixed $\text{sech}^2(\beta\Delta E)$ weighting function, with β^{-1} varying from 1eV to 4eV. Note again the relatively weak dependence of the reaction path for small scale parameters ($\beta^{-1} \approx 2$ - 3 eV) , gradually degrading with increasing β^{-1} as more excited states are included. However, also worth noting is the impact of too small a scale parameter, which can lead to distortions in the reaction path near the transition state (e.g. point P). Such effects occur because the first excited state energy is rapidly increasing near the transition state, which for small β^{-1} implies an abrupt decrease in the number of appreciably weighted excited states. More efficient iterative convergence properties may be achieved by better tailored weighting functions for a given reaction system. In practice, however, this simple first-order treatment already makes it straightforward to obtain reaction paths relatively insensitive to scale parameter and functional weighting, as described in the following section.

IV. Results

We next demonstrate how the DW-MCSCF procedure works when applied to the $F + H_2O \rightarrow HF + OH$ system. DW-MCSCF calculations with a sech^2 weighting function ($\beta^{-1} = 3$ eV) have been performed along the CASSCF reaction path. The results for the 4 lowest states are summarized in Figure 4.5 and indicate several features that are worth noting.

First of all, the potential curves highlight the presence of multiple barriers, avoided crossings and a bound excited state well in the transition state region. Wave function analysis indicates the dominant orbital configurations of the bound state well

to be $F^- + H_2O^+$ and $HF^+ + OH^-$ charge transfer states, on the reactant and product sides of the transition state, respectively. Though only adiabatic curves can be rigorously defined, there are also clearly indications of a diabatic crossing between the first excited $F + H_2O$ reactant state and the $HF^+ + OH^-$ surface, as well as between the $F^- + H_2O^+$ charge transfer channel and the first excited $HF + OH(^2\Pi)$ product channel. There are also indications of a second isolated curve crossing between the third state and fifth state (not shown). These multiple crossings illustrate why such high state averaging proved necessary (at least local to the transition state) and further confirm expectations of strongly non-adiabatic dynamics. Second, despite the presence of multiple crossings, the potential curves (and wave functions) can be obtained as a smooth function of the reaction path. Third, reactant and product channels now achieve the correct degeneracy in the asymptotic limits, i.e., 3-fold and 2-fold degenerate for $F + H_2O$ and HF + OH, respectively.

A quantitative display of dynamic weighting as a function of distance along the reaction path is shown in Figure 4.6, with the adiabatic potentials reproduced in the top panel. As desired, the figure clearly indicates a smooth evolution from i) a 3-state calculation for triply degenerate $F + H_2O$ reactants, ii) through a dynamic mixture near the transition state, into iii) a ~2-state calculation for doubly degenerate HF + OH products. Upon closer inspection of the product asymptotic region, there is a small but finite weighting of the third state ($HF + OH(A^2\Sigma)$). This could be further minimized by choice of β^{-1} scale parameter, but the effect is so small to not incur a significant change in the $OH(^2\Pi)$ energies, and using β^{-1} produces the smoothest reaction path.

To correctly account for spin-orbit effects in the F + H_2O reaction, the Breit-Pauli Hamiltonian[24] is diagonalized using the zero order non-spin-orbit wave functions as a basis. As mentioned previously, the MCSCF wave functions reproduce the experimental spin-orbit splitting as well as the higher level MRCI+Q wave functions, albeit with a 100-fold reduction in computational expense. Using the DW-MCSCF results as basis functions for the spin-orbit Hamiltonian, the 6x6 spin-orbit matrix is therefore evaluated and diagonalized as a function of reaction path geometry. The asymptotic spin-orbit splittings in the reactant channel due to F($^2P_{3/2}$, $_{1/2}$) are calculated to be 390 cm^{-1}, *i.e.,* in good agreement with the experimental values of 404.10 cm^{-1}. Similarly, the spin-orbit splittings for product OH($^2\Pi_{1/2, 3/2}$) are found to be 134 cm^{-1}, in similarly good agreement with the 139.27 cm^{-1} experimental value.

As a final stage, results for the lowest three states from a full MRCI+Q reaction path calculation with spin-orbit interactions are presented in Figure 4.7 and indicate several final points worth noting. First of all, the spin-orbit splitting is now visible on the scale of the plot, and is in good agreement with experiment. Second, the reaction barrier for the ground state has now dropped to about 7 kcal/mol. When corrected for zero point effects at the reactant and transition state, this translates into a barrier around 5 kcal/mol, which is in reasonable agreement with experiment.

As a final note, these adiabatic correlation diagrams offer special relevance for further studies of non-adiabatic reaction dynamics. Specifically, the reactants starting out in the *ground* spin-orbit F($^2P_{3/2}$) and crossing over the ground state barrier correlate exclusively with OH ($^2\Pi_{3/2}$) products in the *ground* spin-orbit state. On the

other hand, the first excited spin-orbit state $F(^2P_{1/2})$ correlates adiabatically over a very high barrier (~60 kcal/mol) with the electronically excited OH ($A^2\Sigma$) product, and therefore should be non-reactive in the pure Born-Oppenheimer limit. This behavior is quite similar to Born-Oppenheimer predictions for F/F* spin-orbit reactivity for the well studied F + H_2, [4,5] and F + Cl_2, [6] systems. However, what is novel about the set of F + H_2O surfaces is the presence of a relatively high barrier (~25 kcal/mol) for reactions adiabatically forming the *first excited* spin-orbit state $OH(^2\Pi_{1/2})$. This suggests that at typical collision energies in a crossed molecular beam, reaction dynamics in the purely adiabatic limit should produce exclusively ground state OH ($^2\Pi_{3/2}$) and that the presence of any excited $OH(^2\Pi_{1/2})$ products must therefore arise from non-adiabatic "surface hopping" dynamics. We are currently investigating this prediction experimentally, taking advantage of high sensitivity laser induced fluorescence (LIF) to probe the spin-orbit and rotational distributions of the nascent product OH. From a theoretical perspective, I will also use the smooth adiabats calculated by the DW-MCSCF method as reference functions for high-level MRCI+Q calculations and thereby compute the non-adiabatic coupling matrix elements relevant for the F + H_2O reaction system. Of special interest will be determining the region of the potential where these non-adiabatic couplings dominate and whether any surface hopping dynamics between OH ($^2\Pi_{3/2}$) and OH ($^2\Pi_{1/2}$) surfaces are restricted to i) long range entrance or exit channel interactions[26], in fact are ii) more strongly localized in the transition state vicinity[27], or are iii) a kinetic effect where angular momentum of molecular rotation and spin-orbit states couple, mixing the two states[28].

V. Summary and Conclusion

DW-MCSCF is an addition to the standard SA-MCSCF calculation that adjusts the weights of included states automatically to account for changes in the electronic spectrum in different regions of a global PES. DW-MCSCF is useful in reactions where i) the degeneracy in the asymptotes is different and ii) there are a number of low-lying states in the transition state region, because it will smoothly adjust the weights among the regions of interest.

The DW-MCSCF algorithm is an approach where a starting guess for the weights is improved upon through iterations of a SA-MCSCF calculation. The process is quite efficient, and converges in only a small number of iterations. Since the MRCI+Q calculations are orders of magnitude longer in computational time, it is worth the extra MCSCF iterations to ensure a smooth set of starting reference wave functions and energies before taking the next steps.

DW-MCSCF is general and can be applied to calculate other PESs where there are a number of important states varies throughout configuration space. Moreover, DW-MCSCF can be easily applied to a PES of any number of dimensions since the weighting function is only a function of the energy of the states (as opposed to nuclear coordinates). The smoothly varying wave functions obtained by DW-MCSCF can then be used as reference functions for MRCI+Q calculations, and non-adiabatic calculations which require derivatives of the wave function.

The example reaction $F(^2P) + H_2O \rightarrow HF + OH(^2\Pi)$ is prototypical of the reactions that are good candidates for DW-MCSCF: i) the reactants are 3-fold degenerate and products are 2-fold, and ii) there are avoided crossings involving low-

lying charge transfer states in the transition state region. Non-adiabatic effects are likely very important in this reaction, so it is imperative that smoothly varying multi-state wave functions are calculated, as the non-adiabatic corrections are functions of derivatives of the wave function. The full 6-D PES of this reaction will be calculated using DW-MCSCF followed by MRCI+Q along with spin-orbit and non-adiabatic corrections to the lowest 3 surfaces.

Tables

Table 4.1. Product, reactant energies and reaction exothermicities as a function of level of theory and basis set size.

	F + H_2O (Hartree)			HF + OH (Hartree)			ΔE (kcal/mol)			
Basis	CASSCF	MRCI	MRCI+Q	CASSCF	MRCI	MRCI+Q	CASSCF	MRCI	MRCI+Q	rel. time
AVDZ	0[a]	-0.325174	-0.349268	-0.009777	-0.346794	-0.372539	-6.13	-13.57	-14.60	1.0
AVTZ	-0.044082	-0.459217	-0.490918	-0.054397	-0.481240	-0.514744	-6.47	-13.82	-14.95	2.6
AVQZ	-0.057301	-0.502245	-0.536145	-0.067061	-0.524344	-0.560164	-6.12	-13.87	-15.07	11.0
AV5Z	-0.060628	-0.516598	-0.551124	-0.070337	-0.538542	-0.574991	-6.09	-13.77	-14.98	57.3
CBS	-0.064583	-0.525946	-0.561136	-0.074483	-0.548033	-0.585155	-6.21	-13.86	-15.07	-

a) Absolute energies stated relative to AVDZ reactant energy: -175.471563 Hartree.

Table 4.2. Product, reactant energies[a] and reaction exothermicities as function of optimizing the AVTZ basis set

Basis	F + H_2O MRCI+Q (Hartree)[a]	HF + OH MRCI+Q (Hartree)[a]	ΔE (kcal/mol)	rel. time
AVTZ[5s4p3d2f]/AVTZ[4s3p2d]	-0.490918	-0.514744	-14.95	2.6
AVTZ[6s4p3d2f]/AVTZ[3s3p2d]	-0.475371	-0.499164	-14.93	2.6
AVTZ[6s4p3d]/VTZ[3s2p1d]	-0.474516	-0.498290	-14.92	2.0
AVTZ[6s4p3d2f]/AVTZ[3s3p]	-0.424399	-0.447828	-14.70	1.4
AVTZ[6s4p3d]/VTZ[3s2p]	-0.423947	-0.447425	-14.73	1.2
+Spin-Orbit	-0.424561	-0.447633	-14.48	-
+ZPE	-0.386702	-0.429889	-16.59	-
Experiment	-	-	-17.61	-

a) Absolute energies relative to AVDZ reactant energy: -175.471563 Hartree.

Table 4.3. The geometry of the transition state at the SA-MCSCF and MRCI+Q level. The lengths and angles are defined in Figure 4.1. Bond lengths are in angstroms, angles in degrees. The basis set used is AVTZ[6s4p3d]/VTZ[3s2p] in a full valence active space.

	R_{HF1}	R_{OH1}	R_{OH2}	A	β	Γ
SA-MCSCF	1.218	1.093	0.974	101.378	139.771	58.158
MRCI+Q	1.350	1.031	0.971	102.551	118.407	69.552

Figures

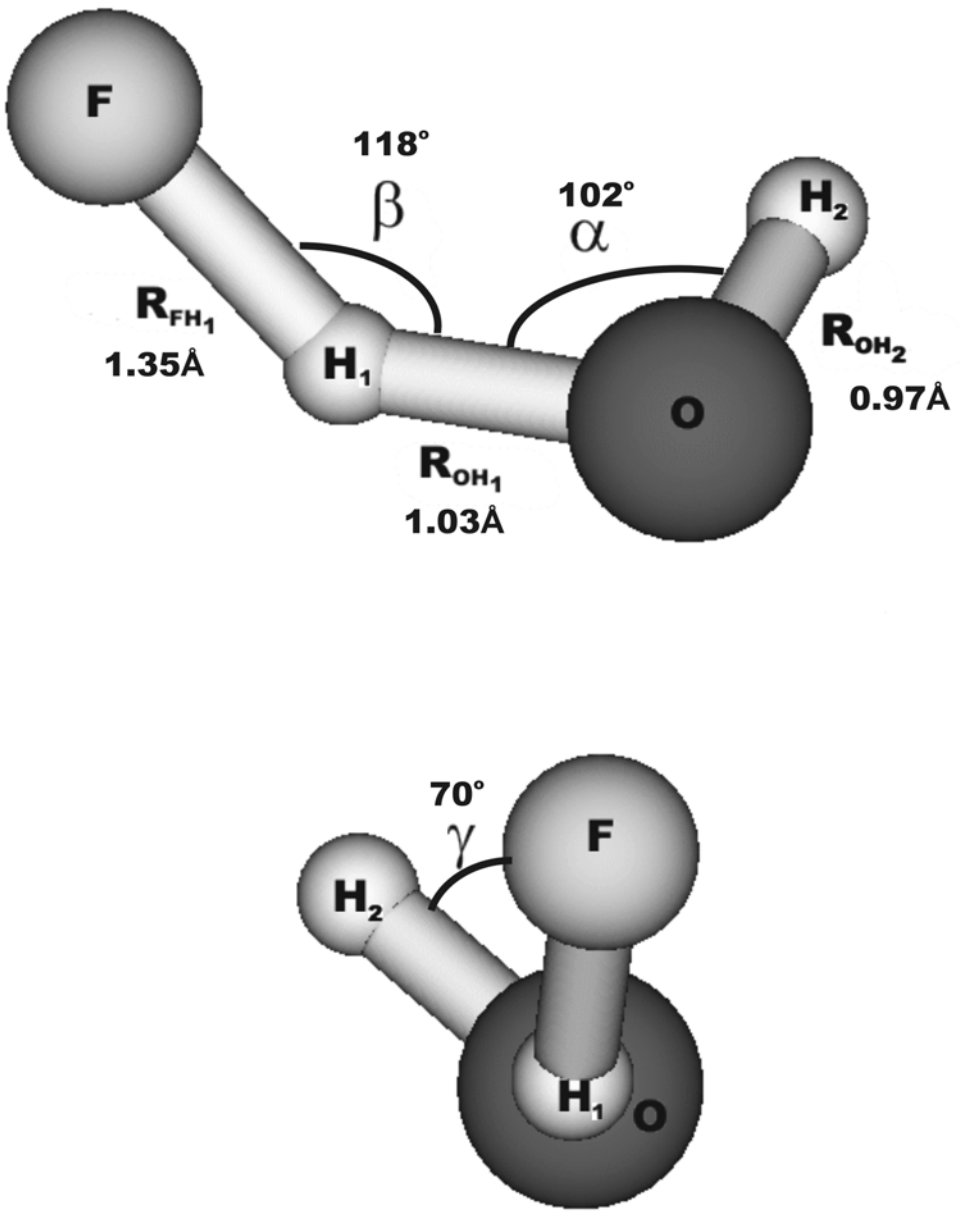

Figure 4.1: The internal coordinates used for specifying F + H_2O geometries. The geometry is given for the 5-state MCSCF transition state.

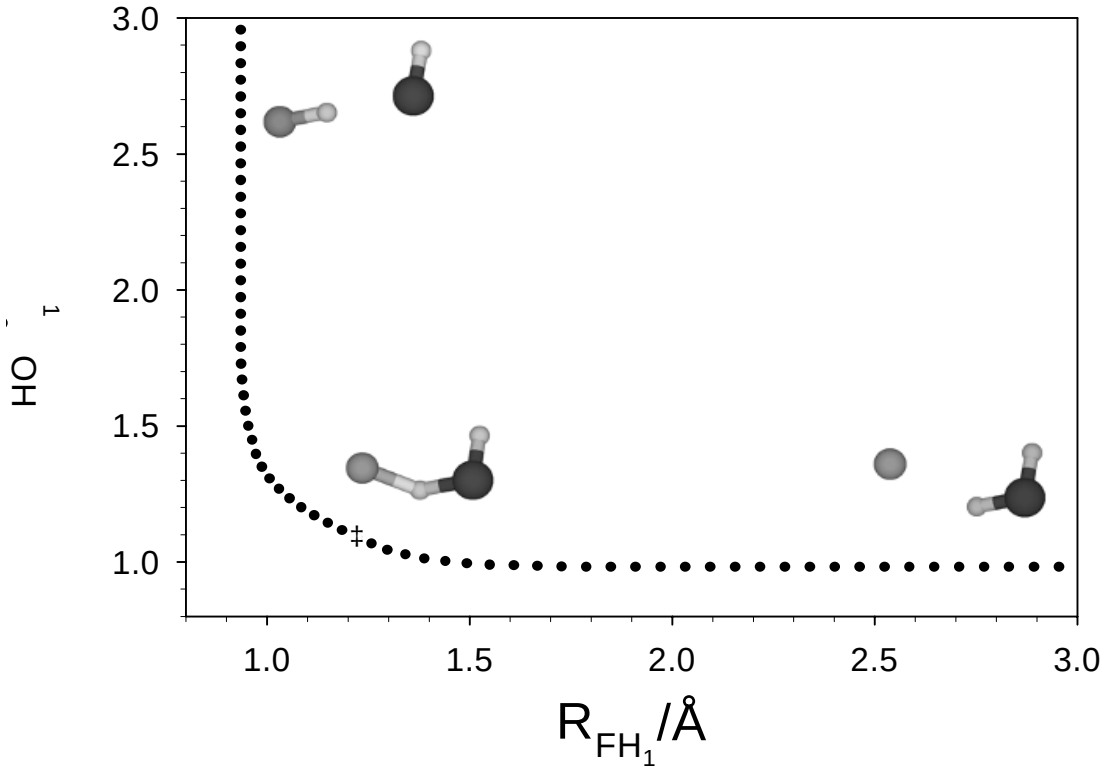

Figure 4.2: A 2D projection (R_{FH1} and R_{OH1} bond distances) of the full 6D reaction path calculated at the 5-state MCSCF level. This 6D reaction path is used throughout the paper.

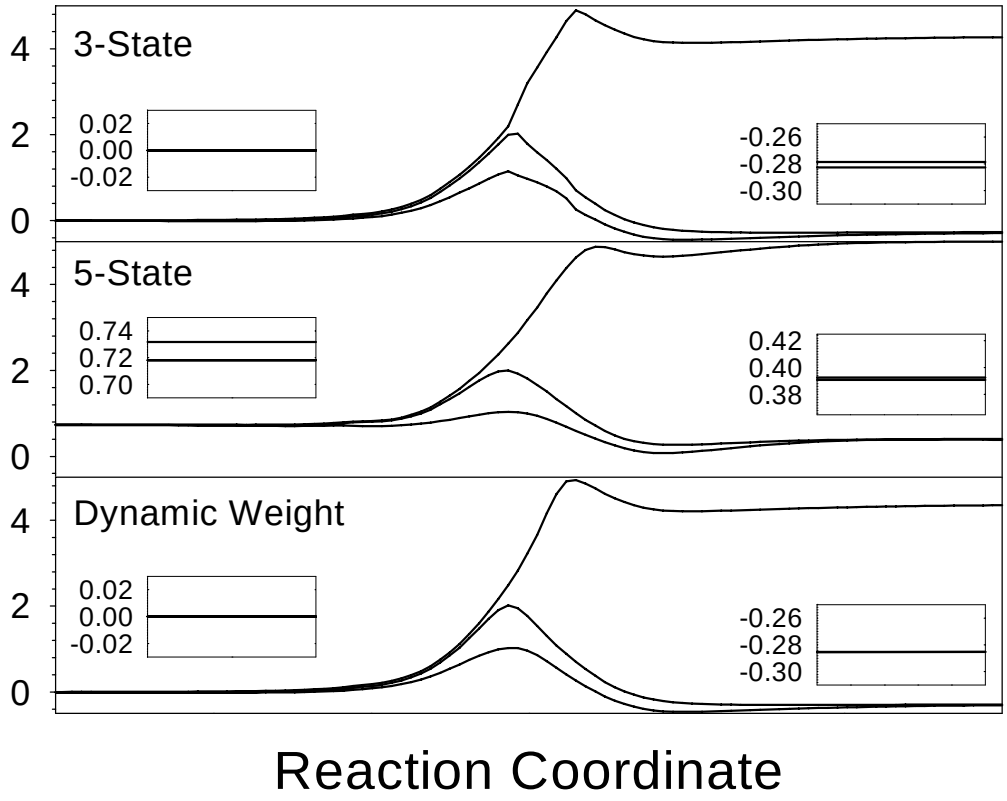

Figure 4.3: Calculated ground and excited state energies along the F + H_2O reaction coordinate for various levels of theory, a) 3-state MCSCF, b) 5-state MCSCF, c) Dynamically weighted MCSCF. The inserts at reactant and product asymptotes indicate a blow up of the energy scale to highlight deviations from perfect 3-fold (reactant) and 2-fold (product) degeneracies. Note that the dynamic weighting method produces the smoothest surface, and also reproduces the correct degeneracy at both asymptotes of the reactants.

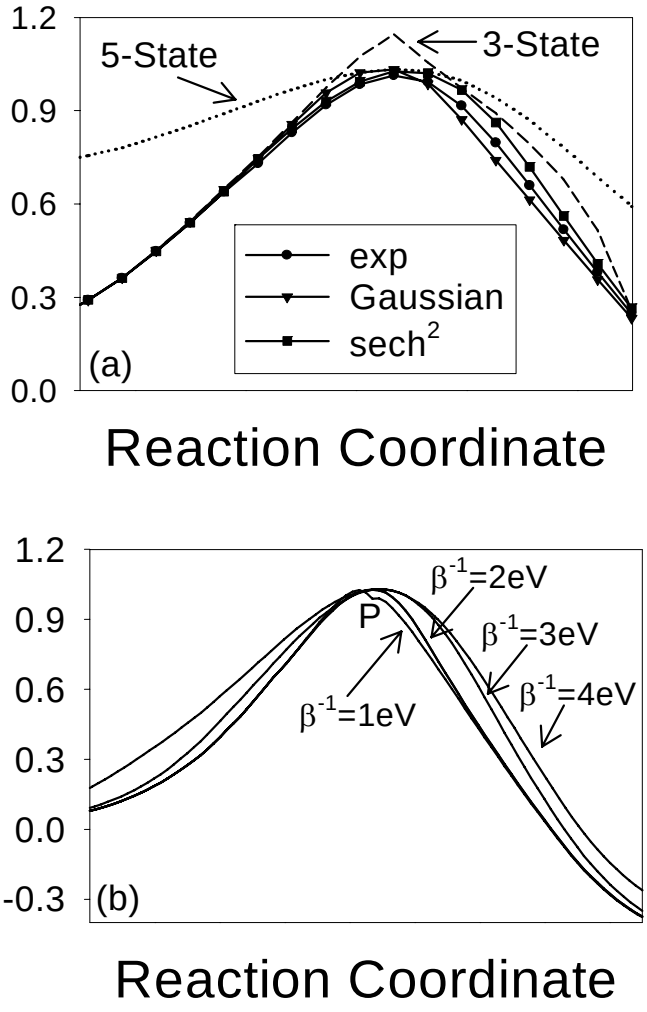

Figure 4.4: Dependence of ground state reaction path energy on weighting function in the transition state region. a) Exponential, Gaussian or $sech^2$ functional form. Note that the choice of the functional form has less of an effect on the surface than the number of states included in a traditional SA-MCSCF. b) Choice of scale parameter β. If β^{-1} is too small, small changes in energies in excited states can cause discontinuities in the ground state (e.g. point P), if β^{-1} is too large, the weights do not decay to 0 in the asymptotes for the excited states. Moderate β^{-1} parameters (*i.e.*,2-3eV) produce smooth curves and converge to ground-state-only asymptotes.

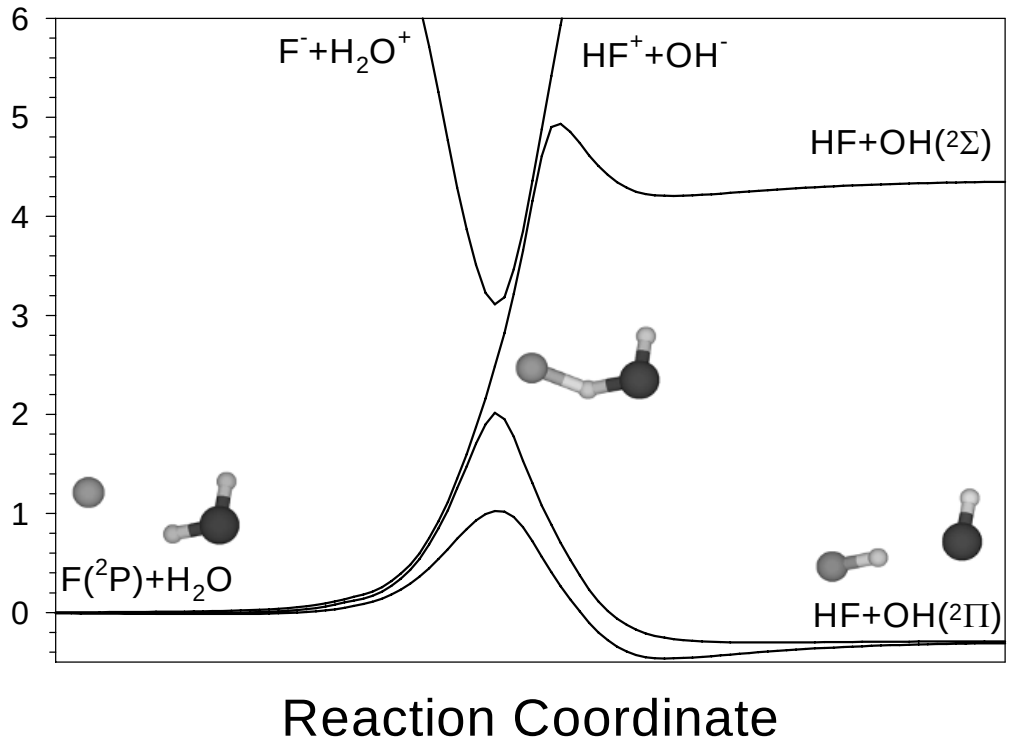

Figure 4.5: The lowest 4 states of the smooth DW-MCSCF reaction path. The energies along the reaction path, not only vary smoothly, but the degeneracies are correctly reproduced in the asymptotes. Also note that there are a number of states interacting in the transition state region.

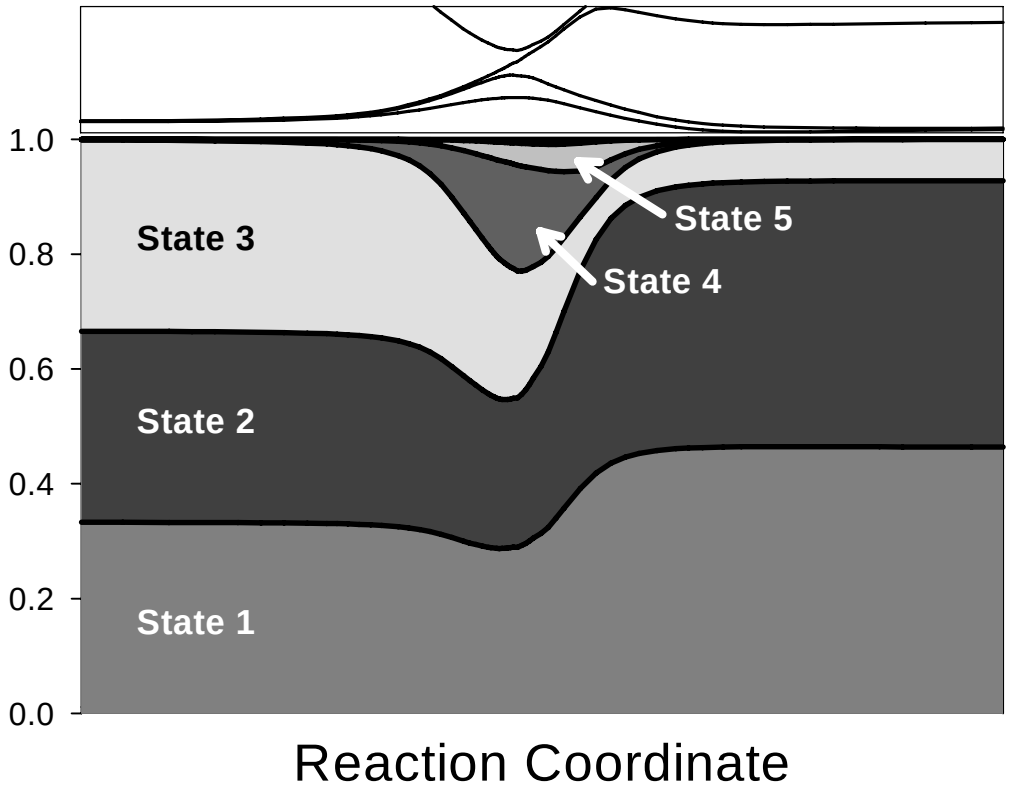

Figure 4.6: Converged weights (normalized to sum to 1) for the DW-MCSCF with β^{-1} = 3. The energies along the reaction path are reproduced at the top to help guide the eye. The weights smoothly vary from $(\frac{1}{3}:\frac{1}{3}:\frac{1}{3})$ to approximately $(\frac{1}{2}:\frac{1}{2}:0)$. During the cross-over through the transition state a fourth and fifth state are briefly introduced. DW-MCSCF automatically included the relevant states in the different regions of the PES.

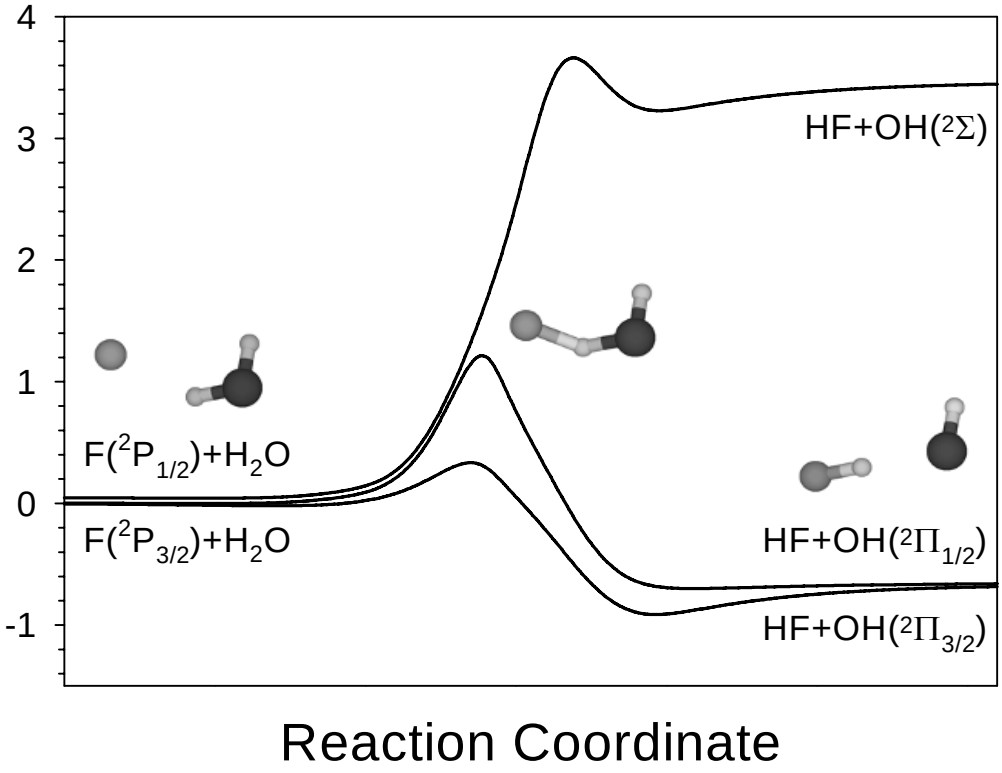

Figure 4.7: MRCI+Q with spin-orbit interactions calculated at the CASSCF reaction path geometries. The smoothly varying DW-MCSCF wave functions are used as reference configurations for MRCI+Q calculations. Note that the lowest barrier (when zero-point energy is included) is experimentally accessible in crossed supersonic jets, but the other barriers are far out of reach.

References

[1] J. M. Bowman and G. C. Schatz, Annual Review of Physical Chemistry **46**, 169 (1995); S. C. Althorpe and D. C. Clary, Annual Review of Physical Chemistry **54**, 493 (2003).

[2] D. H. Zhang and J. Z. H. Zhang, Journal of Chemical Physics **99** (7), 5615 (1993); D. H. Zhang and J. Z. H. Zhang, Journal of Chemical Physics **101** (2), 1146 (1994); D. H. Zhang and J. Z. H. Zhang, Journal of Chemical Physics **100** (4), 2697 (1994); Y. C. Zhang, D. S. Zhang, W. Li, Q. G. Zhang, D. Y. Wang, D. H. Zhang, and J. Z. H. Zhang, Journal of Physical Chemistry **99** (46), 16824 (1995); D. H. Zhang, J. Z. H. Zhang, Y. C. Zhang, D. Y. Wang, and Q. G. Zhang, Journal of Chemical Physics **102** (19), 7400 (1995); D. H. Zhang and J. Z. H. Zhang, Chemical Physics Letters **232** (4), 370 (1995); D. H. Zhang and J. C. Light, Journal of Chemical Physics **105** (3), 1291 (1996); D. H. Zhang and J. C. Light, Journal of Chemical Physics **104** (12), 4544 (1996); W. Zhu, J. Q. Dai, J. Z. H. Zhang, and D. H. Zhang, Journal of Chemical Physics **105** (11), 4881 (1996); Y. C. Zhang, Y. B. Zhang, D. S. Zhang, Q. G. Zhang, D. H. Zhang, and J. Z. H. Zhang, Chinese Science Bulletin **42** (2), 116 (1997); D. H. Zhang and J. C. Light, Journal of the Chemical Society-Faraday Transactions **93** (5), 691 (1997); D. H. Zhang and J. C. Light, Journal of Chemical Physics **106** (2), 551 (1997); J. C. Light and D. H. Zhang, Abstracts of Papers of the American Chemical Society **215**, U201 (1998); D. H. Zhang, J. C. Light, and S. Y. Lee, Journal of Chemical

Physics **109** (1), 79 (1998); R. P. A. Bettens, M. A. Collins, M. J. T. Jordan, and D. H. Zhang, Journal of Chemical Physics **112** (23), 10162 (2000); D. H. Zhang, M. A. Collins, and S. Y. Lee, Science **290** (5493), 961 (2000); Y. M. Li, M. L. Wang, J. Z. H. Zhang, and D. H. Zhang, Journal of Chemical Physics **114** (16), 7013 (2001); M. H. Yang, D. H. Zhang, M. A. Collins, and S. Y. Lee, Journal of Chemical Physics **115** (1), 174 (2001); M. H. Yang, D. H. Zhang, M. A. Collins, and S. Y. Lee, Journal of Chemical Physics **114** (11), 4759 (2001).

[3] M. Brouard, I. Burak, S. Marinakis, D. Minayev, P. O'Keeffe, C. Vallance, F. J. Aoiz, L. Banares, J. F. Castillo, D. H. Zhang, D. Xie, M. Yang, S. Y. Lee, and M. A. Collins, Physical Review Letters **90** (9) (2003); M. Brouard, I. Burak, D. Minayev, P. O'Keeffe, C. Vallance, F. J. Aoiz, L. Banares, J. F. Castillo, D. H. Zhang, and M. A. Collins, Journal of Chemical Physics **118** (3), 1162 (2003).

[4] M. H. Alexander, D. E. Manolopoulos, and H. J. Werner, Journal of Chemical Physics **113** (24), 11084 (2000); M. H. Alexander, Abstracts of Papers of the American Chemical Society **218**, U306 (1999); M. H. Alexander, H. J. Werner, and D. E. Manolopoulos, Journal of Chemical Physics **109** (14), 5710 (1998); S. A. Nizkorodov, W. W. Harper, and D. J. Nesbitt, Faraday Discussions (113), 107 (1999); J. F. Castillo, D. E. Manolopoulos, K. Stark, and H. J. Werner, Journal of Chemical Physics **104** (17), 6531 (1996); F. J. Aoiz, L. Banares, B. MartinezHaya, J. F. Castillo, D. E. Manolopoulos, K.

Stark, and H. J. Werner, Journal of Physical Chemistry A **101** (36), 6403 (1997).

[5] S. A. Nizkorodov, W. W. Harper, W. B. Chapman, B. W. Blackmon, and D. J. Nesbitt, Journal of Chemical Physics **111** (18), 8404 (1999).

[6] M. H. Alexander, G. Capecchi, and H. J. Werner, Science **296** (5568), 715 (2002); M. Alagia, N. Balucani, L. Cartechini, P. Casavecchia, G. G. Volpi, F. J. Aoiz, L. Banares, T. C. Allison, S. L. Mielke, and D. G. Truhlar, Physical Chemistry Chemical Physics **2** (4), 599 (2000).

[7] S. A. Harich, D. W. H. Hwang, X. F. Yang, J. J. Lin, X. M. Yang, and R. N. Dixon, Journal of Chemical Physics **113** (22), 10073 (2000); W. T. Zemke, W. C. Stwalley, J. A. Coxon, and P. G. Hajigeorgiou, Chemical Physics Letters **177** (4-5), 412 (1991).

[8] O. Votava, D. F. Plusquellic, and D. J. Nesbitt, Journal of Chemical Physics **110** (17), 8564 (1999); J. R. Fair, O. Votava, and D. J. Nesbitt, Journal of Chemical Physics **108** (1), 72 (1998); D. F. Plusquellic, O. Votava, and D. J. Nesbitt, Journal of Chemical Physics **109** (16), 6631 (1998); D. F. Plusquellic, O. Votava, and D. J. Nesbitt, Journal of Chemical Physics **107** (16), 6123 (1997); O. Votava, J. R. Fair, D. F. Plusquellic, E. Riedle, and D. J. Nesbitt, Journal of Chemical Physics **107** (21), 8854 (1997).

[9] W. W. Harper, S. A. Nizkorodov, and D. J. Nesbitt, Journal of Chemical Physics **116** (13), 5622 (2002); W. W. Harper, S. A. Nizkorodov, and D. J. Nesbitt, Chemical Physics Letters **335** (5-6), 381 (2001); W. W. Harper, S. A. Nizkorodov, and D. J. Nesbitt, Journal of Chemical Physics **113** (9), 3670

(2000); W. B. Chapman, B. W. Blackmon, S. Nizkorodov, and D. J. Nesbitt, Journal of Chemical Physics **109** (21), 9306 (1998).

[10] T. L. Meyers, D. C. Kitchen, B. Hu, and L. J. Butler, Journal of Chemical Physics **105** (7), 2948 (1996); G. C. G. Waschewsky, P. W. Kash, T. L. Myers, D. C. Kitchen, and L. J. Butler, Journal of the Chemical Society-Faraday Transactions **90** (12), 1581 (1994); P. W. Kash, G. C. G. Waschewsky, L. J. Butler, and M. M. Francl, Journal of Chemical Physics **99** (6), 4479 (1993).

[11] T. C. Allison, S. L. Mielke, D. W. Schwenke, and D. G. Truhlar, Journal of the Chemical Society-Faraday Transactions **93** (5), 825 (1997).

[12] J. C. Tully, in *Dynamics of Molecular Collisions: Part B*, edited by W. H. Miller (Plenum Press, New York, 1976).

[13] J. H. Frederick and C. Woywod, Journal of Chemical Physics **111** (16), 7255 (1999); B. R. Johnson and W. P. Reinhardt, Journal of Chemical Physics **85** (8), 4538 (1986).

[14] H. J. Werner and P. J. Knowles, Journal of Chemical Physics **82** (11), 5053 (1985); P. J. Knowles and H. J. Werner, Chemical Physics Letters **115** (3), 259 (1985).

[15] R. D. Amos, A. Bernhardsson, A. Berning, P. Celani, D. L. Cooper, M. J. O. Deegan, A. J. Dobbyn, F. Eckert, C. Hampel, G. Hetzer, P. J. Knowles, T. Korona, R. Lindh, A. W. Lloyd, S. J. McNicholas, F. R. Manby, W. Meyer, M. E. Mura, A. Nicklass, P. Palmieri, R. Pitzer, G. Rauhut, M. Schutz, U. Schumann, H. Stoll, A. J. Stone, R. Tarroni, T. Thorsteinsson, and H. J.

Werner, MOLPRO, a package of *ab initio* programs designed by H. J. Werner

and P. J. Knowles, version 2002.1 (Birmingham, UK, 2002).

[16] H. J. Werner and P. J. Knowles, Journal of Chemical Physics **89** (9), 5803 (1988); P. J. Knowles and H. J. Werner, Chemical Physics Letters **145** (6), 514 (1988); P. J. Knowles and H. J. Werner, Theoretica Chimica Acta **84** (1-2), 95 (1992).

[17] S. R. Langhoff and E. R. Davidson, International Journal of Quantum Chemistry **8** (1), 61 (1974).

[18] T. H. Dunning, Journal of Chemical Physics **90** (2), 1007 (1989).

[19] T. Helgaker, P. Jorgensen, and J. Olsen, *Molecular Electronic-Structure Theory*. (John Wiley & Sons, LTD, New York, 2000).

[20] K. Stark and H. J. Werner, Journal of Chemical Physics **104** (17), 6515 (1996).

[21] M. A. Collins, Abstracts of Papers of the American Chemical Society **223**, U493 (2002); K. C. Thompson, M. J. T. Jordan, and M. A. Collins, Journal of Chemical Physics **108** (20), 8302 (1998); K. C. Thompson, M. J. T. Jordan, and M. A. Collins, Journal of Chemical Physics **108** (2), 564 (1998); K. C. Thompson and M. A. Collins, Journal of the Chemical Society-Faraday Transactions **93** (5), 871 (1997); M. J. T. Jordan, K. C. Thompson, and M. A. Collins, Journal of Chemical Physics **103** (22), 9669 (1995); M. J. T. Jordan, K. C. Thompson, and M. A. Collins, Journal of Chemical Physics **102** (14),

5647 (1995); J. Ischtwan and M. A. Collins, Journal of Chemical Physics **100** (11), 8080 (1994).

[22] F. Eckert, P. Pulay, and H. J. Werner, Journal of Computational Chemistry **18** (12), 1473 (1997).

[23] F. Eckert and H. J. Werner, Theoretical Chemistry Accounts **100** (1-4), 21 (1998).

[24] A. Berning, M. Schweizer, H. J. Werner, P. J. Knowles, and P. Palmieri, Molecular Physics **98** (21), 1823 (2000).

[25] K. Fukui, Accounts of Chemical Research **14** (12), 363 (1981); K. Yamashita, T. Yamabe, and K. Fukui, Chemical Physics Letters **84** (1), 123 (1981).

[26] A. R. Offer and G. G. Balintkurti, Journal of Chemical Physics **101** (12), 10416 (1994).

[27] T. L. Myers, N. R. Forde, B. Hu, D. C. Kitchen, and L. J. Butler, Journal of Chemical Physics **107** (14), 5361 (1997).

[28] R. N. Zare, in *Angular Momentum* (John Wiley & Sons, New York, 1988), pp. 302.

Chapter 5: Multireference configuration interaction calculations for the $F(^2P) + HCl \rightarrow HF + Cl(^2P)$ reaction: A correlation scaled ground state ($1^2A'$) potential energy surface

I. Introduction

A first principles theoretical understanding of elementary reaction dynamics at the quantum state resolved level has remained a major challenge to the chemical physics community over the last several decades. As a result of this intense interest, there have been impressive advances in both *ab initio* development of accurate potential energy surfaces, as well as methods for numerically exact quantum dynamical calculations on these surfaces. One system that has represented a watershed for reaction dynamics has been the $F(^2P) + H_2 \rightarrow HF + H(^2S)$ reaction, for which there now exists an exceptionally high level potential surface[1,2] and numerous theoretical[3-8] and experimental[9-20] papers on state-to-state reactive scattering. Of particular dynamical interest has been the subtly but importantly different "heavy + light-heavy" isotopic variation on this reaction system, $F(^2P) + HD \rightarrow HF + D(^2S)$, for which long lived scattering resonances in the transition state region have been both predicted[21-31] and experimentally[32] observed. Although there are many contributing factors, inspection of the transition state wave functions offers a simple physical picture of such resonances, classically corresponding to highly excited H atom motion in a quasi bound HF(v = 3)--D state. In essence, this state executes rapid

H atom motion between the F and D atoms, which eventually predissociates into the continuum of states corresponding to HF(v = 2,J) + D. Such efforts have further served to elucidate the considerable complexity and dynamical richness present even in simple H atom transfer reactions and continue to offer challenges for first principles theoretical calculations in larger systems.

The clear observation of transition state resonances in F + HD suggests that there may be similar resonance dynamical effects in the corresponding $F(^2P)$ + hydrogen halide systems. Of particular experimental and theoretical interest is the $F(^2P) + HCl \rightarrow HF + Cl(^2P)$ system, the high-level *ab initio* potential surface which represents the focus of this paper. This reaction has a nearly identical exothermicity (ΔE_{HF+Cl} = -33.1 kcal/mol vs. ΔE_{HF+H} = -31.2 kcal/mol), a thermally accessible barrier height, and yet is still within reach of modern high-level *ab initio* efforts for mapping ground and excited potential surfaces out in full dimensionality. In this work, I present a new benchmark ground state potential energy surface (PES) for the $F(^2P) + HCl \rightarrow HF + Cl(^2P)$ reaction, to accompany experimental direct IR absorption and ion imaging studies currently in progress. In addition to being a prototypically heavy-light-heavy system, the $F(^2P) + HCl \rightarrow HF + Cl(^2P)$ reaction is also important in understanding hydrogen-halide chemical lasers[33] and provides novel opportunities to study non-adiabatic dynamics on multiple electronic surfaces.

Previous theoretical studies on this surface have included quasiclassical trajectory (QCT) calculations performed on an empirical LEPS surface[34], QCT[35]and full dimensional time-dependant wavepacket [36] calculations obtained on a newer *ab initio* (PUMP2/6-311G(3d2f,3p2d)) surface[37], and a LEPS surface created from

recent experimental kinetics information[38]. All previous calculations have focused specifically on the ground ($1^2A'$) electronic state, though study of other F atom abstraction systems has revealed evidence for avoided crossings, charge transfer states, seams of conical intersection, etc. For example, it has been shown that there is significant non-adiabatic behavior for $F(^2P) + H_2 \square HF + H(^2S)$ in the entrance channel[3,23], and there is also direct experimental evidence in 4 atom systems (*i.e.*,$(^2P)F + H_2O \rightarrow HF + OH(^2\Pi)$ that exhibit strong non-adiabatic behavior in both the entrance and exit channels[39]. It is likely that similar effects are present in $F(^2P) + HCl \rightarrow HF + Cl(^2P)$, the dynamics of which clearly necessitate a high-level multireference electronic treatment. In this work, I present a new ground electronic state ($1^2A'$) PES for the $F(^2P) + HCl$ reaction, based on high-level multireference calculations and representing a first step toward multiple fitted surfaces with non-adiabatic coupling, spin-orbit interactions explicitly included.

The $F(^2P) + HCl \rightarrow HF + Cl(^2P)$ reaction presents many of the same challenges seen earlier in the $F(^2P) + H_2O \rightarrow HF + OH(^2\Pi)$ reaction[40], namely the presence of highly electronegative atoms significantly lower the charge transfer (CT) states ($F^- + HCl^+(^2\Pi) \rightarrow HF^+(^2\Pi) + Cl^-$) in the transition state region. This leads to non-adiabatic coupling and avoided crossing behavior between the $1^2A'$ and $2^2A'$, which requires multireference calculations to describe accurately. In light of these considerations, *ab initio* calculations for this PES are obtained via internally contracted multireference configuration interaction (MRCI)[41-43] using reference states taken from a dynamically weighed multiconfigurational self-consistent field (DW-MCSCF)[40] calculation. In addition, extrapolation to the complete basis set (CBS)

limit[44] and correlation energy scaling[45,46] are used to further refine the PES shape and energetics accurately.

As a further source of dynamical richness, the $F(^2P) + HCl \rightarrow HF + Cl(^2P)$ surface is also expected to exhibit conical intersections in both entrance and exit channels. Indeed, this can be anticipated from rather elementary chemistry considerations, as described by Hutson and coworkers[47-49] for open shell radical X-HX complexes. Specifically, well outside the region of chemical reaction, the surface will be asymptotically dominated by dipole-quadrupole and dipole-induced dipole interactions. This results in a state energy ordering of $E(\Sigma) > E(\Pi_x) = E(\Pi_y)$ for the linear approach geometry. In the vicinity of the transition state, however, the lowest energy collinear surface arises from the unfilled p-orbital of the bare F (or Cl) atom in an Σ configuration with respect to the HCl reactant (or HF product), i.e., yielding a reverse energy ordering of $E(\Sigma) < E(\Pi_x) = E(\Pi_y)$. Since the symmetries of the coplanar Π_x and Σ surfaces are reduced to non-crossing $1^2A'$ and $2^2A'$ surfaces for any non-collinear geometry, this necessarily implies the presence of a 3N-5 = 1D "seam" of conical intersections. Of special interest for F + HCl reaction dynamics, these conical intersection seams are both energetically low enough ($E_{crossing}$ = 3-4 kcal/mol) with respect to collision energy (E_{com} = 5 kcal/mol) as well as the $F(^2P)$ + HCl transition state ($E_{TST} \approx 3.8$ kcal/mol) that they are likely play an important role.

The organization of this chapter is as follows: Section II describes the details of the *ab initio* calculations specifically focusing on the $1^2A'$ electronic state. In Section III, I describe the benchmark calculations, with emphasis on the CBS extrapolation and correlation energy scaling that is used to provide an accurate PES.

Section IV presents the details of the analytical fit to the *ab initio* points. In Section V I discuss the interesting aspects of this PES followed by a summary and concluding remarks in Section VI.

II. Details of the Ab Initio Calculations

All calculations are performed using the MOLPRO suite of *ab initio* programs[50]. Since I explicitly need to capture non-adiabatic as well as single surface effects, electronically excited states of the $F(^2P) + HCl \rightarrow HF + Cl(^2P)$ reaction are required. Thus, the *ab initio* methods utilize multireference methods to obtain wavefunctions for non-adiabatic calculations and characterization of the conical intersections. In addition, other 3- and 4-atom systems[40] involving F have indicated large multireference character in the ground state wavefunctions.. In light of these restrictions and past success with the dynamically weighted multiconfigurational self-consistent field (DW-MCSCF)[40] method, the natural choice for this reaction is to use DW-MCSCF along with internally contracted multireference CI (MRCI) [41-43] and the multireference Davidson correction (MRCI+Q)[51-53]. Two separate MRCI+Q calculations are done for each symmetry: one for the $1^2A'$ and $2^2A'$ states and one for the $1^2A''$ state. In this work, I restrict the focus on the ground electronic ($1^2A'$) surface; a more detailed description of all three adiabatic surfaces, as well as the diabatic representation and non-adiabatic coupling between these surfaces will be presented elsewhere.[54]

Residual *ab initio* error due to incomplete basis sets can be corrected by extrapolating to the complete basis set (CBS) limit[44] using the standard aug-cc-pVnZ (n = 2,3,4) basis sets of Woon and Dunning[55-57]. Others[46,58] have shown that an

additional tight (large zeta) d function to the Cl basis set improves the accuracy, but benchmark tests (*vide infra*) show no significant improvement in the $F(^2P) + HCl \rightarrow HF + Cl(^2P)$ system, as calibrated against the precise experimental reaction exothermicity. I therefore elect to use the standard aug-cc-pVnZ (AVnZ, n = 2-4) basis functions and extrapolate to the CBS limit. Based on the benchmark studies of Peterson, this extrapolation is obtained via the three parameter fit[44,46]

$$E(n) = E_{CBS} + Be^{-(n-1)} + Ce^{-(n-1)^2}. \qquad (5.1)$$

This function yields an excellent extrapolation to the CBS limit (see Figure 5.1) as explicitly confirmed by additional calculations for reagent and product asymptotic geometries with basis set extensions up to n = 5.

The MRCI+Q calculations are performed using a full valence complete active space (CAS)[59] reference function with 15 active orbitals (12A',3A"), 6 of which (5A',1A") are uncorrelated. The orbitals are obtained by a state-averaged multiconfiguration SCF (SA-MCSCF)[60,61] calculation with 15 active orbitals (12A', 3A") with 7 (6A', 1A") closed to excitations. A total of 6 states are then included in the SA-MCSCF calculation (4A', 2A"), with the weights determined by the dynamically weighted-MCSCF algorithm. In order to account for the triply degenerate p-hole in both the F and Cl atoms at the asymptote, the SA-MCSCF calculations include all 3 states (2A', 1A"); however, low-lying charge transfer (CT) states (e.g. $F^- + HCl^+(^2\Pi) \rightarrow HF^+(^2\Pi) + Cl^-$) require the inclusion of 2 more A" and 1 more A' state (a total of 6 states) to fully describe the transition state region. As previously demonstrated[40], root flipping as the CT surfaces cross other states along the reaction path makes it extremely challenging to obtain a smooth accurate PES for

a fixed set of SA-MCSCF weights. In DW-MCSCF, on the other hand, the weights for each state are chosen as a function of its energy with respect to the ground state energy at each point in configuration space. The function for the weight based on the energy difference from the ground state is

$$w_i \propto sech^2\left(-\beta\left(E_i - E_0\right)\right) \qquad (5.2)$$

The decay coefficient (β^{-1}) for DW-MCSCF is empirically optimized to be 3eV, though the results prove relatively insensitive to this choice. Most importantly, this method permits one to eliminate spurious discontinuities from root flipping and thereby obtain a smooth reaction path and surface while accurately describing the asymptotes and the transition state. The orbitals obtained from the DW-MCSCF calculation are used as reference states for the internally contracted MRCI calculation.

III. Benchmark Calculations

A. Exothermicity

By way of calibration, I have performed a number of single point calculations at product and reagent asymptotes (F + HCl and HF + Cl) to benchmark how well MRCI+Q predicts the reaction exothermicity, ΔE_{rxn}, with respect to previous lower level methods. Table 5.1 contains a summary of reaction exothermicities calculated by these methods, each for an AVnZ basis set and extrapolated to the CBS limit. To facilitate most the direct comparison with experiment, the energies in Table 5.1 have been corrected for experimental zero-point (5.98 kcal/mol and 4.31 kcal/mol for HF and HCl, respectively) and spin-orbit splittings (1.16 kcal/mol and 2.52 kcal/mol for

F and Cl), which are not included the *ab initio* calculations reported here. The results in Table 5.1 indicate rapid convergence with respect to basis set size ($\Delta E \approx 0.06$ kcal/mol between AVQZ and the CBS limit values). Indeed, Figure 5.1 clearly shows that energies for both reactant and product asymptotes are independently converging to the CBS limit. By way of confirmation, the dotted line in Figure 5.1 represents the CBS extrapolation for AVnZ basis sets with n = 2 - 4, which in fact very closely reproduces the single point calculated values for AV5Z.

It is important to note that although the calculated reaction exothermicity converges nicely to ~-31.0 kcal/mol, the true exothermicity (dashed line) is in fact ~2 kcal/mol lower (-33.06 kcal/mol[62,63]). This is not a limitation in the CBS extrapolation but rather the size of the "complete" active space. This can be readily seen in the incremental shifts in ΔE as a function of basis set size (inset in Figure 5.1), which indicate the CBS extrapolation converging *upward* to a value *higher* than the experimental energy. This arises from incomplete recovery of the full correlation energy at the MRCI+Q level and is reminiscent of the comparable (~ 0.4 kcal/mol) exothermicity discrepancies from benchmark calculations for the F + H_2 surface. Indeed, as demonstrated by Stark and Werner for F + H_2[1], 3pF orbitals must be included in the active space to get results accurate to < 0.1 kcal/mol. For the F + HCl reaction, however, including 3pF orbitals would energetically require also including all 5 of the 3dCl orbitals, increasing the number of occupied orbitals from 15 (12A', 3A") to 24 (18A', 6A"), and making the calculation prohibitively expensive. By way of example, single point AVTZ calculations at reagent and product geometries with this enhanced active space decrease the exothermicity error down to ~0.5 kcal/mol;

however, even this requires more than 2 days on a single 2.4GHz processor, i.e., too long to map out an entire 3D PES. I address below how to systematically compensate for these modest residual discrepancies in correlation energy, but for the moment, simply note that the calculations are quite well converged with respect to basis set by CBS extrapolation for n = [2 - 4].

Building on ideas by Peterson[46] and Truhlar[45], I employ a simple global correlation energy scaling procedure calibrated to match the experimentally known reaction exothermicity. Specifically, I uniformly scale the correlation energy by a constant factor near unity that reproduces the exothermicity exactly while retaining the shape of the PES and not introducing any discontinuities. First, I define correlation energy as the difference between the MRCI+Q energy and the MCSCF energy:

$$E(R)_{CORR} = E(R)_{MRCI+Q} - E(R)_{MCSCF}, \qquad (5.3)$$

where R is a vector of the intermolecular coordinates. The scaled energy is just the sum of the MCSCF energy plus the correlation energy scaled by a factor, γ:

$$E(R)_{SCALED} = E(R)_{MCSCF} + \gamma E(R)_{CORR}. \qquad (5.4)$$

In the limit of $\gamma = 0$, the scaled energy is just the MCSCF energy (i.e., no extra correlation energy is recovered), when $\gamma = 1$ the scaled energy is the MRCI+Q energy (i.e., all correlation energy is recovered). Allowing γ to be greater than unity permits recovery of additional correlation energy, in effect, approximating an increase in active space. The value for γ is empirically chosen to match the reaction exothermicity, i.e.,

$$E(prod)_{SCALED} - E(reac)_{SCALED} = \Delta E_{EXPERIMENT}. \qquad (5.5)$$

The scaling factors (γ) for AVnZ (n = 2 - 4), as well as the CBS extrapolation, monotonically decrease as the basis set becomes more complete. Indeed, at the CBS limit it is close to unity (γ = 1.027) for the A' symmetry, i.e., one only needs to recover an extra 2.7% of the correlation energy to reproduce the experiment. It is worth noting that the scaling values for A' (γ = 1.027) and A" (γ = 1.046) symmetries differ; this is because in the final MRCI+Q calculation, the two lowest ^{2}A' states and the one lowest ^{2}A" state are calculated, resulting in a larger A' reference space. Permitting γ to differ provides additional flexibility for each symmetry species to make up for finite active space size.

By way of example, Fig 5.2 shows the results for correlation energy as defined in Eq. 5.3 along the F + HCl reaction coordinate (described later) for each of the AVnZ basis sets and for the CBS limit. The shaded portion reflects the "extra" amount of energy recovered from the CBS values by correlation scaling. Such a pattern of correlation energy as a function of basis set and reaction coordinate makes it clear that correlation energy scaling is approximately equivalent to increasing the basis size. More quantitatively, the inset in Figure 5.2 shows the ratio of correlation energy for a given basis set to that inferred from a CBS extrapolation. The constancy of this ratio for each basis set provides further support that additional correlation energy is recovered by an almost constant scale factor along the full reaction path. Furthermore, this indicates that the shape of the PES is already quite accurately determined at the MRCI+Q level, with correlation scaling resulting in only minor adjustment of the reaction energetics to match experiment.

B. HF, HCl, and ClF asymptotic potentials

As a further test of the *ab initio* accuracy, the three asymptotic contributions for the $F(^2P) + HCl \rightarrow HF + Cl(^2P)$ surface corresponding to HF, HCl, and ClF have been benchmarked with respect to both basis size and correlation energy scaling. Table 5.2 summarizes the dissociation energies (kcal/mol), bond lengths (A), harmonic frequencies (cm^{-1}), anharmonicities (cm^{-1}), and rotational constants (cm^{-1}) for HF, HCl, and ClF calculated by DW-MCSCF/MCRI+Q for the various AVnZ (n = 2 - 4). The bond dissociation energies for each of the reactant and product channels are both in very satisfactory agreement (~0.1 - 0.2 kcal/mol) with experiment, and are significantly improved by correlation scaling. It is noteworthy that such scaling has relatively little influence on the vibration/rotation diatomic constants, providing additional support that correlation scaling results in only very minor changes in the overall PES topography. Also remarkable is that the single scaling factor chosen to match the experimental exothermicity for F + HCl reproduces properties of the ClF + H channel quite well, despite being quite remote to the reaction path for HF + Cl formation.

C. Transition state

We begin with gradient saddle point searching for the F-H-Cl transition state geometry and barrier height (See Figure 5.3 for transition states at multiple levels of theory and Table 5.3 for a summary of transition state geometries). Previous *ab initio* PES[37] calculations have reported a strongly bent F-H-Cl angle (137^o) and a classical barrier height of 4 - 6 kcal/mol. At the current improved level of theory (MRCI+Q/CBS/Scaled), the transition state geometry is bent even further (123.5^o),

with a classical barrier lowered to 3.8 kcal/mol. I note for later discussion that this is qualitatively different than the slightly bent transition state observed for F + H_2, which has important consequences for the resulting reaction dynamics. Furthermore, the transition state is relatively loose, resulting in zero-point energy along the reaction path that lowers the classical barrier height by $\Delta E \approx 0.9$ kcal/mol. This effectively yields an adiabatic MRCI barrier of ~2.9 kcal/mol.

By way of additional comparison, a single critical point UCCSD(T)/AVQZ calculation[64] also yields a highly bent transition state (118^o), so this novel degree of bending is clearly a robust feature of the true potential surface (see Figure 5.3). Interestingly, such UCCSD(T) calculations suggest an even smaller classical barrier height of 2.2 kcal/mol, though this is obtained using a spin unrestricted basis set. There have been previous temperature dependent studies[65] of F + HCl kinetics by Houston and coworkers, which could in principle help resolve the differences in the MRCI+Q/CBS/Scaled vs. UCCSD(T)/AVQZ barrier values. Unfortunately, the F + HCl experimental results exhibit strongly curved non-Arrhenius behavior, which complicates comparison of empirical activation energies with actual *ab initio* transition state barriers. However, if I examine the CI vector from the MRCI calculations, the MCSCF ground state contribution accounts for only ~60% of the total wave function probability at the transition state, with single excited state amplitudes as large as 0.53. This indicates strong multireference character in the transition state wavefunction and considerable mixing of higher electronic states not reflected in the UCCSD(T) calculation. Furthermore, inclusion of ~0.9 kcal/mol zero point effects would presumably similarly decrease the UCCSD(T)/AVQZ

adiabatic barrier to ~ 1.3 kcal/mol. Such an adiabatic barrier height prediction would already be lower than for F + HD (~ 1.5 kcal/mol[1]), though experimental studies[66] indicate F + HCl to have at least 3 - 4 fold *lower cross sections* for similar collision energies. Therefore, although further high-level surface calculations at the CCSD(T) level could be interesting to pursue, one can be cautiously confident from the present MRCI/Q results that a strongly bent transition state (~123^{o}) with a vibrationally adiabatic barrier height of ~2.9 kcal/mol (before spin-orbit effects) represents a very good approximation to the true values.

D. Reaction path

The reaction path provides a convenient set of benchmark points with which to further verify that my choices of method, basis, correlation scaling, etc are valid throughout configuration space and, in particular, away from the transition state.[67] For simplicity, the reaction path geometries are obtained from a SA-MCSCF ((3 state) calculation, for which analytical gradients are available for efficient reaction path following (MOLPRO does not yet provide analytic gradients for full MRCI+Q) in both product and reagent directions along the path of steepest decent for the lowest state. When the potential gradients in the asymptotic region become too small to follow reliably, the reaction path is simply defined by increasing the F - HCl or HF - Cl center of mass separations toward reactants or products.

Using the coordinates mapped out along the SA-MCSCF reaction path, I next perform a 6 state *dynamically weighted* MCSCF calculation. In Figure 5.4, the energies (a) and normalized dynamical weights (b) along the reaction path are shown as a function of the reaction coordinate[68]. Notice that in each asymptotic region, the

DW-MCSCF method effectively reduces to a ~three-state calculation, i.e., sufficient for accurately describing the triply degenerate p-hole in the lone F or Cl halogen atoms. As the transition state region is entered, however, the two additional F^- + $HCl^+(^2\Pi)$ and $HF^+(^2\Pi)$ + Cl^- charge transfer states rapidly decrease in energy and become significantly weighted in the DW-MCSCF calculation and exhibit strong effects on the reaction path curvature (see Figure 5.4a). As evident in Figures 5.4a, b, dynamical weighting of the 6 lowest states more than ensures that all 5 of the relevant open shell and charge transfer interactions are accounted for throughout the reaction path, and in the transition state region in particular.

An internally contracted MRCI+Q calculation is then performed using the reference states from the DW-MCSCF calculations for each AVnZ n = [2,4] basis set. The energies of both the DW-MCSCF and MRCI+Q calculations are extrapolated as a function of basis set to the CBS limit, with final refinement by scaling of the correlation energies by a constant γ to match experimental exothermicity. As noted earlier, this correlation scaling method only makes minor adjustments in the energetics of the system without influencing the shape of the PES. By way of example, Figure 5.5 presents the energy profile along the reaction path for the series of MCSCF/CBS, MRCI+Q/CBS, and MRCI+Q/CBS/Scaled procedures. The large shift between the MCSCF and MRCI+Q curves is due to the large amount of correlation energy recovered by the MRCI+Q method, in contrast with the very small change (see magnification in Figure 5.5) between MRCI+Q and the MRCI+Q/Scaled methods due to minor additional correlation energy that scaling recovers. Most importantly, this dynamically weighted approach results in smoothly changing

energies along the reaction path, which represents a small but obviously key subset of geometries for dynamics on the full PES.

E. Entrance and exit channel van der Waals wells

As noted in the previous surface calculations[37], there are $1^2A'$ van der Waals complexes in both entrance and exit channels. The entrance channel exhibits a relatively shallow F--HCl well depth (relative to the F + HCl asymptote) of ~0.43 kcal/mol for a linear geometry with R_{HF} = 4.50 a_0 and R_{HCl} = 2.44 a_0. The effective well depth in a full collision should decrease with rotational averaging; this is in good agreement with crossed molecular beam experiments[69], which place the rotationally averaged F + HCl van der Waals well depth at 0.32 kcal/mol. As expected from the larger dipole-quadrupole and dipole-induced dipole interactions[70], the exit channel exhibits a stronger van der Waals well of 1.52 kcal/mol, for a linear geometry with R_{HF} = 1.75 a_0 and R_{HCl} = 4.73 a_0. Interestingly, the CI vectors for both entrance and exit channel wells show significant contributions (~10%) from excited state amplitudes, further supporting the importance of high-level multireference *ab initio* methods in constructing a full potential energy surface.

IV. Potential Energy Surfaces

In order to construct the full 3D potential energy surface, calculations have been performed along a grid of points with the ranges R_{HF} = [1.3 - 15.0] a_0 and R_{HCl} = [1.8 - 15.0] a_0 and $\theta_{F\text{-}H\text{-}Cl}$ = [180, 150, 120, 90, 60, 30, 0], sampling only energies lower than 50 kcal/mol above the entrance channel energy. These 3230 points are chosen on a grid such that the density is maximized in important regions of the

surface (transition state, van der Walls wells) while still sampling a large enough region to get an accurate description of the PES. Also included in the full set are 121 points sampling directly along the reaction path. Following the methods outlined by Aguado and Paniagua,[71] these *ab initio* points are fit to an analytical multibody expansion:

$$V(R_{HF}, R_{HCl}, R_{ClF}) = V^{(1)} + \sum_{i\in\{HF,HCl,ClF\}} V^{(2)}(R_i) + V^{(3)}(R_{HF}, R_{HCl}, R_{ClF}). \quad (5.6)$$

where $V^{(1)}$ is the energy of the separated atoms which was subtracted from the *ab initio* energies, $V^{(2)}$ are the diatomic potentials, and $V^{(3)}$ reflects the remaining 3-body interactions.

A. Two body terms

The two body term is based on a sum of modified Rydberg functions[71]:

$$V^{(2)}(R) = \frac{C_0}{R} e^{-\beta_1^{(2)} R} + \sum_{i=1}^{N} C_i \left(R e^{-\beta_2^{(2)} R} \right)^i . \quad (5.7)$$

where R represents the pairwise interatomic distances between the 3 atoms. *Ab initio* points for each of the diatomics are fit to a 9th order polynomial (N = 9). For the Cl + HF reagent channel, 19 *ab initio* points between R_{HF} = 1.2 a_0 and R_{HF} = 3.0 a_0 have been used, yielding fits with a global RMS deviation of 0.039 kcal/mol. Similarly for HCl, 26 points between R_{HCl} = 1.6 a_0 and R_{HCl} = 4.0 a_0 have been fit to a global RMS of 0.015 kcal/mol. Although the ClF region of the surface is not sampled directly in the reactive scattering experiments, the ClF potential is sampled for 21 points between R_{ClF} = 2.5 a_0 and R_{ClF} = 4.5 a_0, yielding a global diatomic fit with a very satisfactory RMS deviation of ~0.046 kcal/mol.

B. Three body terms

The three body term simply reflects the remaining difference between *ab initio* points after subtracting the diatom $V^{(2)}$ and atom $V^{(1)}$ energies. Since this term must vanish in any of the diatomic asymptotes, a commonly used functional form is simply a linear combination of two-body product functions, i.e.,

$$V^{(3)}(R_1, R_2, R_3) = \sum_{i,j,k}^{M} D_{ijk} \left(R_1 e^{-\beta_1^{(3)} R_1}\right)^i \left(R_2 e^{-\beta_2^{(3)} R_2}\right)^j \left(R_3 e^{-\beta_{31}^{(3)} R_3}\right)^k , \qquad (5.8)$$

where the total order of the polynomial is restricted to $i + j + k \leq M$. The explicit numerical least squares weighting strategy for obtaining this fit is modeled after efforts to develop the Stark-Werner $F + H_2$ surface[1]. Specifically, the *ab initio* points along the reaction path are given a weight of 100. Of the 3230 grid points, the 2200 geometries with energies less than 15 kcal/mol above the entrance channel are weighted by 10, with the remaining 1030 points with energies between 15 and 50 kcal/mol above the entrance channel receiving a weight of 1. The resulting global RMS deviation for least squares fit with a 9th order polynomial (M = 9) is ~0.72 kcal/mol, i.e., 3.5 times better than the previous surface[37], while the RMS deviation for points along the reaction path improves to ~0.29 kcal/mol. A 2D cut through the PES at $\theta = 123.5^{o}$ (i.e., the MRCI+Q/CBS/ Scaled transition state bend angle) is shown in Figure 5.6. As I am restricting my initial focus to the ground state, this does not yet reflect spin-orbit coupling effects, though they will obviously be incorporated in a full non-adiabatic treatment of the lowest three surfaces[54].

Although this fit is already quite good, it is important to note that RMS deviation for F + HCl surface may tend to overestimate how well the surface is in fact

represented. Specifically, the surface has two conical intersection seams in the entrance ($F(^2P)$ + HCl) and exit (HF + $Cl(^2P)$) channels, indeed, even at energies comparable to the transition state. Although a proximity metric in multiple dimensions is not uniquely defined, the points on the conical intersection seam that are "closest" to the reaction path (as simply evaluated by sum of Euclidian displacements for each atom) are $R_{HF} = 3.578\ a_0$, $R_{HCl} = 2.459\ a_0$, E = 3.55 kcal/mol in the entrance channel and $R_{HF} = 2.166\ a_0$, $R_{HCl} = 2.770\ a_0$, E = -3.23 kcal/mol in the exit channel. These conical intersection seams introduce regions of derivative discontinuities in the adiabatic PES, which is precisely where the least squares multibody expansion deviates most from the *ab initio* values. Indeed, in some respects, these are the most dynamically interesting regions of the multiple surfaces and are clearly responsible for the role of non-adiabaticity in the reaction dynamics. A more complete treatment of such non-adiabatic effects therefore requires simultaneous diabitization and fitting of all three lowest surfaces, which is outside the scope of this paper and will be presented elsewhere.[54]

V. Discussion

As has been noted in other PESs for reaction systems with open highly electronegative open shell atoms[40], the electronic wavefunction can be highly multireferential, i.e., significant amplitudes of excited reference state configurations become mixed with the ground state. The *absence* of such mixing (i.e., single reference behavior) can be quantified by χ, the amplitude of the ground reference configuration in the final MRCI+Q wavefunction. To further demonstrate the crucial importance of multireference methods in the F + HCl PES, Figure 5.7 plots the

magnitude of the ground state reference configuration (*i.e.*,χ^2) as a function of the reaction coordinate. The strong and highly structured decrease in χ^2 clearly indicates that excited reference configurations constitute a significant portion of the wave function in the broad vicinity around the transition state. Interestingly, there are two structured dips in the χ^2 plot where the excited state admixture is greatest; these correspond quite nicely to points along the reaction coordinate closest to the conical intersection seams (marked with a *). Clearly, significant mixing of excited configurations is taking place over the entire barrier region of the surface, further underscoring that single reference *ab initio* methods cannot be expected to adequately describe the electronic wavefunction.

The importance of these conical intersection seams in F + HCl dynamics will depend on how intimately the full 3D wavefunction samples these regions on the way toward reaction. The extent of this sampling is not immediately obvious, since the conical intersections occur only for a collinear configuration ($\theta = 0^o$, 180^o), and yet the transition state is quite strongly bent ($\theta = 123.5^o$). To provide more insight into this question, 2D contour plots as a function of R_{HF} and R_{HCl} are shown in Fig, 5.8, for both collinear and transition state bending angles. The dashed lines in Fig 5.8b represent the coordinates of the conical intersection seams, with the asterisks indicating the positions closest to the (bent) reaction path. These points clearly occur high up on the reaction barrier and for R_{HF} and R_{HCl} bond lengths quite comparable to those of the transition state.

Based on the above discussion, one relevant question is therefore the "stiffness" of the bending potential, evaluated near the transition state bond lengths.

Figure 5.9 displays 1D cuts through the full potential as a function of the bend angle θ. The dashed line cut is for R_{HF} and R_{HCl} coordinates fixed at the optimized transition state values. The strongly bent nature of the transition state is clearly evident with a modest ~3 kcal/mol higher barrier at the linear configuration. However, this substantially underestimates the energetic proximity to the conical intersection seam; specifically, if one also adjusts R_{HCl} and R_{HF} to the conical intersection values represented by the two asterisks, the energies drop to 3.55 kcal/mol and -3.23 (referenced to the F + HCl asymptotic entrance channel). Thus even the *higher* of these two points on the seam is *lower* than the transition state by ~0.25 kcal/mol. Simply stated, *all* reagents with sufficient energy to surmount the classical reaction barrier have energetic access to non-adiabatic seam regions for both reagent and product channel sides of the transition state.

A more relevant angular slice through the potential is therefore at the RHCl and RHF geometries associated with the two conical intersection seam values closest to the transition state. Such a slice is also displayed in Fig 5.9 for the (higher energy) reagent channel seam region, which now indicates a much softer bending potential and even lower barrier (~ 1 kcal/mol) to the linear configuration than at the transition state bond lengths. Note that the *barrier* at linearity on this second curve now explicitly corresponds to a point *directly on* the conical intersection seam. Furthermore, this curve intersects with the reaction path (point marked "P") at an energy only 0.9 kcal/mol below this linear conical intersection, underscoring the energetic proximity of reactants to these regions of high non-adiabaticity. A more quantitative metric for how accessible the conical intersection region is to reagents

along the reaction path can be obtained by solving for the ground state 1D angular wave function at fixed R_{HCl} and R_{HF}. Since the F-H-Cl moment of inertia becomes singular at the linear configuration, this requires taking advantage of the rigid bender methods developed by Hougen, Bunker and Johns. Using these methods, the lowest several eigenenergies have been calculated and are displayed for both the transition state and conical intersection curves in Figure 5.9. Note that linear conical intersection region becomes classically accessible even for a few quanta of bend excitation. A more detailed investigation of these conical intersections with full spin-orbit effects and fitting of the resulting diabatic $2^2A'$ and $1^2A''$ surfaces is explored in the next chapter.[54]

The most striking aspect of the $F(^2P) + HCl \rightarrow HF + Cl(^2P)$ PES is the sharply bent MRCI+Q/CBS/Scaled transition state geometry of 123.5^o. This feature is qualitatively reiterated at any level calculation, from previous single reference surface calculations ($\theta \approx 137^o$) to single point UCCSD(T)/AVQZ (118^o) calculations. Fig 5.8 exhibits the typical "early" barrier expected for a strongly exothermic reaction. However, both the barrier height and "early" vs. "late" nature of the transition state changes quite dramatically with the F-HCl bend angle θ. As noted previously by Skodje and coworkers,[64] this strongly bent transition state can have a significant influence on the reaction dynamics, specifically in *reducing* the reaction cross section for $J_{HCl} \gg 0$ reagents.

A simple picture for such behavior can be obtained as follows. 2D transition state geometries and barrier heights have been obtained from the full 3D surface at a fixed angle, varying only the two bond length coordinates R_{HCl} and R_{HF}. These

effective transition state barrier heights and HCl bond lengths are plotted as a function of θ in Figure 5.10a. For more collinear geometries (θ ≈ 180), the 2D barrier height and transition state HCl bond length prove to be relatively insensitive to θ. Furthermore, rHCl remains quite close to the free equilibrium value, as characteristic of "early barrier" behavior even out to near the transition state bend angle (θ ≈ 123.5). For more strongly bent geometries (θ < 120), however, the 2D transition state HCl bond length grows dramatically with decreasing θ, implying a rapid shift from "early" to "late" barrier dynamics, accompanied by a similarly precipitous increase in the 2D barrier height. By way of example, the shaded portion in Fig 5.10a displays the relatively small range of F-H-Cl angles that correspond to 2D barriers below a typical 5 kcal/mol experimental collision energy. Alternatively stated, the strongly bent transition state nature of the F + HCl PES translates into a strongly *reduced* angular acceptance window for reaction, resulting in anomalously small cross sections even for an "early" barrier process at energies well above the transition state threshold.

Indeed, the strongly bent nature of the F-H-Cl transition state generates additional dynamical restrictions on the reaction probabilities. As a simple physical picture for this, consider a collision of F with HCl oriented initially in a bent configuration. Particularly for such a "heavy + light-heavy" mass combination, this presents a large moment arm for prerotating the HCl reagent in the entrance channel, thereby decreasing θ below the optimum transition state angle. From Fig 5.10a, this "entrance channel rotation" translates into higher effective barrier heights, thereby shutting off the probability of a successful reaction. To quantify how large these "entrance channel rotation" effects might be during a F + HCl collision, preliminary

classical trajectory simulations have been performed on the current PES. Initial conditions are chosen such that the F atom initial velocity is directly toward the H atom at 5.0 kcal/mol center of mass collision energy (i.e., 1.2 kcal/mol above threshold) for an initial F-HCl bend angle between 60^o and 180^o. The resulting F-H-Cl bending angle is then recorded at the location of closest approach of the F atom to the HCl center of mass. Results of this sample trajectory analysis are shown in Figure 10b, where the change in angle $\Delta\theta$ at the closest approach distance has been plotted against the initial F-H-Cl angle. Noteworthy is that for all incident angles, $\Delta\theta$ is quite large and negative (*i.e.,* the F-H-Cl angle becomes more bent). In conjunction with Figure 5.10a, this implies a large increase in the effective barrier height, which begins to explain the exceptionally low probability of reactive trajectories observed even above threshold.

Indeed, based on this elementary classical analysis, a successful reaction would require collision at very nearly collinear geometries to "prerotate" the HCl into the appropriate transition state bend angle. This range of angles is indicated by the steeply rising edge feature in Fig 5.10b, which translates into a considerable narrowing of reactive acceptance window at 5.0 kcal/mol, specifically from $\theta \approx 33^o$ to $\theta \approx 2^o$. Furthermore, when one takes the correct $\sin(\theta)$ area element into account, this model predicts a reactive event with only 0.21% of the hard sphere cross section. The dashed line in Figure 5.10b shows similar predicted deflection plots for trajectories with the H atom replaced with D. As expected, the deflection is somewhat decreased due to the more massive D atom but still quite large and sampling a region of the configuration space where the barrier is too large to react. Note that such a dynamical

picture due to pre-rotation into the transition state is most appropriate for *non-rotating* HCl reagent molecules. This is a likely explanation for observations obtained from classical and full 3-D quantum dynamics on this surface[64] , which show very small cross sections for reactions starting in $J_{HCl} = 0$ but which *increase* dramatically with $J_{HCl}>0$. Whether such a simple picture for the role of transition state bending angle effects will be dynamically relevant in other reaction systems represents an interesting question for further exploration.

VI. Summary and Conclusion

This chapter presents results from high-level *ab initio* calculations on the $1^2A'$ electronic state for the $F(^2P) + HCl \rightarrow HF + Cl(^2P)$ reaction, along with an analytical fit to this surface in full 3D. The *ab initio* data for the analytical fit are calculated at a grid of 3D points using *dynamically weighted* MCSCF methods with 6 states, followed by high-level multireference (MRCI+Q) methods for a series of correlation-consistent basis sets (AVnZ, n = 2,3,4). These results are then extrapolated to the complete basis set limit (CBS), with a single global correlation scaling parameter to match theoretical and experimental exothermicities. Sequential fits of this surface to atom, pairwise, and full three body terms have been obtained and reported for the ground adiabatic state. This represents a necessary first step toward obtaining all multistate diabatic electronic surfaces for use in quantum scattering calculations and rigorous comparison with state-resolved experimental data.

The successful extraction of this full 3D surface demonstrates the robust applicability of DW-MCSCF method to obtain multiple smooth potentials in systems with strongly avoided crossings and charge transfer character at the transition state.

Furthermore, the nominally "ground" electronic state wave function proves to be highly multireference in character, particularly in the chemically important region near the transition state. This underscores the importance of multireference methods in open shell reaction dynamics, particularly for highly electronegative atoms with strong charge transfer contributions and permits extraction of a much improved surface for comparison with previous single reference state methods. A simple one-parameter correlation scaling procedure is introduced that recovers relatively minor correlation energy effects due to frozen core orbitals, benchmarked to match the experimentally measured exothermicity.

This surface exhibits several intriguing dynamical features for further exploration. First of all, elementary chemical arguments are presented for open shell halogen/H atom abstraction reactions that predict the appearance of conical intersections close to the transition state region. The presence of two such seams of conical intersections is confirmed in the *ab initio* calculations, occurring at R_{HCl} and R_{HF} bond lengths close to and energies slightly below the transition state values. Most importantly, this may suggest a major role for multiple electronic surfaces and non-adiabatic effects for F + HCl even under thermal reaction conditions. In fact, the temperature dependent studies by Houston and coworkers indicate a curiously non-Arrhenius kinetic behavior. One plausible speculation is that this could arise from non-adiabatic hopping effects due to temperature dependent access to the entrance and exit conical intersection seams on the surface. This would be extremely interesting to explore, both by full multisurface dynamics calculations as well as rovibrational and spin orbit state-resolved scattering experiments.

Second, the transition state is quite strongly bent, with a F-H-Cl bend angle of $\theta \approx 123.5^{o}$. This is in contrast with the more nearly linear transition states observed for F + H_2 surfaces and may have a significant impact on the reaction dynamics in multiple ways. For example, 2D slices (R_{HF}, R_{HCl}) of the potential surface for a fixed bend angle indicate a dramatic *increase* in the effective transition state barrier and R_{HCl} bond length with *decreasing* θ below 120. This is consistent with rapid shift from early to late barrier dynamics as the F-H-Cl angle becomes more bent, which, particularly for a heavy + light-heavy mass combination, is likely to occur naturally in the entrance channel. This is further verified by trajectory calculations, which reveal a strong "entrance channel rotation" of the HCl reagent, greatly narrowing the angular window of acceptance for scaling the transition state and achieving successful reaction. Such strongly bent transition states clearly offer a novel platform and testing ground for predictions of reaction dynamics as a function of rotational and vibrational quantum state, one of many directions which may prove interesting to pursue with the availability of the present surface.

Tables

Table 5.1: ΔE_{rxn} in kcal/mol of $F(^2P) + HCl \rightarrow HF + Cl(^2P)$ calculated by various *ab initio* methods. Calculated energies are corrected for zero-point and spin-orbit which are not included in the single surface *ab initio* calculations. The experimental ΔE is -33.060 +/- 0.001 kcal/mol.

Method	Basis				Error (CBS)
	AVDZ	AVTZ	AVQZ	CBS	
HF	-19.3	-18.83	-18.67	-18.57	-14.49
MCSCF	-23.1	-22.87	-22.75	-22.68	-10.38
MRCI	-30.41	-29.98	-29.91	-29.87	-3.19
MRCI+Q	-31.33	-31.04	-30.94	-30.88	-2.18

Table 5.2: Diatomic constants from *ab initio* PES calculated at MRCI+Q/AVnZ compared with the correlation scaled values and experiment.

	Basis	D_e (kcal/mol)	D_o kcal/mol)	ZPE (kcal/mol)	r_e(A)	ω_e (cm^{-1})	$\omega_e x_e$ (cm^{-1})	B_e (cm^{-1})	α_e (cm^{-1})
HF	AVDZ	133.84	128.10	5.74	0.9260	4038.1	76.8	20.6086	0.707
	AVTZ	138.08	132.24	5.84	0.9217	4118.6	77.1	20.8440	0.695
	AVQZ	139.61	133.74	5.87	0.9185	4134.6	77.1	20.9766	0.700
	CBS	140.50	134.61	5.89	0.9165	4143.2	77.1	21.0599	0.705
	Scaled	141.58	135.69	5.89	0.9164	4143.0	76.4	21.0586	0.701
	expt.	141.63	135.65	5.98	0.9168	4138.3	89.9	20.9557	0.798
HCl	AVDZ	100.29	96.08	4.21	1.2938	2966.9	49.0	10.3740	0.299
	AVTZ	104.18	99.95	4.23	1.2790	2975.5	47.5	10.6048	0.301
	AVQZ	105.75	101.52	4.23	1.2775	2976.2	46.1	10.6291	0.297
	CBS	106.67	102.44	4.23	1.2769	2978.2	45.6	10.6388	0.295
	scaled	107.35	103.11	4.24	1.2766	2980.2	45.4	10.6433	0.294
	expt.	107.36	103.05	4.31	1.2746	2990.9	52.8	10.5934	0.307
ClF	AVDZ	51.44	50.34	1.09	1.6847	770.2	6.5	0.4828	0.004
	AVTZ	56.86	55.74	1.12	1.6455	787.7	6.0	0.5060	0.005
	AVQZ	59.16	58.02	1.14	1.6362	803.2	5.9	0.5118	0.004
	CBS	60.54	59.39	1.15	1.6315	811.7	5.8	0.5148	0.004
	scaled	61.73	60.57	1.16	1.6304	816.3	5.8	0.5155	0.004
	expt.	61.50	60.30	1.13	1.6283	786.2	6.2	0.5165	0.004

Table 5.3: The geometries and energies of the transition state for a range of methods and basis sets. In particular, the transition state geometry is strongly bent at all levels of theory.

Method	Basis	Bend Angle (degree)	$\Delta E^{\ddagger}$ (kcal/mol)
UMP2[37]	6-311G(3d2f,3p2d)	137.4	6.2
PUMP2[37]	6-311G(3d2f,3p2d)	137.4	4.7
PUMP4[37]	6-311G(3d2f,3p2d)	137.4	4.0
UCCSD(T)[64]	AVQZ	118.0	2.2
MRCI+Q	AVDZ	126.2	4.2
	AVTZ	126.4	4.2
	AVQZ	125.9	4.2
	CBS	125.7	4.2
	Scaled	123.5	3.8

Figures

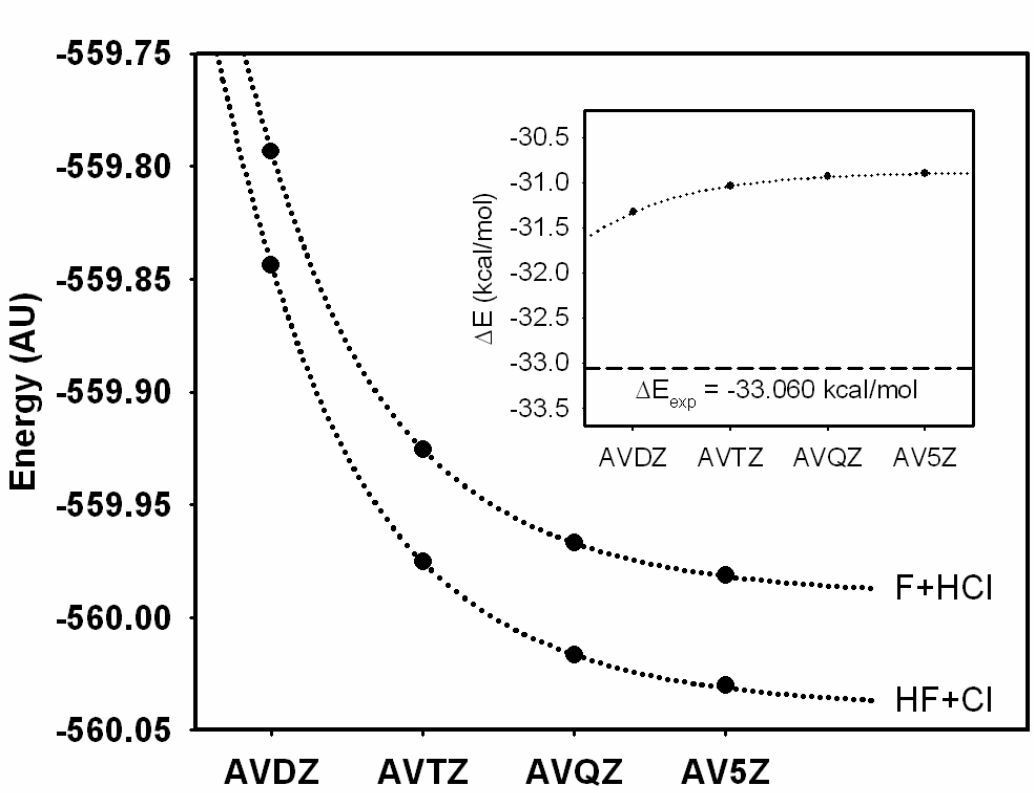

Figure 5.1: AVnZ (n = 2-5) extrapolation for F(^{2}P) + HCl and HF + Cl(^{2}P) energies to the CBS limit, indicating clear convergence (see inset) in the exothermicity (ΔE) as a function of n. The residual error in ΔE (dashed line) is due to active space size in the MRCI+Q calculations, as included in correlation scaling

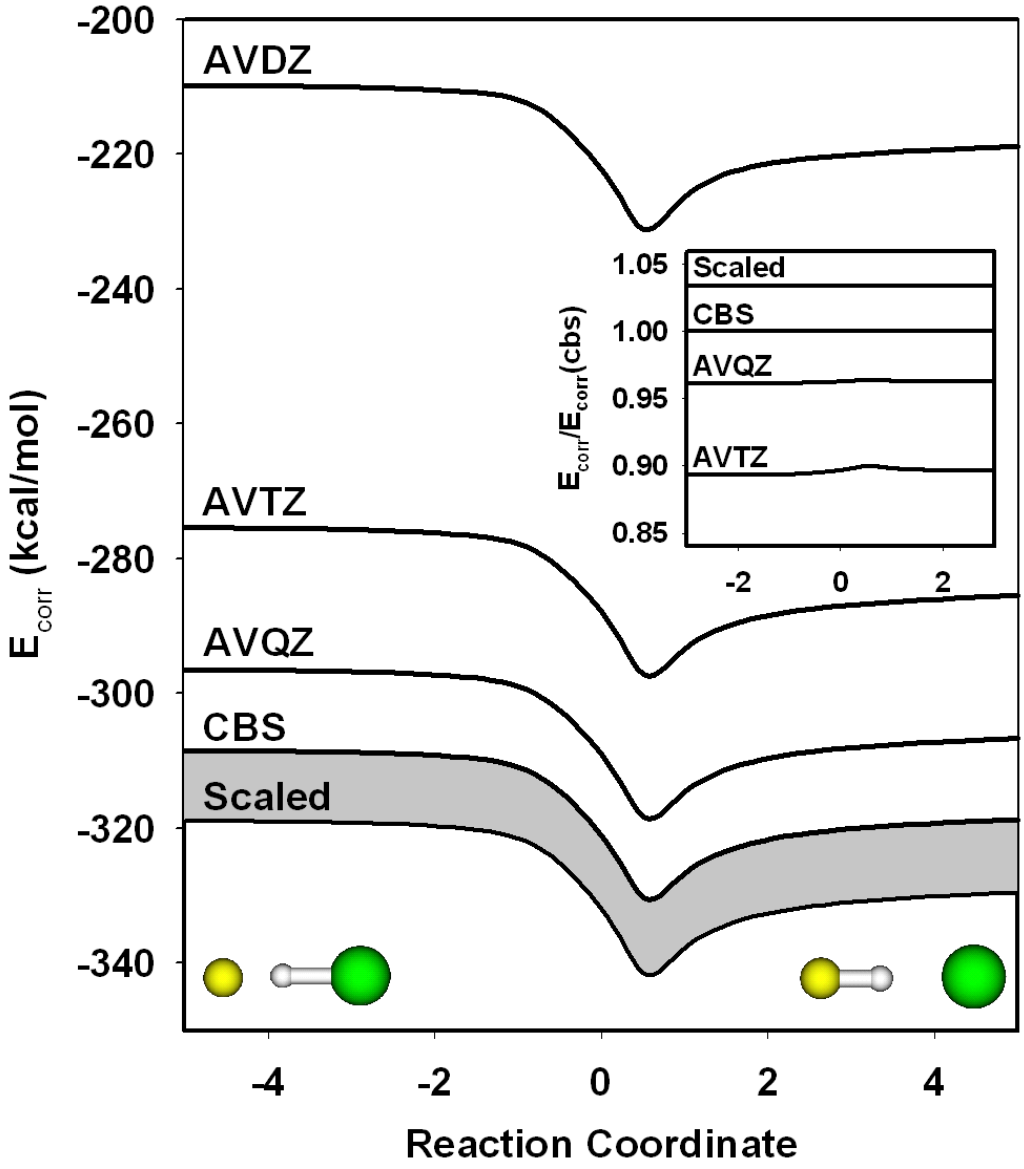

Figure 5.2: Correlation energy (E_{MRCI}-E_{MCSCF}) recovered for each basis set, AVnZ. - The nearly constant ratio of recovered correlation energy relative to the CBS extrapolation (see inset) illustrates how correlation scaling effectively mimics a larger active space.

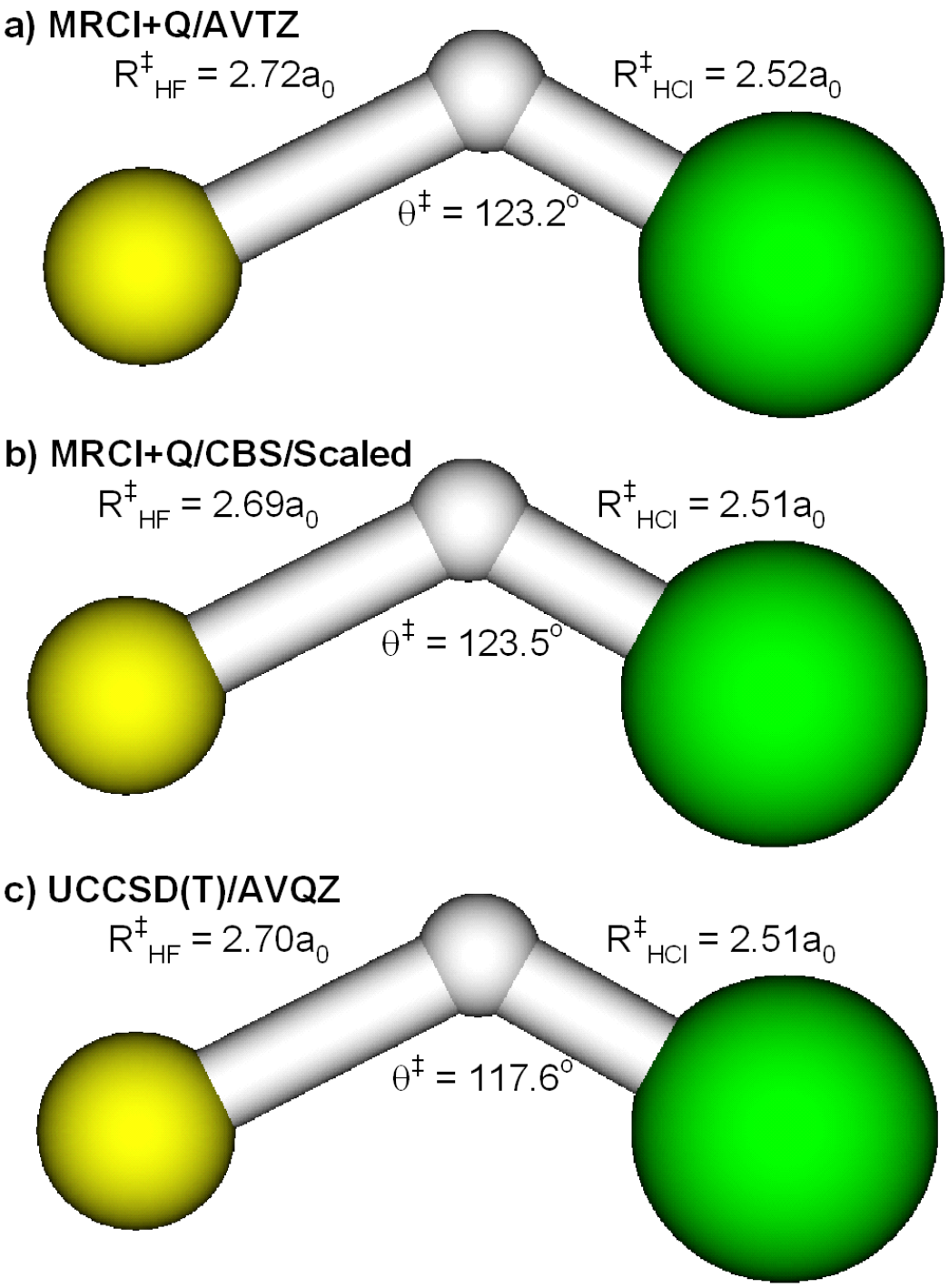

Figure 5.3: F-H-Cl transition state geometry at various levels of theory, all confirming a sharply bent transition state: (a) MRCI+Q/AVTZ; (b) MRCI+Q/CBS/Scaled; UCCSD(T)/AVQZ.

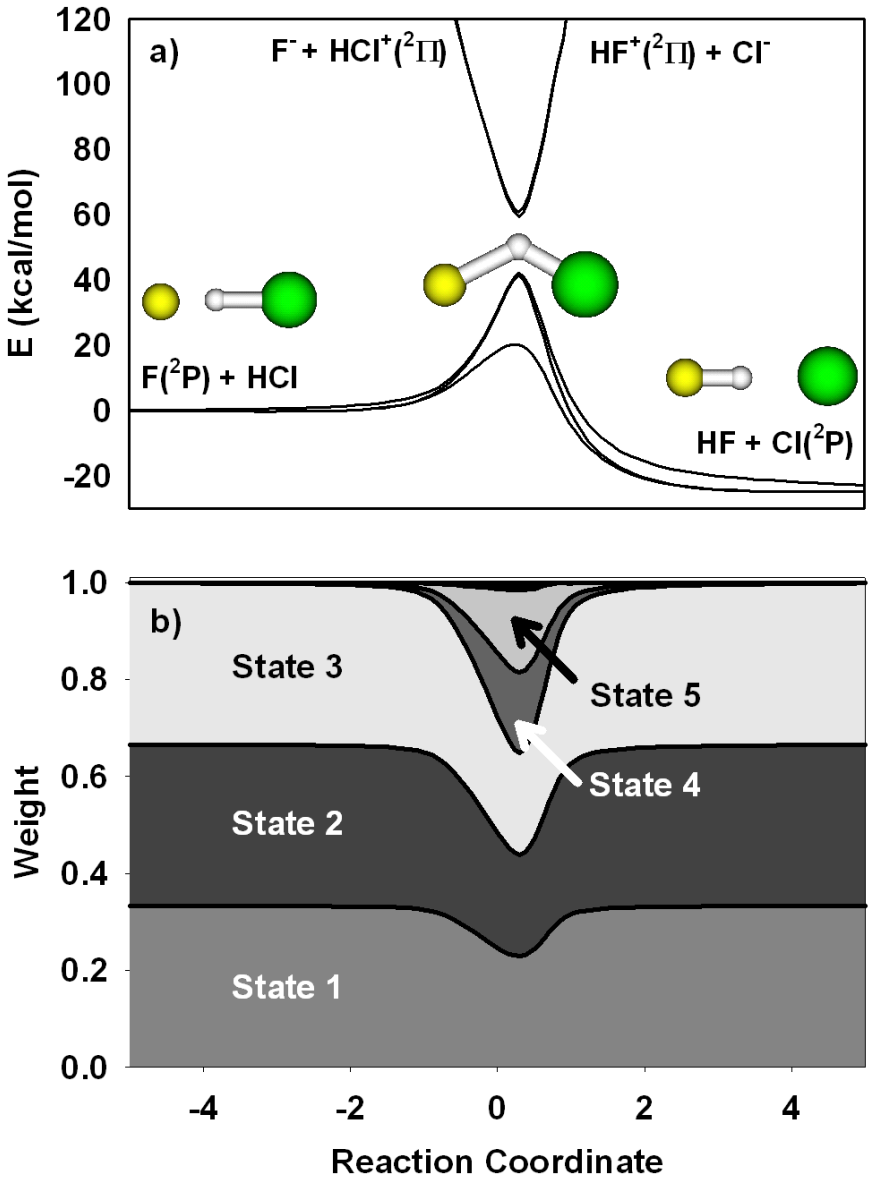

Figure 5.4: The DW-MCSCF energies (a) and weights (b) as a function of reaction coordinate, with up to 6 states dynamically weighted. Note the strongly avoided crossings of F^- + $HCl(^2\Pi)^+$ and $HF(^2\Pi)^+$ + Cl^- charge transfer (CT) states with surfaces correlating to the ground state (^2P) asymptotes. Note also the smooth weight adjustment from a 3-state calculation at either asymptote to > 5 states near the transition state geometry.

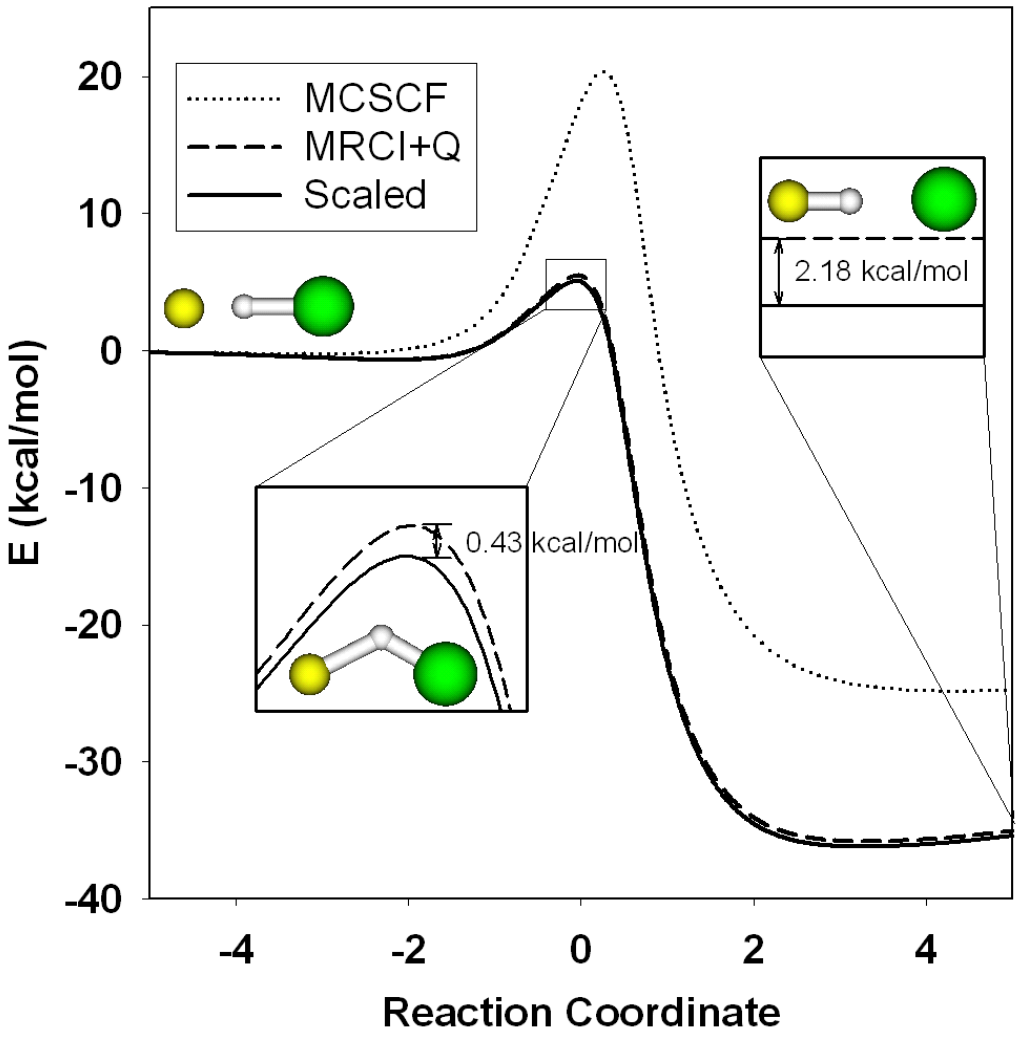

Figure 5.5: $1^2A'$ reaction path at the MCSCF, MRCI+Q, and correlation scaled levels, indicating relatively minor effects due to correlation scaling. Such scaling makes up for 2.18 kcal/mol in ΔE and lowers the barrier by 0.43 kcal mol.

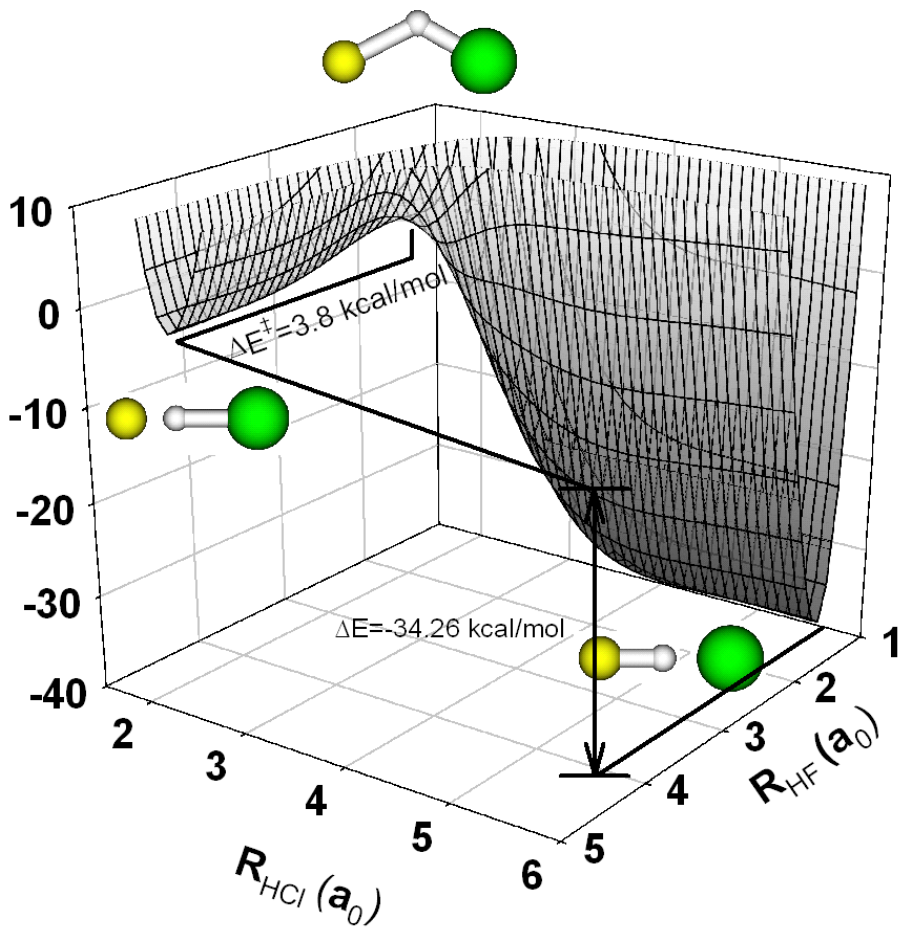

Figure 5.6: 2D slice (θ = 123.5°) of the fitted $1^2A'$ surface with global RMS of 0.79 kcal/mol.

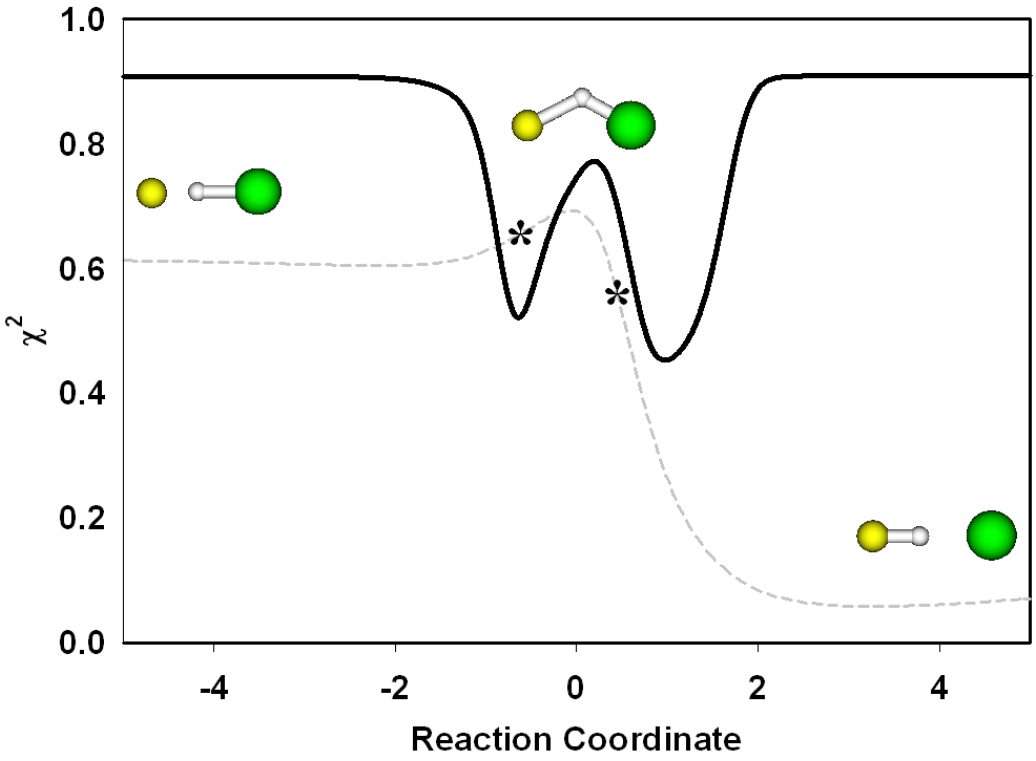

Figure 5.7: Ground reference state coefficient in the MRCI+Q wavefunction, indicating strong admixture of excited state character near the transition state geometries closest to the conical intersection (marked by asterisks).

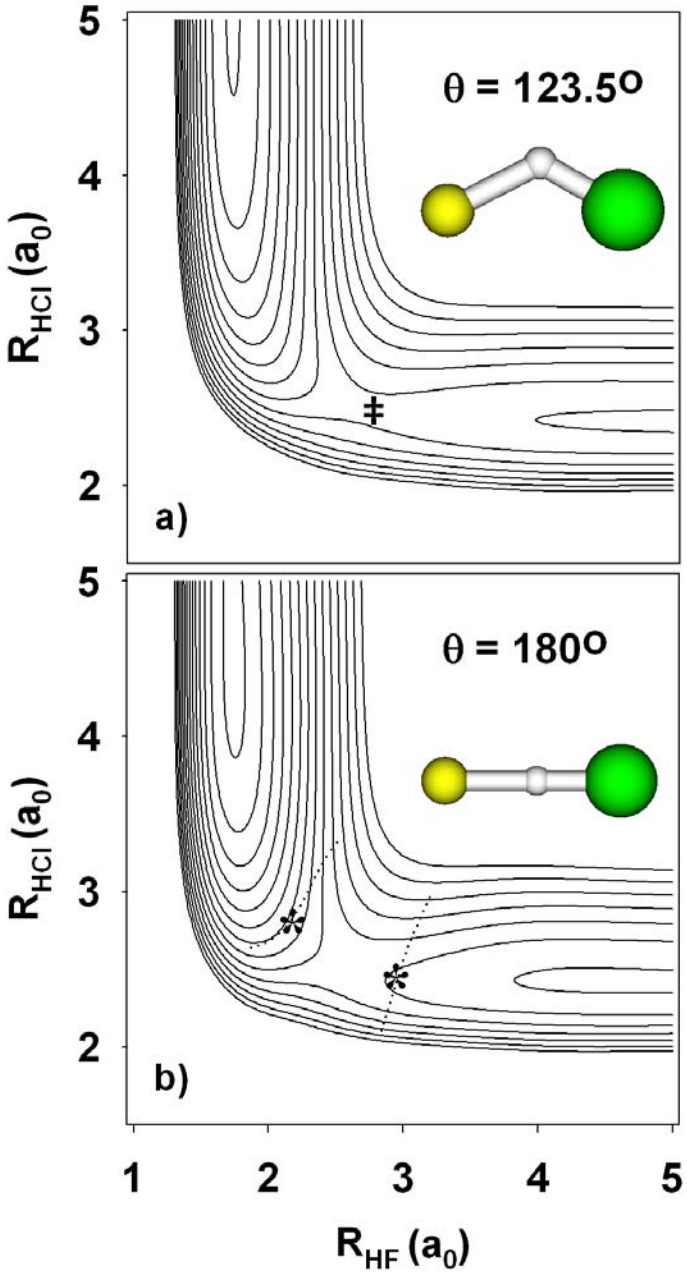

Figure 5.8: $1^2A'$ PES R_{HF} vs. R_{HCl} contours for (a) transition state ($\theta = 123.5^o$) and (b) collinear ($\theta = 180^o$) bend angles. Conical intersection seams occur to each side of the transition state; the seam location closest to the reaction path is marked by the asterisk. Contour spacing is 5 kcal/mol with respect to F + HCl(R_e).

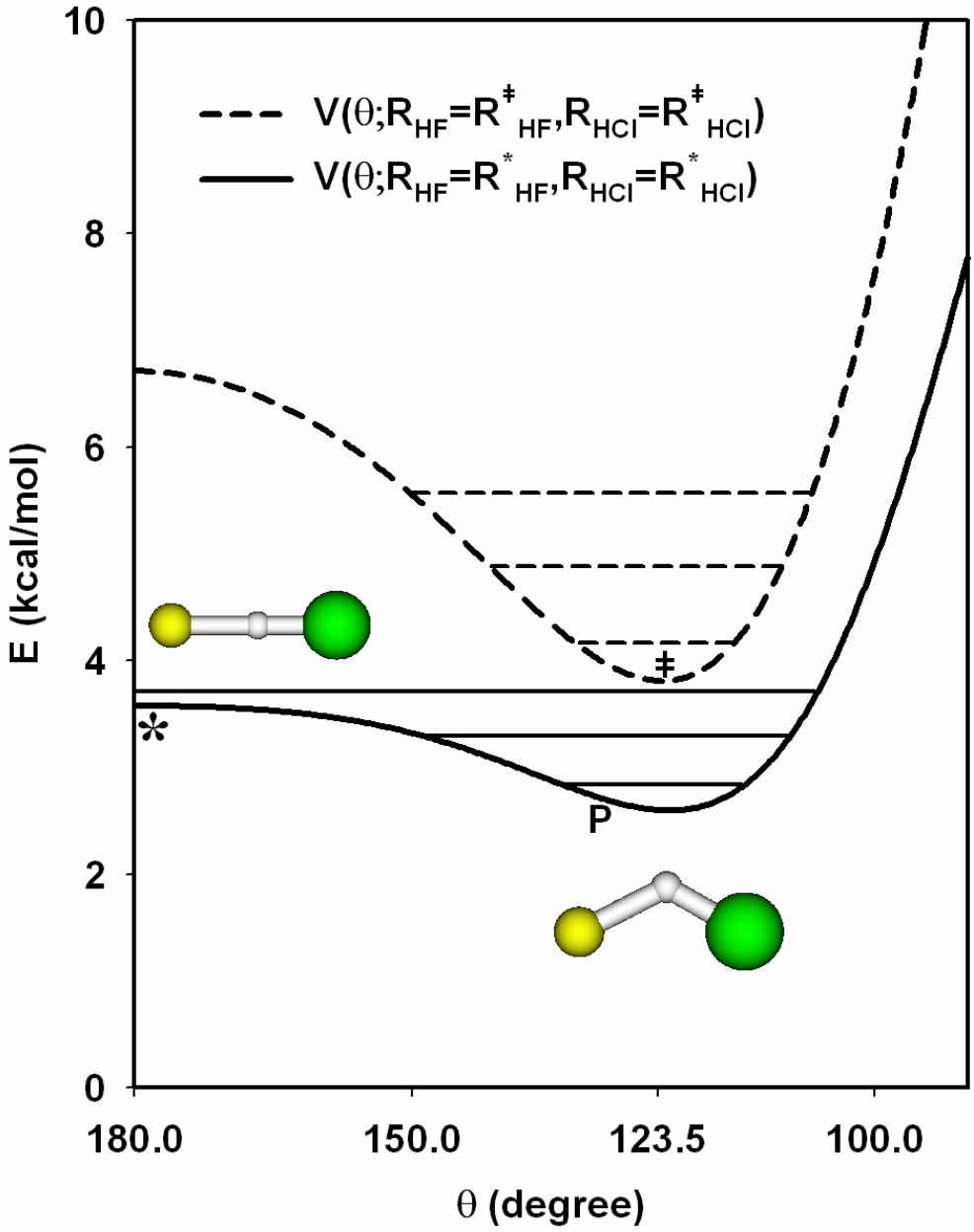

Figure 5.9: F-H-Cl bending potential corresponding to transition state (dashed) and conical intersection seam (solid) R_{HF} and R_{HCl} bond lengths, with eigenvalues obtained from a rigid bender analysis. Note that the conical intersection is lower than the transition state with only a ~1 kcal/mol barrier to linearity from the reaction path.

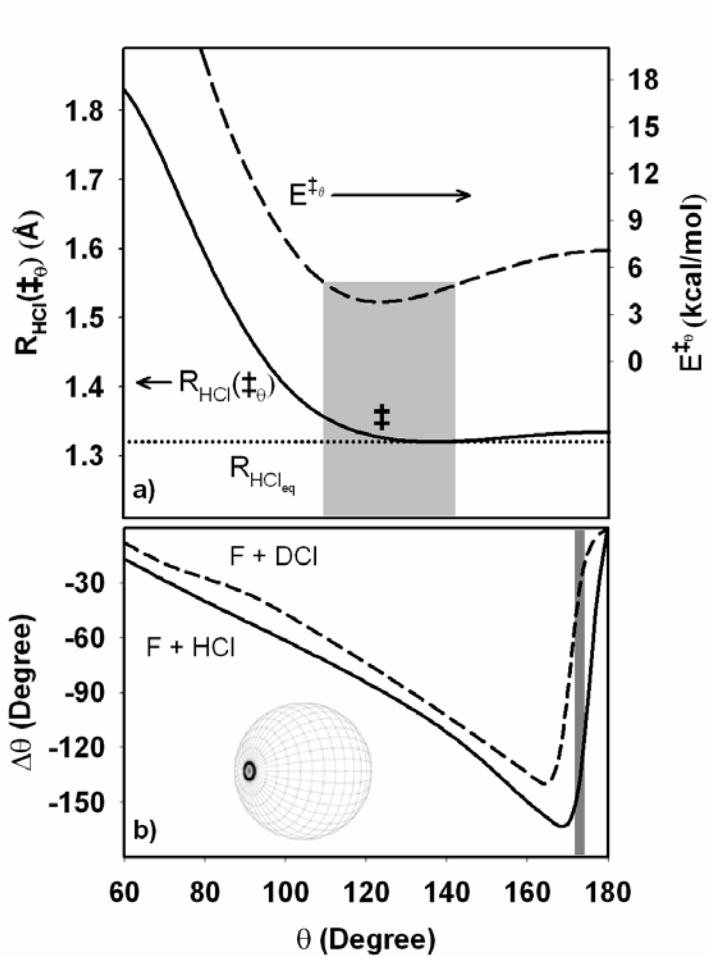

Figure5.10: a) 2D effective transition state barrier height (solid) and HCl bond length (dashed) as a function of F-H-Cl bending angle (dotted line is R_e for HCl). As θ decreases below ~120°, both the HCl bond length and barrier height increase dramatically from transition state values, characteristic of a shift from an "early" to "late" transition state. b) Trajectory analysis for F-HCl angular deflection (Δθ) as a function of initial bend angle, θ. For J = 0, only a very narrow range (dark grey) of incident scattering angles are successfully "prerotated" (light grey) into the appropriately bent transition state angle to react.

References

[1] K. Stark and H. J. Werner, J. Chem. Phys. **104**, 6515 (1996).

[2] M. Hayes, M. Gustafsson, A. M. Mebel, and R. T. Skodje, Chem. Phys. **308**, 259 (2005).

[3] Y. R. Tzeng and M. H. Alexander, J. Chem. Phys. **121**, 5812 (2004).

[4] Y. Zhang, T. X. Xie, K. L. Han, and J. Z. H. Zhang, J. Chem. Phys. **119**, 12921 (2003).

[5] S. D. Chao and R. T. Skodje, J. Chem. Phys. **113**, 3487 (2000).

[6] M. H. Alexander, H. J. Werner, and D. E. Manolopoulos, J. Chem. Phys. **109**, 5710 (1998).

[7] F. J. Aoiz, L. Banares, B. MartinezHaya, J. F. Castillo, D. E. Manolopoulos, K. Stark, and H. J. Werner, J. Phys. Chem. A **101**, 6403 (1997).

[8] J. F. Castillo, D. E. Manolopoulos, K. Stark, and H. J. Werner, J. Chem. Phys. **104**, 6531 (1996).

[9] S. A. Nizkorodov, W. W. Harper, W. B. Chapman, B. W. Blackmon, and D. J. Nesbitt, J. Chem. Phys. **111**, 8404 (1999).

[10] S. A. Nizkorodov, W. W. Harper, and D. J. Nesbitt, Faraday Disc. **113**, 107 (1999).

[11] W. B. Chapman, B. W. Blackmon, S. Nizkorodov, and D. J. Nesbitt, J. Chem. Phys. **109**, 9306 (1998).

[12] W. B. Chapman, B. W. Blackmon, and D. J. Nesbitt, J. Chem. Phys. **107**, 8193 (1997).

[13] M. Baer, M. Faubel, B. Martinez-Haya, L. Rusin, U. Tappe, and J. P. Toennies, J. Chem. Phys. **110**, 10231 (1999).

[14] M. Baer, M. Faubel, B. Martinez-Haya, L. Y. Rusin, U. Tappe, and J. P. Toennies, J. Chem. Phys. **108**, 9694 (1998).

[15] L. Y. Rusin and J. P. Toennies, Phys. Chem. Chem. Phys. **2**, 501 (2000).

[16] G. Dharmasena, K. Copeland, J. H. Young, R. A. Lasell, T. R. Phillips, G. A. Parker, and M. Keil, J. Phys. Chem. A **101**, 6429 (1997).

[17] G. Dharmasena, T. R. Phillips, K. N. Shokhirev, G. A. Parker, and M. Keil, J. Chem. Phys. **106**, 9950 (1997).

[18] M. Faubel, L. Rusin, S. Schlemmer, F. Sondermann, U. Tappe, and J. P. Toennies, J. Chem. Phys. **101**, 2106 (1994).

[19] D. M. Neumark, A. M. Wodtke, G. N. Robinson, C. C. Hayden, and Y. T. Lee, J. Chem. Phys. **82**, 3045 (1985).

[20] D. M. Neumark, A. M. Wodtke, G. N. Robinson, C. C. Hayden, K. Shobatake, R. K. Sparks, T. P. Schafer, and Y. T. Lee, J. Chem. Phys. **82**, 3067 (1985).

[21] H. Kornweitz and A. Persky, J. Phys. Chem. A **108**, 8599 (2004).

[22] Y. R. Tzeng and M. H. Alexander, J. Chem. Phys. **121**, 5183 (2004).

[23] Y. R. Tzeng and M. Alexander, Phys. Chem. Chem. Phys. **6**, 5018 (2004).

[24] Y. Zhang, T. X. Xie, K. L. Han, and J. Z. H. Zhang, J. Chem. Phys. **120**, 6000 (2004).

[25] T. X. Xie, Y. Zhang, M. Y. Zhao, and K. L. Han, Phys. Chem. Chem. Phys. **5**, 2034 (2003).

[26] S. C. Althorpe, J. Phys. Chem. A **107**, 7152 (2003).

[27] S. C. Althorpe, Chem. Phys. Lett. **370**, 443 (2003).

[28] S. H. Lee, F. Dong, and K. P. Liu, J. Chem. Phys. **116**, 7839 (2002).

[29] K. P. Liu, Nuc. Phys. A **684**, 247C (2001).

[30] R. T. Skodje, D. Skouteris, D. E. Manolopoulos, S. H. Lee, F. Dong, and K. P. Liu, Phys. Rev. Lett. **85**, 1206 (2000).

[31] R. T. Skodje, D. Skouteris, D. E. Manolopoulos, S. H. Lee, F. Dong, and K. Liu, J. Chem. Phys. **112**, 4536 (2000).

[32] W. W. Harper, S. A. Nizkorodov, and D. J. Nesbitt, J. Chem. Phys. **116**, 5622 (2002).

[33] O. D. Krogh and G. C. Pimentel, J. Chem. Phys. **67**, 2993 (1977).

[34] A. M. G. Ding, L. J. Kirsch, D. S. Perry, J. C. Polanyi, and J. L. Schreiber, Faraday Disc. Chem. Soc. **55**, 252 (1973).

[35] R. Sayos, J. Hernando, R. Francia, and M. Gonzalez, Phys. Chem. Chem. Phys. **2**, 523 (2000).

[36] B. Y. Tang, B. H. Yang, K. L. Han, R. Q. Zhang, and J. Z. H. Zhang, J. Chem. Phys. **113**, 10105 (2000).

[37] R. Sayos, J. Hernando, J. Hijazo, and M. Gonzalez, Phys. Chem. Chem. Phys. **1**, 947 (1999).

[38] H. Kornweitz and A. Persky, J. Phys. Chem. A **108**, 140 (2004).

[39] D. J. Nesbitt, M. P. Deskevich, M. Wocjik, M. Ziemkiewicz, A. Zolot, and E. Whitney, Abstracts Of Papers Of The American Chemical Society **227**, U334 (2004).

[40] M. P. Deskevich, D. J. Nesbitt, and H. J. Werner, J. Chem. Phys. **120**, 7281 (2004).

[41] H. J. Werner and P. J. Knowles, J. Chem. Phys. **89**, 5803 (1988).

[42] P. J. Knowles and H. J. Werner, Chem. Phys. Lett. **145**, 514 (1988).

[43] P. J. Knowles and H. J. Werner, Theoretica Chimica Acta **84**, 95 (1992).

[44] K. A. Peterson, D. E. Woon, and T. H. Dunning, J. Chem. Phys. **100**, 7410 (1994).

[45] F. B. Brown and D. G. Truhlar, Chem. Phys. Lett. **117**, 307 (1985).

[46] B. Ramachandran and K. A. Peterson, J. Chem. Phys. **119**, 9590 (2003).

[47] M. Meuwly and J. M. Hutson, J. Chem. Phys. **119**, 8873 (2003).

[48] M. L. Dubernet and J. M. Hutson, J. Chem. Phys. **101**, 1939 (1994).

[49] M. L. Dubernet and J. M. Hutson, J. Phys. Chem. **98**, 5844 (1994).

[50] H.-J. Werner, P. J. Knowles, R. Lindh, M. Schutz, P. Celani, T. Korona, F. R. Manby, G. Rauhut, R. D. Amos, A. Bernhardsson, A. Berning, D. L. Cooper, M. J. O. Deegan, A. J. Dobbyn, F. Eckert, C. Hampel, G. Hetzer, A. W. Lloyd, S. J. McNicholas, W. Meyer, M. E. Mura, A. Nicklass, P. Palmieri, R. Pitzer, U. Schumann, H. Stoll, A. J. Stone, R. Tarroni, and T. Thorsteinsson, Molpro, version 2002.6, a package of *ab initio* programs (see http://www.Molpro.Net) (Birmingham, UK, 2003).

[51] S. R. Langhoff and E. R. Davidson, Int. J. Quantum Chem. **8**, 61 (1974).

[52] M. R. A. Blomberg and P. E. M. Siegbahn, J. Chem. Phys. **78**, 5682 (1983).

[53] J. Simons, J. Phys. Chem. **93**, 626 (1989).

[54] M. P. Deskevich and D. J. Nesbitt (work in progress).

[55] D. E. Woon and T. H. Dunning, J. Chem. Phys. **98**, 1358 (1993).

[56] T. H. Dunning, J. Chem. Phys. **90**, 1007 (1989).

[57] R. A. Kendall, T. H. Dunning, and R. J. Harrison, J. Chem. Phys. **96**, 6796 (1992).

[58] T. H. Dunning, K. A. Peterson, and A. K. Wilson, J. Chem. Phys. **114**, 9244 (2001).

[59] L. M. Cheung, K. R. Sundberg, and K. Ruedenberg, Int. J. Quantum Chem. **16**, 1103 (1979).

[60] H. J. Werner and P. J. Knowles, J. Chem. Phys. **82**, 5053 (1985).

[61] P. J. Knowles and H. J. Werner, Chem. Phys. Lett. **115**, 259 (1985).

[62] J. D. D. Martin and J. W. Hepburn, J. Chem. Phys. **109**, 8139 (1998).

[63] W. T. Zemke, W. C. Stwalley, J. A. Coxon, and P. G. Hajigeorgiou, Chem. Phys. Lett. **177**, 412 (1991).

[64] M. Y. Hayes, M. P. Deskevich, D. J. Nesbitt, K. Takahashi, and R. T. Skodje, J. Chem. Phys.(in press) (2005).

[65] E. Wurzberg and P. L. Houston, J. Chem. Phys. **72**, 5915 (1980).

[66] A. Zolot and D. J. Nesbitt (work in progress).

[67] F. Eckert and H. J. Werner, Theor. Chem. Acc. **100**, 21 (1998).

[68] K. Fukui, Acc. Chem. Res. **14**, 363 (1981).

[69] V. Aquilanti, D. Cappelletti, F. Pirani, L. Y. Rusin, M. B. Sevryuk, and J. P. Toennies, J. Phys. Chem. **95**, 8248 (1991).

[70] J. M. Hutson, J. Chem. Phys. **89**, 4550 (1988).

[71] A. Aguado, C. Tablero, and M. Paniagua, Comput. Phys. Comm. **108**, 259 (1998).

Chapter 6: Multireference configuration interaction calculations for $F(^2P) + HCl \rightarrow HF + Cl(^2P)$ reaction: Correlation-scaled diabatic potential energy surfaces.

I. Introduction

Understanding reaction dynamics at the quantum state resolved level has been a major challenge to the theoretical and experimental chemical physics community for many years. As a result of such interest, there has been much development towards both accurate *ab initio* potentials and numerically exact quantum dynamical calculations on these surfaces. One particularly well-studied system is the $F(^2P) + H_2 \rightarrow HF + H(^2S)$ reaction, for which there now exists an exceptionally accurate potential surface[1,2] from the Werner group, as well as numerous theoretical[3-8] calculations and experimental[9-20] papers on state-to-state reactive scattering. Also of interest has been the similar but notably different "heavy + light-heavy" isotopic variation on this reaction system, $F(^2P) + HD \rightarrow HF + D(^2S)$, for which long sought-after quantum transition state resonances have been both predicted [21-31] and experimentally[32] observed. In particular, stabilization calculations at the resonance energy in the transition state region yield a resonance wave function that can be described classically as an excited H atom motion in a quasi bound HF(v = 3)--D state. As a simple physical picture, the light H atom executes rapid oscillations between the relatively heavy F and D atoms, eventually predissociating into states corresponding to HF(v = 2,J) + D. Ongoing theoretical and experimental work on this

H atom transfer triatomic system has revealed the considerable dynamical sophistication still to be found even in "simple" heavy + light-heavy reactions, which continue to offer fundamental challenges for first principles theoretical calculations.

The clear observation of transition state resonance dynamics in F + HD suggests that there may be similar resonances in other heavy + light-heavy reaction systems such as $F(^2P)$ + HX. One such reaction of particular interest is the $F(^2P)$ + HCl → HF + $Cl(^2P)$ system, the high-level benchmark calculations of 3-state adiabatic and diabatic potential energy surfaces which represent the primary focus of this chapter. The reason for this choice is several-fold. First of all, $F(^2P)$ + HCl → HF + $Cl(^2P)$ has a very nearly identical exothermicity to the $F(^2P)$ + HD → HF + $D(^2S)$ reaction ($\Delta E_{HF + Cl}$ = -33.1 kcal/mol vs $\Delta E_{HF + H}$ = -31.2 kcal.mol), as well as an experimentally accessible barrier height of E_{barr} = 3-5 kcal/mol. Secondly, the total electron count (N_{elec} = 27) and number of nuclear degrees of freedom are challenging but still manageable with modern high-level multireference configuration interaction (MRCI) *ab initio* efforts for mapping ground and excited potential surfaces out in full dimensionality. Thirdly, simple electrostatic arguments predict the presence of non-adiabatic surface crossings and 1D seams of conical intersections that should be energetically accessible at typical reactive collision energies. Finally, the open shell halogen in the $F(^2P)$ + HCl → HF + $Cl(^2P)$ reaction has multiple spin-orbit configurations of products and reactants in the entrance and exit channels, which provides a potential experimental handle to distinguish surface hopping events as well as novel opportunities to study non-adiabatic dynamics on multiple electronic surfaces.

Previous theoretical studies on this surface have included quasiclassical trajectory (QCT) calculations performed on an empirical LEPS surface[33], QCT[34]and full dimensional time-dependant wavepacket [35] calculations obtained on a newer *ab initio* (PUMP2/6-311G(3d2f,3p2d)) surface[36], a LEPS surface created from recent experimental kinetics information[37], and a correlation-scaled MRCI surface from our group[38]. All previous calculations[33-35] have focused specifically on the ground ($1^2A'$) electronic state, though study of other F atom abstraction systems has revealed evidence for avoided crossings, charge transfer states, seams of conical intersection, etc. For example, it has been shown that there is significant non-adiabatic behavior for $F(^2P) + H_2$->$HF + H(^2S)$ in the entrance channel[3,23], and there is also direct experimental evidence in 4 atom systems (i.e. $F (^2P) + H_2O \rightarrow HF + OH(^2\Pi)$ that exhibit strong non-adiabatic coupling behavior in both the entrance and exit channels[39]. It is likely that similar effects are present in $F(^2P) + HCl \rightarrow HF + Cl(^2P)$, the dynamics of which clearly necessitate a high-level multireference electronic treatment. In this work, I present a new 3-state ($1^2\Sigma$, $1^2\Pi_x$, $1^2\Pi_y$) diabatic PES for the $F(^2P) + HCl$ reaction, based on high-level multireference calculations including spin-orbit contributions.

The $F(^2P) + HCl \rightarrow HF + Cl(^2P)$ reaction presents many of the same challenges seen earlier in the $F(^2P) + H_2O \rightarrow HF + OH(^2\Pi)$ reaction[40], namely, the presence of highly electronegative atoms that significantly lower the charge transfer (CT) state (i.e. $F^- + HCl^+ (^2\Pi)$ and $HF^+ (^2\Pi) + Cl^-$) energies in the barrier region. In addition, there is significant non-adiabatic coupling and avoided crossing behavior between the $1^2A'$ and $2^2A'$ surfaces, which requires explicit multireference

calculations to describe accurately. In light of these considerations, *ab initio* calculations for this PES are obtained via internally contracted multireference configuration interaction (MRCI)[41-43] methods using reference states taken from a dynamically weighed multiconfigurational self-consistent field (DW-MCSCF)[40] calculation. In addition, extrapolation to the complete basis set (CBS) limit[44] and correlation energy scaling[45,46] are used to further refine the PES shape as well as accurately reproduce the experimentally determined energetics.

As a further source of dynamical richness, the $F(^2P) + HCl \rightarrow HF + Cl(^2P)$ surfaces exhibit conical intersection seams in both entrance and exit channels. This can be explained by elementary chemistry considerations, as described by Hutson and coworkers[47-49] for open shell radical X-HX complexes. This is most readily understood by first considering the collinear limit, with z as the molecular axis and electronic states classified in the $C_{\infty v}$ symmetry group, followed by bending of the triatomic away from linearity in the xz plane and consequent reduction to the C_s symmetry group. Far outside the region of significant chemical reaction, the surfaces will be asymptotically dominated by electrostatic dipole-quadrupole and dipole-induced dipole interactions. For a collinear configuration of atoms, this results in an energy ordering where the Σ state (with the unfilled p orbital *parallel* to the z-axis) lies above the doubly degenerate Π_x, Π_y states (unfilled p-hole *perpendicular* to the z-axis). However, for the reaction to occur over the lowest barrier, the unfilled p-orbital must be approximately parallel to the reaction coordinate to participate in the H atom transfer. Thus, in the vicinity of the transition state, the lowest energy barrier (again in $C_{\infty v}$) must arise from a Σ configuration of the F (or Cl) atom with respect to the

HCl (or HF), thereby reversing the asymptotic Σ and Π ordering of states with respect to the reactant (or product) channels. Since the symmetries of the Π_x and Σ surfaces are reduced to non-crossing $1^2A'$ and $2^2A'$ surfaces for any non-collinear geometry, this necessarily results in a 3N-5 = 1-D seam of conical intersections in both the entrance channel and exit channel. As will be shown in this work, these conical intersection seams for the F + HCl → HF + Cl system are energetically quite low ($E_{crossing}$ = 3-4 kcal/mol) with respect to the collision energy (E_{com} = 5 kcal/mol) as well as the F(^{2}P) + HCl transition state ($E_{TST} \approx 3.8$ kcal/mol). Thus, although such arguments for the existence of conical intersections are quite generally true for ^{2}P + closed shell systems, these intersections for F + HCl → Cl + HF are energetically accessible in *all* reactive encounters and therefore likely to be of significant relevance in accurately describing the reaction dynamics.

The organization of this chapter is as follows: Section II describes the details of the *ab initio* calculations, including a discussion on the CBS extrapolation and correlation energy scaling that is used to provide an accurate PES. In Section III, I discuss the adiabatic potential energy surfaces, followed by Section IV, detailing the creation of and analytical fit to the diabatic energies with a discussion on the inclusion of spin-orbit effects in the diabatic basis. In Section V, I discuss the interesting aspects of this PES followed by a summary and concluding remarks in Section VI.

II. Ab Initio Background

All calculations are performed using the MOLPRO suite of *ab initio* programs[50]. Since I explicitly need to account for non-adiabatic as well as single

surface effects, electronically excited states of the F(^{2}P) + HCl → HF + Cl(^{2}P) reaction are required. Thus, the *ab initio* methods employed include multireference methods to obtain wavefunctions for non-adiabatic calculations and characterization of the conical intersections. In addition, other 3- and 4-atom systems involving F have indicated large multireference character in the ground state wavefunctions[38,40]. In light of these restrictions and past success with the dynamically weighted multiconfigurational self-consistent field (DW-MCSCF) method, the natural choice for this reaction is to use DW-MCSCF along with internally contracted multireference CI (MRCI) and the multireference Davidson correction (MRCI+Q). As the MRCI calculations only correlate electrons in orbitals of the same symmerty, separate adiabatic MRCI+Q calculations are performed for each C_s symmetry: one for the 1^2A' and 2^2A' states together and one for the 1^2A" state.

Residual *ab initio* error due to incomplete basis sets can be corrected by extrapolating to the complete basis set (CBS) limit[44] using the standard aug-cc-pVnZ (n = 2,3,4) basis sets of Woon and Dunning[51-53]. Based on the benchmark surface studies of O(^{3}P) + HCl by Peterson[44,46], this extrapolation is obtained via the three parameter fit

$$E(n) = E_{CBS} + Be^{-(n-1)} + Ce^{-(n-1)^2} . \qquad (6.1)$$

This function yields an excellent extrapolation to the CBS limit as explicitly confirmed by additional calculations for reagent and product asymptotic geometries with basis set extensions up to n = 5. The absolute energy difference between the CBS extrapolation for n = 2 - 4 and n = 2 - 5 was ~0.39 kcal/mol for both the entrance

and exit channel asymptotic calculations; a fuller description of the CBS extrapolation procedure is given in previous work on the ground state PES.[38]

The adiabatic MRCI+Q calculations are performed using a full valence complete active space[54] (CAS) reference function with 15 active orbitals (12A',3A"), 6 of which (5A',1A") are uncorrelated. The orbitals are obtained by a state-averaged multiconfiguration SCF (SA-MCSCF) calculation with 15 active orbitals (12A', 3A") with 7 (6A', 1A") closed to excitations. A total of 6 states are then included in the SA-MCSCF calculation (4A', 2A"), with the weights determined by the DW-MCSCF algorithm. In order to account for the triply degenerate p-hole in both the F and Cl atoms at the asymptote, the SA-MCSCF calculations include all 3 states (2A', 1A"); however, low-lying charge transfer (CT) states (e.g. $F^- + HCl^+ (^2\Pi) \rightarrow HF^+ (^2\Pi) + Cl^-$) require the inclusion of 2 more A" and 1 more A' state (a total of 6 states) to fully describe the transition state region. As previously demonstrated[40], root flipping as the CT surfaces cross other states along the reaction path makes it extremely challenging to obtain a smooth accurate PES for a fixed set of SA-MCSCF weights. In DW-MCSCF, on the other hand, the weights for each state are chosen as a function of its energy with respect to the ground state energy at each point in configuration space. The function for the weight based on the energy difference from the ground state is

$$w_i \propto sech^2\left(-\beta\left(E_i - E_0\right)\right) \qquad (6.2)$$

The decay coefficient (β^{-1}) for DW-MCSCF is empirically chosen to be 3eV. In the SA-MCSCF calculations, at the transition state, the CT states are about 2eV above the ground state, and from our group's previous F + H_2O calculations[40] with similar energetics, it is known that a 3eV DW-MCSCF decay works well. Most importantly,

this method permits one to eliminate spurious discontinuities from root flipping and thereby obtain a smooth reaction path and surface while accurately describing both asymptotic and transition state regions. The orbitals obtained from the DW-MCSCF calculation are then used as reference states for the internally contracted MRCI calculation. The benefit of using the DW-MCSCF procure is that the lowest MRCI states that arise from the DW-MCSCF orbitals are smoothly changing as a function of reaction coordinate. However, it is impossible to completely eliminate discontinuities in the upper MRCI states without an unreasonably large decay coefficient. As noted in previous F + H_2O work[40], the relative smoothness of the DW-MCSCF energies is controlled by the β^{-1} parameter. A larger β^{-1}, correlates to smoother curves, although accuracy at the asymptotes suffers when β^{-1} is too large. In this work, the 3eV choice of β^{-1} reflects the smoothest $1^2A'$, $2^2A'$, and $1^2A''$ curves that could be obtained while still accurately describing the asymptotic energies. By the way of an example, in the absence of spin-orbit contributions, the three lowest asymptotic F + HCl (and HF + Cl) states should be exactly degenerate. When β^{-1} is equal to 3eV, these three states at both asymptotes are degenerate to within $2x10^{-6}$ kcal/mol; however, a slightly larger β^{-1} of 5eV yields states that are only degenerate to 0.06 kcal/mol.

Building on ideas by Peterson and coworkers[46] and Truhlar and coworkers[45], I employ a simple global correlation energy scaling procedure calibrated to match the experimentally known reaction exothermicity. Specifically, the correlation energy is uniformly scaled by a constant factor near one that reproduces the exothermicity exactly while retaining the shape of the PES and not introducing any discontinuities.

The scaled energy is simply the sum of the MCSCF energy plus the correlation energy scaled by a factor, γ:

$$E(R)_{SCALED} = E(R)_{MCSCF} + \gamma E(R)_{CORR}. \qquad (6.3)$$

In the limit of γ = 0, the scaled energy is just the MCSCF energy (i.e., no extra correlation energy is recovered), and when γ = 1, the scaled energy is the MRCI+Q energy (i.e., all correlation energy is recovered). Allowing γ to be greater than one permits recovery of additional correlation energy, in effect, approximating an increase in active space. The scaling factor (γ) at the CBS limit determined in previous work[38] is close to unity (γ = 1.027) for the A' symmetry; i.e., one only needs to recover an extra 2.7% of the correlation energy to reproduce the experiment.

III. Adiabatic Surface Calculations

In the $F(^2P)$ + HCl → HF + $Cl(^2P)$ reaction, there are 3 low-lying adiabatic potential energy surfaces that correlate to the spin-orbit split, $F(^2P_{3/2})$ + HCl and $F^*(^2P_{1/2})$ + HCl in the entrance channel and HF + $Cl(^2P_{3/2})$ and HF + $Cl^*(^2P_{1/2})$ in the exit channel. The overall calculational strategy is as follows. First of all, in the Born-Oppenheimer approximation, *ab initio* methods directly yield the adiabatic energies for arbitrarily slowly moving nuclei, with non-adiabatic coupling between the surfaces arising from derivatives of the wave function with respect to 3N-6 displacements. To facilitate later dynamical calculations, however, it proves convenient to express these (3x3) adiabatic surfaces in an equivalent (3x3) diabatic representation with off-diagonal coupling terms mixing the 1A' and 2A' states. This choice of diabatic representation is in general non-unique, but can be calculated

simply in MOLPRO by constraining the diabats to converge onto the appropriate adiabatic states for collinear and asymptotic geometries. Secondly, I need to include spin-orbit interaction due to ^{2}P orbital angular momentum in the F and Cl atoms. Since this interaction is relatively weak, this is initially neglected this in the calculation of both adiabatic and diabatic surfaces, but it is later included explicitly via Breit-Pauli spin-orbit matrix elements[55] to generate a 6x6 matrix representation of the 3 doubly degenerate spin-orbit states.

In order to construct the full 3D potential energy surface, adiabatic calculations have been performed along a grid of points with the ranges R_{HF} = [1.3 - 15.0] a_0 and R_{HCl} = [1.8 - 15.0] a_0 and $\theta_{F\text{-}H\text{-}Cl}$ = [180, 150, 120, 90, 60, 30, 0] degrees, sampling only energies lower than 50 kcal/mol above the entrance channel. The resulting 3230 points are chosen such that the density is maximized in the most important regions of the surface (i.e., the transition state and van der Walls well regions), while still sampling a large enough region to get an accurate global description of the PES. Also included in this full set are 121 points sampling directly along the reaction path.

Figure 6.1 shows the energies of these three adiabatic surfaces (with the spin-orbit interactions included) as a function of the 1^2A' reaction coordinate. The lowest adiabat has a barrier of ~5 kcal/mol, which is lowered to 3.8 kcal/mol when vibrationally adiabatic zero-point energies in orthogonal coordinates are taken into account.[38] By way of contrast, the 2^2A' and 1^2A'' surfaces both have much higher barriers of about 25 kcal/mol. The two high barriers are the result of an avoided crossing from the relatively low energy CT states that correspond to $F^- + HCl^+$ ($^2\Pi$)

→ HF^+ ($^2\Pi$) + Cl^-, as clearly revealed in the DW-MCSCF calculations. Indeed, it is precisely the interaction among these states that necessitated the inclusion of up to 6 states in the DW-MCSCF calculation described earlier. A key result of this analysis is that at experimental collision energies of ~5 kcal/mol, only reactions over the lowest barrier are energetically permitted. Such adiabatic surface correlations make unambiguous predictions about the reaction dynamics. For example, in absence of non-adiabatic surface hopping, spin-orbit excited F would be completely non-reactive at 5 kcal/mol and any product Cl would be formed exclusively in the ground spin-orbit state. As I shall show later, this is largely true but not entirely accurate due to non-adiabatic coupling between the $1^2A'$ and $2^2A'$ surfaces.

For the special case of 3 atoms in a linear configuration, the three lowest adiabatic states, $1^2A'$, $2^2A'$, and $1^2A''$, transform according to three different symmetries, $1^2\Sigma$, $1^2\Pi_x$, and $1^2\Pi_y$, respectively. By the Wigner non-crossing rule, the $1^2A'$ and $2^2A'$ states couple and avoid for any non-collinear geometry. However, these surfaces can and indeed do cross as $1^2\Sigma$ and $1^2\Pi_x$ states when the molecule is collinear, thereby creating a 1D manifold of conical intersections. As noted in the introduction, the F(^{2}P) + HCl → HF + Cl(^{2}P) reaction exhibits two conical intersection seams (one in the entrance channel, and one in the exit channel). Figure 6.2 illustrates the nature of the conical intersection region in the exit channel. When the $\theta_{F\text{-}H\text{-}Cl}$ is 180^o (see Figure 6.2a), there is a 1-D "seam" of geometries (solid black line) at which the $1^2\Sigma$ and $1^2\Pi_x$ states cross (or, alternately, the $1^2A'$ and $2^2A'$ states touch) and are exactly degenerate. As $\theta_{F\text{-}H\text{-}Cl}$ bends away from linearity (Figure 6.2b), however, the symmetries are reduced from $1^2\Sigma$ and $1^2\Pi_x$ to $1^2A'$ and $2^2A'$, thereby

avoiding one another in a classic conical intersection. Of particular dynamical interest is that this seam occurs at energies *lower* than the ground transition state barrier, and though clearly for a collinear as opposed to the bent transition state geometry, not dramatically far away from the reaction path. Thus essentially *all* reactive collisions (with the exception of tunneling events) have sufficient energy to sample the conical intersection region.

This energetic proximity of adiabatic electronic surfaces implies significant derivatives in the wavefunctions with respect to motion along the reaction coordinate. Specifically, when the molecule is bent, the $1^2A'$ ($2^2A'$) state correlates adiabatically with the lower (higher) of the $1^2\Sigma$ and $1^2\Pi_x$ states, respectively. As mentioned previously, when the F atom is far away, the lower state is approximately "Π-like", but switches to a "Σ-like" state as the F approaches HCl. (Σ and Π are not rigorous quantum labels for anything except the collinear geometry, but nevertheless offer useful qualitative descriptors.) The region in which the electrons rearrange from Π-like to Σ-like states is the region of the avoided crossing. The time required for electron rearrangement compared to the time over which the nuclei approach governs the role of non-adiabatic surface hopping dynamics, as first described in 1-D systems by Landau and Zener. Simply stated, at sufficiently low energies, the electrons quickly rearrange to remain on the same adiabatic surface. However, at higher energies where nuclei move on time scales competitive with electron rearrangement, non-adiabatic transitions to a different adiabatic surface can result. Explicit calculation of these transitions requires a full multiple electronic surface treatment to determine the role of non-adiabatic contributions to the reaction dynamics, as will be

demonstrated later in Section V. However, these calculations prove to be more tractable in the corresponding diabatic basis, the extraction of which is discussed in the next section.

IV. Diabatic Potential Energy Surfaces

A. Diabatic Surface and Non-Adiabatic Coupling Calculations

In contrast to the adiabatic representation, the diabatic state reflects a specific representation for which the wavefunctions do not change rapidly in the vicinity of a crossing. The key advantage of this approach is that off-diagonal coupling between the diabatic states can be treated as independent of nuclear velocities. Though the choice of such a representation is not unique, there are several methods for obtaining well-behaved diabatic electronic and associated coupling surfaces from adiabatic *ab initio* calculations. Shatz and coworkers[56] have developed a method to approximate the mixing angle, χ, from matrix elements of the electronic angular momentum operator. With this mixing angle, the transformation from adiabatic to diabatic energies can be described by a simple 3x3 rotation

$$\begin{bmatrix} |\Sigma\rangle \\ |\Pi_x\rangle \\ |\Pi_y\rangle \end{bmatrix} = \begin{bmatrix} \cos\chi & -\sin\chi & 0 \\ \sin\chi & \cos\chi & 0 \\ 0 & 0 & 1 \end{bmatrix} \begin{bmatrix} |1A'\rangle \\ |2A'\rangle \\ |1A''\rangle \end{bmatrix} \qquad (6.4)$$

where $|1A'\rangle$, $|2A'\rangle$, and $|1A''\rangle$ are the adiabatic *ab initio* energies. The corresponding potential in the diabatic basis is then reported as a 3x3 matrix[57]:

$$V = \begin{bmatrix} & |\Sigma\rangle & |\Pi_x\rangle & |\Pi_y\rangle \\ |\Sigma\rangle & V_\Sigma & \beta & 0 \\ |\Pi_x\rangle & \beta & V_{\Pi x} & 0 \\ |\Pi_y\rangle & 0 & 0 & V_{\Pi y} \end{bmatrix} \qquad (6.5)$$

Here the diagonal terms represent diabatic energies of $|\Sigma\rangle, |\Pi_x\rangle$, and $|\Pi_y\rangle$ respectively, where β is the coupling surface between $|\Sigma\rangle$ and $|\Pi_x\rangle$ states and directly related to the mixing angle by $2\chi = \tan^{-1}[2\beta/(V_\Sigma - V_{\Pi x})]$. It is worth stressing that the labels $|\Sigma\rangle$, $|\Pi_x\rangle$, and $|\Pi_y\rangle$ are rigorously valid only for collinear geometries, which therefore have a unique axis around which the electronic angular momentum can be defined. More precisely, these labels denote the corresponding 1^2A', 2^2A' and 1^2A" diabatic surfaces with which these states correlate upon bending away from collinearity.

The mixing angle is determined through MOLPRO subroutines, which calculate χ by directly examining the electronic wavefunctions[58-60]. Simply stated, the adiabatic *ab initio* energies at each geometry are calculated for aug-cc-pVnZ bases (n = 2,3,4), extrapolated to the CBS limit via Equation 6.1 and further refined by correlation energy scaling via Equation 6.3. These adiabatic energies are then transformed to the diabatic basis using the mixing angle obtained from the highest level aug-cc-pVQZ *ab initio* calculation. However, sensitivity to basis set level is extremely small, with less than 1%.variation in mixing angles for all three AVnZ (n = 2,3,4).

As the specific choice of diabatic representation is non-unique, I use the following method to ensure that the resultant diabatic surfaces are internally self-

consistent. At linear geometries, the coupling among the three states must vanish identically, since all three ($1^2\Sigma$, $1^2\Pi_x$, and $1^2\Pi_y$) are of different symmetries. For each fixed R_{HF} and R_{HCl} geometry, therefore, I make a 1D angular sweep from $\theta_{F\text{-}H\text{-}Cl}$ = 180° to 0 °. I start at $\theta_{F\text{-}H\text{-}Cl}$ = 180° with diabatic states, $|\Sigma\rangle$, $|\Pi_x\rangle$, and $|\Pi_y\rangle$, defined to be the adiabatic states, $|1A'\rangle$, $|2A'\rangle$, and $|1A''\rangle$. In the spirit of the diabatic representation, calculations at each subsequent non-collinear angle proceed first by maximizing overlap with the previous orbital, determining the mixing angle via MOLPRO, and iterating for a series of $\theta_{F\text{-}H\text{-}Cl}$ = [120°,90 °,60 °,30 °,0 °] angles. As a test of self-consistency of the diabitization process, the resulting $|\Sigma\rangle$ and $|\Pi_x\rangle$ diabatic states can now in general cross, but must converge smoothly onto the adiabatic states, $|1A'\rangle$, $|2A'\rangle$, at both $\theta_{F\text{-}H\text{-}Cl}$ = 180° and 0° collinear geometries. In addition, at a few select geometries, $\theta_{F\text{-}H\text{-}Cl}$ was swept in 1° increments and compared to the 30° steps at the same points. Variations in the mixing angle were less than 1% between the 1° and 30° angular sweeps, indicating excellent convergence of χ.

Figure 6.3 shows sample adiabatic/diabatic results from calculations in the exit channel, where R_{HF} is fixed at the HF equilibrium value (3.4 a_0) for R_{HCl} at 6.6 a_0. As expected, the coupling vanishes at both $\theta_{F\text{-}H\text{-}Cl}$ = 180° (and $\theta_{F\text{-}H\text{-}Cl}$ = 0°), resulting in identical diabatic and adiabatic energies. At $\theta_{F\text{-}H\text{-}Cl}$ = 180°, the Π state is lower in energy than the Σ state, due to dipole-quadrupole and dipole-induced dipole interactions (i.e., the p-hole perpendicular to the partially positive H end of the HF).[47-49] As $\theta_{F\text{-}H\text{-}Cl}$ sequentially decreases from 180°, the Σ state (p-hole pointing preferentially parallel to the reaction coordinate) drops in energy due to interaction

with the partially negative F on the HF. Note that as $\theta_{F\text{-}H\text{-}Cl}$ is swept from 180^o to 0^o, the adiabatic 1A' and 2A' states exhibit an avoided crossing in the precise area where the Σ and Π states swap energy ordering.

Similarly, diabatic energy crossings (and adiabatic avoided crossings) of the $^2\Sigma$ and $^2\Pi$ states also occur as a function of the reaction coordinate, as shown in Figure 6.4a, Note that in the asymptotes, the low-energy states always correlate with the Π (blue) surface, due to the same electrostatic arguments given above. As the reagents get closer toward the transition state, the Σ-like state must be lower in energy for the H abstraction to occur.[47-49] Notice again that in the region where the diabatic surface are crossing, the adiabatic surfaces avoid strongly. It is in this region where, adiabatically, the p-hole is moving from a Π-like state (pointing away from the diatomic) to a Σ-like state (pointing towards the diatomic). Figure 6.4b shows a similar plot of the reaction path, but this time with the geometry artificially constrained to be collinear ($\theta_{F\text{-}H\text{-}Cl} = 180^o$), for which the adiabatic and diabatic energies are necessarily the same. The adiabats do not avoid in this case because they are all of different symmetry ($^2\Sigma$, $^2\Pi_x$, $^2\Pi_y$ as opposed to the bent geometry case of ^{2}A' and ^{2}A'').

B. Spin-orbit Calculations

The spin-orbit terms are calculated identically as described by Alexander and coworkers[61] for the F + H_2 → HF + H multistate surface. In this method, first the Breit-Pauli spin-orbit operator[55] is used to calculate the adiabatic spin-orbit states[62] using the unperturbed adiabatic states as a basis. The Breit-Pauli spin-orbit operator

generates an adiabatic spin-orbit matrix (H_{SO}), which is then transformed into a diabatic spin-orbit matrix using the known mixing angle. This procedure results into two additional A and B surfaces as a function of coordinates (θ, R_{HF}, R_{HCl}), obtained from the diabatic orbitals via:

$$A = i\left\langle \Pi_y \left| H_{SO} \right| \Pi_x \right\rangle \quad (6.6)$$

and

$$B = \left\langle \overline{\Pi_x} \left| H_{SO} \right| \Sigma \right\rangle \quad (6.7)$$

where the absence (presence) of a bar over a state signifies an electron spin projection of $+{}^1/_2$ ($-{}^1/_2$). After inclusion of spin-orbit terms, the final potential is represented as a 6x6 matrix:

$$V = \begin{bmatrix} & |\Sigma\rangle & |\overline{\Sigma}\rangle & |\Pi_x\rangle & |\overline{\Pi_x}\rangle & |\Pi_y\rangle & |\overline{\Pi_y}\rangle \\ |\Sigma\rangle & V_\Sigma & 0 & \beta & B & 0 & 0 \\ |\overline{\Sigma}\rangle & 0 & V_{\Pi x} & B & \beta & 0 & 0 \\ |\Pi_x\rangle & \beta & B & V_{\Pi y} & 0 & A & 0 \\ |\overline{\Pi_x}\rangle & B & \beta & 0 & V_\Sigma & 0 & -A \\ |\Pi_y\rangle & 0 & 0 & A & 0 & V_{\Pi x_x} & 0 \\ |\overline{\Pi_y}\rangle & 0 & 0 & 0 & -A & 0 & V_{\Pi y} \end{bmatrix} \quad (6.8)$$

The 6 parameters obtained from this adiabatic to diabatic transformation (V_Σ, $V_{\Pi x}$, $V_{\Pi y}$, β, A, and B) are then fit to analytical functions of θ, R_{HF}, and R_{HCl} as described below. A FORTRAN subroutine and complete listing of least-squares coefficients for calculating this matrix and the lowest three diabatic and adiabatic PES's will be made available though EPAPS[63].

C. Analytical fits of the diabatic PES

Following the methods outlined by Aguado and Paniagua[64], the diabatic surface energies, V_{Σ}, $V_{\Pi x}$, and $V_{\Pi y}$, are least-squares fit to a multibody expansion in pairwise displacement coordinates:

$$V(R_{HF}, R_{HCl}, R_{ClF}) = V^{(1)} + \sum_{i \in \{HF, HCl, ClF\}} V^{(2)}(R_i) + V^{(3)}(R_{HF}, R_{HCl}, R_{ClF}). \quad (6.9)$$

where $V^{(1)}(R_{HF}, R_{HCl}, R_{ClF})$ represents the energy zero for three separated atoms (i.e., subtracted from each *ab initio* energy), $V^{(2)}$ (R_i) are diatomic potentials for in the asymptotic pairwise limit, and $V^{(3)}(R_{HF}, R_{HCl}, R_{ClF})$ reflects the remaining 3-body interactions.

The two body interaction term is based on a sum of modified Rydberg functions[64]:

$$V^{(2)}(R) = \frac{C_0}{R} e^{-\alpha_1 R} + \sum_{i=1}^{N} C_i \left(R e^{-\alpha_2 R}\right)^i . \quad (6.10)$$

where R represents the pairwise interatomic distances between the 3 atoms. *Ab initio* points for each of the diatomics are fit to a N^{th} order polynomial with N = 9. For the Cl + HF reagent channel, 19 *ab initio* points between R_{HF} = 1.2 a_0 and R_{HF} = 3.0 a_0 have been used, yielding a least-squares fits for α_1, α_2 and C_i (i = 0,9) with a global RMS deviation of 0.039 kcal/mol. Similarly for HCl, 26 points between R_{HCl} = 1.6 a_0 and R_{HCl} = 4.0 a_0 have been fit to a global RMS of 0.015 kcal/mol. Although the ClF region is not energetically sampled in reactive scattering experiments at typical collision energies, the ClF potential is also obtained for 21 points between R_{ClF} = 2.5 a_0 and R_{ClF} = 4.5 a_0, yielding a global diatomic fit with a RMS deviation of ~0.046 kcal/mol.

The three body term simply reflects the remaining difference between *ab initio* points after subtracting the diatom $V^{(2)}$ and atom $V^{(1)}$ energies. Since this term must vanish in any of the diatomic asymptotes, a commonly used functional form is simply a linear combination of two-body product functions, i.e.,

$$V^{(3)}(R_1, R_2, R_3) = \sum_{i,j,k}^{M} D_{ijk} \left(R_1 e^{-\beta_1^{(3)} R_1}\right)^i \left(R_2 e^{-\beta_2^{(3)} R_2}\right)^j \left(R_3 e^{-\beta_{31}^{(3)} R_3}\right)^k , \qquad (6.11)$$

with the total order of the polynomial restricted to $i + j + k \leq M$. The explicit numerical least-squares weighting strategy for obtaining this fit is modeled after efforts developing the Stark-Werner F + H_2 surface. First of all, *ab initio* points along the reaction path are the most important and given the highest weight of 100. Of the remaining 3230 grid points, the 2200 geometries with energies less than 15 kcal/mol above the F + HCl entrance channel are weighted 10-fold, with the remaining 1030 points with energies between 15 and 50 kcal/mol receiving a weight of 1. For the V_Σ surface, the resulting global RMS deviation for a least-squares fit with a 12^{th} order polynomial (M = 12) is ~0.31 kcal/mol, with RMS deviations for $V_{\Pi x}$ and $V_{\Pi y}$ surfaces of ~0.35 kcal/mol and ~0.34 kcal/mol respectively. However, the errors in such a fitting process prove to have non-Gaussian tails, for which a simple RMS metric can substantially overestimate the importance of the deviations. By way of example, the inset in Figure 6.7a displays the explicit error histogram for the V_Σ surface least-squares fit, which exhibits a substantially improved FWHM metric of ~0.049 kcal/mol, i.e., nearly an order of magnitude better than the RMS value. Furthermore, the surface fit quality for geometries along the reaction coordinate is ~0.005 kcal/mol, reflecting improvement by yet another order of magnitude.

The above comparison speaks to the presence of residual errors in the least-squares fitted surface, but in regions that are generally much higher in energy and away from the reaction path sampled at typical collision conditions. There appear to be two contributions. The first is due to the strongly exothermic nature of the potential, for which the above weighting strategy necessarily includes product state regions high up on the repulsive walls. Secondly, analysis of the residual errors indicates that regions > 20 kcal/mol above the barrier are less well fit, due specifically to $V_{\Pi x}$ and $V_{\Pi y}$ surfaces in the transition state region. These surfaces are much higher in energy (~30 kcal/mol) than the V_{Σ} surface (~5 kcal/mol) and are influenced by multiple and rapid avoided crossings with excited charge transfer states. These effects can be compensated for by including additional electronic states in the DW-MCSCF prodecure and/or utilizing a faster decay parameter (~5-6 eV). However, both options would degrade PES accuracy in the physically relevant regions corresponding to typical collision energies at or near the transition state.

D. Diabatic coupling and spin-orbit fits

Slices of the diabatic coupling, β, are shown in Figure 6.8 for three different F-H-Cl bend angles, revealing the basic surface topography. Based on these observations, the surface is fit to a 3 body-like term given by the sum of i) a simple polynomial that creates a steep repulsive wall as R_{HF} and R_{HCl} become small and ii) a direct product of distributed Gaussians in R_{HF} and R_{HCl} and sin(nθ):

$$\beta(R_{HF}, R_{HCl}, \theta) = \frac{a_0 \sin(\theta)}{(R_{HF} + R_{HCl})^4} + \sum_{in} a_{in} g_i(R_{HF_i}, R_{HCl_i}, \sigma_i) \sin(n\theta) \,. \quad (6.12)$$

As required, the functional dependence of β on sin(nθ) ensures identically zero coupling between diabats for molecules in the linear configuration (θ = 0, 180). The first term represents an empirical 4th order polynomial "wall" for non linear molecules as R_{HF} and R_{Cl} approach zero, with an a_0 value least-squares fit to the data. With the large dynamic range terms covered in Equation 6.12, the remaining surface can then be efficiently fitted by normalized 2D Gaussians, $g(R_{HF_i}, R_{HCl_i}, \sigma_i)$, centered on (R_{HF_i}, R_{HCl_i}) with a width of σ_i.. The direct product grid of 134 Gaussians with sin(nθ) (n = 1-3) functions results in a total of 402 basis functions for the least-squares fit. The R_{HF}, R_{HCl} grid of Gaussians is shown explicitly in Figure 6.6, with σ_i for each grid point being 0.6411 of the grid spacing. This choice of σ_i arises from a desire to minimize the coupling (or overlap) of the Gaussian basis functions, while still having them wide enough to fill out the space between the grid points. The weights for the 3230 *ab initio* points are chosen such that large weights correspond to large values of the diabatic coupling. Specifically, guided by simple perturbation theory, the weight of each *ab initio* point is taken to be proportional to $\beta/(V_{\Sigma}-V_{\Pi\xi})$ with a cutoff dynamic range of 0.1 and 1,000. The RMS residuals of such a least-squares fit to the *ab initio* points are 0.064 kcal/mol on a range of 0 - 15 to kcal/mol.

Similar to the above analysis of the β surface, the two spin-orbit surfaces, A and B, are fit with a product of distributed Gaussian and angular terms as in Equation 6.12. However since there is now spin-orbit interaction asymmetry between the asymptotic F + HCl and Cl + HF limits, an additional offset term S must be included:

$$A(orB)\left(R_{HF}, R_{HCl}, \theta\right) = S(R_{HCl} - R_{HF}) + \sum_{il} a_{il}\, g(R_{HF\,i}, R_{HCl_i}, \sigma_i) P_l(\cos(\theta_i)) \quad (6.13)$$

Here g is a normalized Gaussian, P_l is a Legendre function (with l = 0, 1) , and the offset, S, is in the form of a switching function because the two asymptotes (F + HCl and HF + Cl) have a constant non-zero value . Since these surfaces must converge on F and Cl spin-orbit values at the reactant and product asymptotes, respectively, a simple switching function for A is used:

$$S(\Delta R) = \frac{(A_{Cl} - A_F)}{2}\tanh(\alpha \Delta R) + \frac{(A_{Cl} + A_F)}{2}, \qquad (6.14)$$

with a correspondingly similar expression for B. In Equation 6.14, A_X is the asymptotic value of $i\langle \Pi_y | H_{SO} | \Pi_x \rangle$ for the X atom asymptote where $A_F = 124.14$ cm^{-1} and $A_{Cl} = 272.29$ cm^{-1}. At the asymptotes, the B spin-orbit term, $\langle \overline{\Pi_x} | H_{SO} | \Sigma \rangle$, is conveniently identical to the A term[61], so the corresponding switching functions for A and B use the same parameters. Based on these correct spin-orbit asymptotic values for the switching functions plus 202 distributed Gaussian functions in the interaction region, the RMS residuals of the fit are 3.1 cm^{-1} for the A surface, and 2.8 cm^{-1} for the B surface, both on a range of ~275 cm^{-1}.

V. Discussion

The presence of low-lying conical intersections in the adiabatic surface[38] prompts the calculation of diabatic surfaces to be used in full 3-D quantum dynamics calculations. Figure 6.5b shows the contours (3 kcal/mol spacing) of the collinear potential energy surface of the 1^2A' state along with two dashed lines representing the location of the conical intersection, that is, the coordinates where the 1^2A' and 2^2A'

states have equal energies at $\theta = 180^o$, or, equivalently, where the V_Σ and $V_{\Pi x}$ surfaces cross at $\theta = 180^o$.

Note that conical intersections in both the entrance and exit channels occur at energies *lower* than that of the transition state. (Figure 6.5a shows the contours of the $1^2A'$ surface at the transition state angle $\theta = 123.5^o$.) Specifically, the barrier to reaction on the $1^2A'$ surface is 3.8 kcal/mol, with the conical intersection energies dropping as low as 3.55 kcal/mol and -3.23 kcal/mol in the entrance and exit channels respectively[38]. Stated simply, this means that any collision with enough energy to cross the barrier and react also has enough energy to access the conical intersection and interact with the excited $2^2A'$ surface. It is for precisely this reason that each of the lowest three diabatic surfaces are calculated.

The diabatic surfaces are composed of transformations of the three lowest adiabatic surfaces. V_Σ (Σ-like) and $V_{\Pi x}$ (Π-like) are mixtures of the $1^2A'$ and $2^2A'$ surfaces while $V_{\Pi y}$ is identical to the $1^2A''$ surface, which, by symmetry, does not have any interaction with the two A' surfaces. The contours of V_Σ, $V_{\Pi x}$, and $V_{\Pi y}$ at the transition state angle are shown in Figure 6.7. The coupling between V_Σ and $V_{\Pi x}$ is represented in the β surface shown in Figure 6.8 at three angles. At $\theta = 180^o$ (and $\theta = 0^o$, not shown), the β surface is identically 0 because coupling between the surfaces is prohibited by symmetry. As seen in Figure 6.8, $\theta = 150^o$ and 120^o, the value of the β surface is non-zero and significant in the region of the reaction path. The magnitude of the coupling is more easily seen in Figure 6.9, where it is plotted as a function of the reaction coordinate. The two coupled diabatic curves are shown along with the value of β (using the right y-axis) along the reaction path. The

coupling (β) is the largest in the steep descent out of the transition state towards the reactants. This is reminiscent of the large non-adiabatic coupling seen in the F + H_2O reaction[40],where the OH spin-orbit excited state is observed in greater populations[39] than would be predicted in an adiabatic model. In the F + HCl reaction, the two A' states correlate to the Cl($^2P_{3/2}$) and Cl*($^2P_{1/2}$) spin-orbit states asymptotically; thus, as in the F + H_2O reaction, non-adiabatic coupling between these two surfaces may produce an experimentally detectable amount of Cl* even if the reaction only has enough energy to cross the lowest adiabatic barrier.

To estimate the approximate coupling between the electronic surfaces at the ~5 kcal/mol experimental collision energies, I start with the simplest approach and use the well known Lendau-Zener model[65] to predict the probability of surface hopping along the 1-D F(^2P) + HCl → Cl(^2P) + HF reaction coordinate. In this elementary calculation, it is assumed that the reaction has just enough energy to get over the lowest adiabatic barrier (similar to the experimental conditions). As the system travels along the reaction path, the probability of surface hopping (i.e., exiting on a different surface than the molecules entered on) can be estimated based on i) the semiclassical velocity, ii) slope difference between the crossing diabats and iii) the strength of the coupling.[65] The Lendau-Zener model assumes constant velocity and constant coupling along the reaction path; this is approximated as the values of the velocity and coupling at the points along the reaction path where the diabats cross. Since the diabats cross in *both* the entrance and exit channels, the two crossing probabilities are considered independently. In the entrance channel, this surface hopping probability at 5 kcal/mol collision energy is ~0.1. Thus, ~10% of the

reagents entering on the *excited* state ($F(^2P_{1/2}*)$) surface with sufficient energy do indeed cross to the lower state and react, with 90% remaining on the upper state surface and being reflected from the higher adiabatic barrier. Similarly, the exit channel non-adiabatic contributions can be interpreted by considering all reactions that cross the lowest barrier. The Landau-Zener expressions predict products moving over the transition state barrier to have a small but finite probability (5%) of emerging on the *excited* state $Cl^*(^2P_{1/2})$ surface. Despite the simplicity of the model, this range of numbers (5%-10%) is certainly qualitatively consistent with full 3D non-adiabatic calculations of spin-orbit vs. ground state reactivity for the corresponding $F/F^* + H_2$ reaction.

The Landau-Zener model is exact only for i) constant semiclassical velocity and ii) constant non-adiabatic coupling, which is not rigorously the case for any realistic molecular system. To get a more quantitative feel for the non-adiabaticity of the reaction, therefore, I present preliminary results from a more sophisticated model based on a 1-D wavepacket constrained along the reaction coordinate. Simply stated, I propagate a 1-D Gaussian wavepacket in time along the 1-D $F(^2P) + HCl \rightarrow Cl(^2P) + HF$ reaction coordinate using a standard grid representation[66]. To propagate a wave function in time, the relation

$$\Psi(t_0 + \Delta t) = e^{(-i\hat{H}\Delta t)}\Psi(t_0), \quad (6.15)$$

is expanded in a suitable Chebychev polynomial basis[67,68] which operates on the wave function at $t = t_0$ and results in the wave function at $t = t_0 + \Delta t$. As described by Rush and Wiberg[69], the effective mass along the constrained 1D reaction coordinate can be readily calculated at each point based on large amplitude motion (LAM) Hamiltonian

methods of Hougen, Bunker and Johns. An attenuating operator is used[70,71] to prevent reflection of the wavepacket at the end of the grid, with the probability flux calculated for each of the electronic surfaces as the wavepacket evolves in time.

By using such wavepacket propagation methods, I am able to include the coupling between not only between V_Σ and $V_{\Pi x}$ surfaces, but also the additional coupling with the $V_{\Pi y}$ surface that occurs upon inclusion of spin-orbit interactions. Since the potential in Equation 6.8 is a non-Hermetian operator, I switch from the Cartesian Σ, Π_x, Π_y basis to a the signed notation Σ, Π_{-1}, and Π_1 using the standard relations[72]. In this basis, the potential is a Hermetian block diagonal 6x6 matrix[61]:

$$V = \begin{bmatrix} & |\Sigma\rangle & |\Pi_1\rangle & |\Pi_{-1}\rangle & |\overline{\Sigma}\rangle & |\overline{\Pi_1}\rangle & |\overline{\Pi_{-1}}\rangle \\ |\Sigma\rangle & V_\Sigma & -V_1 - i\sqrt{2}B & V_1 & 0 & 0 & 0 \\ |\Pi_1\rangle & -V_1 + i\sqrt{2}B & V_\Pi + A & V_2 & 0 & 0 & 0 \\ |\Pi_{-1}\rangle & V_1 & V_2 & V_\Pi - A & 0 & 0 & 0 \\ |\overline{\Sigma}\rangle & 0 & 0 & 0 & V_\Sigma & -V_1 + i\sqrt{2}B & V_1 \\ |\overline{\Pi_1}\rangle & 0 & 0 & 0 & -V_1 - i\sqrt{2}B & V_\Pi + A & V_2 \\ |\overline{\Pi_{-1}}\rangle & 0 & 0 & 0 & V_1 & V_2 & V_\Pi - A \end{bmatrix}, \quad (6.16)$$

where $V_\Pi = (V_{\Pi x} + V_{\Pi y}) / 2$, $V_1 = \beta / 2^{1/2}$, and $V_2 = (V_{\Pi y} - V_{\Pi x}) / 2$. However, only the upper (or lower) block of the matrix is necessary for wavepacket propagation, with the remaining elements offering redundant dynamical information on the degenerate α and β spin-orbit pair[73].

By way of demonstration, I present sample results from two wavepacket calculations on this 1-D grid. The first corresponds to a Gaussian wavepacket started at the transition state with no momentum (p = 0 au, Δp = 2 au), which then evolves in both forward and backward directions to reagents and products. Although, the

calculation was performed in the signed diabatic basis, the results are shown in the adiabatic basis. At each point the diabatic basis is diagonalized and the resulting eigenvectors are used to transform the wave packed probability from diabatic to adiabatic states. The results in Figure 6.10 start at t = 0 with all of the probability on the lowest adiabatic surface at the transition state. Subsequent panels reveal snapshots of $|\Psi|^2$ evolution up to 100 fs, with the bottom panel displaying the total accumulated flux passing through each point for the full calculation. It is clear that probability is coupled primarily between the first and second lowest adiabats, both of which correlate asymptotically with the ground Cl($^2P_{3/2}$) state. There is transient minor coupling in the entrance well region of wavepacket flux into the third adiabat, but this asymptotically results in only ~1% probability for non-adiabatic transfer to the spin-orbit excited Cl*($^2P_{1/2}$) state (Cl:Cl* = 0.993:0.007). It is worth noting that once the wavepacket has propagated appreciably away from the transition state, the flux map indicates that probability for each of the adiabats is effectively frozen in.

The issue of non-adiabatic reactivity can be addressed more explicitly by starting the wavepacket in one spin-orbit asymptote and measuring the flux that emerges in each of the final spin-orbit states. For wavepackets starting on the F($^2P_{3/2}$) surface with enough momentum to cross the barrier (p = 22 au, Δp = 2 au), the total normalized flux accumulated in the Cl($^2P_{3/2}$) and Cl*($^2P_{1/2}$) states state is 0.511 and 0.005, respectively. Thus half of the wavepacket reacts (the remaining probability reflected back to reactants), again with about ~1% non-adiabatic surface hopping probability. Conversely, I can start the wavepacket on the spin-orbit excited F*($^2P_{1/2}$) state and monitor reaction to form Cl and Cl* product channels. Note that the only

way for $F^*(^2P_{1/2})$ to react is to undergo a non-adiabatic transition in the entrance channel, since the barrier that adiabatically correlates with $F^*(^2P_{1/2})$ + HCl is ~25 kcal/mol, or about 20 kcal/mol too high for the mean collision energy. As expected, the non-adiabatic reaction probability is small, corresponding to 2.8% product formation in the $Cl(^2P_{3/2})$ (2.72%) and $Cl^*(^2P_{1/2})$ (0.03%) states. In comparison with the 52% reactivity for wavepackets starting on the ground spin-orbit state surface, this would indicate $F^*(^2P_{1/2})$ to be ~5% as reactive as $F(^2P_{3/2})$ and in qualitative agreement with the above Landau-Zener predictions.

This 1D reaction path model also permits mapping out the reactivity of $F(^2P_{3/2})$ and $F^*(^2P_{1/2})$ as a function of energy. Recall from Figure 6.10 that there are two adiabatic states correlating asymptotically with *ground* spin order $F(^2P_{3/2})$ and $Cl(^2P_{3/2})$, with barriers denoted in energetic order by E_1 and E_2. Conversely, the single adiabatic state correlating with spin-orbit *excited* $F^*(^2P_{1/2})$ and $Cl^*(^2P_{1/2})$ exhibits a barrier height E_3, where $E_3 \approx E_2$ and both $E_2, E_3 >> E_1$. For these calculations, I therefore start the reactants in each of the three adiabatic reactant states and compute the total flux in any product ($Cl(^2P_{3/2})$ or $Cl^*(^2P_{1/2})$) exit channels. The results of these wavepacket calculations are shown in Figure 6.11a, where solid lines represent the reaction probability (i.e. sum of the flux in the all of the three exit channels) and vertical dashed lines denote the positions of the three adiabatic energy barriers. Careful inspection reveals the lowest barrier in this plot is to be $E_1 \approx 5.1$ kcal/mol, not the 3.8 kcal/mol value stated earlier. This is because reaction path geometries are calculated from analytic derivatives on the DW-MCSCF surface, and thus are not in the exact same place as obtained with MRCI methods (for which MOLPRO does not

yet provide analytic gradients). However, this only shifts the reaction thresholds and has no bearing on the qualitative behavior.

As expected, both reactants correlating with the ground spin-orbit state $F(^2P_{3/2})$ start yielding significant reaction probability as the energy is increased above the E_1 barrier. The finite (~5-10%) F* reactivity at these low energies is due to non-adiabatic coupling that transfers reactants from the F* surface to (both) F surfaces prior to the transition state. As the energy is increased further to the higher E_2 and E_3 barriers, all incoming states become chemically reactive, reaching 100% reactivity asymptotically. For comparison, also included in Figure 6.11a are dotted lines that represent purely adiabatic reactivity levels, for a calculation in which the non-adiabatic coupling is arbitrarily set to 0. The difference between dotted and solid lines therefore reflects the non-trivial changes in reactivity due to non-adiabatic coupling.

It is worth noting that the above wavepacket calculations reflect a non-collinear reaction path and thus do not sample the energetically accessible conical intersections. I can therefore take these model calculations one step further to illustrate the possible importance of conical intersections on the reaction dynamics. By way of example, Figure 6.11b shows the results of the same wavepacket calculations as in 11a, however in these calculations, the 1-D path the wavepacket is now constrained to a collinear reaction path. Note that a direct wavepacket sampling of the conical intersection seam results in a preferential reactivity of spin-orbit excited F* vs F at low energies. This occurs because F* now *adiabatically* crosses down to the F states and can therefore react over the lowest barrier. Conversely, a wavepacket

starting in one of the F ground spin-orbit states transfers adiabatically to F* at the conical intersection seam and therefore to react must cross one of the two higher barriers. Such dramatic differences between collinear versus the full reaction path dynamics speak to the crucial role of conical intersection seams in the F + HCl system on controlling the low energy reactivity of F*.

VI. Summary and Conclusion

This chapter presents results for high-level *ab initio* calculations on the three lowest diabatic electronic states for the $F(^2P) + HCl \rightarrow HF + Cl(^2P)$ reaction, along with an analytical fit to these surfaces in full 3D and inclusion of spin-orbit effects. The *ab initio* data for the analytical fit are calculated at a grid of 3D points using *dynamically weighted* MCSCF methods, followed by high-level multireference (MRCI+Q) methods for a series of correlation-consistent basis sets (AVnZ, n = 2,3,4). These results are then extrapolated to the complete basis set limit (CBS), with a single global correlation scaling parameter to reproduce the experimentally well-known exothermicity. The adiabatic surfaces reveal extensive seams of conical intersections, as predicted from simple orbital considerations for X + HY halogen atom abstraction processes. For use in multiple surface quantum reactive scattering dynamical calculations, these surfaces have been systematically converted into a diabatic representation. The uniqueness of this transformation is maintained by requiring diabatic and adiabatic surfaces to match at both theta = 0 and 180 configurations, which is equivalent to forcing the coupling matrix elements between the diabatic surfaces to vanish for collinear geometries. Sequential full 3D fits of these surfaces to atom, pairwise and full three body terms have been obtained and

reported for the three lowest diabatic surfaces, as well as explicit inclusion of spin-orbit effects via Breit-Pauli matrix operators that yield excellent agreement with experiment. By way of preliminary tests, 1-D wavepacket calculations have been performed along the $F(^2P) + HCl \rightarrow HF + Cl(^2P)$ reaction coordinate to estimate the extent of non-adiabatic coupling and reactivity for both ground $F(^2P_{3/2})$ and spin-orbit excited $F^*(^2P_{1/2})$ atomic species. The goal of this work has been a benchmark set of multistate *ab initio* potential energy surfaces for the $F(^2P) + HCl \rightarrow HF + Cl(^2P)$ system, that should provide much stimulation for further theoretical and experimental exploration.

Figures

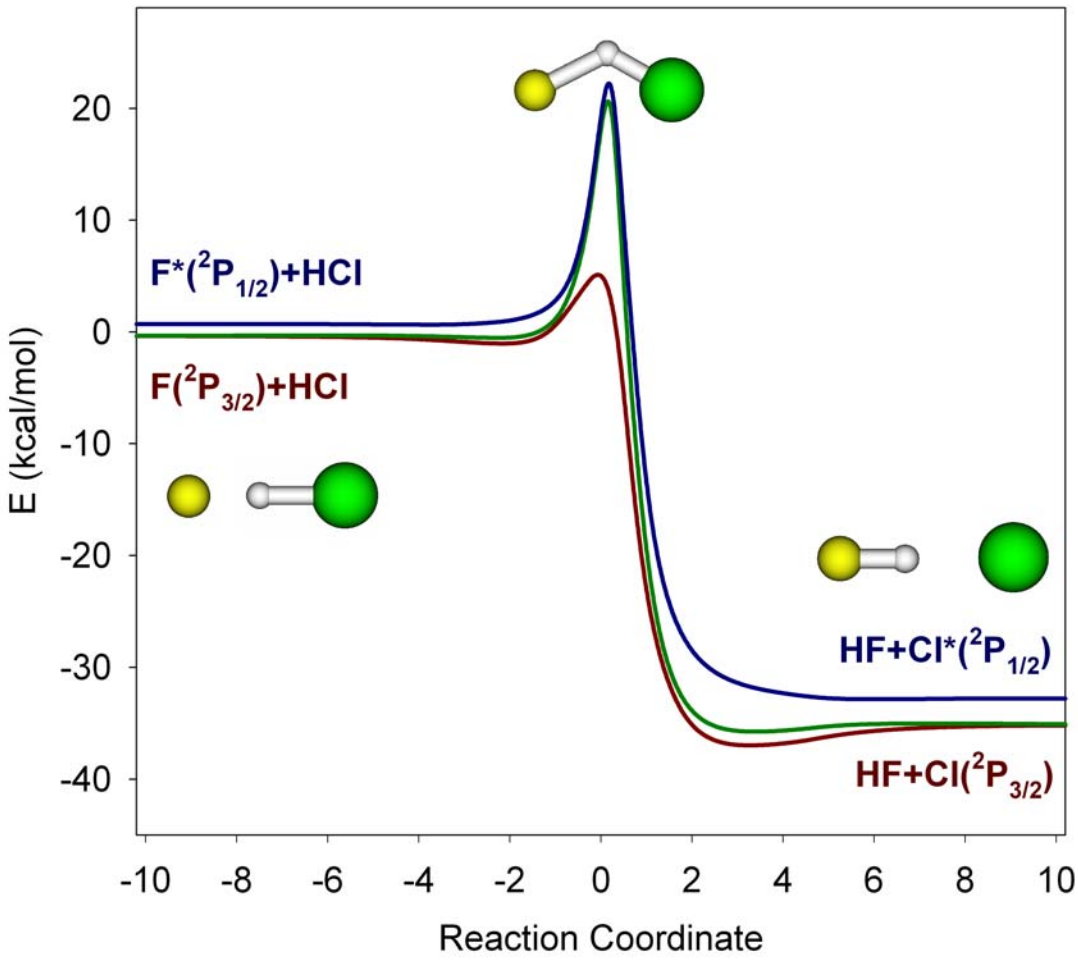

Figure 6.1: Three lowest adiabats along the reaction path for the F(^{2}P) + HCl → HF + Cl(^{2}P) system, obtained by high-level DW-MCSCF, MRCI+Q and CBS methods. The lowest two correlate with ground state F and Cl, while the highest one correlates asymptotically with spin-orbit excited F* and Cl* species. In the adiabatic limit, only the lowest spin-orbit ground state can react over a barrier accessible at experimental collision energies.

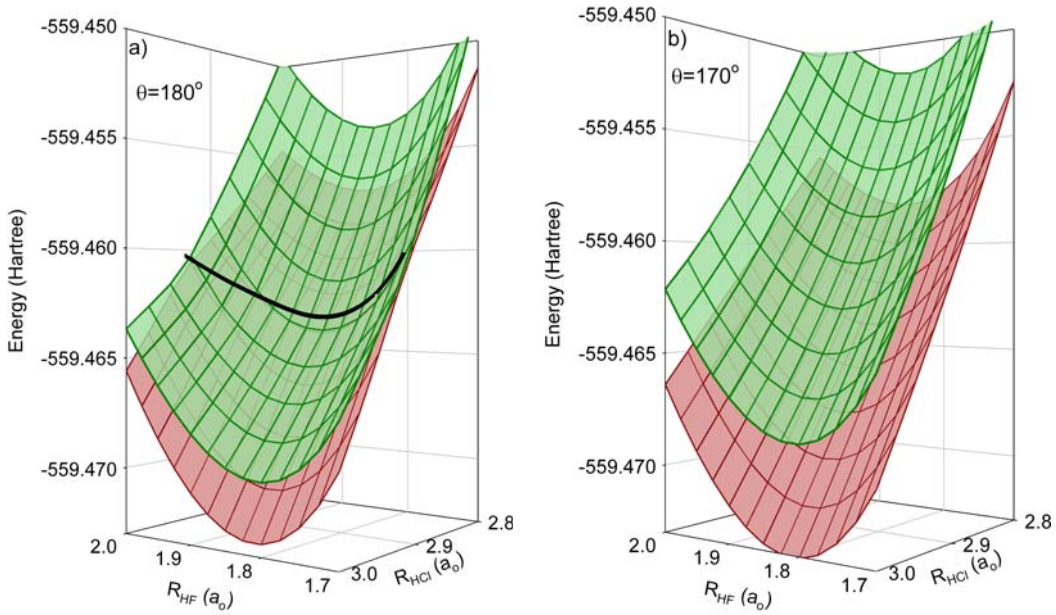

Figure 6.2: 2D slices through two full 3D A' adiabats. a) The region near the conical intersection seam (solid black line) at θ=180°, which by symmetry becomes b) an avoided crossing for any non-collinear geometry (θ=170°).

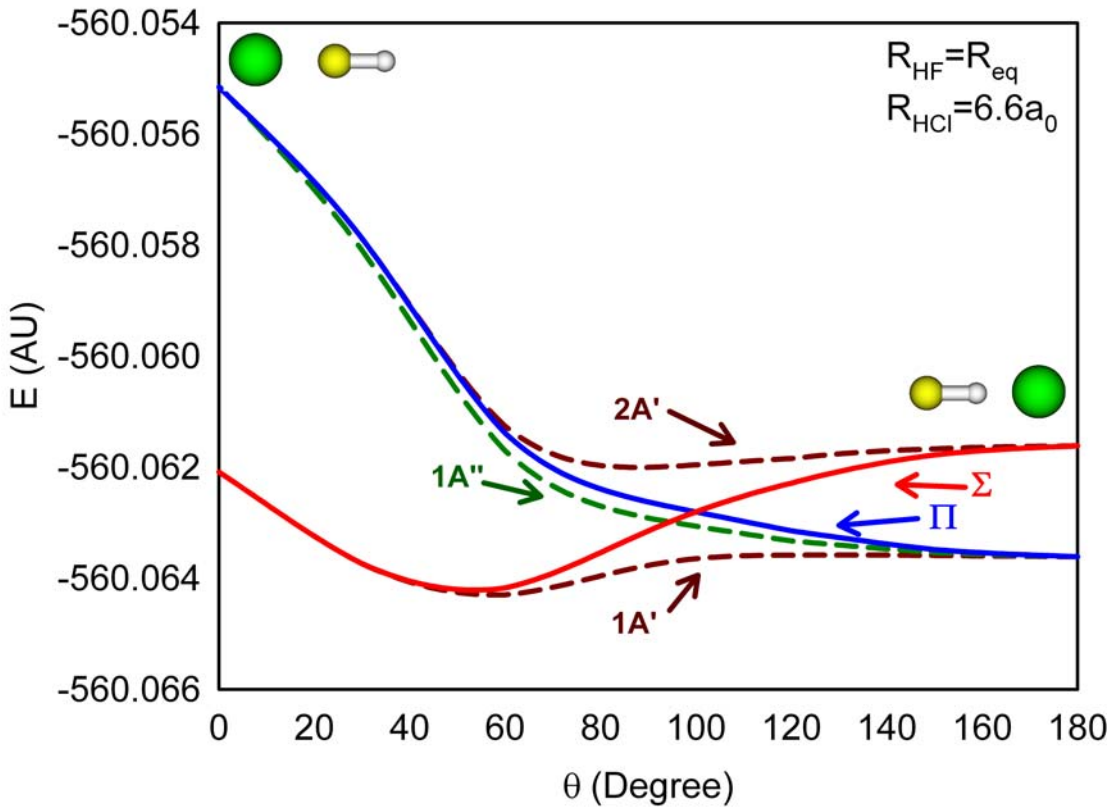

Figure 6.3: A 1D angular cut through full 3D adiabatic and diabatic surfaces in the exit channel, with R_{HF}=Req and R_{HCl}=6.6 a0. The adiabats and diabats are asymptotically equal at collinear geometries, but strongly avoid as the symmetry is lowered from $C_{\infty v}$.

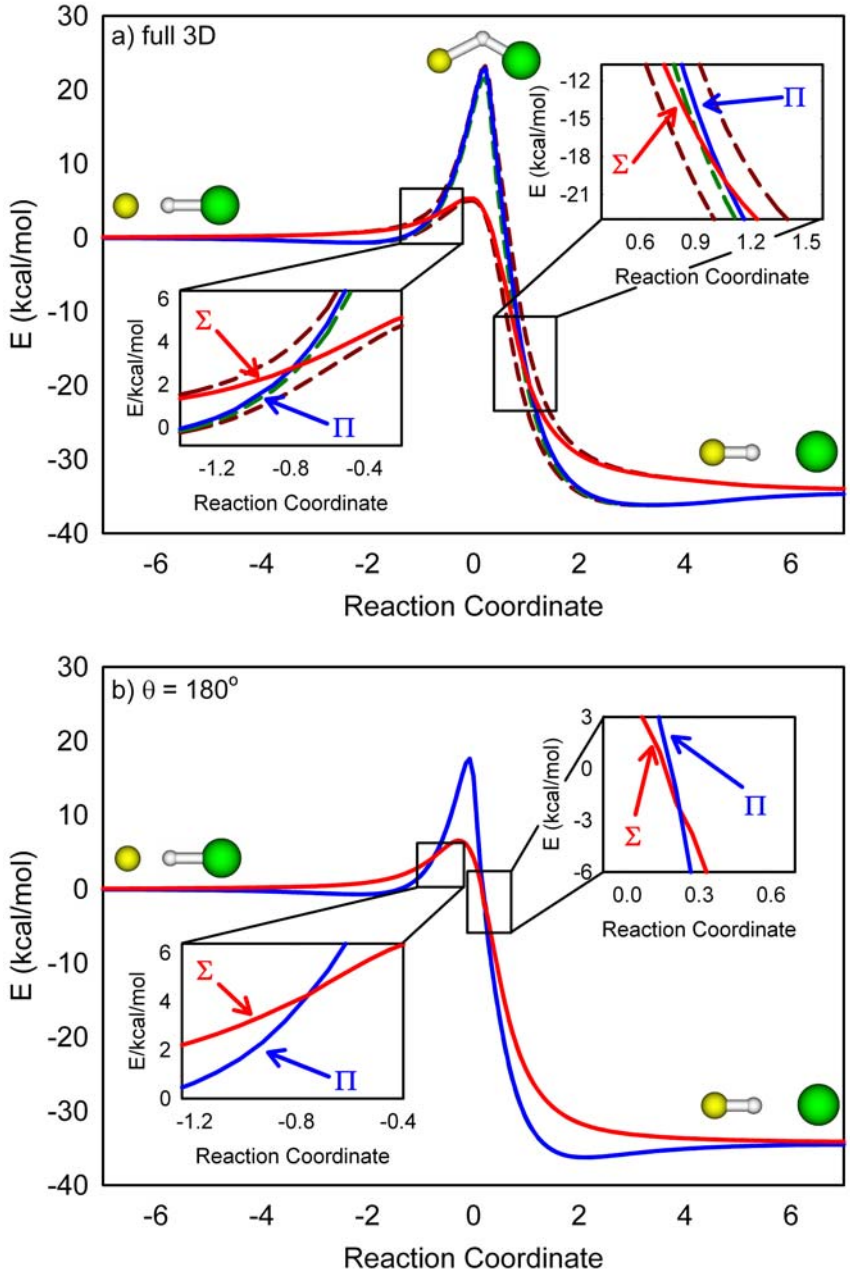

Figure 6.4: Adiabats (dashed lines) and diabats (solid lines) calculated along the reaction path a) in full 3D and b) with θ constrained at 180°. In full 3D the adiabats avoid where the diabats cross, whereas for a collinear geometry the adiabats and diabats overlap perfectly at each point along the conical intersection seam due to zero coupling.

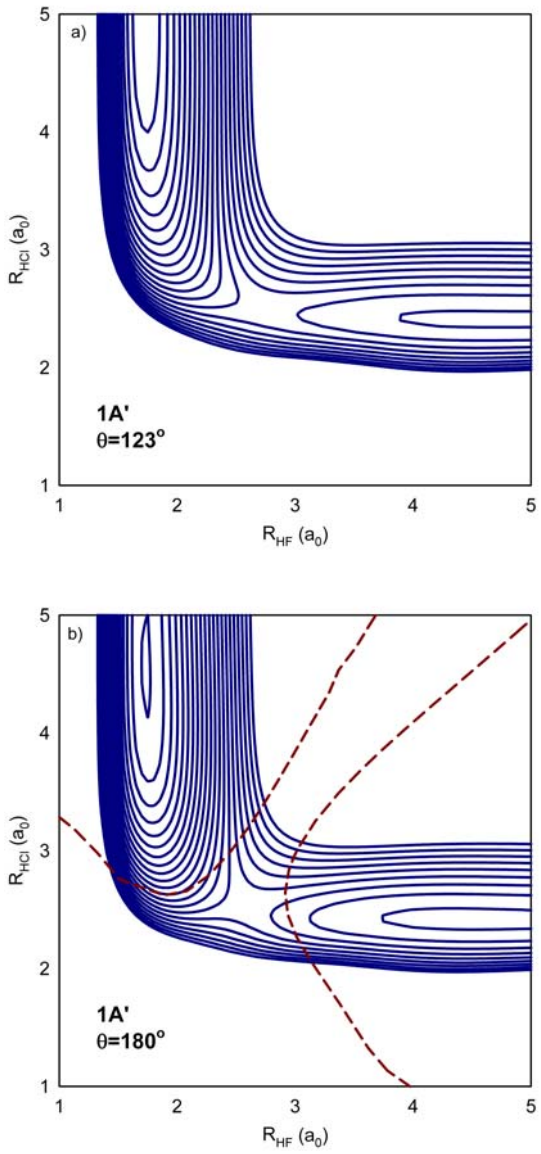

Figure 6.5: A 2D R_{HF}, R_{HCl} contour plot for the ground state adiabatic surface at both a) transition state (θ=123^o) and b) collinear (θ=180^o) geometries. In b) the conical intersection seams are shown with dashed lines. Contour spacing is 3 kcal/mol with respect to zero at reactant entrance channel.

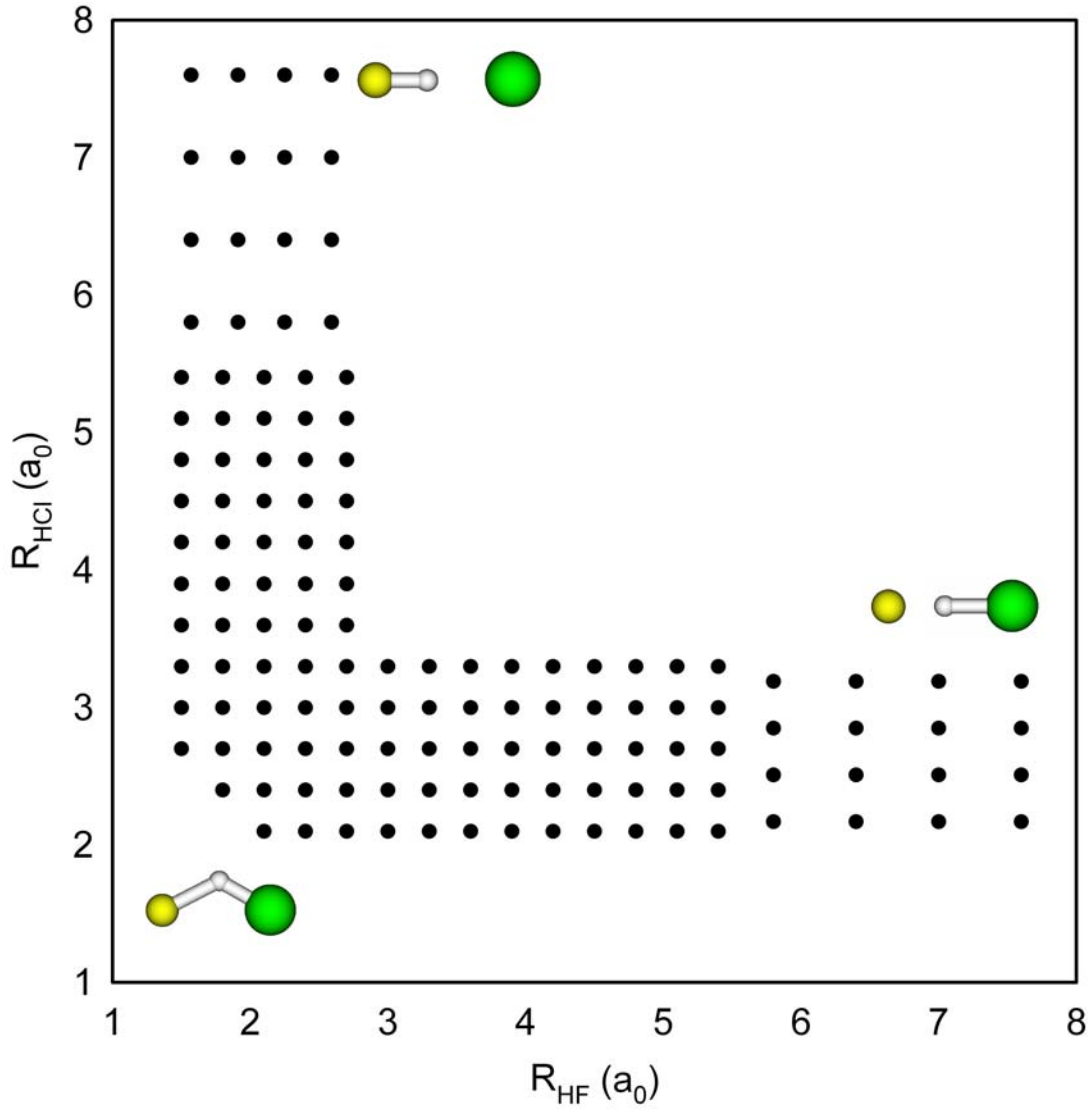

Figure 6.6: Grid of distributed Gaussian locations used to fit the β coupling surface. Angular dependence is fitted at each point (R_{HF}, R_{HCl}) by a linear combination of sin(nθ) functions.

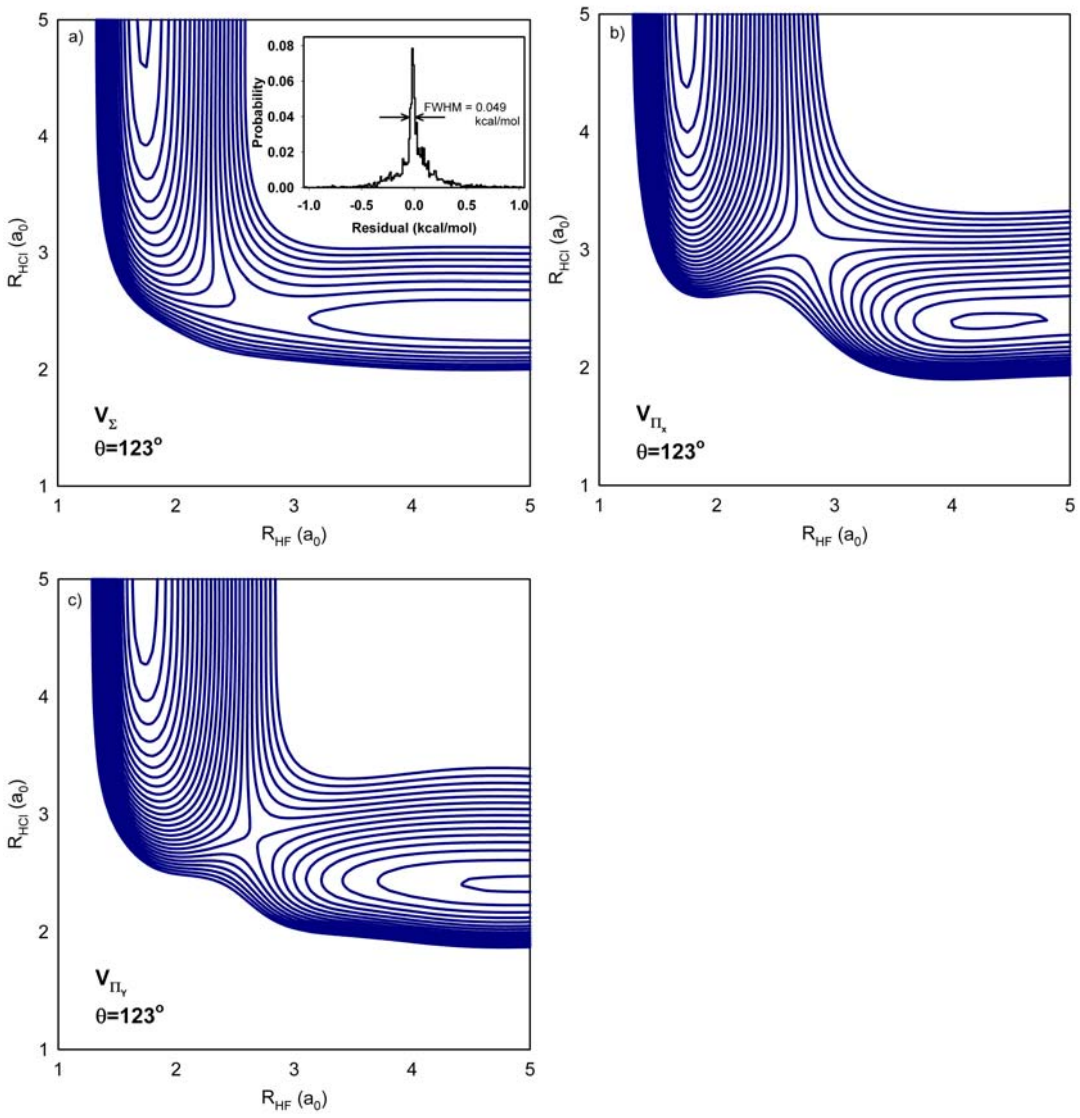

Figure 6.7: 2D contours (at θ=123°) for the a) V_Σ, b) $V_{\Pi x}$, and c) $V_{\Pi y}$ diabats with 3 kcal/mol spacing. A sample histogram of residuals for fitting the V_Σ function is also shown in a). The values are not distributed normally, which is why the RMS (0.34 kcal/mol) is considerably larger than the FWHM (0.049 kcal/mol).

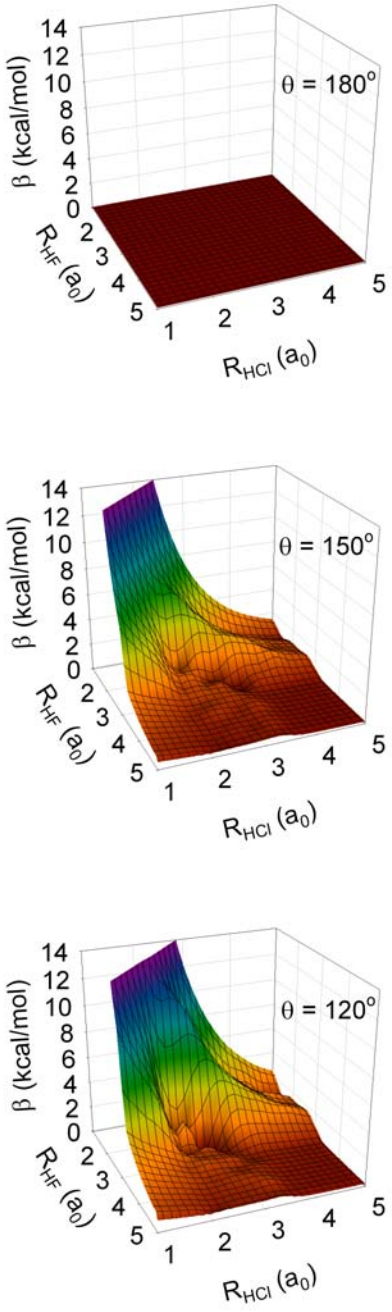

Figure 6.8: Sample 2D slices through the full 3D β coupling surface between V_{Σ} and $V_{\Pi x}$ diabats at a) θ=180°, b) θ=150°, and c) θ=120°. Note that for collinear geometry, β vanishes identically but grows rapidly as the molecule becomes bent.

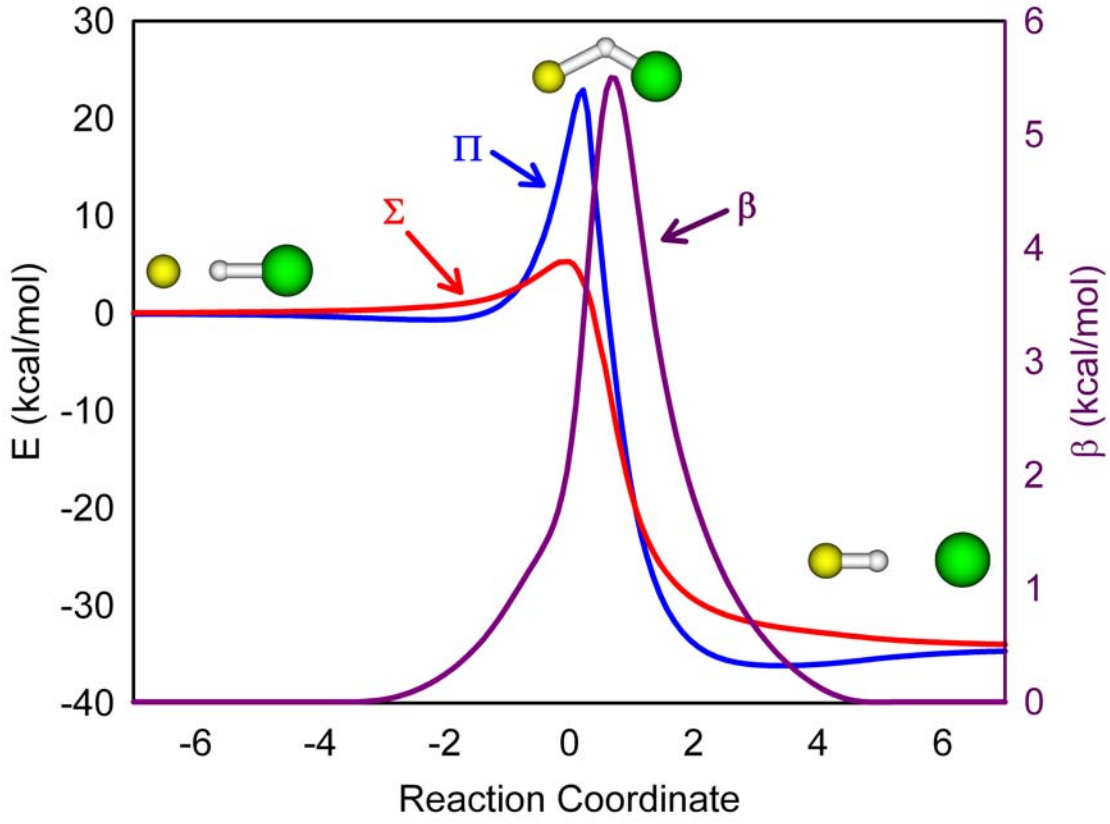

Figure 6.9: V_{Σ} and $V_{\Pi x}$ diabats along the reaction path (scale to left), and the β coupling between the diabats (scale to right). Note the strong peaking of diabatic coupling immediately in the *post* transition state region, due to rapid change in electronic character for the newly formed bond.

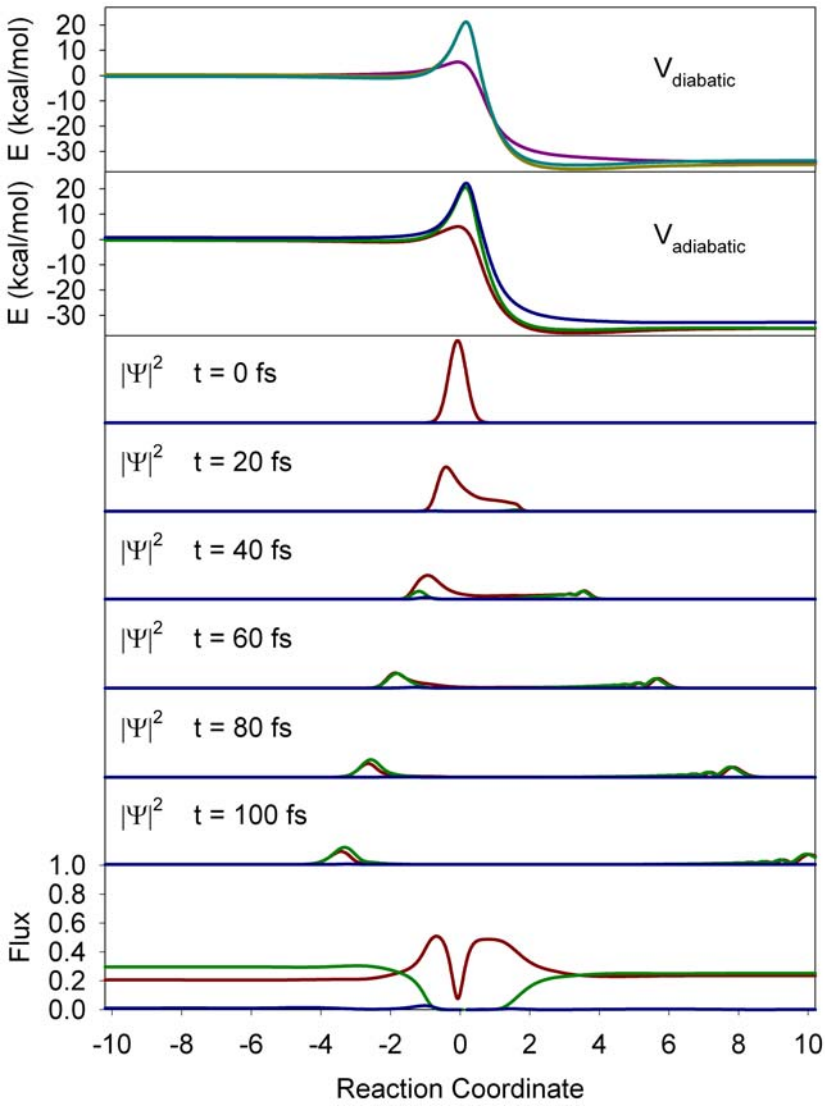

Figure 6.10: Sample results starting at the transition state (p=0 au, Δp=2 au) for multistate 1D wavepacket propagation along the F + HCl → HF + Cl reaction coordinate. The top panel displays adiabatic energies, the middle panels reveal snapshots of $|\Psi|^2$ out to 100 fs, and the bottom panel accounts for the total flux that passed by each point on each surface.

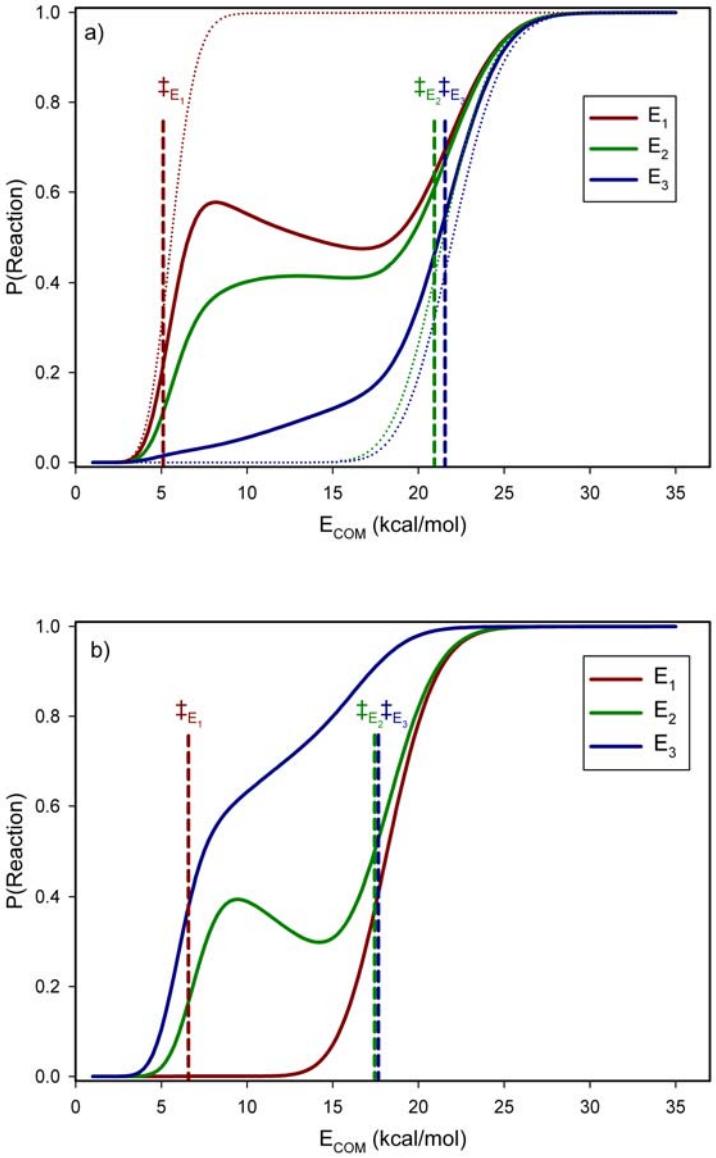

Figure 6.11: Reaction dynamics for ground F and spin-orbit excited F* as a function of energy. a) Reaction probability of F and F* along the reaction path (solid lines), with dotted lines representing probability if non-adiabatic coupling is set to 0. b) Reaction probability of F and F* along a 2D reaction path with θ constrained to be 180°. The dramatically increased reactivity of F* vs F results from the presence of conical intersection seams sampled at collinear geometries.

References

[1] K. Stark and H. J. Werner, J. Chem. Phys. **104**, 6515 (1996).

[2] M. Hayes, M. Gustafsson, A. M. Mebel, and R. T. Skodje, Chem. Phys. **308**, 259 (2005).

[3] Y. R. Tzeng and M. H. Alexander, J. Chem. Phys. **121**, 5812 (2004).

[4] Y. Zhang, T. X. Xie, K. L. Han, and J. Z. H. Zhang, J. Chem. Phys. **119**, 12921 (2003).

[5] S. D. Chao and R. T. Skodje, J. Chem. Phys. **113**, 3487 (2000).

[6] M. H. Alexander, H. J. Werner, and D. E. Manolopoulos, J. Chem. Phys. **109**, 5710 (1998).

[7] F. J. Aoiz, L. Banares, B. MartinezHaya, J. F. Castillo, D. E. Manolopoulos, K. Stark, and H. J. Werner, J. Phys. Chem. A **101**, 6403 (1997).

[8] J. F. Castillo, D. E. Manolopoulos, K. Stark, and H. J. Werner, J. Chem. Phys. **104**, 6531 (1996).

[9] S. A. Nizkorodov, W. W. Harper, W. B. Chapman, B. W. Blackmon, and D. J. Nesbitt, J. Chem. Phys. **111**, 8404 (1999).

[10] S. A. Nizkorodov, W. W. Harper, and D. J. Nesbitt, Faraday Disc. **113**, 107 (1999).

[11] W. B. Chapman, B. W. Blackmon, S. Nizkorodov, and D. J. Nesbitt, J. Chem. Phys. **109**, 9306 (1998).

[12] W. B. Chapman, B. W. Blackmon, and D. J. Nesbitt, J. Chem. Phys. **107**, 8193 (1997).

[13] M. Baer, M. Faubel, B. Martinez-Haya, L. Rusin, U. Tappe, and J. P. Toennies, J. Chem. Phys. **110**, 10231 (1999).

[14] M. Baer, M. Faubel, B. Martinez-Haya, L. Y. Rusin, U. Tappe, and J. P. Toennies, J. Chem. Phys. **108**, 9694 (1998).

[15] L. Y. Rusin and J. P. Toennies, Phys. Chem. Chem. Phys. **2**, 501 (2000).

[16] G. Dharmasena, K. Copeland, J. H. Young, R. A. Lasell, T. R. Phillips, G. A. Parker, and M. Keil, J. Phys. Chem. A **101**, 6429 (1997).

[17] G. Dharmasena, T. R. Phillips, K. N. Shokhirev, G. A. Parker, and M. Keil, J. Chem. Phys. **106**, 9950 (1997).

[18] M. Faubel, L. Rusin, S. Schlemmer, F. Sondermann, U. Tappe, and J. P. Toennies, J. Chem. Phys. **101**, 2106 (1994).

[19] D. M. Neumark, A. M. Wodtke, G. N. Robinson, C. C. Hayden, and Y. T. Lee, J. Chem. Phys. **82**, 3045 (1985).

[20] D. M. Neumark, A. M. Wodtke, G. N. Robinson, C. C. Hayden, K. Shobatake, R. K. Sparks, T. P. Schafer, and Y. T. Lee, J. Chem. Phys. **82**, 3067 (1985).

[21] H. Kornweitz and A. Persky, J. Phys. Chem. A **108**, 8599 (2004).

[22] Y. R. Tzeng and M. H. Alexander, J. Chem. Phys. **121**, 5183 (2004).

[23] Y. R. Tzeng and M. Alexander, Phys. Chem. Chem. Phys. **6**, 5018 (2004).

[24] Y. Zhang, T. X. Xie, K. L. Han, and J. Z. H. Zhang, J. Chem. Phys. **120**, 6000 (2004).

[25] T. X. Xie, Y. Zhang, M. Y. Zhao, and K. L. Han, Phys. Chem. Chem. Phys. **5**, 2034 (2003).

[26] S. C. Althorpe, J. Phys. Chem. A **107**, 7152 (2003).

[27] S. C. Althorpe, Chem. Phys. Lett. **370**, 443 (2003).

[28] S. H. Lee, F. Dong, and K. P. Liu, J. Chem. Phys. **116**, 7839 (2002).

[29] K. P. Liu, Nuc. Phys. A **684**, 247C (2001).

[30] R. T. Skodje, D. Skouteris, D. E. Manolopoulos, S. H. Lee, F. Dong, and K. P. Liu, Phys. Rev. Lett. **85**, 1206 (2000).

[31] R. T. Skodje, D. Skouteris, D. E. Manolopoulos, S. H. Lee, F. Dong, and K. Liu, J. Chem. Phys. **112**, 4536 (2000).

[32] W. W. Harper, S. A. Nizkorodov, and D. J. Nesbitt, J. Chem. Phys. **116**, 5622 (2002).

[33] A. M. G. Ding, L. J. Kirsch, D. S. Perry, J. C. Polanyi, and J. L. Schreiber, Faraday Disc. Chem. Soc. **55**, 252 (1973).

[34] R. Sayos, J. Hernando, R. Francia, and M. Gonzalez, Phys. Chem. Chem. Phys. **2**, 523 (2000).

[35] B. Y. Tang, B. H. Yang, K. L. Han, R. Q. Zhang, and J. Z. H. Zhang, J. Chem. Phys. **113**, 10105 (2000).

[36] R. Sayos, J. Hernando, J. Hijazo, and M. Gonzalez, Phys. Chem. Chem. Phys. **1**, 947 (1999).

[37] H. Kornweitz and A. Persky, J. Phys. Chem. A **108**, 140 (2004).

[38] M. P. Deskevich, M. Y. Hayes, K. Takahashi, R. T. Skodje, and D. J. Nesbitt, Journal Of Chemical Physics **124**, (2006).

[39] M. Ziemkiewicz, M. Wojcik, and D. J. Nesbitt, J. Chem. Phys. **123**, 224307 (2005).

[40] M. P. Deskevich, D. J. Nesbitt, and H. J. Werner, J. Chem. Phys. **120**, 7281 (2004).

[41] H. J. Werner and P. J. Knowles, J. Chem. Phys. **89**, 5803 (1988).

[42] P. J. Knowles and H. J. Werner, Chem. Phys. Lett. **145**, 514 (1988).

[43] P. J. Knowles and H. J. Werner, Theoretica Chimica Acta **84**, 95 (1992).

[44] K. A. Peterson, D. E. Woon, and T. H. Dunning, J. Chem. Phys. **100**, 7410 (1994).

[45] F. B. Brown and D. G. Truhlar, Chem. Phys. Lett. **117**, 307 (1985).

[46] B. Ramachandran and K. A. Peterson, J. Chem. Phys. **119**, 9590 (2003).

[47] M. Meuwly and J. M. Hutson, J. Chem. Phys. **119**, 8873 (2003).

[48] M. L. Dubernet and J. M. Hutson, J. Chem. Phys. **101**, 1939 (1994).

[49] M. L. Dubernet and J. M. Hutson, J. Phys. Chem. **98**, 5844 (1994).

[50] H.-J. Werner, P. J. Knowles, R. Lindh, M. Schutz, P. Celani, T. Korona, F. R. Manby, G. Rauhut, R. D. Amos, A. Bernhardsson, A. Berning, D. L. Cooper, M. J. O. Deegan, A. J. Dobbyn, F. Eckert, C. Hampel, G. Hetzer, A. W. Lloyd, S. J. McNicholas, W. Meyer, M. E. Mura, A. Nicklass, P. Palmieri, R. Pitzer, U. Schumann, H. Stoll, A. J. Stone, R. Tarroni, and T. Thorsteinsson, Molpro, version 2002.6, a package of ab initio programs (see http://www.Molpro.Net) (Birmingham, UK, 2003).

[51] D. E. Woon and T. H. Dunning, J. Chem. Phys. **98**, 1358 (1993).

[52] T. H. Dunning, J. Chem. Phys. **90**, 1007 (1989).

[53] R. A. Kendall, T. H. Dunning, and R. J. Harrison, J. Chem. Phys. **96**, 6796 (1992).

[54] L. M. Cheung, K. R. Sundberg, and K. Ruedenberg, Int. J. Quantum Chem. **16**, 1103 (1979).

[55] A. Berning, M. Schweizer, H. J. Werner, P. J. Knowles, and P. Palmieri, Molecular Physics **98**, 1823 (2000).

[56] A. J. Dobbyn, J. N. L. Connor, N. A. Besley, P. J. Knowles, and G. C. Schatz, Physical Chemistry Chemical Physics957.

[57] M. H. Alexander, J. Chem. Phys. **99**, 6014 (1993).

[58] H. J. Werner and W. Meyer, J. Chem. Phys. **74**, 5802 (1981).

[59] H. J. Werner, B. Follmeg, and M. H. Alexander, J. Chem. Phys. **89**, 3139 (1988).

[60] D. Simah, B. Hartke, and H. J. Werner, J. Chem. Phys. **111**, 4523 (1999).

[61] M. H. Alexander, D. E. Manolopoulos, and H. J. Werner, J. Chem. Phys. **113**, 11084 (2000).

[62] A. Berning, M. Schweizer, H. J. Werner, P. J. Knowles, and P. Palmieri, Molecular Physics **98**, 1823 (2000).

[63] See epaps document no xxx for a complete listing of the functional form and least squares coefficients for the pes. This document can be reached via a direct link in the online article's htms reference section or via the epaps homepage (http://www.Aip.Org/pubservs/epaps.Html)

[64] A. Aguado, C. Tablero, and M. Paniagua, Comput. Phys. Comm. **108**, 259 (1998).

[65] M. S. Child, *Molecular collision theory*. (Academic Press, New York, 1974).

[66] D. Kosloff and R. Kosloff, Journal Of Computational Physics **52**, 35 (1983).

[67] H. Talezer and R. Kosloff, Journal Of Chemical Physics **81**, 3967 (1984).

[68] J. R. Fair, D. Schaefer, R. Kosloff, and D. J. Nesbitt, J. Chem. Phys. **116**, 1406 (2002).

[69] D. J. Rush and K. B. Wiberg, Journal Of Physical Chemistry A **101**, 3143 (1997).

[70] V. A. Mandelshtam and H. S. Taylor, Journal Of Chemical Physics **103**, 2903 (1995).

[71] V. A. Mandelshtam and H. S. Taylor, Journal Of Chemical Physics **102**, 7390 (1995).

[72] R. N. Zare, *Angular momentum*. (John Wiley & Sons, New York, 1988).

[73] M. Tinkham, *Group theory and quantum mechanics*. (McGraw-Hill, New York, 1964).